Uniaxial Stress Effects in Zincblende and Wurtzite GaAs Nanowires: an Optical Spectroscopy Study

Inauguraldissertation

zur
Erlangung der Würde eines Doktors der Philosophie
vorgelegt der
Philosophisch-Naturwissenschaftlichen Fakultät
der Universität Basel

von

Giorgio Signorello
von Palermo (Italien)

UNI
BASEL

Basel, 2014

Genehmigt von der Philosophisch-Naturwissenschaftlichen Fakultät
auf Antrag von
Prof. Dr. C. Schönenberger
Dr. H. Riel
Prof. Dr. A. Fontcuberta i Morral
Prof. Dr. L. Samuelson

Basel, den 17. September 2013

Prof. Dr. Jörg Schibler
Dekan

“When it is dark enough,
you can see the stars.”

Ralph Waldo Emerson

Summary

To tackle two of the biggest challenges that the semiconductor industry faces today, i.e. the future of CMOS scaling and the limits in bandwidth and energy of the current technology of interconnects, the semiconductor industry is shifting its focus towards nonplanar nanoscale structures, the introduction of novel materials and strain engineering. Inspired by these developments, we have explored the synergistic interplay of strain effects in III-V nanoscale devices. GaAs was chosen as the ideal material system to study: zincblende GaAs is the material that enabled the first solid-state lasers and light-emitting devices and, in the nanowire form, promises exceptional mechanics and a large range of elastic deformation. When grown at nanoscale dimensions, novel crystal structures such as wurtzite can be synthesized, and new degrees of freedom to tailor electronic and optoelectonic properties become available.

We have shown that by tuning the strain continuously, from tension to compression and up to 3.5 %, the photoluminescence (PL) of zincblende GaAs nanowires can be red-shifted by 290 meV. We have observed a much more pronounced PL shift in tension than in compression in these nanowires and have attributed this phenomenon to the different symmetry character of the top valence band: heavy hole under tension, light hole under compression. Fingerprints of symmetry breaking due to the anisotropic nature of the nanowire deformation were found also in the Raman spectra, which allowed the unambiguous identification of distinct phonon contributions. Because of the linear relation with stress, the energy shift of the Raman peaks were used to determine the axial strain induced in the nanowire and to infer information about the Poisson ratio in the [111] direction (0.16±0.04). To test the consistency of the $k \cdot p$ model with the measurement, we extracted the band-edge deformation potentials ($a = -8.6\,\mathrm{eV} \pm 0.7\,\mathrm{eV}$ as well as $d = -5.2\,\mathrm{eV} \pm 0.7\,\mathrm{eV}$), which are consistent with those of bulk GaAs and with our initial assumptions.

Even larger shifts of the PL could be demonstrated in wurtzite nanowires. We showed a remarkable energy shift of the PL due to transitions between the bright conduction band and the heavy-hole band (345 meV) or the light-hole band (257 meV), by varying the strain over a range of 2 %. For the first time, we demonstrated that uniaxial stress can be used to induce a transition

on the band structure from a direct bandgap to a pseudodirect bandgap configuration. In the latter configuration, the relation between energy and the wave-vector is indistinguishable from that of direct bandgap materials: the conduction band minimum and the valence band maximum are located at the Γ-point and the respective wavefunctions overlap strongly in the wave-vector space. However, because of symmetry reasons, the optical dipole transitions between these states occur with low probability and the material is a poor light emitter, like indirect bandgap materials. Leveraging the strain degree of freedom, both direct and pseudodirect bandgap configurations can be achieved on wurtzite GaAs nanowires: when tensile stress is applied, the direct configuration can be obtained and the nanowires emit light efficiently; upon compression, the pseudodirect configuration is achieved and light emission can be suppressed by more than three orders of magnitude. The splitting between the dark and bright conduction bands could be tuned continuously over a range of more than 230 meV. Using the Raman scattering spectra as relative strain gauge and fitting the optical transition energies to a $k \cdot p$ model, we were able to determine all band-structure parameters of the wurtzite GaAs nanowire in unstrained conditions, i.e. the crystal field (197 meV±50 meV) and spin-orbit splitting (293 meV±129 meV), the bandgap (1.41 eV±8 meV) and, for the first time, the splitting between the bright and the dark conduction bands (33 meV±47 meV). The Poisson ratio along the c-axis (0.17±0.17) and the phonon deformation potentials of the GaAs and AlGaAs optical phonons have also been determined.

This body of results constitutes a solid foundation for understanding strain effects on the optical and electronic properties of III-V nanowires. Their implications promise to have high technological relevance, being at the foundation of a new generation of functional strain devices.

Contents

1

Introduction

“There are those who look at things the way they are,
and ask why...
I dream of things that never were,
and ask why not?”

Robert Kennedy

In the past 35 years, the scaling of metal-oxide-semiconductor field effect transistors (MOSFETs)[1] has powered the information technology revolution, enabling to double the device density, lowering cost per function and increasing the computational performance of integrated circuits every two to three years. As the device dimensions, i.e. the technology node, shrink below 100 nm, new physical phenomena start to interfere with traditional scaling laws[2]. The gate fails to control the charge carrier density at the semiconductor-dielectric interface (short-channel effect). Charge carriers interact increasingly more with the ionic lattice causing a velocity saturation. Leakage currents from the gate to the channel increase with ever thinner oxide thicknesses. Dielectric breakdown lowers the maximum voltage applicable across the gate oxide of the transistor.

To overcome such performance limitations and deliver the MOSFET performance increase, a combination of different strategies has been proposed: strain engineering, novel materials and novel device structures. Strain engineering has been the dominant method to deliver enhanced MOSFET performance during the last decade, offering a low-cost and low-risk solution and maintaining the traditional fabrication processes[3–8]. Strain has been a topic of interest in semiconductor research since 1950. Three years after the demonstration of the first point-contact transistor, John Bardeen and William Shockley developed the deformation potential theory to model the coupling between acoustic waves and electrons in solids[9]. With subsequent developments[10,11], such theory allowed to correctly predict physical effects like the increase in carrier velocity due to band warping, or the lower interband scattering due to the band degeneracy lifting[12]. The introduction of novel channel materials has also been explored as a method to increase the transistor performance. For example, III-V alloys offer electron mobilities higher than silicon up to 10 times, exceptionally high charge carrier velocities and outstanding frequency response. To improve the electrostatic control over the transistor channel with decreasing device dimensions, novel device structures have also been proposed. The industry is following a clear trend, moving away from planar device structures towards fins and nanowire channel devices with wrapped around gates. The effect of quantization is also expected to play a dominant role to obtain injection velocities significantly greater than bulk[13,14].

Elaborating and implementing strategies to permit the scaling of MOSFETs is not the only concern of the semiconductor industry. Since the power dissipated in electrical interconnects is rising above 80 % of the total energy used in the chip and the amount of heat that can be removed from each chip is saturating, there is a strong interest to develop new ideas around the distribution of information on and between integrated circuits. Integrating photonics on chip offers solutions to face these challenging power limits[15,16]. The integration of key photonic components, like p-i-n and avalanche photo-detectors or optical modulators, has been demonstrated using indirect bandgap semiconductors employed in traditional fabrication processes[17–20]. On the other end, the integration of a light source on silicon presents bigger challenges which can be tackled, once more, by using a combination of strain engineering, novel materials and nanostructured devices.

Strain engineering enabled to control and enhance the performance of III-V based optoelectronic devices. By modifying the energy bandgap, the valence and conduction band density of states, and the electronic wavefunction, strain made possible to tune the wavelength of emission[21], reduce the threshold current[22,23], suppress the Auger recombination[24] and intervalence band absorption processes[25], control the polarization[26], and improve the overall efficiency of solid state lasers[27]. More recently, high anisotropic strain has been used to achieve a direct bandgap configuration in germanium[28–30], enabling the integration of a light source based on traditional group IV materials directly on silicon[31,32].

The nanowire geometry allows a direct integration of III-V materials on silicon[33–35] and offers a broader parameter space and opportunities to explore. Because of the small cross-section dimension of a nanowire, the mismatch of lattice constant and thermal expansion coefficient have a reduced impact on the crystal growth and quality. Increasing efforts in understanding the bottom-up growth of these structures[36–38] enabled unprecedented control over the morphology[39–44] and crystal structures[45,46] and alloy composition[47–50], leading to the synthesis of materials not available in bulk form, with novel optical properties[51,52]. The scope of nanowire research has also expanded beyond the above mentioned technological applications, enabling the realization of individually addressable entangled single photons sources[53–57], state-of-the-art photo-detectors[58–60] with single photon sensitivity[61], and found application in energy harvesting and photovoltaics[62–69].

Studying strain effects on novel III-V nanowires and nanostructured materials is therefore essential for the future information and communication technologies, having a strong influence on the future of MOSFET scaling and enabling on-chip optical communication. The impact of the discoveries generated by this research has a potentially broader range of influence, scientifically and technologically.

This thesis is devoted to studying uniaxial stress effects on GaAs nanowires. We chose this material as a model system for solid state light-emitting applications and focused our attention to experiments where a combination of nanoscale dimensions, novel materials and strain have a synergistic interplay. Recent theoretical calculations and experiments have highlighted that GaAs Zincblende nanowires exhibit enhanced mechanical properties and very high elastic range of deformation[70–73], which are a necessary requirement for enhanced effects on the band structure and on the optical and electronic properties. GaAs nanowires can also be grown with novel crystal structures, i.e. Wurtzite GaAs, not available in bulk or thin film form: the electronic bandstructure of this material is still highly controversial. We will show how uniaxial stress experiments can be used to disentangle and provide a clearer picture of the bandstructure.

The chapters 2 to 4 provide a concise but self-contained theoretical background, describing the concepts of mechanics and solid state physics that are needed to fully appreciate the experimental work. The chapters 5 to 8 are dedicated to the description of the instrumentation used, of the measurements performed, and to the physical interpretation and discussion of the results.

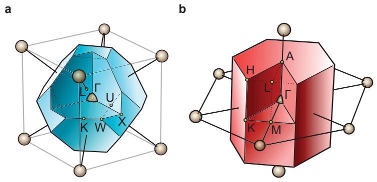

Chapter 2

We provide a general description of GaAs Zincblende and Wurtzite crystals. We describe their crystal structure, show the differences between their Brillouin zones, illustrate their bulk electronic band structure and dedicate special attention to the band states in proximity of the Γ-point. Finally we provide a description of the vibrational spectrum, showing the phonon dispersion relations and describing the corresponding geometries of atomic displacement.

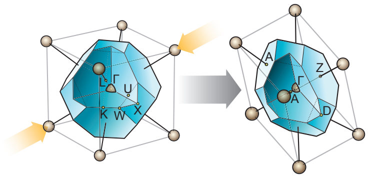

Chapter 3

The effects of strain on the band structure and lattice dynamics are treated here. We provide the basic definitions of stress, strain, compliance and stiffness tensors, derive the expression of the strain tensor upon uniaxial stress and decompose it into isotropic and deviatoric components. We describe the effect of strain on the conduction and valence band states using a $k \cdot p$ model, and on energy of the optical phonons using the deformation potential theory.

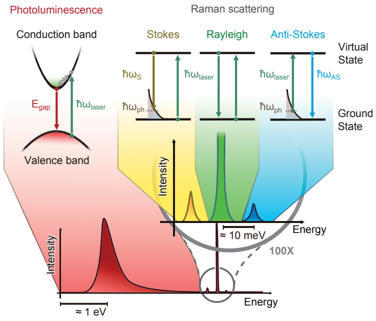

Chapter 4

We explain how strain effects can be observed experimentally using optical spectroscopy. We show how to model the photoluminescence lineshape and how to extract bandstructure parameters and other observables. We give a classical description of the Raman scattering process and show how to isolate the contribution of phonons with different symmetry using the polarization dependence of the Raman selection rules.

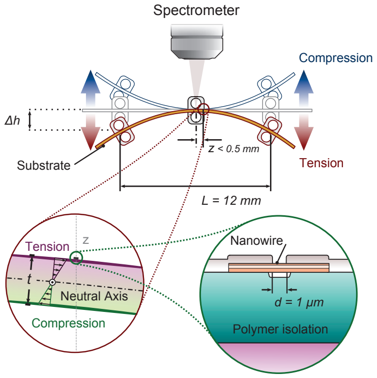

Chapter 5

The methods and the procedures used to perform the experiments are described here. We briefly summarize the methods used to grow Zincblende and Wurtzite nanowires, describe the steps used and highlight the challenges that were overcome to fabricate the nanowire strain devices. A brief description of the strain mechanism is given, followed by the analysis of the optical spectroscopy setup. We conclude the chapter with a summary of the nanoscale size effects that are expected for the particular nanowires employed in our experiment.

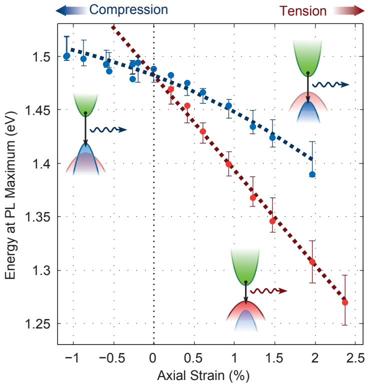

Chapter 6

The strain effects on Zincblende GaAs nanowires are studied: we demonstrate remarkable shifts of the energy bandgap by polarized photoluminescence measurements, explain how Raman spectroscopy can be used to fully characterize the strain tensor and the nanowire mechanical properties and provide a consistency check of our analysis by calculating the band edge deformation potentials of the nanowire. Finally we show the maximum strain and photoluminescence shift that can be obtained in such nanowire structures.

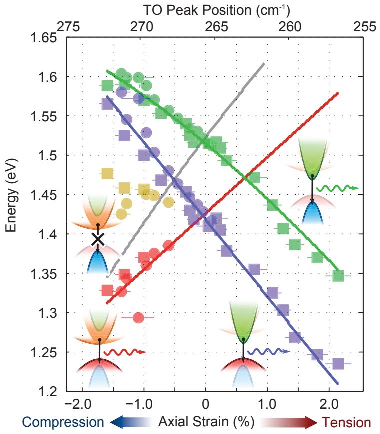

Chapter 7

The effect of strain on a Wurtzite GaAs nanowire is studied by photoluminescence and Raman spectroscopy: we show that uniaxial stress can cause a reversible quenching of the photoluminescence, which has been assigned to a direct-to-pseudodirect bandgap transition. By analyzing the results with a theoretical model, we could clarify the band structure of these crystals and resolve a controversial discussion about the energy and symmetry of the valence and conduction band states. Mechanical properties and phonon deformation potentials of the nanowire are also determined.

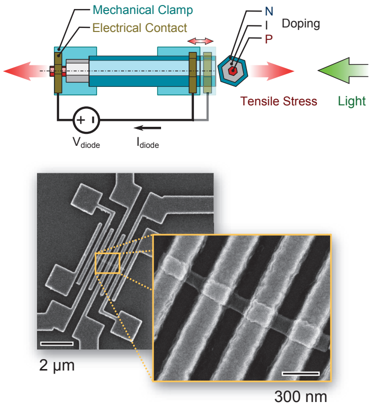

Chapter 8

We conclude this thesis summarizing our initial goals and the technical challenges that had to be overcome, providing an overview of the results of Zincblende and Wurtzite nanowires, and comparing them to each others. Finally we describe our vision of a new generation of devices which leverage the strain degree of freedom to achieve novel functionalities.

2

Electronic and Vibrational Properties of Zincblende and Wurtzite GaAs

This chapter provides the fundamentals concepts about the crystal structure and physical properties of Zincblende and Wurtzite crystals. We will describe the electronic bandstructure, the energy and atomic displacement of the optical phonons of these III-V crystals.

2.1 Crystal Structure

The structure of Zincblende and Wurtzite crystals can be defined using two different Bravais lattices and basis sets of atoms per unit cell. The Zincblende structure is constructed with the face centered cubic (FCC) lattice and a base set of two atoms, one of the group III, like Gallium (Ga), and one of the group V, like Arsenic (As). One lattice parameter a, i.e. the length of the edge of the cube, is needed to define the FCC lattice. The Wurtzite structure is created instead with a base set of four atoms associated to an hexagonal lattice, which is completely specified by the length of the edge of the hexagon a and the height of the parallelepiped c. The unit cells of Zincblende and Wurtzite crystals are represented in figure 2.1 and discussed with further detail in appendix A.

Even if appearing different at first sight, the two crystal structures have very much in common. In both structures every atom of group III is located

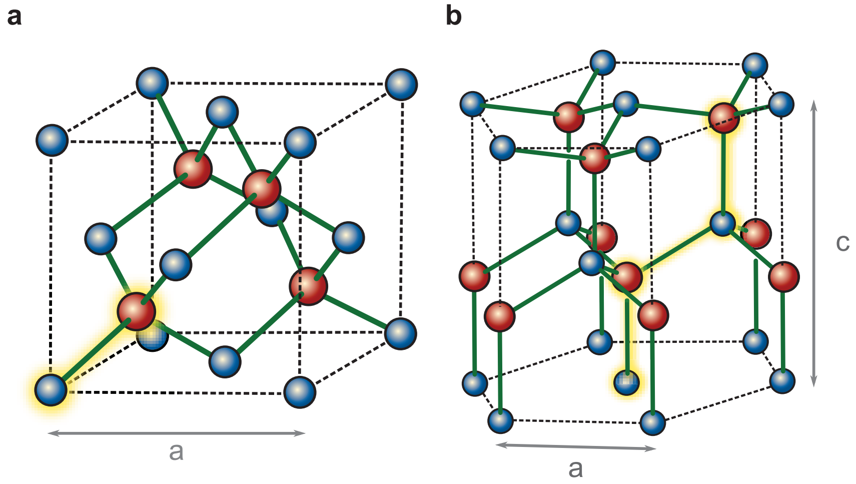

Figure 2.1: Unit cells of Zincblende (a) and Wurtzite (b) crystals. Atoms of the group III and V are shown in red and blue, respectively. The atoms constituting the base set are highlighted in yellow.

at the center of a regular tetrahedron, forming bonds with four atoms of the group V. The similarity between the two structures becomes even more evident if one rotates the Zincblende unit cell, orienting the z-axis parallel to the cubic [111] direction, and the x-axis and y-axis along [110] and $[11\bar{2}]$: both crystals are formed by stacking triangular lattices formed by the coordination tetrahedra on top of each others. Birmann highlighted that one can leverage such similarity and generate the Zincblende crystal shown in figure 2.2, using a basis containing six atoms and an hexagonal lattice, like in the Wurtzite case[74,75]. This definition highlights that the only difference between the two crystal structures resides on the sequence of stacking of tetrahedral planes, which is ABCABC for Zincblende and ABABAB for Wurtzite.

2.2 Electronic Band Structure

The Schrödinger equation that describes the dynamics of electrons and nuclei of Zincblende and Wurtzite semiconductors constitutes a very complex many-body problem and simplified solutions can be obtained only by using a number of assumptions. The valence electrons can be considered separately from the ionic lattice, constituted by the nuclei and the core electrons. Under the adiabatic approximation, the valence electrons experience only the potential generated by the static ionic lattice. With the mean field approximation, all valence electrons experience the same average potential

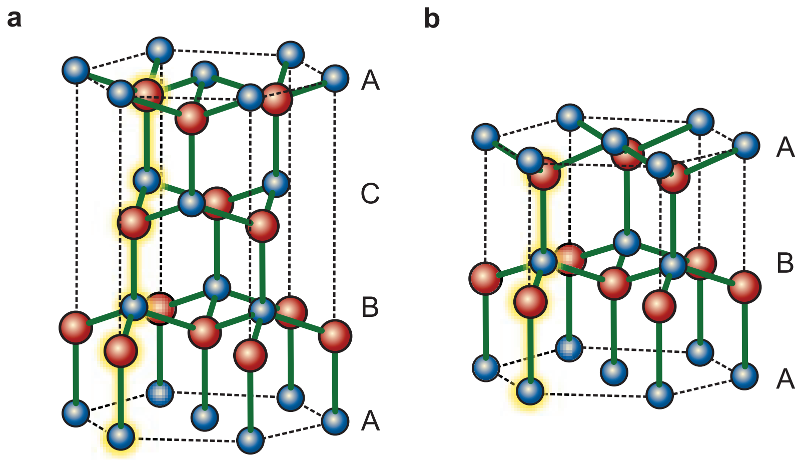

Figure 2.2: Defining the Zincblende crystal structure with the Birmann unit cell (a) highlights its similarity with the Wurtzite structure (b). In both structures, the base set is highlighted in yellow.

$V(\mathbf{r})$ generated by the ionic lattice and by the remaining valence electrons. Within these assumptions the Schrödinger equation for each single electron can be rewritten as[76]:

$$\mathscr{H}_{1e}\Phi_n(\mathbf{r}) = \left(\frac{p^2}{2m} + V(\mathbf{r})\right)\Phi_n(\mathbf{r}) = E_n\Phi_n(\mathbf{r}) \,, \tag{2.1}$$

where $\mathscr{H}_{1e}$ is the one-electron Hamiltonian while $\Phi_n(r)$ and E_n denote the wave-function and energy of an electron in the eigenstate n, which can only accommodate two electrons with opposite spin.

The mean-field potential $V(\mathbf{r})$ will have the translational symmetry of the crystal itself and the electron wave-functions can be written as the sum of plane waves, with wave-vector $\mathbf{k}$, times an envelope function $\psi_{n\mathbf{k}}(\mathbf{r})$ that has the same periodicity as the crystal:

$$\Phi_n(\mathbf{r}) = \sum_{\mathbf{k}} \psi_{n\mathbf{k}}(\mathbf{r})\, e^{i\mathbf{k}\cdot\mathbf{r}} \,. \tag{2.2}$$

The periodic solutions and the energy spectrum E_n can be defined within a finite region of wave-vector space $\mathbf{k}$, with the symmetry of the reciprocal lattice, i.e. the Brillouin zone.

Figure 2.3 shows the reciprocal lattice and Brillouin zones for a FCC lattice (a) and for an hexagonal lattice (b): the high symmetry points at the surface are marked with capital latin letters, while the center is indicated in both structures with the greek letter Γ. Using these definitions, it is possible

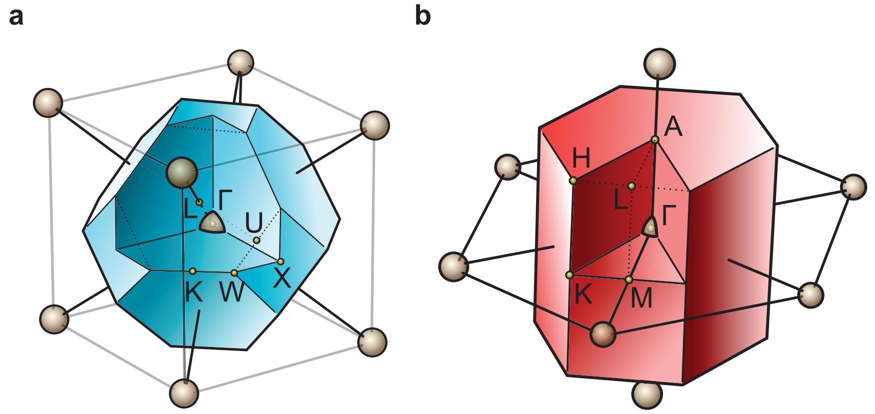

Figure 2.3: Brillouin zones for (a) Zincblende and (b) Wurtzite crystals.

to represent the dependence of $E_n(\mathbf{k})$ on the wave-vector along lines that connect high symmetry points within the Brillouin zone.

2.2.1 Band Structure of Zincblende GaAs

Density Functional Theory (DFT) can be used to calculate the energy-momentum relation of Zincblende GaAs[77]. The energy values along the high symmetry directions are shown in figure 2.4a. The energy levels that determine optical and electrical properties of the material are highlighted with a dashed line and magnified in a sketch in figure 2.3b.

The valence band states, i.e. the highest occupied electronic states, are characterized by quadratic relation between energy and wave-vector and one can describe them as free charged particle with modified "effective" mass. The two valence bands with the highest energy are degenerate at the Γ-point but have a different energy wave-vector relation: the heavy hole band is associated to an effective mass m_{hh} that, depending on the direction of the wave-vector, ranges between 0.33 m_e and 0.81 m_e [*]. The light hole band instead has overall a smaller effective mass m_{lh}, which ranges between 0.080 m_e and 0.094 m_e, depending on the wave-vector direction[78]. A third band, called split-off hole, has an almost isotropic effective mass $m_{\mathrm{so}} \approx 0.182\, m_e$ and is found at lower energy compared to the heavy hole and light hole states. This energy difference (340 meV) is a manifestation of the spin-orbit interaction, i.e. the interaction of the spin of the electron with its own angular momentum. The conduction band states, formed by the lowest unoccupied electronic states, also have a minimum energy at the Γ-point and parabolic energy wave-vector relation, with $m_{\mathrm{cb}} \approx 0.066\, m_e$. The

---

[*] m_e is the mass of a free electron.

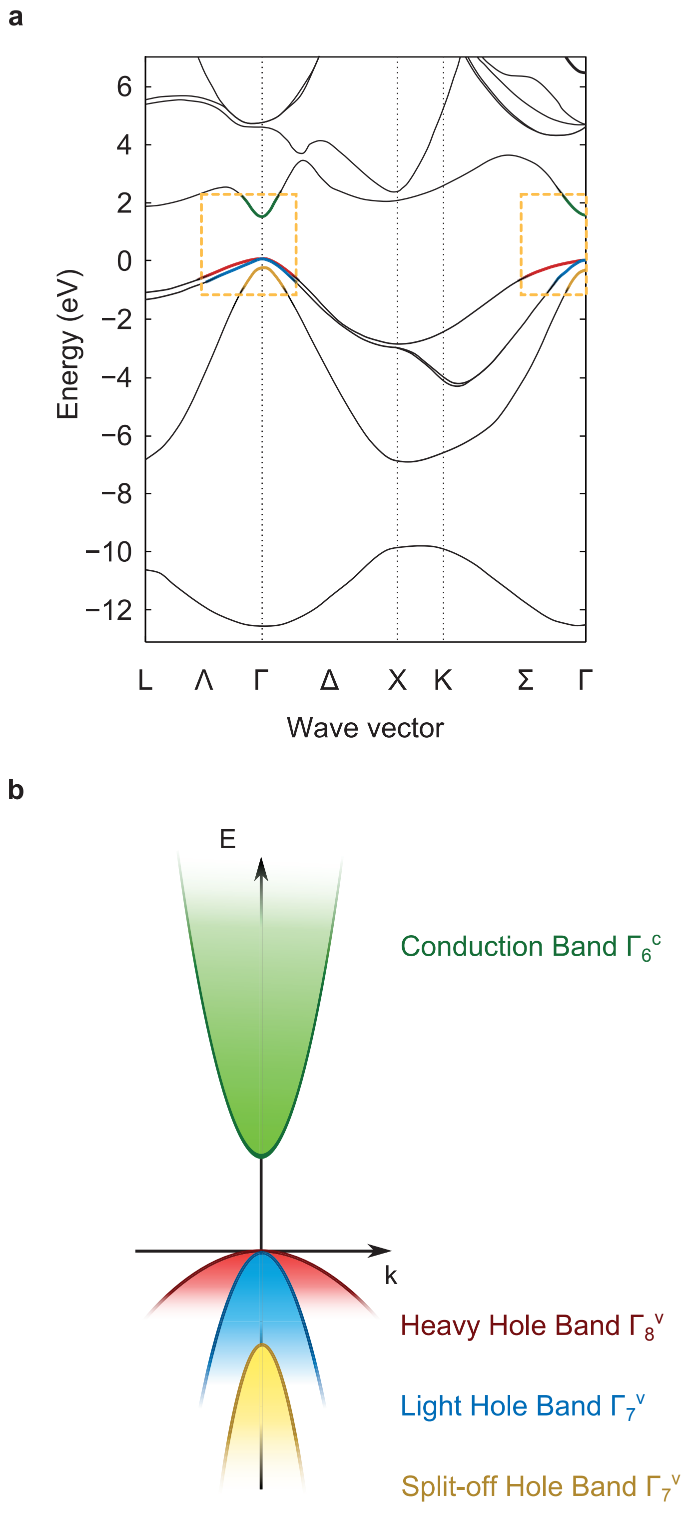

Figure 2.4: Bandstructure of Zincblende GaAs crystals. (a) *Ab-initio* calculation of the energy wave-vector relation, represented along high symmetry directions of the Brilluoin zone[76,77]. (b) Effective mass approximation and symmetry of the bands in proximity of the Γ-point.

energy difference between the conduction band minimum and the valence band maximum, i.e. the energy bandgap, depends strongly on the crystal temperature[79] and varies from 1.519 eV at few mK to 1.43 eV at 300 K in Zincblende GaAs. Other local conduction band minima are located at the L-point (1.71 eV at 300 K), and at the X-point (1.90 eV at 300 K).

2.2.2 Band Structure of Wurtzite GaAs

Unlike Zincblende GaAs, which has been extensively studied, the bandstructure of Wurtzite GaAs is still object of a lively discussion in the scientific community. Parameters like the energy bandgap, the energy difference between bright and dark conduction bands, the spin-orbit and crystal field splitting (which determine the energy difference between heavy-hole, light-hole and split-off holes) are still object of debate and of intense experimental and theoretical research. One of the outcome of this thesis is to provide, through strain measurements, a methodology to determine these parameters with higher accuracy.

The energy wave-vector relation $E_n(\mathbf{k})$ calculated for Wurtzite GaAs is shown in figure 2.5[80]. Since the Wurtzite unit cell has twice as many atoms compared to Zincblende, $E_n(\mathbf{k})$ has twice as many states per value of wave-vector $\mathbf{k}$. Like in Zincblende, the valence band states are also described by three bands with parabolic energy wave-vector relation. However, because of the lower symmetry compared to Zincblende, heavy and light hole states do not have the same energy at the Γ-point and are separated by $\approx$100 meV as predicted by several *ab-initio* calculations[80,81]. Unoccupied states are found with lowest energy at the Γ-point and form two bands, which are labeled as bright conduction band and dark conduction band for reasons that will be clear when discussing the optical transitions. While the bright conduction band is characterized by an almost isotropic effective mass $m_{\text{bright}} \approx 0.065\, m_e$, the dark conduction band is highly anisotropic: if the wave-vector is aligned parallel to the c-axis, from the Γ to the A-point of the Brilluoin zone, the effective mass is $m_{\text{dark},\parallel} \approx 1.06\, m_e$. This value is approximately ten times higher than $m_{\text{dark},\perp} \approx 0.11 m_e$, the value of effective mass in the directions orthogonal to the c-axis, from the Γ to the M-point[81]. Like in GaAs Zincblende, other local minima are present in the conduction band, at the L, M and A point.

We would like to emphasize here that, using the alternative definition of unit cell shown in §2.1, it is possible to describe Zincblende and Wurtzite crystals on the same Brillouin zone and establish exact relations between the electronic states of the two structures. While the electronic state found at the Γ-point are unaffected by the redefinition, two states found at the L-point of Zincblende are shown to “fold” back into the Γ-point of the new

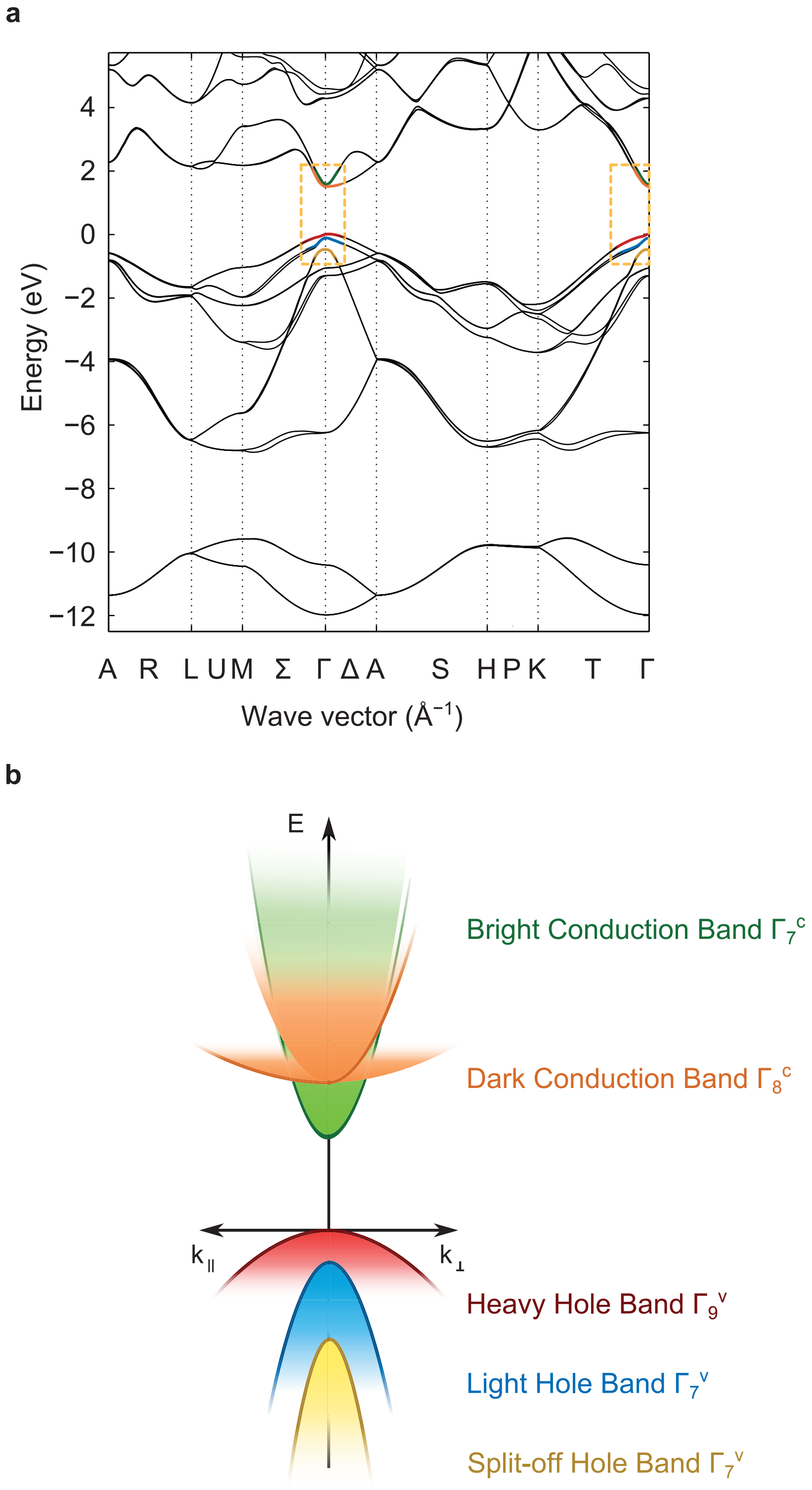

Figure 2.5: Bandstructure of Wurtzite GaAs crystals. (a) *Ab-initio* calculation of the Energy wave-vector relation represented along high symmetry directions of the Brillouin zone[80]. (b) Effective mass approximation and symmetry of the bands in proximity of the Γ-point.

unit cell. After such transformation, the relation between the conduction band states in Zincblende and Wurtzite is evident: the bright conduction band is related to the conduction band minimum found in Zincblende, while the dark conduction band is related to the minimum found in Zincblende at the L-point in the [111] direction.

2.3 Phonons and Vibrational Modes

We now shift our focus to the vibrational properties of Zincblende and Wurtzite GaAs crystals. To gather information about the lattice dynamics of a generic crystal we need to go back and consider the Hamiltonian of the crystal. We have explained in §2.2 how to separate it into an electronic and an ionic lattice part, to get simplified solution of the electronic bandstructure.

In the adiabatic approximation, the Hamiltonian of the ionic lattice $\mathscr{H}_{\text{ion}}$ can be expressed as a function of the electric field in the crystal and of the atomic displacements from the equilibrium position[82]. We can identify with $\xi_\alpha\binom{l}{k}$ the component α of the atomic displacement ξ of the of the atoms k in the unit cell l. For simplicity, we will consider the ideal case of an infinite lattice and allow $l = (l_1, l_2, l_3)$ to assume any integer value. The label k instead will have a finite number of values, to cover the n atoms of the unit cell. Finally, we indicate with E_μ the component μ and of the electric field vector $\mathbf{E}$. Since the equilibrium position is going to be a minimum in energy, the Hamiltonian can be approximated with a quadratic function of E_μ and $\xi_\alpha\binom{l}{k}$ and assume the following expression (in the Einstein tensor notation, discussed in §B.2):

$$\mathscr{H}_{\text{ion}} = \mathscr{H}_{\text{ion}}^{(0)} + \frac{1}{2} m_k \dot{\xi}_\alpha\binom{l}{k}\dot{\xi}_\alpha\binom{l}{k} + \frac{1}{2}\Phi_{\alpha\beta}\binom{l\,l'}{k\,k'}\xi_\alpha\binom{l}{k}\xi_\beta\binom{l'}{k'} - \\ - M_{\mu\alpha}\binom{l}{k}\xi_\alpha\binom{l}{k}E_\mu - \frac{1}{2}A_{\mu\nu}^{(0)}E_\mu E_\nu \; . \tag{2.3}$$

The first term, $\mathscr{H}_{\text{ion}}^{(0)}$, represents the energy of the lattice in the equilibrium configuration. The second term of the Hamiltonian represents the kinetic energy due to the lattice oscillations, i.e. the variation in time of the displacements ξ_α of the atoms k, with mass m_k, across the unit cells l. The third term of the Hamiltoninan represents a purely elastic contribution to the potential energy and $\Phi_{\alpha\beta}\binom{l\,l'}{k\,k'}$ represent the force constant between the atom k of the unite cell l and the atom k' of the unit cell l'. The dipole moment term $M_{\mu\alpha}\binom{l}{k}$ represents the component α of the force acting on the atom in position $\binom{l}{k}$ because of the presence of a component in direction μ

of the electric field $\mathbf{E}$. The polarizability term $A^{(0)}_{\mu\nu}$ represents the energy due to the polarization of the lattice under the electric field $\mathbf{E}$.

By differentiating the potential energy term against the atomic displacement $\xi_\alpha\binom{l}{k}$, we can get the equations of dynamics of the crystal lattice:

$$m_k\ddot{\xi}_\alpha\binom{l}{k} = \Phi_{\alpha\beta}\binom{l\,l'}{k\,k'}\xi_\beta\binom{l'}{k'} - M_{\mu\alpha}\binom{l}{k}E_\mu \,. \tag{2.4}$$

To obtain information about the lattice dynamics, we have to solve the system of equation (2.4). We can drammatically reduce the complexity of this system, by considering plane wave solutions and by noticing that $\Phi_{\alpha\beta}\binom{l\,l'}{k\,k'}$ and $M_{\mu\alpha}\binom{l}{k}$ posses the same translational symmetry properties of the crystal. As in the case of for the Bloch theorem, we can look for solutions to the lattice dynamics problem that have plane wave form:

$$\xi_\alpha\binom{l}{k} = \frac{1}{\sqrt{m_k}} w_\alpha(k) e^{i\left[2\pi\mathbf{q}\cdot\mathbf{x}\binom{l}{k}-\omega t\right]} \,, \tag{2.5}$$

where the wave-vector $\mathbf{q}$ is defined within the Brillouin zone. For each value of wave-vector $\mathbf{q}$ in the Brilluoin zone, the lattice dynamics problem will return as many vibration energies as degrees of freedom in the unit cell.

These solutions can be divided in two groups, i.e. acoustic and optical vibrational modes. The acoustic modes are characterized by atomic displacements that displace the center of mass of the unit cell, keeping the unit cell undeformed. There can only be three of such kind of vibration modes, one per degree of freedom that defines the position of the unit cell. The corresponding dispersion relation follows a liner dependence on the wave vector $\mathbf{q}$ and, in proximity of the Γ-point, will have negligible angular frequency ω. The remaining $3n-3$ optical vibrational modes are characterized by atomic displacements that preserve the position of the center of mass of the unit cell but distort the cell geometry. These phonons have finite energy for $\mathbf{q} \approx \mathbf{0}$ and, because of this feature, can be visible in optical experiments. Further details on the solution to the lattice dynamics problem are described in appendix C. We will now describe the specific solutions to the lattice dynamics problem for Zincblende and Wurtzite crystals.

2.3.1 Lattice Vibrations in GaAs Zincblende Crystals

The relation between the energy of the vibration modes and the wave-vector $\mathbf{q}$, also known as phonon dispersion relation, is represented for the case of Zincblende GaAs in figure 2.6. We have seen in §2.1 that Zincblende unit cell can be described with a base set of two atoms: the lattice dynamics of the unit cell problem will be described by a linear combination of six vibration modes. Three of them are acoustic modes and are characterized by a linear

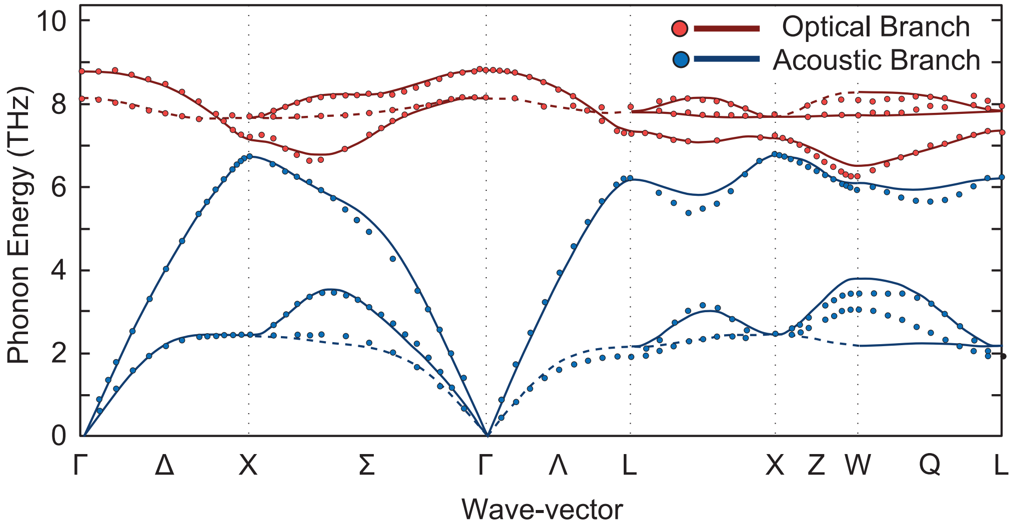

Figure 2.6: Phonon dispersion relations of a GaAs Zincblende crystal obtained by inelastic neutron scattering[76].

dispersion relation. The remaining $3 \times 2 - 3 = 3$ degrees of freedom will be associated to optical modes, which have a finite energy spectrum at the Γ-point and share the same symmetry character, indicated with F_{2g} in the notation of Loudon[83]. Their atomic displacements are sketched in figure 2.7.

Along high symmetry directions the optical modes can be further distinguished into transversal optical (TO) and longitudinal optical (LO) modes. TO modes are characterized by atomic displacements of each atom in the unit cell that are orthogonal to the direction of the phonon wave-vector **q**. In the LO modes instead, the displacement of each atom of the unit cell occurs in the same direction of the phonon wave vector. To better understand this concept, we can consider at the unit cell displacements in figure 2.7 and associate them to a wave-vector oriented along the long edge of the page, in the vertical direction. The atomic displacement shown in (a) would then represent the LO mode, while (b) and (c) would show the displacements of the two TO modes.

In materials like silicon or germanium, where the unit cell is populated by atoms of the same chemical specie, LO and TO modes are degenerate. However, this degeneracy cannot be observed in III-V alloys. Because of the finite dipole moment between the group III and the group V atom, the lattice vibrations can induce a macroscopic electric field in the direction of the phonon wave-vector[82]. While for TO modes such macroscopic electric field is orthogonal to the polarization vector associated with the vibration mode,

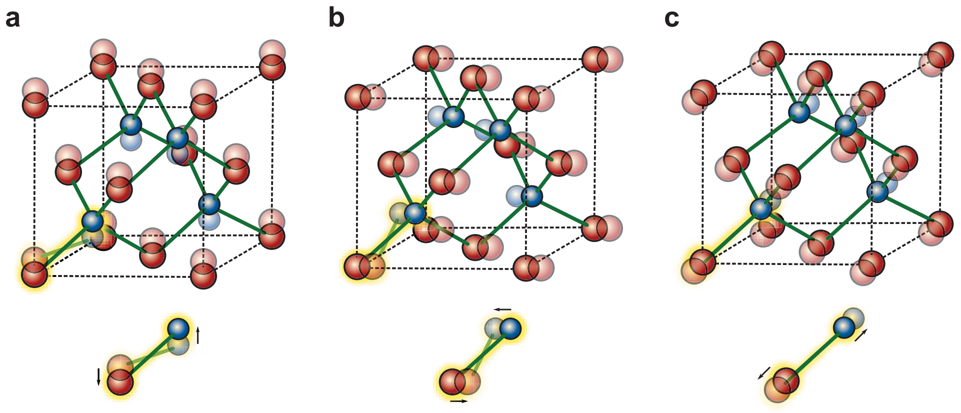

Figure 2.7: Atomic displacements of the three optical vibrational modes of Zincblende crystals at the Γ-point.

Zincblende Phonon Mode	Raman Shift (cm^{-1})	Activity
F_{2g} (TO)	268	IR + Raman
F_{2g} (LO)	292	IR + Raman

Table 2.1: Energy and activity of the optical modes of Zincblende GaAs. The mode symmetry is given in the notation of Loudon[83].

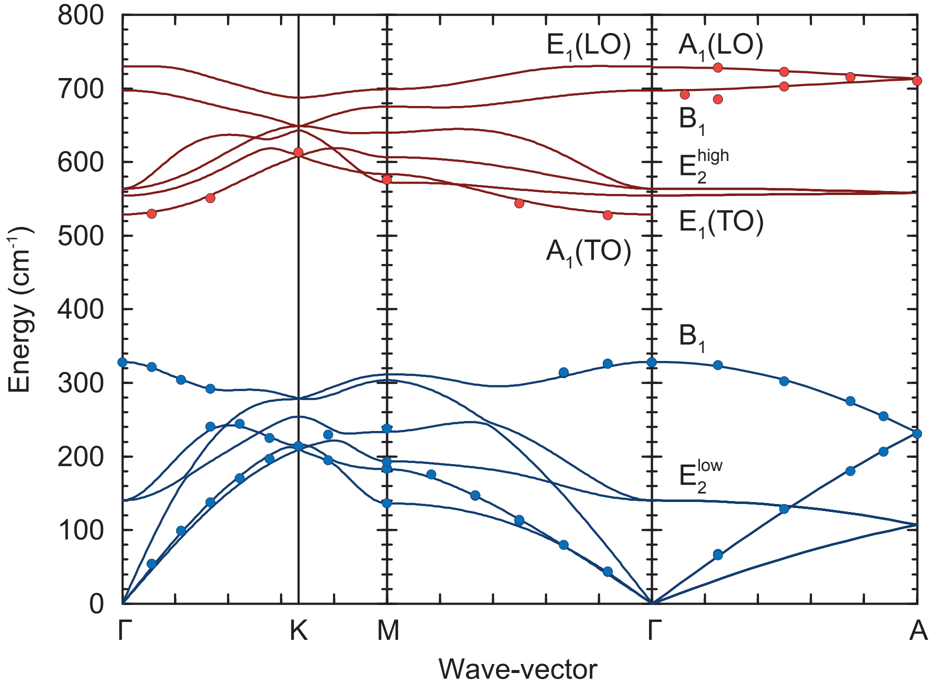

Figure 2.8: Phonon dispertion relations in Wurtzite GaN obtained by inelastic X-ray scattering[84].

for LO modes the macroscopic electric field and the polarization vector are parallel. Because of this configuration, an extra energy term is associated to the LO phonons as well as a higher vibrational frequency compared to the TO phonon. The LO-TO energy splitting can be considered as a manifestation of the piezoelectric activity of the unit cell. The energies of the TO and LO phonons for Zincblende GaAs, in proximity of the Γ-point, are summarized in table 2.1.

2.3.2 Lattice Vibrations in GaAs Wurtzite Crystals

To our knowledge, the phonon dispersion relations have not been measured yet in Wurtzite GaAs. An idea of the higher degree complexity and reacher structure can be obtained considering the dispersion relation of Wurtzite GaN, shown in figure 2.8. Wurtzite crystals are composed by a unit cell containing four atoms and $4 \times 3 = 12$ vibrational modes for each value of wave-vector describe the lattice dynamics of these crystals. Apart from the three acoustic branches, $12 - 3 = 9$ optical modes are going to have finite energy at the Γ-point. Because of the greater number of atoms in the unit cell and the lower degree of symmetry transformations that relate the atoms with one another compared to Zincblende, Wurtzite crystals have a greater number of symmetries that are used to identify the vibration modes. The possible unit cell atomic displacements and the respective symmetries are shown in figure 2.9.

Like in Zincblende, a set of three lattice vibrations are both Raman and infrared active and have symmetry A_1 and E_1. The displacement of the A_1 phonons is parallel to the c-axis. For the E_1 phonons, the displacements occur orthogonally to the c-axis, within the hexagonal plane. The vibration modes with symmetry B_1 are called silent modes, since they are neither Raman nor infrared active and do not provide any feature in optical spectroscopy experiments. The vibration modes with symmetry E_2 are only Raman active and can be grouped according to their energies in two sets, E_2^{high} and E_2^{low}. Each set contains two degenerate modes. Following similar folding relations as the one used for the electronic states, these phonons can be associated to the phonons found at the [111] and $[\bar{1}\bar{1}\bar{1}]$ point in Zincblende: two E_2^{high} phonons correspond to the Zincblende zone-edge phonons described by the optical branch while the two E_2^{low} phonon corresponds instead to the Zincblende zone-edge phonons described by the acoustic branch. The Wurtzite symmetry is a sufficient condition to enable the Raman activity of these phonons, the observation of which provides an experimental proof of the hexagonal symmetry of the crystal structure.

As in the case of Zincblende, Wurtzite GaAs has a finite dipole moment which can interact with the macroscopic electric field of the vibration modes and provide an extra energy contribution. For the infrared active modes, i.e. the modes with symmetry A_1 and E_1, this energy term provides a finite contribution which lifts the degeneracy of LO and TO phonons. The contribution is instead identically zero for the non polar modes, with symmetry E_2 and B_1. In table 2.2 we have summarized the energy and Raman activity of the different phonons in GaAs Wurtzite at the Γ-point.

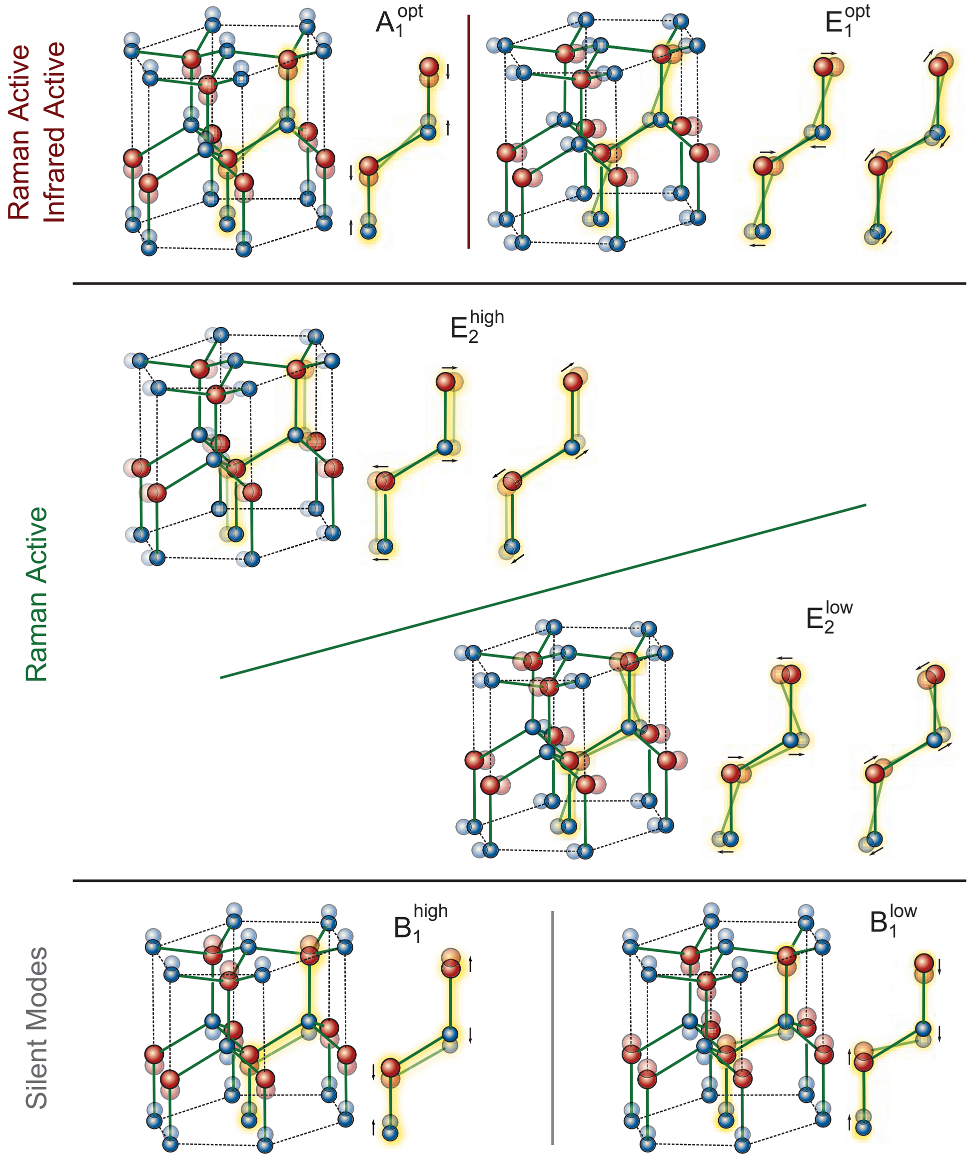

Figure 2.9: Atomic displacements of the optical phonons in Wurtzite crystals at the Γ-point.

Wurtzite Phonon Mode	Raman Shift (cm^{-1})	Activity
A_1 (LO)	291	IR + Raman
E_1 (LO)	≈ 293	IR + Raman
A_1 (TO)	≈ 265	IR + Raman
E_1 (TO)	267	IR + Raman
E_2^{High}	259	Raman
B_1^{High}	234	Silent
B_1^{Low}	206	Silent
E_2^{low}	59	Raman

Table 2.2: Energy and activity of optical phonons in Wurtzite GaAs[85]. The phonon symmetry is given in the notation of Loudon[83].

3

Strain Effects in Semiconductors

This chapter describes the fundamentals about the effects of strain on the crystal structure, electronic structure and vibrational properties of Zincblende and Wurtzite crystals. Mechanical quantities like stress and strain are defined and their correlation through the compliance and stiffness tensors are specified in both crystal structures. We describe how strain can be used to manipulate the electronic bandstructure. In conclusion, we concentrate on the effect of strain on the vibrational properties of these crystals and illustrate its effect on the energy of the optical phonons.

3.1 Mechanical Properties of Zincblende and Wurtzite Crystals

In this section we will introduce mechanical quantities such as the stress and strain tensors, define the notation needed to handle these quantities mathematically, see how they are related to each others and to the electric field and the polarization through the elastic compliance tensor, the stiffness tensor and the piezoelectric tensor[86]. We will also show the relations between the elements of these tensors in Zincblende and Wurtzite crystals.

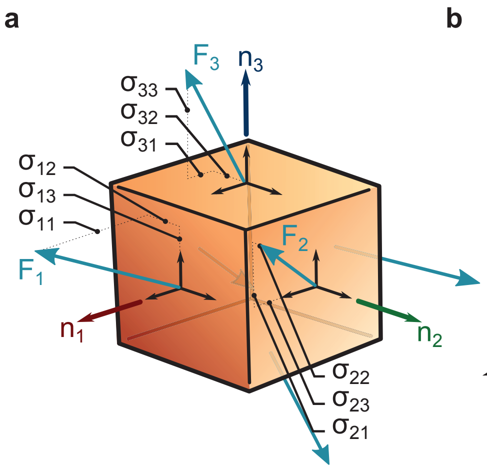

Figure 3.1: Definitions of stress tensor (a) and strain tensor (b).

3.1.1 Stress Tensor

Consider a unit cube within the body of a material, like in figure 3.1a. The interaction of the material within the cube with the external environment can be described by forces acting on the faces of the cube. If the condition of mechanical equilibrium is met, we will only need to define the forces $\mathbf{F}_1$, $\mathbf{F}_2$ and $\mathbf{F}_3$ for the faces of the cube whose normal vectors are $\mathbf{n}_1$, $\mathbf{n}_2$ and $\mathbf{n}_3$. Each force $\mathbf{F}_i$ will scale with the area of the face of the cube and can be represented by its Cartesian components, oriented along the directions $\mathbf{n}_i$. For example, the force $\mathbf{F}_1$, acting on the surface of the cube normal to vector $\mathbf{n}_1$, can be decomposed into three components $F_{1,1}$, $F_{1,2}$ and $F_{1,3}$. We indicate with σ_{ij} the ratio between the j component of the force $\mathbf{F}_i$ and the area of the face of the cube normal to the vector $\mathbf{n}_i$. The collection of such elements in a 3×3 array represents the stress tensor.

Since two indexes are needed to define it, the stress tensor is a second rank tensor. Each index can assume the value of 1, 2 or 3, standing for the x,y and z axes of a Cartesian reference system. It follows from the definition that a positive stress component corresponds to a tensile stress, while negative one corresponds to compressive stress. The hypothesis of mechanical equilibrium imposes also conditions on the stress tensor. For the sum of the forces and of the moments to be zero, σ_{ij} must be symmetric upon permutation of the indexes:

$$\sigma_{ij} = \sigma_{ji} \ . \tag{3.1}$$

3.1.2 Strain Tensor

Consider a body that undergoes some deformation, like in figure 3.1b. Each point **x** within the body can be defined by its coordinates x_j with respect to a fixed origin and set of reference axes. The deformation of the body can be defined in terms of displacement vector **u** (with components u_i) of the point **x**. We define the displacement tensor e_{ij} as:

$$e_{ij} = \frac{\partial u_i}{\partial x_j} \, . \tag{3.2}$$

The displacement tensor e_{ij} is a linear map that specifies how the displacement vector **u** varies upon the variation of the point **x**. The coordinate of the point $\mathbf{x}'$, after the body deformation, can be related to the one before deformation **x** by the following expression:

$$x'_j = \sum_i (1 + e_{ij}) x_i \, . \tag{3.3}$$

The displacement tensor e_{ij} can be decomposed in two parts:

- the component ϖ_{ij}, antisymmetric upon exchange of the indexes i and j, represent a rigid rotation of the body:

$$\varpi_{ij} = \tfrac{1}{2}(e_{ij} - e_{ji}) \, ; \tag{3.4}$$

- the component ε_{ij}, obtained calculating the symmetric part of the displacement tensor, represents the real deformation of the body and is called strain tensor:

$$\varepsilon_{ij} = \tfrac{1}{2}(e_{ij} + e_{ji}) \, . \tag{3.5}$$

3.1.3 Compliance and Stiffness Tensor

When a crystal is subject to a system of small forces, it is possible to define a linear relation between the components of the stress tensor σ_{ij} and the body deformation, described by the strain tensor ε_{kl}:

$$\varepsilon_{ij} = \sum_{k,l=1}^{3} S_{ijkl} \, \sigma_{kl} \, ,$$

or in Einsteins notation (see §B.2 in the appendix):

$$\varepsilon_{ij} = S_{ijkl} \, \sigma_{kl} \, . \tag{3.6}$$

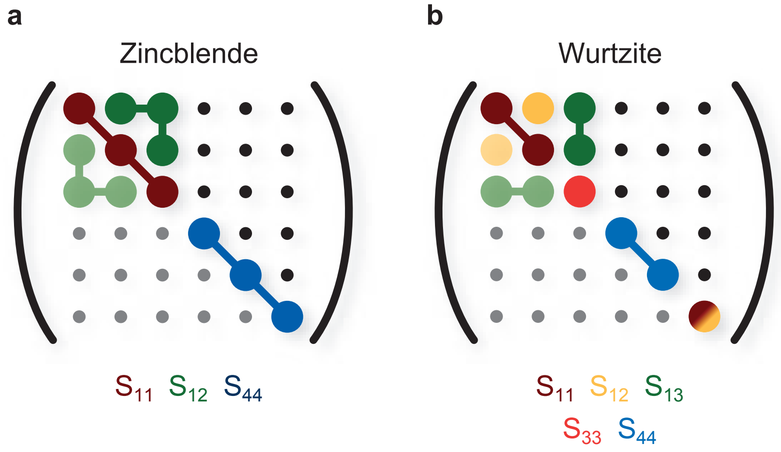

Figure 3.2: Relationship between the compliance tensor elements in (a) Zincblende and (b) Wurtzite crystals[86].

S_{ijkl} is the elastic compliance tensor and generalizes the Hooke's relation between force and displacement in a solid body. This tensor is also an example of a fourth rank tensor property of a material. The dual relation, between strain and stress, defines instead the stiffness tensor C_{ijkl}:

$$\sigma_{kl} = C_{ijkl}\,\varepsilon_{ij}\ . \tag{3.7}$$

Compliance and stiffness tensors are generally represented by $3 \times 3 \times 3 \times 3$ arrays. However, symmetry relationships between their components can be used to represent these fourth rank tensors in a more compact form.

Stress and strain tensors are symmetric upon permutation of the indexes, i.e. only six parameters are needed to fully define σ_{ij} and ε_{ij}. The Voigt notation (see §B.3 in the appendix) exploits such relations and represent in form of column vector only the independent components of the second rank tensors. Using the Voigt notation, the fourth rank tensor assumes the general form of a 6×6 matrix. The application of symmetry operations characteristic of a material leave, by definition, the material and its physical properties unchanged. As we show in figure 3.2, the application of symmetry operations introduces further relationships between the 36 parameters of the fourth rank tensors[86]. In Zincblende crystals, the compliance tensor is described by three parameters: S_{11}, S_{12} and S_{44} while in Wurtzite crystals the number of components increases to five: S_{11}, S_{12}, S_{13}, S_{33}, S_{44}. The element S_{66} is related to the S_{11} and S_{12} by the following relation:

$$S_{66} = 2(S_{11} + S_{12})\ .$$

Stiffness Constant (GPa)	Zincblende	Wurtzite
C_{11}	118	145.5
C_{12}	53.8	45.0
C_{44}	59.4	154.7
C_{13}		35.9
C_{33}		41.3

Table 3.1: Stiffness tensor elements in Zincblende and Wurtzite GaAs. The Wurtzite compliance constants have been calculated using the Martin's relation[87,88].

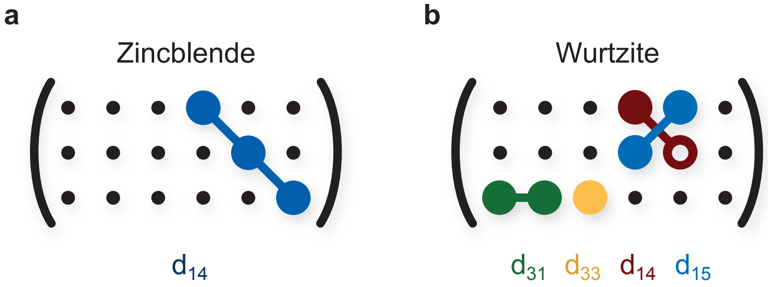

Figure 3.3: Relations between the piezoelectric tensor elements in Zincblende (a) and Wurtzite (b) crystals. In the Wurtzite case, the constants d_{14} (red filled circle) and d_{25} (red hollow circle) have the same magnitude but opposite sign.

In table 3.1 we have collected the value of the stiffness tensor for GaAs Zincblende and Wurtzite. While the values reported for Zincblende have been measured in bulk samples, the corresponding values for Wurtzite have been obtained using a theoretical method proposed by Martin[87].

3.1.4 Piezoelectricity

Strictly speaking, stress-strain relations like the one in equations (3.6, 3.7) can only be defined in materials where the unit cell does not possess a finite dipole moment. III-V materials do not belong to this category and the mechanics and electrostatics of these materials have to be treated jointly. Electric field E_m, dielectric polarization P_n, stress and strain are coupled together in the following system of equations:

$$\sigma_{ij} = C_{ijkl}\,\varepsilon_{kl} - d_{ijm}\,E_m \tag{3.8}$$

$$P_n = d_{nij}\,\varepsilon_{ij} + A_{nm}\,E_m \tag{3.9}$$

where C_{ijkl} is the stiffness tensor and A_{nm} represents the dielectric polarization of the material while the tensor d_{ijm} is called piezoelectric tensor. This tensor property allows to express the state of stress generated in a material by the application of an electric field, as well as the variation in polarization of a material due to the strain component of deformation. The piezoelectric tensor is a third rank tensor and can be represented with a 3×6 matrix, expressing the stress or strain in Voigt notation.

Like the compliance and stiffness tensor, the form of the piezoelectric tensor depends on the symmetry of the crystal. Figure 3.3 shows the relations between the elements of the piezoelectric tensor for Zincblende and Wurtzite crystals. The only non zero elements of the piezoelectric tensor in Zincblende GaAs are d_{14}, d_{25} and d_{36} and are all equal to a single constant whose value[88] is $-0.155\,\mathrm{C\,m^{-2}}$. In Wurtzite crystals, because of the lower number of symmetry operation, more tensor elements are different than zero: d_{33}, $d_{31} = d_{32}$, $d_{14} = -d_{25}$ and $d_{15} = -d_{24}$. Up to our knowledge, the piezoelectric coefficients in GaAs Wurtzite have not been determined yet.

3.1.5 Uniaxial Stress and Strain Decomposition

The experiments described in this thesis deal with a specific form of the stress tensor called the uniaxial stress. This state of stress is obtained by applying to a material a compression or tension oriented along a single axis. Because of the specific details of our experiment, the axis of stress coincides also with the nanowire growth direction. In a system of reference where the z-axis is aligned along the stress axis, while the x and y axis are orthogonal to it, we can express the stress in tensor and Voigt notation with the following relations:

$$\sigma_{ij} = \begin{bmatrix} 0 & 0 & 0 \\ 0 & 0 & 0 \\ 0 & 0 & \sigma_{\parallel} \end{bmatrix} \leftrightarrow \sigma_I = \begin{bmatrix} 0 \\ 0 \\ \sigma_{\parallel} \\ 0 \\ 0 \end{bmatrix}. \tag{3.10}$$

To obtain the respective strain tensor we can use equation (3.6) and the expression of the compliance tensor for Zincblende and Wurtzite crystals. Details about these calculations are provided in §B.3.1 and §B.3.2, in the the appendix. If the reference system is chosen like in the definition of the uniaxial stress tensor, it is possible to show that the strain tensor can be expressed in the following diagonal form in both Zincblende and Wurtzite crystals:

$$\varepsilon_{ij}^{\mathrm{NW}} = \begin{bmatrix} \varepsilon_{\perp} & 0 & 0 \\ 0 & \varepsilon_{\perp} & 0 \\ 0 & 0 & \varepsilon_{\parallel} \end{bmatrix}. \tag{3.11}$$

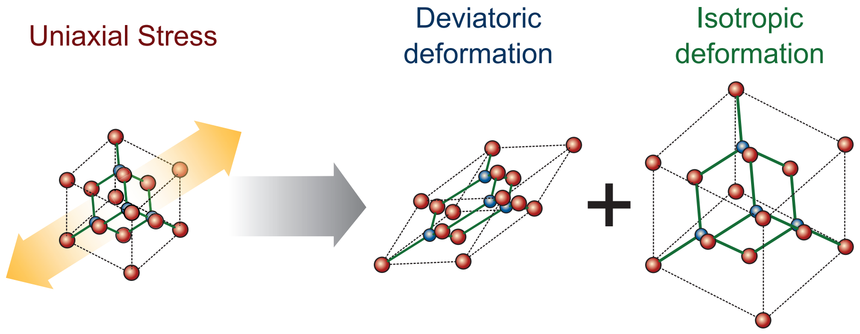

Figure 3.4: Deformation of the Zincblende unit cell upon the application of uniaxial stress along the [111] direction. The unit cell deformation can be decomposed into a deviatoric component and an isotropic component.

The strain tensor is a function of two parameters, the nanowire elongation $\varepsilon_\parallel$ and the Poisson ratio ν defined with the following relation:

$$\nu = -\frac{\varepsilon_\perp}{\varepsilon_\parallel} \, . \tag{3.12}$$

It's important to remark that the Poisson ratio ν can vary significantly with the direction of application of stress: no single value characterizes entirely Wurtzite and Zincblende materials.

We now introduce a decomposition of the strain tensor that is going to be instrumental to characterize the strain effects on the electronic bandstructure and vibrational spectra of semiconductors[76]. The strain tensor can be decomposed into a sum of two different types of deformations: the isotropic component $\varepsilon_{ij}^{\mathrm{iso}}$, and the deviatoric component $\varepsilon_{ij}^{\mathrm{dev}}$

$$\varepsilon_{ij} = \varepsilon_{ij}^{\mathrm{iso}} + \varepsilon_{ij}^{\mathrm{dev}} \, . \tag{3.13}$$

Isotropic component of strain $\varepsilon_{ij}^{\mathrm{iso}}$ captures the variation of volume of the crystal upon the application of stress. This component of the strain tensor preserves the symmetry and aspect ratio of the unit cell and is proportional to the unitary second rank tensor:

$$\varepsilon_{ij}^{\mathrm{iso}} = \begin{bmatrix} 1 & & \\ & 1 & \\ & & 1 \end{bmatrix} h\varepsilon_\parallel \, , \qquad h = \frac{1-2\nu}{3} \, . \tag{3.14}$$

The term h represents the portion of elongation that gets converted into isotropic mode of deformation and is limited between zero and unity. Using

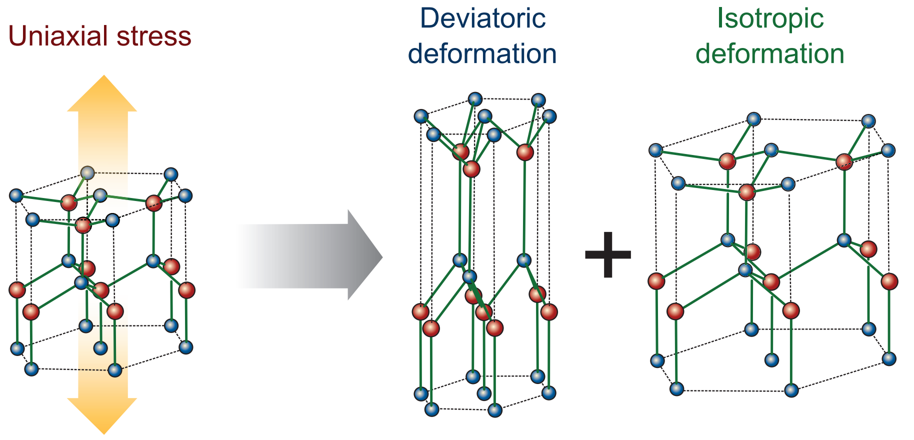

Figure 3.5: Deformation of the Wurtzite unit cell upon the application of uniaxial stress along the c-axis. The deformation, described by the strain tensor, can be decomposed into a deviatoric component and an isotropic component.

simple algebra, these limits can be directly transferred to the Poisson ratio:

$$0 \leqslant \frac{1-2\nu}{3} \leqslant 1 \;\Rightarrow\; -1 \leqslant \nu \leqslant \frac{1}{2} \,. \tag{3.15}$$

The deviatoric strain component $\varepsilon_{ij}^{\text{dev}}$ captures the distortion of the unit cell geometry that occurs without variation in volume. We can write this strain component in the stress reference system as:

$$\varepsilon_{ij}^{\text{dev}} = \begin{bmatrix} -\frac{1}{2} & & \\ & -\frac{1}{2} & \\ & & 1 \end{bmatrix} (1-h)\varepsilon_{\|} \,, \qquad (1-h) = \frac{2\,(1+\nu)}{3} \,. \tag{3.16}$$

Figure 3.4 shows the effect of uniaxial stress, applied along the [111] direction, on the Zincblende unit cell and the decomposition of the crystal deformation in isotropic and deviatoric components. The deviatoric part of the stress reduces the symmetry of the crystal from cubic (T_d^2 in Schönflies notation) to tetragonal (C_{3v}^2 in Schönflies notation). The effect of uniaxial stress, applied along the c-axis, on the Wurtzite unit cell is shown in figure 3.5. The deviatoric deformation modifies the c-a ratio but, in contrast with the Zincblende case, maintains the hexagonal symmetry of the unit cell (C_{6v}^4 in Schönflies notation).

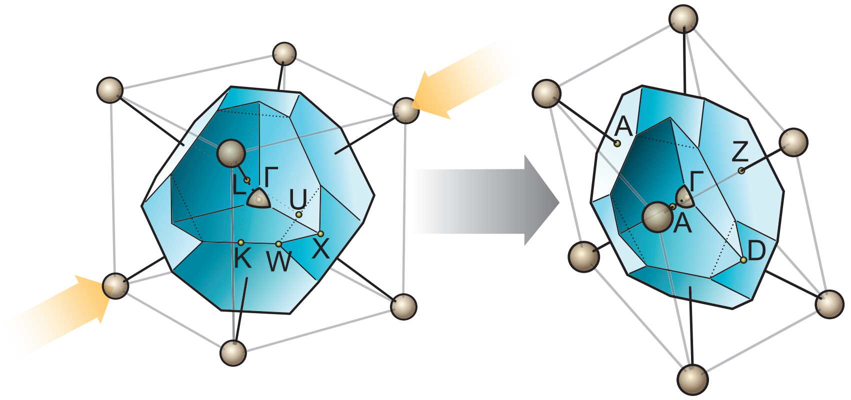

Figure 3.6: Effect of [111] uniaxial tensile stress on the geometry of the Brillouin zone of Zincblende crystals.

3.2 Strain Effects on the Electronic Band Structure

In this section we are going to discuss the effect of strain on the band structure of Zincblende and Wurtzite GaAs crystals. We will first describe how strain can influence the dimensions and geometry of the Brillouin zone. We will then concentrate on the states at the Γ-point, where the valence and conduction band states are located for both Zincblende and Wurtzite crystals. In the neighborhood of this reciprocal space region we can approximate the Hamiltonian with a special form of perturbation theory, introduced by John Bardeen and Frederick Seitz[89,90] and further developed by Evan Kane[10]: the $\mathbf{k} \cdot \mathbf{p}$ method.

3.2.1 Strain Effect on the Brillouin Zone

The crystal deformation will have a strong effect on the periodicity and value of the potential $V(\mathbf{r})$ and, therefore, on the Brilluoin zone shape and on the energy wave-vector relation. When uniaxial stress is applied to a Zincblende crystal along the [111] direction, the volume of the Brillouin zone will change with inverse proportionality with the volume variation of the unit cell, which is captured by the isotropic component of strain. The deviatoric component of strain reduces the symmetry of the crystal from cubic to tetragonal and affects the Brillouin zone shape, which will undergo a deformation shown in figure 3.6. As the Zincblende crystal elongates along the [111] direction and shrinks in the orthogonal directions, the Brilluoin zone undergoes the opposite transformation, contracting along the wave-vector direction parallel to [111] and expanding orthogonally to it. The hexagon corresponding to this direction grows in area while the squares where the X-points are laying are deformed by strain into rectangles. The symmetry relations between the eight L-points are lost with the onset of the deformation: the wave vectors associated to the L-point have to be distinguished between the two-fold degenerate Z-points, aligned along the [111] direction, and the remaining six-fold degenerate A-points. The X-points still maintain their symmetry relation and, in the new Brillouin zone, are labeled as D-points.

When tensile uniaxial stress is applied to Wurtzite crystals along the c-axis, the volume of the Brillouin zone will change as in the Zincblende case. The aspect ratio of the Brillouin zone will change inversely with the variation of c-a ratio but, unlike Zincblende, the shape and symmetry of the Brillouin zone are maintained by the deformation.

3.2.2 $\mathbf{k} \cdot \mathbf{p}$ Hamiltonian in GaAs Zincblende

We now can shift our attention to the energy of the conduction and valence band states and study how they can be influenced by strain. In close proximity of the Γ-point, the one electron Hamiltonian $\mathscr{H}_{1e}$ can be approximated with perturbation theory. By incorporating the wavefunctions in Bloch form (2.2) in equation (2.1) and including spin-orbit interaction term, proportional to $\nabla V \times \mathbf{p} \cdot \sigma$, we can simplify the Hamiltonian with the following expression:

$$\left(\frac{p^2}{2m} + V(\mathbf{r}) + \frac{\hbar^2 k^2}{2m} + \frac{\hbar}{2m}\mathbf{k}\cdot\mathbf{p} + \frac{\hbar}{4m^2c^2}\nabla V \times \mathbf{p}\cdot\sigma\right)\psi_{n\mathbf{k}}(\mathbf{r}) = E_n\psi_{n\mathbf{k}}(\mathbf{r})\,. \tag{3.17}$$

Following David Gershoni[78,91], we can introduce a basis set constituted by s-like states for the conduction band minimum and three degenerate p-like states for the valence band. Each state will have double multiplicity, to take into account of the two spin states.

$$\begin{aligned} &\psi_1 = |s\uparrow\rangle \quad \psi_2 = |p_x\uparrow\rangle \quad \psi_3 = |p_y\uparrow\rangle \quad \psi_4 = |p_z\uparrow\rangle \\ &\psi_5 = |s\downarrow\rangle \quad \psi_6 = |p_x\downarrow\rangle \quad \psi_7 = |p_y\downarrow\rangle \quad \psi_8 = |p_z\downarrow\rangle \end{aligned} \tag{3.18}$$

Using this set as a basis of representation, the Hamiltonian (3.17) assumes the form of a 8×8 matrix:

$$\mathscr{H} = \begin{bmatrix} \mathscr{G}_0 + \mathscr{G}_k + \mathscr{G}_{\mathrm{so}} + \mathscr{G}_\varepsilon & \mathscr{J} \\ -\mathscr{J}^* & {\mathscr{G}_0}^* + {\mathscr{G}_k}^* + {\mathscr{G}_{\mathrm{so}}}^* + {\mathscr{G}_\varepsilon}^* \end{bmatrix}, \tag{3.19}$$

where the blocks $\mathscr{G}_0$, $\mathscr{G}_k$, $\mathscr{G}_{\mathrm{so}}$, $\mathscr{G}_\varepsilon$ and $\mathscr{J}$ are defined by the following relations:

$$\mathscr{G}_0 = \begin{bmatrix} E_c & iP\,k_x & iP\,k_y & iP\,k_z \\ -iP\,k_x & E_v & 0 & 0 \\ -iP\,k_y & 0 & E_v & 0 \\ -iP\,k_z & 0 & 0 & E_v \end{bmatrix} , \tag{3.20}$$

$$\mathscr{G}_k = \begin{bmatrix} A'\left({k_x}^2+{k_y}^2+{k_z}^2\right) & 0 & 0 & 0 \\ 0 & L'{k_x}^2+M\left({k_y}^2+{k_z}^2\right) & N'k_xk_y & N'k_xk_z \\ 0 & N'k_xk_y & L'{k_y}^2+M\left({k_x}^2+{k_z}^2\right) & N'k_yk_z \\ 0 & N'k_xk_z & N'k_yk_z & L'{k_z}^2+M\left({k_x}^2+{k_y}^2\right) \end{bmatrix} , \tag{3.21}$$

$$\mathscr{G}_{\mathrm{so}} = -\frac{\Delta}{3}\begin{bmatrix} 0 & 0 & 0 & 0 \\ 0 & 0 & i & 0 \\ 0 & -i & 0 & 0 \\ 0 & 0 & 0 & 0 \end{bmatrix} , \tag{3.22}$$

$$\mathscr{G}_\varepsilon = \begin{bmatrix} a_c\left(\varepsilon_{xx}+\varepsilon_{yy}+\varepsilon_{zz}\right) & iP\sum_j \varepsilon_{xj}k_j & iP\sum_j \varepsilon_{yj}k_j & iP\sum_j \varepsilon_{zj}k_j \\ -iP\sum_j \varepsilon_{xj}k_j & l'\varepsilon_{xx}+m\left(\varepsilon_{yy}+\varepsilon_{zz}\right) & n\varepsilon_{xy} & n\varepsilon_{xz} \\ -iP\sum_j \varepsilon_{yj}k_j & n\varepsilon_{xy} & l\varepsilon_{yy}+m\left(\varepsilon_{xx}+\varepsilon_{zz}\right) & n\varepsilon_{yz} \\ -iP\sum_j \varepsilon_{zj}k_j & n\varepsilon_{xz} & n\varepsilon_{yz} & l\varepsilon_{zz}+m\left(\varepsilon_{xx}+\varepsilon_{yy}\right) \end{bmatrix} , \tag{3.23}$$

$$\mathscr{J} = -\frac{\Delta}{3}\begin{bmatrix} 0 & 0 & 0 & 0 \\ 0 & 0 & 0 & -1 \\ 0 & 0 & 0 & i \\ 0 & -1 & i & 0 \end{bmatrix} . \tag{3.24}$$

The parameters A', L', M and N' are related to the Luttinger parameters γ_i through the following set of equations:

$$\begin{aligned} L' &= -\frac{\hbar^2}{2m_e}\left(1+\gamma_1+4\gamma_2\right)+\frac{P^2}{E_g} , \\ M &= -\frac{\hbar^2}{2m_e}\left(1+\gamma_1-2\gamma_2\right) , \\ N' &= -\frac{3\hbar^2}{2m_e}\gamma_3+\frac{P^2}{E_g} , \\ E_p &= -\frac{2m_e}{\hbar^2}P^2 , \\ E_g &= E_c-\left(E_{v'}+\tfrac{1}{3}\Delta\right) . \end{aligned} \tag{3.25}$$

The Luttinger parameters γ_i are most known for their relation with the effective masses of the conduction band electrons m_{cb} and of heavy-holes m_{hh}, light-holes m_{lh} and split-off holes m_{so}:

$$\begin{gathered}
\frac{m_e}{m_{\mathrm{hh}[100]}} = \gamma_1 - 2\gamma_2 \ , \ \frac{m_e}{m_{\mathrm{hh}[111]}} = \gamma_1 - 2\gamma_3 \ , \\
\frac{m_e}{m_{\mathrm{lh}[100]}} = \gamma_1 + 2\gamma_2 \ , \ \frac{m_e}{m_{\mathrm{lh}[111]}} = \gamma_1 + 2\gamma_3 \ , \\
\frac{m_e}{m_{\mathrm{cb}}} = -\frac{2m}{\hbar^2}\left(A' + \frac{P^2}{E_g}\frac{E_g + \frac{2}{3}\Delta}{E_g + \Delta}\right) \ , \\
\frac{m_e}{m_{\mathrm{so}}} = \gamma_1 - \frac{2m}{\hbar^2}\frac{P^2}{E_g}\frac{\frac{1}{3}\Delta}{E_g + \Delta} \ .
\end{gathered} \tag{3.26}$$

The constants l, m and n that have been used to define $\mathscr{G}_\varepsilon$ are related to a set of band-edge deformation potentials:

$$a_v = \frac{1}{3}\left(1 + 2m\right) \ , \quad b_v = \frac{1}{3}\left(1 - m\right) \ , \quad d_v = \frac{1}{\sqrt{3}} n \ . \tag{3.27}$$

The constants a_c and a_v are the conduction band and valence band hydrostatic deformation potentials, and describe how the conduction band and valence band shift in energy because of the isotropic component of the strain tensor. The constants b_v and d_v are called valence band deviatoric deformation potentials, and define the splitting in energy that occurs between the valence band states because of the deviatoric component of strain induced by a uniaxial stress, respectively along the [100] and [111] directions. A summary of the parameters used to describe Zincblende GaAs with $k \cdot p$ have been collected in table 3.2.

Using the $k \cdot p$ framework it is possible to calculate the energies E_n and wavefunctions $\psi_{n\mathbf{k}}$ of the one electron Hamiltonian, by computing the eigenvalues and eigenvectors of the matrix (3.19) for any desired value of wavevector $\mathbf{k}$ and strain ε_{ij}. The energies and wave-functions of the conduction and valence band states of the unstrained Zincblende crystal can be found explicitly at the Γ-point: such set of solutions, called the Kramers set, is represented in table 3.3. The Kramers set permits also to define unequivocally what is meant with state of heavy-hole, light-hole and split-off hole. These states are also labeled by $|J, J_z\rangle$, using their associated total angular momentum J and projection J_z along a quantization axis.

We now have all the instruments to study the variation of the the conduction and valence band energies and states, evaluated at the Γ-point, as uniaxial stress is applied. We have written a MATLAB code that implements the $k \cdot p$ Hamiltonian (3.19) with the above mentioned matrix formalism and

$k \cdot p$ parameter	GaAs Zincblende
E_g	1.42 eV
Δ_0	341 meV
E_p	28.8 eV
${}^{m_\mathrm{el}}/_{m}$	0.0665
γ_1	6.790
γ_2	1.924
γ_3	2.782
a_c	−7.1 eV
a_v	2.67 eV
a_g	−9.77 eV
b_v	−1.7 eV
d_v	−4.55 eV

Table 3.2: Parameters used to describe bulk GaAs Zincblende with a 8 band $k \cdot p$ model[78].

Name	Energy	Kramers Set
Conduction Band Electron	E_c	$\left\|\frac{1}{2},\frac{1}{2}\right\rangle = \|s\uparrow\rangle$ $\left\|\frac{1}{2},-\frac{1}{2}\right\rangle = \|s\downarrow\rangle$
Heavy Hole	$E'_\mathrm{v} + \frac{1}{3}\Delta$	$\left\|\frac{3}{2},\frac{1}{2}\right\rangle = \sqrt{\frac{1}{2}}\,[\|x\uparrow\rangle + i\|y\uparrow\rangle]$ $\left\|\frac{3}{2},-\frac{1}{2}\right\rangle = \sqrt{\frac{1}{2}}\,[\|x\downarrow\rangle - i\|y\downarrow\rangle]$
Light Hole	$E'_\mathrm{v} + \frac{1}{3}\Delta$	$\left\|\frac{3}{2},\frac{1}{2}\right\rangle = \sqrt{\frac{1}{6}}\,[\|x\downarrow\rangle + i\|y\downarrow\rangle] - \sqrt{\frac{2}{3}}\|z\uparrow\rangle$ $\left\|\frac{3}{2},-\frac{1}{2}\right\rangle = -\sqrt{\frac{1}{6}}\,[\|x\uparrow\rangle - i\|y\uparrow\rangle] - \sqrt{\frac{2}{3}}\|z\downarrow\rangle$
Split-off Hole	$E'_\mathrm{v} - \frac{2}{3}\Delta$	$\left\|\frac{1}{2},\frac{1}{2}\right\rangle = \sqrt{\frac{1}{3}}\,[\|x\downarrow\rangle + i\|y\downarrow\rangle + \|z\uparrow\rangle]$ $\left\|\frac{1}{2},-\frac{1}{2}\right\rangle = -\sqrt{\frac{1}{3}}\,[\|x\uparrow\rangle - i\|y\uparrow\rangle - \|z\downarrow\rangle]$

Table 3.3: Eigenvalues and eigenstates of the Hamiltonian (3.19), forming the Kramers set.

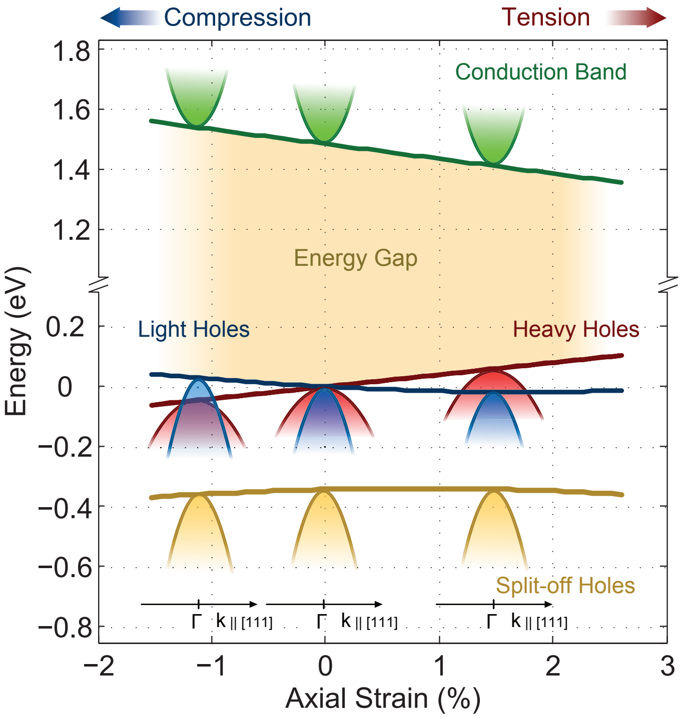

Figure 3.7: Effect of uniaxial stress on the energy of the conduction band minimum and valence band maxima of Zincblende GaAs.

uses the expression of the strain tensor of equation (3.11). To identify the nature of the bands, we have calculated the projection of the eigenvalues into the Kramers set, where the direction of uniaxial stress is taken as quantization axis.

Figure 3.7 shows the effect of strain on the conduction band and valence band energies at the Γ-point. The conduction band shifts linearly with stress, decreasing in energy when tensile stress is applied and increasing upon compression. The heavy hole band shifts also linearly, but with opposite slope compared to the conduction band. The light hole and split-off hole states mix under the influence of stress and undergo the non-linear shifts. When tensile stress is applied, the heavy hole becomes the highest in energy among the valence bands and the energy bandgap is shown to decrease linearly. Under compression, the light-hole states have instead the highest energy and shift with a slope similar to the one of the conduction band: upon this type of compression, no significant bandgap variation is expected.

Using the strain decomposition and the definitions in equations (3.12, 3.14), the energy shift of conduction band E^{cb}, of the heavy-hole band E^{hh} and of the light hole-band E^{lh} can be expressed as a function of axial strain $\varepsilon_{\parallel}$ and approximated with second order polynomials[92]:

$$E^{\mathrm{cb}} = E_0^{\mathrm{cb}} + 3a_c h\,\varepsilon_{\parallel}\ ,$$

$$E^{\mathrm{hh}} = E_{\mathrm{v}}' + \tfrac{1}{3}\Delta + \left[3a_v h + \frac{\sqrt{3}}{2}d_v(1-h)\right]\varepsilon_{\parallel}\ , \tag{3.28}$$

$$E^{\mathrm{lh}} = E_{\mathrm{v}}' + \tfrac{1}{3}\Delta + \left[3a_v h - \frac{\sqrt{3}}{2}d_v(1-h)\right]\varepsilon_{\parallel} - \frac{1}{2\Delta_0}\left[\sqrt{3}d_v(1-h)\,\varepsilon_{\parallel}\right]^2\ .$$

We will show in chapter 6 how these model can be used to interpret the photoluminescence spectra of Zincblende GaAs nanowires subject to uniaxial stress.

3.2.3 k · p Hamiltonian in GaAs Wurtzite

To study the effect of strain on the conduction and valence band states of Wurtzite GaAs we can follow the same methodology used in the Zincblende case and include some variation that captures the characteristics of the Wurtzite structure[93,94]. In proximity of the Γ-point, the valence band states of Wurtzite GaAs crystals can be described by heavy hole, light hole and split-off hole states. Unlike the Zincblende case, the Hamiltonian has to include terms that lift the degeneracy between light and heavy holes. To accurately describe the conduction band states, both bright and dark conduction band states have to be included*.

Inspired by the results of Zincblende, we can use the Kramers set directly as base for the expression of the Hamiltonian (3.17) in matrix form: this set will be formed by three p-like states for the valence band (p_x,p_y and p_z), one s-like state for the bright conduction band and one f-like state ($f_{x(x^2-3y^2)}$) for the dark conduction band:

$$\begin{array}{ccc}
 & \psi_1 = i|f_{\text{dark}}\uparrow\rangle \qquad \psi_2 = i|s_{\text{bright}}\uparrow\rangle & \\
\psi_3 = \frac{-1}{\sqrt{2}}|p_x + ip_y\uparrow\rangle & \psi_4 = \frac{1}{\sqrt{2}}|p_x - ip_y\uparrow\rangle & \psi_5 = |p_z\uparrow\rangle \\
 & \psi_6 = i|f_{\text{dark}}\downarrow\rangle \qquad \psi_7 = i|s_{\text{bright}}\downarrow\rangle & \\
\psi_8 = \frac{1}{\sqrt{2}}|p_x - ip_y\downarrow\rangle & \psi_9 = \frac{-1}{\sqrt{2}}|p_x + ip_y\downarrow\rangle & \psi_{10} = |p_z\downarrow\rangle
\end{array} \tag{3.29}$$

The Hamiltonian assumes the form of a 10×10 matrix:

$$\mathscr{H} = \begin{bmatrix} \mathscr{G}_0 + \mathscr{G}_{\text{so}} + \mathscr{G}_{k,\varepsilon} & \mathscr{J} \\ -\mathscr{J}^* & {\mathscr{G}_0}^* + {\mathscr{G}_{k,\varepsilon}}^* + {\mathscr{G}_{\text{SO}}}^* \end{bmatrix},$$

constituted by four blocks of 5×5 matrices, defined in the following way:

$$\mathscr{G}_0 = \begin{bmatrix} E_c + \Delta E_c & 0 & 0 & 0 & 0 \\ 0 & E_c & \frac{-1}{\sqrt{2}}P_{b2}\left(k_x + ik_y\right) & \frac{1}{\sqrt{2}}P_{b2}\left(k_x - ik_y\right) & P_{b1}k_z \\ 0 & \frac{-1}{\sqrt{2}}P_{b2}\left(k_x - ik_y\right) & E_v + \Delta_1 & 0 & 0 \\ 0 & \frac{1}{\sqrt{2}}P_{b2}\left(k_x + ik_y\right) & 0 & E_v + \Delta_1 & 0 \\ 0 & P_{b1}k_z & 0 & 0 & E_v \end{bmatrix}, \tag{3.30}$$

$$\mathscr{G}_{\text{so}} = -\Delta_2 \begin{bmatrix} 0 & 0 & 0 & 0 & 0 \\ 0 & 0 & 0 & 0 & 0 \\ 0 & 0 & -1 & 0 & 0 \\ 0 & 0 & 0 & 1 & 0 \\ 0 & 0 & 0 & 0 & 0 \end{bmatrix}, \tag{3.31}$$

---

[*] The heavy-hole states have symmetry Γ_9^v, while both light and split-off hole states have symmetry Γ_7^v. The bright conduction band has symmetry Γ_7^c while the dark conduction band has symmetry Γ_8^c. The symmetry character are given in the Wurtzite double group notation. More details about the symmetry notation are provided in chapter 4.

$$\mathscr{J} = \begin{bmatrix} 0 & 0 & \frac{-1}{\sqrt{2}} P_{b2}\left(k_x + ik_y\right) & 0 & 0 \\ 0 & 0 & 0 & 0 & 0 \\ \frac{-1}{\sqrt{2}} P_{b2}\left(k_x - ik_y\right) & 0 & 0 & 0 & 0 \\ 0 & 0 & 0 & 0 & \sqrt{2}\Delta_3 \\ 0 & 0 & 0 & \sqrt{2}\Delta_3 & 0 \end{bmatrix} , \quad (3.32)$$

$$\mathscr{G}_{k,\varepsilon} = \begin{bmatrix} \Upsilon_d & 0 & 0 & 0 & 0 \\ 0 & \Upsilon_b & 0 & 0 & 0 \\ 0 & 0 & \Lambda + \Theta & -K & H \\ 0 & 0 & -K^* & \Lambda + \Theta & -H^* \\ 0 & 0 & H^* & -H & \Lambda \end{bmatrix} . \quad (3.33)$$

The term $\mathscr{G}_{k,\varepsilon}$ contains the wave-vector and strain dependence of the Hamiltonian and is expressed as function of the terms Λ, Θ, H, K defined in the following way:

$$\begin{aligned} \Lambda &= A_1 k_z^2 + A_2 k_\perp^2 + D_1 \varepsilon_{zz} + D_2 \varepsilon_\perp , \\ \Theta &= A_3 k_z^2 + A_4 k_\perp^2 + D_3 \varepsilon_{zz} + D_4 \varepsilon_\perp , \\ H &= i\left(A_6 k_z k_+ + D_6 \varepsilon_{z+} + A_7 k_+\right) , \\ K &= A_5 k_+^2 + D_5 \varepsilon_+ , \\ \Upsilon_d &= A_{d\|} k_z^2 + A_{d\perp} k_\perp^2 + \Xi_{d\|} \varepsilon_{zz} + \Xi_{d\perp} \varepsilon_\perp , \\ \Upsilon_b &= A_{b\|} k_z^2 + A_{b\perp} k_\perp^2 + \Xi_{b\|} \varepsilon_{zz} + \Xi_{b\perp} \varepsilon_\perp . \end{aligned} \quad (3.34)$$

Stress and wave-vector components are defined with the help of the following relations:

$$\begin{aligned} k_\perp^2 &= k_x^2 + k_y^2 , \\ \varepsilon_\perp &= \varepsilon_{xx} + \varepsilon_{yy} , \\ k_+ &= k_x + ik_y , \\ \varepsilon_{z+} &= \varepsilon_{zx} + i\varepsilon_{zy} , \\ \varepsilon_+ &= \varepsilon_{xx} - \varepsilon_{yy} + 2i\varepsilon_{xy} . \end{aligned} \quad (3.35)$$

The set of parameters needed to define the $k \cdot p$ Hamiltonian in GaAs Wurtzite crystals are summarized in table 3.4 while the optical deformation

Parameter	GaAs Wurtzite
E_g	1.42 eV
Δ_cr	196±16 meV
Δ_so	343±5 meV
$m_{\mathrm{b}\parallel}/m$	0.06
$m_{\mathrm{b}\perp}/m$	0.075
$m_{\mathrm{d}\parallel}/m$	1.06
$m_{\mathrm{d}\perp}/m$	0.017
A_1	$-18.39\ \frac{\hbar^2}{2m}$
A_2	$-1.87\ \frac{\hbar^2}{2m}$
A_3	$17.05\ \frac{\hbar^2}{2m}$
A_4	$-6.26\ \frac{\hbar^2}{2m}$
A_5	$6.83\ \frac{\hbar^2}{2m}$
A_6	$-7.27\ \frac{\hbar^2}{2m}$
A_7	$0.035\ \frac{e^2}{2}$

Table 3.4: $k \cdot p$ parameters for GaAs Wurtzite, estimated with *ab-initio* density functional theory[81].

potentials are collected in table 3.5.

Using this matrix representation it is possible to calculate the energy and the wave-functions, respectively, as eigenvalues and eigenvectors for any arbitrary value of strain and wave-vector in proximity of the Γ-point. For simplicity, we will now consider only how the eigen-energies change at the Γ-point as uniaxial stress is applied. The Hamiltonian assumes a block diagonal form and both dark and bright conduction bands undergo linear shifts with stress:

$$\begin{aligned} E_\mathrm{dark} &= E_c + \Delta E_c + \Xi_{d\|}\varepsilon_{zz} + \Xi_{d\perp}\varepsilon_\perp \\ E_\mathrm{bright} &= E_c + \Xi_{b\|}\varepsilon_{zz} + \Xi_{b\perp}\varepsilon_\perp \end{aligned} \tag{3.36}$$

The energy of the valence band states E_hh, E_lh and E_so varies with strain

Deformation potentials	LDA	GW
$\Xi_{d,h} - \Xi_{b,h}$	5.69 eV	5.16 eV
$\Xi_{d,u}$	19.1 eV	21.0 eV
$\Xi_{b,h} - D_1 - 2D_2$	−7.60 eV	−8.25 eV
D_3	7.57 eV	7.68 eV

Table 3.5: Optical deformation potentials calculated by different *ab-initio* methods[81].

according to the following relations:

$$\begin{aligned} E_{\mathrm{hh}} &= E_v + \Delta_1 + \Delta_2 + \Lambda + \Theta \,, \\ E_{\mathrm{lh}} &= E_v + \Lambda + \tfrac{1}{2}[\Delta_1 + \Theta - \Delta_2] + \sqrt{\tfrac{1}{4}(\Delta_1 + \Theta - \Delta_2)^2 + 2{\Delta_3}^2} \,, \\ E_{\mathrm{so}} &= E_v + \Lambda + \tfrac{1}{2}[\Delta_1 + \Theta - \Delta_2] - \sqrt{\tfrac{1}{4}(\Delta_1 + \Theta - \Delta_2)^2 + 2{\Delta_3}^2} \,. \end{aligned} \tag{3.37}$$

For GaAs Wurtzite crystals, one can introduce the cubic approximation[93,94], consisting on the following relations between the $k \cdot p$ parameters:

$$\begin{gathered} \Xi_{b\|} = \Xi_{b\perp} = \Xi_b \,, \quad \Delta_2 = \Delta_3 \,, \\ D_1 - D_2 = -D_3 = 2D_4 \,, \quad D_3 + 4D_5 = \sqrt{2}D_6, \,, \\ A_1 - A_2 = A_3 = 2A_4 \,, \quad A_3 + 4A_5 = \sqrt{2}A_6 \,. \end{gathered} \tag{3.38}$$

This approximation ignores the anisotropy in the spin-orbit coupling between different bands, and uses a single crystal-field splitting Δ_{cr} and spin-orbit splitting Δ_{so} to characterize the Wurtzite bandstructure:

$$\Delta_{\mathrm{cr}} = \Delta_1 \,, \quad \Delta_{\mathrm{so}} = 3\Delta_2 = 3\Delta_3 \,. \tag{3.39}$$

In unstrained conditions, the energy difference between the valence band states and the heavy hole level will only depend on the crystal-field splitting Δ_{cr} and spin-orbit splitting Δ_{so}, according to the following set of relations:

$$\begin{aligned} E_{\mathrm{lh}} - E_{\mathrm{hh}} &= \tfrac{1}{2}\left\{\Delta_{\mathrm{cr}} + \Delta_{\mathrm{so}} - \sqrt{(\Delta_{\mathrm{cr}} + \Delta_{\mathrm{so}})^2 - \tfrac{8}{3}\Delta_{\mathrm{cr}}\Delta_{\mathrm{so}}}\right\} , \\ E_{\mathrm{so}} - E_{\mathrm{hh}} &= \tfrac{1}{2}\left\{\Delta_{\mathrm{cr}} + \Delta_{\mathrm{so}} + \sqrt{(\Delta_{\mathrm{cr}} + \Delta_{\mathrm{so}})^2 - \tfrac{8}{3}\Delta_{\mathrm{cr}}\Delta_{\mathrm{so}}}\right\} . \end{aligned} \tag{3.40}$$

We can now consider the effect of strain, studying the difference between the energy levels defined in equation (3.37), using the same methodology that led to equation (3.40). We discover that the strain dependence resides only through the term Θ. One can lump Θ together with Δ_1 and define a strain-dependent crystal-field splitting:

$$\Delta'_{\mathrm{cr}} = \Delta_1 + D_3\varepsilon_{zz} + D_4\varepsilon_{\perp} \, . \tag{3.41}$$

We deduce that the strain affects the energy difference between valence band states only by varying the crystal field splitting as shown in (3.41). Furthermore, the model does not capture the variation of the spin-orbit interaction induced by strain. The energy difference between the valence band states assumes the form of equation (3.40) also when strain is applied, substituting the crystal field splitting Δ_{cr} with its strain dependent version of equation (3.41).

The combined effect of hydrostatic and deviatoric strain on the energy of conduction and valence band levels is summarized by the following relations and shown in figure 3.8:

$$\begin{gathered}
E_{\mathrm{b}} = E_c + 3\Xi_b h\varepsilon_{\parallel} \\
E_{\mathrm{d}} = E_c + \Delta E_c + \left(\Xi_{d\parallel} + 2\Xi_{d\perp}\right) h\varepsilon_{\parallel} + \left(\Xi_{d\parallel} - \Xi_{d\perp}\right)(1-h)\varepsilon_{\parallel} \\
E_{\mathrm{hh}} = E_v + \Delta_1 + \Delta_2 + (D_1 + 2D_2)\, h\varepsilon_{\parallel} + \tfrac{1}{2} D_3(1-h)\varepsilon_{\parallel} \\
\Delta_{\mathrm{cr},\varepsilon} = \Delta_1 + \tfrac{3}{2} D_3(1-h)\varepsilon_{\parallel} \\
E_{\mathrm{lh}} - E_{\mathrm{hh}} = \tfrac{1}{2}\left\{\Delta_{\mathrm{cr}} + \Delta_{\mathrm{so}} - \sqrt{(\Delta_{\mathrm{cr}} + \Delta_{\mathrm{so}})^2 - \tfrac{8}{3}\Delta_{\mathrm{cr}}\Delta_{\mathrm{so}}}\right\} \\
E_{\mathrm{so}} - E_{\mathrm{hh}} = \tfrac{1}{2}\left\{\Delta_{\mathrm{cr}} + \Delta_{\mathrm{so}} + \sqrt{(\Delta_{\mathrm{cr}} + \Delta_{\mathrm{so}})^2 - \tfrac{8}{3}\Delta_{\mathrm{cr}}\Delta_{\mathrm{so}}}\right\}
\end{gathered} \tag{3.42}$$

The conduction band states and heavy hole states undergo linear shifts with stress: the bright conduction band edge decreases linearly in energy when tensile stress is applied, while the heavy hole band and the dark conduction band follow the opposite trend and increase their energy with tension. Light hole and split-off band mix under the influence of stress and undergo non-linear shifts.

The bright conduction band is energetically favorable when tensile stress is applied to the crystal. On the contrary, when compressive stress is applied, the dark conduction band becomes energetically favorable. When assuming this configuration, the semiconductor is said to have a pseudodirect bandgap: like direct bandgap materials, conduction and valence bands have both ex-

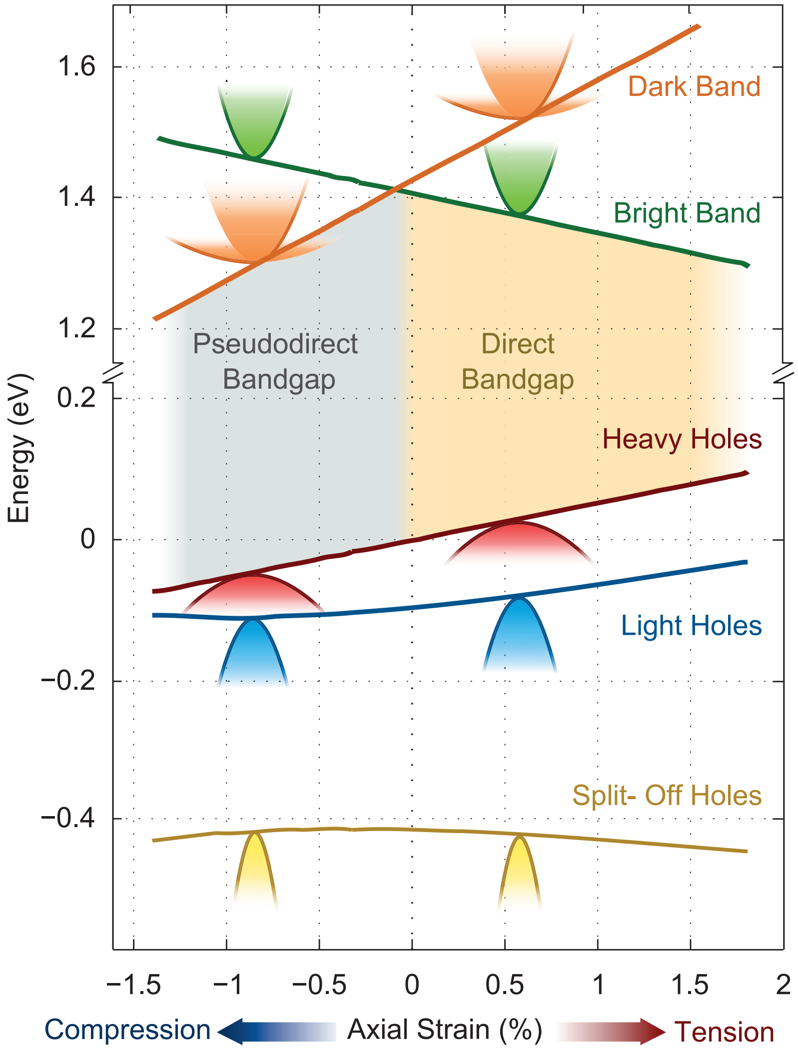

Figure 3.8: Uniaxial stress effect on the energy of the conduction and valence band states of bulk GaAs Wurtzite crystals at the Γ-point, calculated with the $k \cdot p$ model.

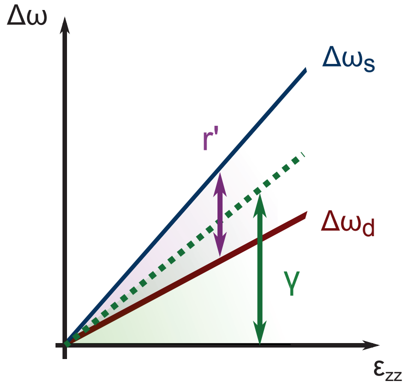

Figure 3.9: Freqeuncy shift of the optical phonons of Zincblende under uniaxial stress. The effect of isotropic and deviatoric deformation are represented using the mode Grüneisen parameters γ and r'.

trema at the Γ-point but, because of symmetry arguments described in §4.2, the most populated conduction band is not efficiently coupled to the valence band states through optical dipole transitions. We will see in chapter 7 how such a phenomenon can be observed in Wurtzite GaAs nanowires subject to uniaxial stress.

3.3 Strain Effects on the Lattice Vibrations

We now consider the effects of stress and strain on the energy of the vibration modes of Wurtzite and Zincblende crystals. To do so we need to consider an an-harmonic expansion of the ionic Hamiltonian, up to the third order in the atomic displacements and electric field. Upon the application of stress, a new equilibrium and energy minimum has to be found and a new equation of the dynamics of the strained crystal is obtained (a detailed treatment is given in appendix C.2). The new dynamics equation has a form similar to the one shown in equation (2.4):

$$m_k \ddot{u}_\alpha\binom{l}{k} = \hat{\Phi}_{\alpha\beta}\binom{l\,l'}{k\,k'} u_\beta\binom{l'}{k'} - E_\mu \hat{M}_{\mu\alpha}\binom{l}{k} \tag{3.43}$$

where the spring constant tensor $\hat{\Phi}_{\alpha\beta}\binom{l\,l'}{k\,k'}$ and the dipole moment $\hat{M}_{\mu\alpha}\binom{l}{k}$ are modified by the influence of strain, according to the following relations:

$$\hat{\Phi}_{\alpha\beta}\binom{l\,l'}{k\,k'} = \Phi^{(0)}_{\alpha\beta}\binom{l\,l'}{k\,k'} + \hat{\Phi}^{(1)}_{\alpha\beta\gamma\delta}\binom{l\,l'}{k\,k'}\varepsilon_{\gamma\delta} \tag{3.44}$$

$$\hat{M}_{\mu\alpha}\binom{l}{k} = M^{(0)}_{\mu\alpha}\binom{l}{k} + M^{(1)}_{\mu\alpha\gamma\delta}\binom{l}{k}\varepsilon_{\gamma\delta} \tag{3.45}$$

3.3.1 Uniaxial Stress Effects on the Optical Phonons of Zincblende Crystals

We now consider how the dynamic equation (3.44) simplifies in the case of optical phonons of a Zincblende crystal. To do that we neglect, in first approximation, the effect of the macroscopic electric field and dipole moment $\hat{M}_{\mu\alpha}\binom{l}{k}$. The angular frequency of vibration of the strained Zincblende crystal can be found as eigenvalues of the following matrix:

$$\begin{bmatrix} {\omega_{F_{2g}}}^2 - \omega^2 & & \\ & {\omega_{F_{2g}}}^2 - \omega^2 & \\ & & {\omega_{F_{2g}}}^2 - \omega^2 \end{bmatrix} +$$

$$+ \begin{bmatrix} p\varepsilon_{xx} + q(\varepsilon_{yy} + \varepsilon_{zz}) & r\varepsilon_{xy} & r\varepsilon_{xz} \\ r\varepsilon_{xy} & p\varepsilon_{yy} + q(\varepsilon_{xx} + \varepsilon_{zz}) & r\varepsilon_{yz} \\ r\varepsilon_{xz} & r\varepsilon_{yz} & p\varepsilon_{zz} + q(\varepsilon_{xx} + \varepsilon_{yy}) \end{bmatrix} , \tag{3.46}$$

where $\omega_{F_{2g}}$ is the angular frequency of the TO or LO phonon, which are degenerate because of our initial assumption. The constants p, q and r define the relative shift of the phonon frequencies upon the application of strain and are called phonon deformation potentials. We now determine the effect of uniaxial stress and make use of the strain decomposition into isotropic and deviatoric component, described in §3.1.5.

The isotropic component of stress keeps the triple degeneracy of the F_{2g} optical phonons and maintains equation (3.46) in diagonal form. All vibration modes shift in energy equally, according to the following relation:

$$\Delta\omega_{\text{iso}} \approx \frac{\omega^2 - {\omega_{F_{2g}}}^2}{2\omega_{F_{2g}}} = \frac{p+2q}{2\omega_{F_{2g}}}\, h\, \varepsilon_{\parallel} \; . \tag{3.47}$$

The quantity $p + 2q$ is called isotropic phonon deformation potential. The ratio of this quantity with the square of the unstrained phonon frequency is known as mode Grüneisen parameter γ [95], which is often used to describe hydrostatic strain effects[†]:

$$\gamma = -\frac{p+2q}{6{\omega_{F_{2g}}}^2} \; . \tag{3.48}$$

The deviatoric component of the strain tensor breaks the symmetry of the unit cell and, with it, the degeneracy of the phonons: equation (3.46)

[†] Eduard Grüneisen defined these constants while studying the effect of temperature on the vibrational frequency and the lattice contribution to specific heat of crystals.

assumes a non-diagonal form. However, by applying a rotation of the cubic coordinate system which makes the [111] direction become the new z-axis, it is possible to restore the diagonal form. Strain separates the optical phonons in a doublet, formed by the two phonons that have displacement orthogonal to the stress direction, and a singlet, consisting of the phonon mode with displacement aligned in the stress direction. The energy difference between them, induced by the deviatoric strain, can be expressed with the following relation:

$$\Delta\omega_{\mathrm{dev}} = \omega_{\mathrm{s}} - \omega_{\mathrm{d}} \approx \frac{3r}{2\omega_{F_{2g}}} \left(1 - h\right) \varepsilon_{\parallel} \, . \tag{3.49}$$

In the same spirit of the definition of γ, we define a deviatoric mode Grüneisen parameter r':

$$r' = -\frac{r}{{\omega_{F_{2g}}}^2} \, . \tag{3.50}$$

The compound frequency shift of the singlet phonon $\Delta\omega_s$ and of the doublet phonons $\Delta\omega_d$, due to isotropic and deviatoric strain components, is shown in figure 3.9 and can be expressed, in terms of γ and r', with the following relations:

$$\begin{cases} \frac{\Delta\omega_s}{\omega_{F_{2g}}} = [-3\gamma h + r'(1-h)]\varepsilon_{\parallel} \; ; \\ \frac{\Delta\omega_d}{\omega_{F_{2g}}} = [-3\gamma h - \frac{1}{2} r'(1-h)]\varepsilon_{\parallel} \; . \end{cases} \tag{3.51}$$

Finally we can include the effect of the macroscopic electric field and the effect of strain on the LO-TO splitting. This term can be fully determined considering the variation of dipole moment $M^{(1)}_{\mu\alpha\gamma\delta}\binom{l}{k}\varepsilon_{\gamma\delta}$ and polarizability of the material. Wickboldt et al.[96] have shown that the strain effects on the splitting between TO and LO phonons of Zincblende crystals can be fully characterized by considering a two set of constants, (p_T, q_T, r_T) for the transversal optical phonons, and (p_L, q_L, r_L) for the longitudinal optical phonons. The difference between the two sets describes how the microscopic electric field effect varies by the introduction of strain. In table 3.6 we have collected the corresponding mode Grüneisen parameters necessary to characterize the effect of uniaxial stress along the [111] direction in GaAs Zincblende. We will discuss in chapter 6 which combination of phonon deformation potentials has to be used for the particular orientation of the wave-vector $\mathbf{q}$ and scattering configuration of the experiment.

3.3.2 Uniaxial Stress Effects on the Optical Phonons of Wurtzite Crystals

Using the same theoretical treatment as the one used for Zincblende crystals, it is in principle possible to fully characterize the effect of strain on the

γ_T	γ_L	r'_T	r'_L
1.35	1.07	−0.88	−0.53

Table 3.6: Phonon deformation potentials necessary to describe the effect of uniaxial stress along the [111] direction in Zincblende GaAs[96].

optical phonons of Wurtzite crystals. However, the increased number of atoms per unit cell makes the treatment more complicated. To the best of our knowledge, an expression similar to equation (3.46) has never been proposed to describe the effect of a generic strain and a full characterization of the phonon deformation potentials in GaAs Wurtzite has not been object of experimental measurement yet. Briggs and Ramdas have treated both theoretically and experimentally the influence of uniaxial stress in Wurtzite CdSe[97]. As in the Zincblende case, a linear relation between strain and angular frequency of the phonons is observed. They have also shown that, if the uniaxial stress breaks the symmetry of the Wurtzite unit cell, the doubly degenerate E_1 and E_2 phonon modes split in energy.

If the effect of macroscopic electric field is neglected, it is possible to show (see §C.2.2 in appendix) that uniaxial stress applied along the c-axis induces the following shifts on the E_1, A_1 and E_2 optical phonons of Wurtzite crystals:

$$\begin{cases} \Delta\omega_{E_1} = \omega_{E_1}[\gamma_{E_1} h + \zeta_{E_1}(1-h)]\varepsilon_{\parallel} \\ \Delta\omega_{A_1} = \omega_{A_1}[\gamma_{A_1} h + \zeta_{A_1}(1-h)]\varepsilon_{\parallel} \\ \Delta\omega_{E_2^{\text{high}}} = \omega_{E_2^{\text{high}}}[\gamma_{E_2^{\text{high}}} h + \zeta_{E_2^{\text{high}}}(1-h)]\varepsilon_{\parallel} \end{cases} \tag{3.52}$$

The constants γ_{E_1}, γ_{A_1} and $\gamma_{E_2^{\text{high}}}$ represent the hydrostatic mode Grüneisen parameters for the optical phonon modes of symmetry E_1, A_1 and E_2^{high}, while ζ_{E_1}, ζ_{A_1} and $\zeta_{E_2^{\text{high}}}$ are the corresponding deviatoric mode Grüneisen parameters . Notice that since the symmetry of the unit cell is preserved upon deformation, E_1 and E_2 phonons maintain their double degeneracy.

4

Optical Spectroscopy

Optical spectroscopy is a very powerful tool that permits to investigate the bandstructure and the lattice dynamics of semiconductors, and has been used in this thesis to characterize the effects of strain on nanowires. Two interaction paths between light and matter are represented in figure 4.1. The process that permits photoluminescence (PL) spectroscopy is shown on the left part of the figure and can be used to gather information about the electronic bandstructure of the material. On the right part of the figure are instead represented the processes responsible for Raman scattering, which can be used to obtain information about the lattice dynamics.

4.1 The Fermi Golden Rule

In a photoluminescence experiment, a sample is excited using a light source, e.g. a laser, and the light emitted by the sample is collected and measured as a function of wavelength. If the energy of the excitation photons is higher than the bandgap of the semiconductor, electrons can be excited to the conduction band, creating a hole in the valence band. In this way a non-equilibrium distribution of electron-hole pairs can be established. As a result of the interaction with other charge carriers, with the vibration of the lattice or other scatterers, electrons and holes can thermalize and reach, respectively, the bottom of the conduction band or the top of the valence band and, from this state, recombine radiatively by the spontaneous emission of

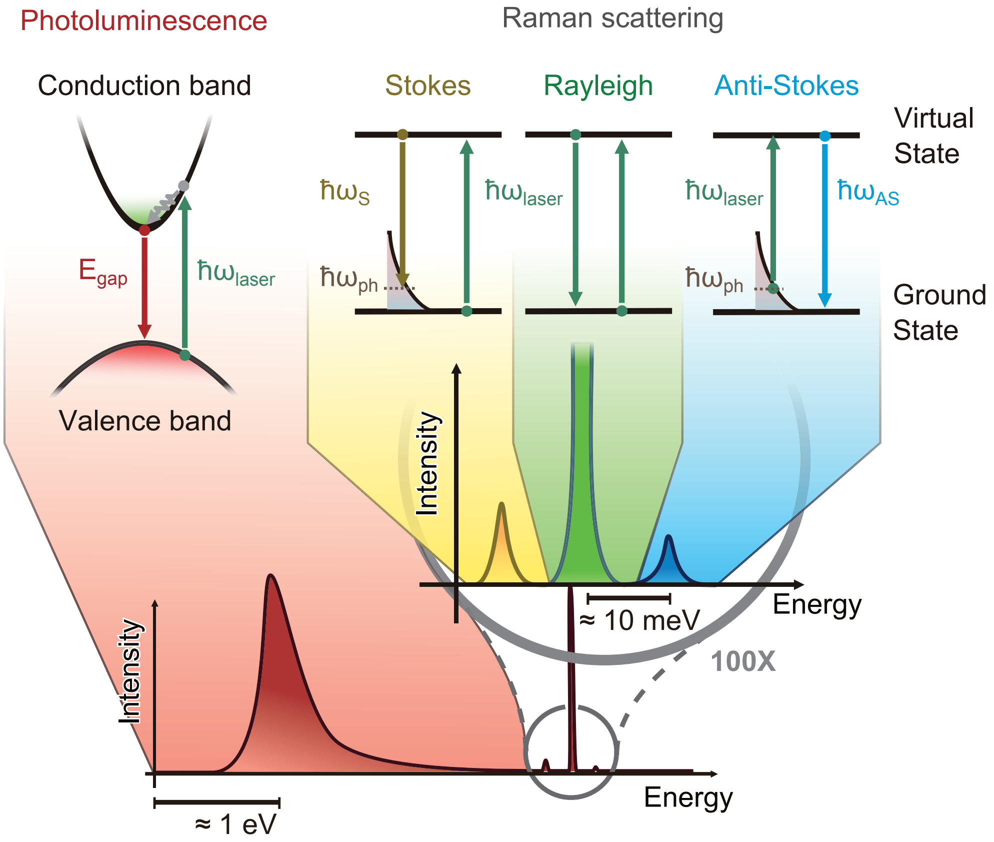

Figure 4.1: Schematic representation of the processes involved in photoluminescence and Raman spectroscopy.

a photon. The interaction between the semiconducting material and the electromagnetic field can be treated in the semi-classical approximation, using Maxwell's equations to describe the electromagnetic field and the mean field Hamiltonian $\mathscr{H}_{1e}$ in equation (2.1) to treat the valence electrons. In the semiclassical picture, the electron-radiation Hamiltonian $\mathscr{H}_{\text{e-R}}$ can be expressed in the dipole approximation with the following expression:

$$\mathscr{H}_{\text{e-R}} = \frac{e}{m_e c} \mathbf{A} \cdot \mathbf{p} \,, \tag{4.1}$$

where e is the electric charge, m_e is the free electron mass, c is the speed of light and $\mathbf{A}$ is the vector potential, related to the electric field $\mathbf{E}$ of a photon with wave-vector $\mathbf{q}$ and angular frequency ω and given by the following relation:

$$A = -\frac{E}{2q} \left[e^{i(\mathbf{q}\cdot\mathbf{r}-\omega t)} + e^{-i(\mathbf{q}\cdot\mathbf{r}-\omega t)} \right] \,. \tag{4.2}$$

The emission of a photon is described by the recombination rate R between electrons from the conduction band $|\psi_c\rangle$ and holes of the valence band $|\psi_v\rangle$ and formalized by the Fermi golden rule[76]:

$$R = \frac{2\pi}{\hbar} \sum_{\mathbf{k_v},\mathbf{k_c}} |\langle\psi_c|\mathscr{H}_{\text{e-R}}|\psi_v\rangle|^2 \, \delta\left(E_c(\mathbf{k_c}) - E_v(\mathbf{k_v}) - \hbar\omega\right) \delta\left(\mathbf{k_v} - \mathbf{k_c}, \mathbf{q}\right) \,. \tag{4.3}$$

Equation (4.3) describes all the conditions that need to occur for efficient light emission. Since the momentum $\mathbf{q}$ carried by photons is much smaller than the momentum of the charge carriers, the momentum conservation term can be approximated by:

$$\delta\left(\mathbf{k_v} - \mathbf{k_c}, \mathbf{q}\right) \approx \delta\left(\mathbf{k_v} - \mathbf{k_c}, \mathbf{0}\right) \,, \tag{4.4}$$

and the optical transitions from the conduction to the valence band are described by vertical lines in the energy wave-vector diagram of the semiconductor, as shown schematically in the left part of figure 4.1. Moreover, the square of the matrix element $\langle\psi_c|\mathscr{H}_{\text{e-R}}|\psi_v\rangle$ must be as big as possible. The electron and hole wave functions have to be located with high probability density in the same point of the Brillouin zone: conduction and valence bands of III-V semiconductors, in both Zincblende and Wurtzite, have local extrema at the Γ-point and ensure that this condition is met. The symmetry of the states involved in the radiative transition plays a more critical role, "selecting" whether an optical transition is possible, with a finite matrix element, or is forbidden, with a matrix element equal to zero. Group theory arguments can be used to determine in a simple way whether the matrix elements can be finite or not.

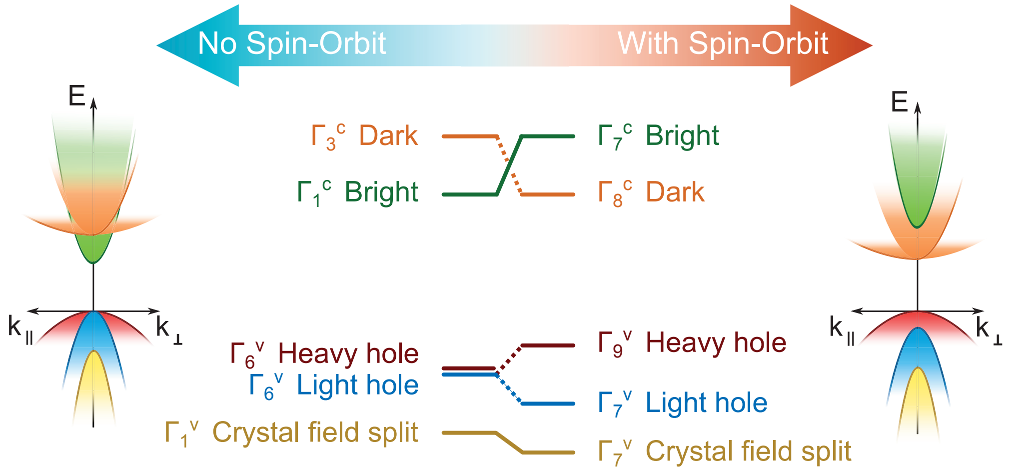

Figure 4.2: Effect of the inclusion or exclusion of the spin-orbit interaction on the energy and symmetry of conduction and valence band levels. Symmetry characters are expressed in BSW and double group notations[98].

4.2 Selection Rules in Wurtzite and Zincblende Crystals

We have explained in §3.2.2 and §3.2.3 that the bandstructure of Zincblende and Wurtzite crystals can be represented, around the Γ-point, by a combination of *s*-like, *p*-like and *f*-like states. In particular, we have seen that all of these symmetry characters are needed to accurately describe the conduction and valence band states of Wurtzite GaAs, giving to this crystal the richest variety of possible combinations of band-to-band transitions. We will now proceed considering the selection rules for the dipole transitions in Wurtzite crystals and, later on, generalize these results to the case of Zincblende.

Since uniaxial stress applied along the *c*-axis does not change the symmetry of the unit cell of Wurtzite crystals, the set of selection rules presented here will characterize radiative processes in unstrained conditions as well as when uniaxial stress is applied. For simplicity of calculation, we will neglect at first the spin degree of freedom and, with it, any spin-orbit interaction effect. This assumption allows us to reduce by half the number of possible symmetry operations and symmetry characters of the material, making the matrix element analysis very simple. In the $k \cdot p$ framework, treated in §3.2.3, this assumption consists also in forcing to zero the parameter Δ_{so}, or Δ_2 and Δ_3 without the cubic approximation. The simplification has also an effect on the band energies, summarized in figure 4.2: light hole and heavy hole

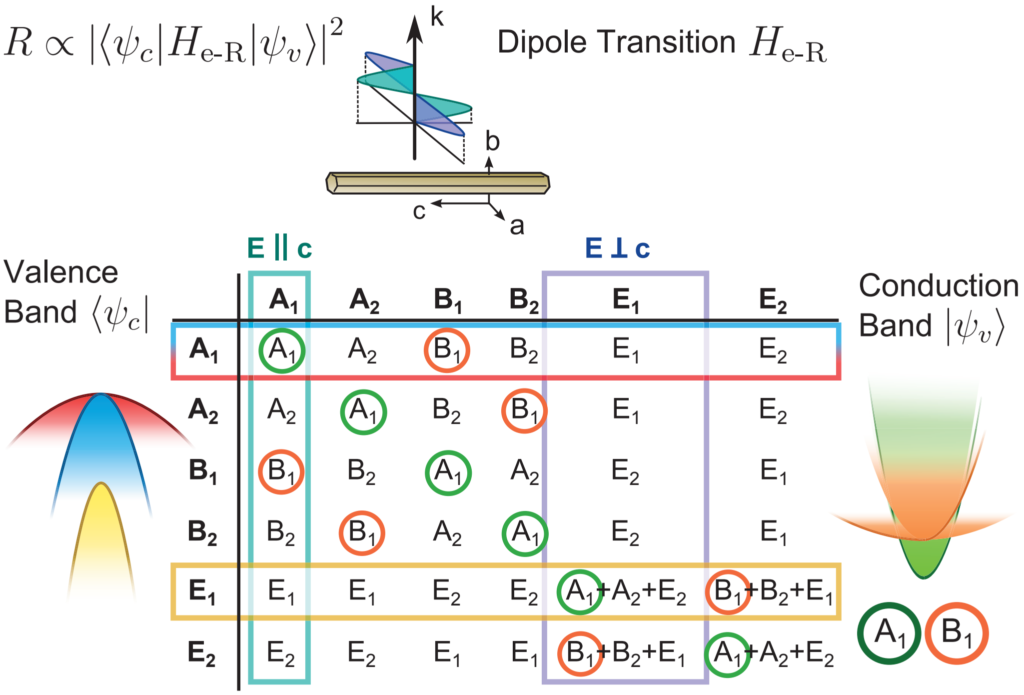

	A_1	**A_2**	**B_1**	**B_2**	**E_1**	**E_2**
A_1	A_1	A_2	B_1	B_2	E_1	E_2
A_2	A_2	A_1	B_2	B_1	E_1	E_2
B_1	B_1	B_2	A_1	A_2	E_2	E_1
B_2	B_2	B_1	A_2	A_1	E_2	E_1
E_1	E_1	E_1	E_2	E_2	$A_1+A_2+E_2$	$B_1+B_2+E_1$
E_2	E_2	E_2	E_1	E_1	$B_1+B_2+E_1$	$A_1+A_2+E_2$

Figure 4.3: Determining the optical selection rules in Wurtzite crystals using the C_{6v} group multiplication table. Spin-orbit interaction effects are not considered in this formalism.

states become degenerate while the split-off band is found at lower energy because of the crystal field splitting $\Delta_{\mathrm{cr}} = \Delta_1$. According to *ab-initio* calculations, "switching" on or off the spin-orbit interaction has also the effect of favoring different conduction band states. If the spin-orbit interaction is allowed, the dark conduction band is expected to have lowest energy; if the spin-orbit interaction is not considered, the bright conduction band is favored[80].

To determine whether the matrix element $\langle \psi_c | \mathscr{H}_{\text{e-R}} | \psi_v \rangle$ is identically zero we neglect the spin-orbit effects and use the multiplication table of the symmetry group of the Wurtzite unit cell, that is C_{6v} in the Schönflies notation. This table is shown in figure 4.3. As a first step of our calculation, we identify the symmetry of the electric states and of the dipole operator. The symmetry of the dark conduction band will be E_2 in Schönflies notation (Γ_3^C in the BSW notation of Bouckaert, Smoluchowski and Wigner[98]), while the bright conduction band will have symmetry $A_1(\Gamma_1^C)$. The heavy hole and light hole bands will have symmetry A_1 (Γ_6^V) while the split-off band will have symmetry Γ_1^V (B_1). The dipole operator can be decomposed in two components, parallel to the *c*-axis of Wurtzite unit cell and with symmetry $A_1(\Gamma_1)$, and orthogonal to the c-axis with symmetry $E_1(\Gamma_6)$. The symmetry of the dipole operator acting on the valence band is obtained from the multiplication table, as the element at the intersection between rows, where we define the valence band symmetry, and columns, where we identify the dipole operator symmetry. Finally we highlight with circles the symbols of the symmetry of the conduction band.

For the matrix element $\langle \psi_c | \mathscr{H}_{\text{e-R}} | \psi_v \rangle$ to be different than zero, the symmetry of the dipole operator acting on the valence band has to be the same as the one of the conduction band: this occurs only at a common intersection between the highlighted rows (valence band symmetry), columns (dipole operator symmetry) and highlighted symbols (conduction band symmetry). Inspecting the multiplication table in figure 4.3, it is easy to recognize that transitions are only possible from the bright conduction band Γ_1. The valence band involved in the transition can be distinguished using the light polarization: transitions into Γ_1 will be polarized parallel to the c-axis, while transitions into Γ_6 will be polarized orthogonally to the c-axis. Since no intersection is found with the symbol of the dark conduction band Γ_3, all dipole transitions from this band are forbidden. This justifies the nomenclature "dark" and "bright" introduced in §2.2 and used to identify the conduction bands in Wurtzite GaAs.

If spin-orbit interaction is taken into account, light hole and split-off hole states mix and acquire the same symmetry. The new symmetry operation doubles also the number of symmetry characters and, with it, the dimension of the multiplication table[99]. The possible transitions in the double-group

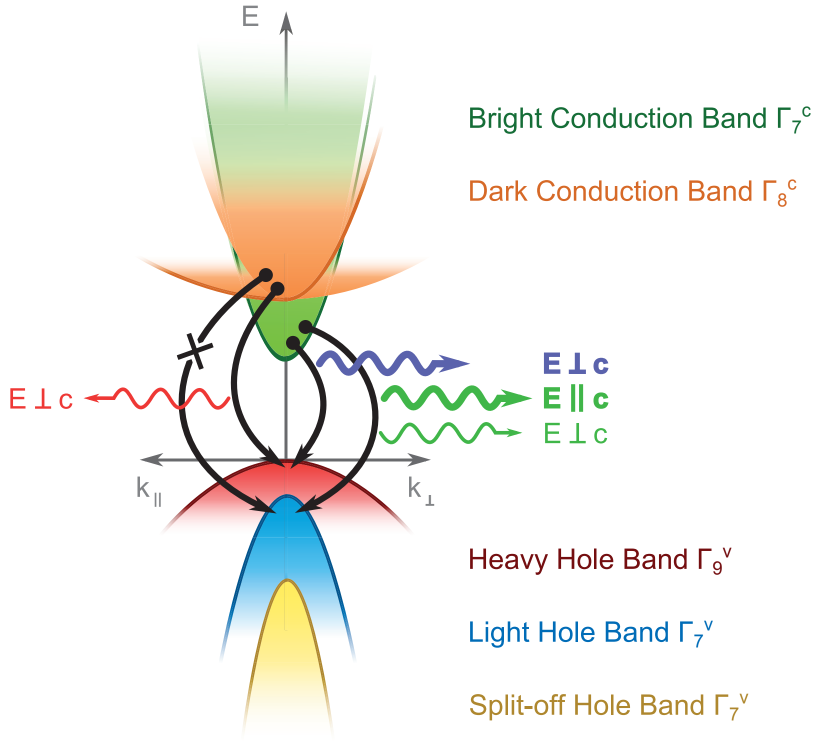

Figure 4.4: Summary of the optical selection rules in Wurtzite crystals in the double group notation. Spin-orbit interaction effects are included.

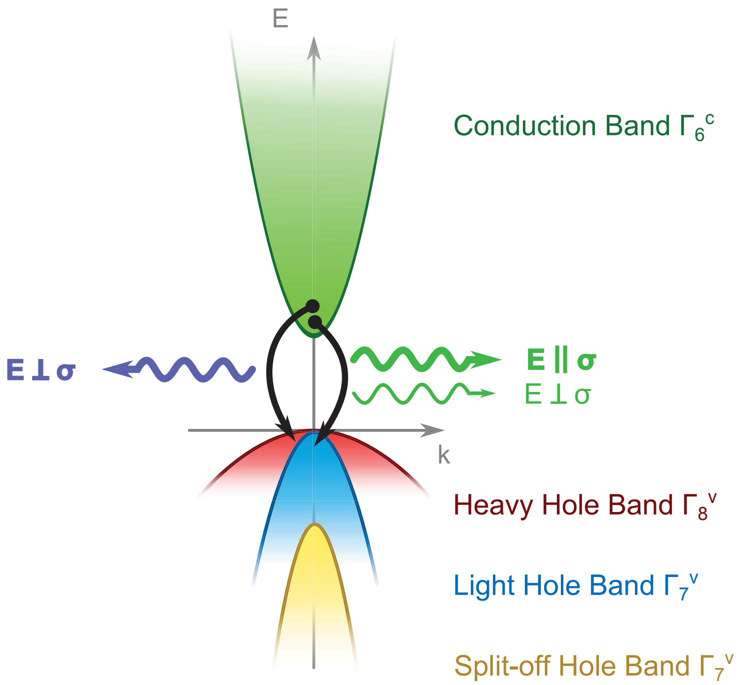

Figure 4.5: Summary of the optical selection rules in Zincblende crystals in the double group notation. Spin-orbit interaction effects are included.

are summarized in figure 4.4. The set of transitions possible when neglecting the spin-orbit effects maintain their polarization properties and are labeled using bold symbols and fonts. The transitions between the bright conduction band and the heavy hole band have polarization orthogonal to the *c*-axis, while the transitions between the bright conduction band and the light hole band have polarization parallel to the *c*-axis. The set of transitions possible only if the spin degree of freedom is taken into account, using the Wurtzite double group, are represented with a thin symbols and their oscillator strength is expected to be small: transitions between the bright conduction band and the light hole become possible also with polarization orthogonal to the c-axis and, interestingly, transitions between the dark conduction band and the heavy hole band become allowed.

Arguments and results similar to the ones shown in this section can be obtained in the case of Zincblende crystals, the selection rules of which are shown in figure 4.5. If no stress is applied the heavy hole and light hole states degenerate, because of the cubic symmetry: radiative transitions between conduction band and valence band can occur in all polarization directions with equal probability. As soon as strain is applied, the degeneracy between heavy hole and light hole states is lifted: optical transitions into heavy hole states will occur exclusively with polarization orthogonal to the uniaxial stress direction. Transitions into the light hole states will instead occur predominantly with polarization parallel to the stress direction.

4.3 Modeling the Photoluminescence Line-shape

For each possible combination of conduction band state $|\psi_c\rangle$ and valence band state $|\psi_v\rangle$ associated with a finite matrix element, the conditions for light emission are met and the respective electron-hole pairs can recombine radiatively. Equation (4.3) completely defines this process and can be used to derive the spectral line-shape of the photoluminescence. The summation over the wave-vectors $\mathbf{k} = \mathbf{k_v} - \mathbf{k_c}$ can be replaced with an integral over the energies and the matrix element of each transition has to be multiplied by the joint density of states D_{j}, that is the function specifying the number of electron-hole pair states found in a given energy interval.

We have seen in §2.2, §3.2.2 and §3.2.3, that all conduction band and valence band states can be described in proximity of the Γ-point with the effective mass approximation, also when stress is applied to the crystal. For every pair of conduction band and valence band states one can define a joint density of states contribution D_{j} that follows a square root dependence on energy according to the following equation:

$$D_{\mathrm{j}} = \begin{cases} \frac{\mu_{\mathrm{eff}}^{\frac{3}{2}}}{2\pi^2}\sqrt{E - E_{\mathrm{gap}}} & , E > E_{\mathrm{gap}} \, , \\ 0 & , E < E_{\mathrm{gap}} \, . \end{cases} \tag{4.5}$$

where the reduced effective mass μ_{eff} is defined from the effective mass of the conduction band $m_{\mathrm{eff,c}}$ and of the valence band $m_{\mathrm{eff,v}}$ by[*]:

$$\frac{1}{\mu_{\mathrm{eff}}} = \frac{1}{m_{\mathrm{eff,c}}} + \frac{1}{m_{\mathrm{eff,v}}} \, . \tag{4.6}$$

Under low laser excitation intensity, the electrons and holes reach a quasi-equilibrium condition that can be approximated by Boltzmann distributions:

$$f \propto e^{-\frac{E}{k_{\mathrm{B}}T}} \, . \tag{4.7}$$

The distribution of possible optical transitions D_{PL} is proportional to the

---

[*] Notice that the definition of D_{j} is valid in the hypothesis of with isotropic effective masses. Considering explicitly the effective mass anisotropy only varies the pre-factor in the equation (4.5) and does not affect its energy dependence.

following expression:

$$D_{\mathrm{PL}}(E) \propto \begin{cases} \sqrt{E - E_{\mathrm{g}}}\, e^{-\frac{E - E_{\mathrm{g}}}{k_{\mathrm{B}} T}} & , \ E \geqslant E_{\mathrm{g}} \, ; \\ 0 & , \ E < E_{\mathrm{g}} \, . \end{cases} \tag{4.8}$$

This expression would also represent the experimental photoluminescence lineshape in case of infinitely long-lived conduction band states and very weak coupling between conduction and valence band states. However, several mechanisms can limit the lifetime of the transition and broaden the photoluminescence spectrum: the Heisenberg uncertainty introduces a broadening due to the finite lifetime of the transitions; thermal effects or interaction with defects can also induce an energy broadening of the optical transitions. To model these different mechanisms, we introduce a Gaussian broadening function $g(E)$:

$$g(E) = \frac{1}{\sqrt{2\pi \mathit{\Delta} E^2}} e^{-\frac{E^2}{2\mathit{\Delta} E^2}} \, , \tag{4.9}$$

where $\mathit{\Delta} E$ represents the energy broadening. The final photoluminescence lineshape can be obtained by the convolution integral of the transition distribution $D_{\mathrm{PL}}(E)$ with the Gaussian broadening function $g(E)$:

$$I_{\mathrm{PL}}(\hbar\omega) = \int D_{\mathrm{PL}}(E) g(E - \hbar\omega) dE \, . \tag{4.10}$$

It is therefore possible to extract many valuable parameters by fitting the experimental spectra with relation (4.10) using a least-square algorithm. An example of such fitting is given in figure 4.6 for the case of the photoluminescence of a GaAs Wurtzite nanowire. The raw spectrum, represented with a thin black line, has been acquired at room temperature with polarization parallel to the Wurtzite c-axis. The optical transitions between the bright conduction band and the heavy hole band and between the bright conduction band and the light hole band are visible and provide two joint density of states contributions D_{j}, shown respectively in red and blue. The population of both states is given by a single Boltzmann distribution, shown in green. The resulting distribution of possible optical transitions D_{PL} is represented with a shaded curve in light blue. The broadening is represented in brown and the result of the convolution integral of equation (4.10) is represented with a red dashed line.

As a result of the fitting, it is possible to gather information such as the energy gap between conduction and valence band states, determine an accurate energy difference between the valence band states, assess the broadening $\mathit{\Delta} E$ of the radiative recombination and the effective temperature T of the

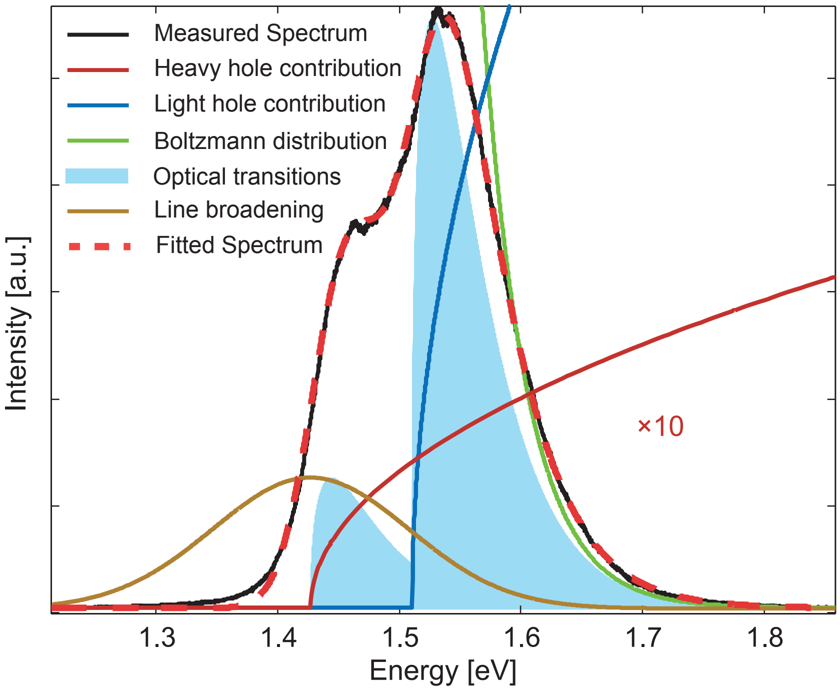

Figure 4.6: Deconvolution of the photoluminescence spectrum of a Wurtzite GaAs nanowire. The heavy hole joint density of states contribution (continuous red line) is enlarged by a factor of 10.

electron-hole pairs. If the laser excitation intensity is high, electron-electron or hole-hole interactions will increase and so will the temperature of the electron-hole pairs: the temperature extracted in this cases can be higher than the lattice temperature. Fitting the experimental spectra with the lineshape or equation (4.10) can provide further information about whether or not the charge carriers have reached thermal equilibrium with the lattice.

4.4 Raman Scattering

Optical spectroscopy can provide valuable information about the lattice dynamics through inelastic light scattering processes, known as Raman scattering. These scattering processes, sketched in the left part of figure 4.1, can be understood using a completely classical picture to describe the electromagnetic field as well as the lattice vibrations. The electromagnetic field associated with the light impinging on the semiconductor can be described by a sinusoidal wave with amplitude E_0, polarization direction $\mathbf{e}_i$, frequency ω_i and wave-vector $\mathbf{k}_i$:

$$\mathbf{E} = \mathbf{e}_i E_0 \cos(\mathbf{k}_i \cdot \mathbf{r} - \omega_i t) \;\rightarrow\quad E_\mu = e_{i\mu} E_0 \cos(\mathbf{k}_i \cdot \mathbf{r} - \omega_i t)\,. \tag{4.11}$$

Because of the finite electric susceptibility χ, a finite polarization $\mathbf{P}$ will be induced in the material according to the following expression (in Einstein tensor notation):

$$P_\nu = \chi_{\nu\mu} E_\mu\,. \tag{4.12}$$

The atomic displacements of the different normal modes can modulate the susceptibility of the semiconductor. Each one provides its own contribution to the susceptibility:

$$\chi_{\nu\mu} = \chi^{(0)}_{\nu\mu} + \frac{\partial \chi_{\nu\mu}}{\partial \mathbf{w}} \mathbf{w}\,. \tag{4.13}$$

The first term in equation (4.13) describes the static susceptibility, while the second represents the modulation by an atomic displacement $\mathbf{w}$. The resulting polarization vector P_ν can be expressed as the sum of two terms:

$$P_\nu = P_\nu^{\text{elastic}} + P_\nu^{\text{inelastic}}\,. \tag{4.14}$$

The first term describes the elastic scattering, i.e. Rayleigh scattering, by the medium and is represented on the center of figure 4.1:

$$P_\nu^{\text{elastic}} = \chi^{(0)}_{\nu\mu} E_\mu = \chi^{(0)}_{\nu\mu} e_{i\mu} E_0 \cos(\mathbf{k}_i \cdot \mathbf{r} - \omega_i t)\,. \tag{4.15}$$

The second term represents instead the inelastic scattering, or Raman scattering, by the lattice vibration modes with displacement $\mathbf{w}$. We can write the atomic oscillation in plane wave form,

$$\mathbf{w} = \mathbf{w_0} \cos\left(\mathbf{q} \cdot \mathbf{R}_l - \omega_p t\right) \ . \tag{4.16}$$

and express the inelastic scattering term of the polarization with the following relation:

$$P_\nu^{\text{inelastic}} = \frac{\partial \chi_{\nu\mu}}{\partial \mathbf{w}} \mathbf{w_0} E_\mu = \frac{\partial \chi_{\mu\nu}}{\partial \mathbf{w}} \mathbf{w_0}\; e_{i\,\mu}\, E_0 \cos(\mathbf{q} \cdot \mathbf{r} - \omega_p t) \cos(\mathbf{k}_i \cdot \mathbf{r} - \omega_i t) \ . \tag{4.17}$$

The lattice vibration and electric field interfere with one another, giving rise to two terms of inelastic scattering:

$$\begin{aligned} P_\nu^{\text{inelastic}} &= \frac{1}{2} \frac{\partial \chi_{\mu\nu}}{\partial \mathbf{w}} \mathrm{w}_0\; e_{i\,\mu} E_0 \left[\cos\left((\mathbf{q} - \mathbf{k}_i) \cdot \mathbf{r} - (\omega_i - \omega_p) t\right) + \right. \\ &\left. + \cos\left((\mathbf{q} + \mathbf{k}_i) \cdot \mathbf{r} - (\omega_i + \omega_p) t\right)\right] \ . \end{aligned} \tag{4.18}$$

The argument of the two cosines represent the momentum and energy conservation in the scattering event.

$$\mathbf{k}_s = \mathbf{q} \pm \mathbf{k}_i \ , \quad \omega_s = \omega_i \pm \omega_p \ . \tag{4.19}$$

The term with angular frequency $\omega_s = \omega_i + \omega_p$ describes the Anti-Stokes scattering events (shown on the right side of figure 4.1), in which a vibration excitation is absorbed and the scattered photon has higher energy compared to the one of the incoming photon. The term with angular frequency $\omega_s = \omega_i - \omega_p$, describes instead the Stokes scattering events, where the incoming photon excites a lattice vibration of the crystal and the scattered photon is characterized by a lower energy compared to the one of the incoming photon. In this work we will only investigate the Stokes part of the Raman spectrum.

Since the momenta of the scattered light $\mathbf{k}_s$ and of the excitation light $\mathbf{k}_i$ are very small compared to the vibration mode momentum $\mathbf{q}$, Raman scattering will only provide information about the vibration modes at the Γ-point. The intensity of inelastically scattered light in direction $\mathbf{e}_s$ can be expressed in terms of the inelastic component of the polarization vector:

$$I_{\text{inelastic}} \propto \left|\mathbf{e}_s \cdot \mathbf{P}^{\text{inelastic}}\right|^2 = \left|e_{s\,\nu} \frac{1}{2} \frac{\partial \chi_{\mu\nu}}{\partial \mathbf{w}} \mathrm{w}_0 e_{i\,\mu}\right|^2 {E_0}^2 \ . \tag{4.20}$$

Equation (4.20) summarizes different properties of the Raman scattering process. The intensity of the features of a Raman spectrum will increase linearly with the intensity of the excitation beam and will depend strongly on the direction of incoming polarization $\mathbf{e}_i$ and scattered polarization $\mathbf{e}_s$.

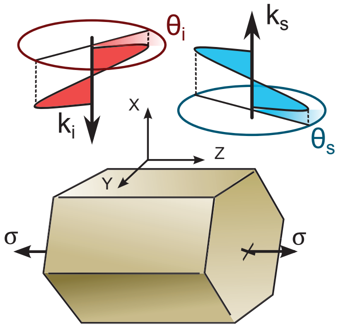

Figure 4.7: Schematic representation of the back-scattering geometry used in the strain experiments.

For each vibration mode $\mathbf{w}_i$ one can identify a second rank Raman tensor $\mathfrak{R}^{\mathbf{w}_i}_{\mu\nu}$, defined by the following equation:

$$\mathfrak{R}^{\mathbf{w}_i}_{\mu\nu} = \frac{1}{2}\frac{\partial\chi_{\mu\nu}}{\partial\mathbf{w_i}} \; . \tag{4.21}$$

For a particular orientation of incoming and scattered polarization, the intensity of the Raman peak due to the phonon $\mathbf{w}_i$ will be proportional to $|\mathbf{e}_s\mathfrak{R}^{\mathbf{w}_i}\mathbf{e}_i|^2$.

4.4.1 Scattering Geometry

Because of the transversal nature of the electromagnetic waves, the scattering geometry imposes strong limits on which phonon contribution can be visible in a Raman spectrum. The polarization vector $\mathbf{e}_i$ of the laser excitation can assume any direction within the plane normal to the wave-vector $\mathbf{k}_i$. The same argument is true for light detected by the spectrometer, i.e. the same geometrical relation holds for the polarization vector $\mathbf{e}_s$ and wave-vector $\mathbf{k}_s$. It is good practice to specify whether a polarized excitation and detection have been used to acquire a Raman spectrum and, if this is the case, define the scattering geometry by specifying the orientation of the wave-vectors $\mathbf{k}_i$ and $\mathbf{k}_s$ and of the polarization vectors $\mathbf{e}_i$ and $\mathbf{e}_s$ with respect to an orthogonal reference system. For this definition, we have used the following notation introduced by Damen et al.[100]:

$$\mathbf{k}_i\,(\mathbf{e}_i,\mathbf{e}_s)\,\mathbf{k}_s \; . \tag{4.22}$$

The Raman spectra discussed in this thesis have been acquired using the back-scattering geometry shown in figure 4.7: the nanowire lays with its long axis parallel to the substrate surface and a high numerical aperture objective is used to excite and collect the scattered light. We can define a scattering reference system, in which the x-axis defines the direction of the incoming and scattered beam, while the z-axis is oriented parallel to the direction of uniaxial stress. The wave-vector $\mathbf{k}_s$ is oriented in the same orientation of x, while $\mathbf{k}_i$ has opposite direction. Because of the momentum conservation, the phonon wave-vector $\mathbf{q}$ is defined by the scattering geometry and is oriented parallel but with opposite direction compared to the x-axis.

The polarization vectors $\mathbf{e}_i$ and $\mathbf{e}_s$ can assume any orientation within the y-z plane and can be uniquely defined by the angles θ_i and θ_s, formed by the polarization vectors with the z-axis. Using this convention, we now can represent the contribution of individual phonons to a polarized Raman spectrum, by plotting the ratio between incoming and scattered intensity as a function of the angles θ_i and θ_s in a two-dimensional plot. This method will be used to analyze the similarities and differences between the Raman selection rules in Zincblende and Wurtzite crystals.

4.4.2 Raman Scattering Selection Rules in Zincblende Crystals

We have discussed in §2.3.1 that the optical phonons of Zincblende crystals can be expressed as a linear combination of phonons with symmetry F_{2g}. Using the FCC lattice as reference system we can express the Raman tensors $\mathfrak{R}^{\mathbf{w}_i}$ with the following expressions[101]:

$$\mathfrak{R}_x^{F_{2g}} = \begin{bmatrix} 0 & 0 & 0 \\ 0 & 0 & d \\ 0 & d & 0 \end{bmatrix}, \quad \mathfrak{R}_y^{F_{2g}} = \begin{bmatrix} 0 & 0 & d \\ 0 & 0 & 0 \\ d & 0 & 0 \end{bmatrix}, \quad \mathfrak{R}_z^{F_{2g}} = \begin{bmatrix} 0 & d & 0 \\ d & 0 & 0 \\ 0 & 0 & 0 \end{bmatrix}. \tag{4.23}$$

Notice that, since the phonons are also infrared active and have translational symmetry, the Raman tensors in equation (4.23) can be lumped in a $3\times3\times3$ matrix, which has the symmetry properties of a third rank tensor. It is not surprising that such matrix is defined by a single constant, like the piezoelectric tensor of Zincblende crystals. We can push this analogy further and use the transformation laws of third rank tensors, described in §B.1, to express the Raman tensor in the scattering reference system rather than in the cubic one. Once this transformation is performed, its is straightforward to calculate the contribution to the intensity of the Raman spectrum of the different phonons in a two-dimensional plot $I(\theta_i, \theta_s)$, using equation (4.20).

In Figure 4.8 we represent the Raman selection rules in the case in which the laser light impinges along the $[1\bar{1}0]$ direction, on one of the hexagonal

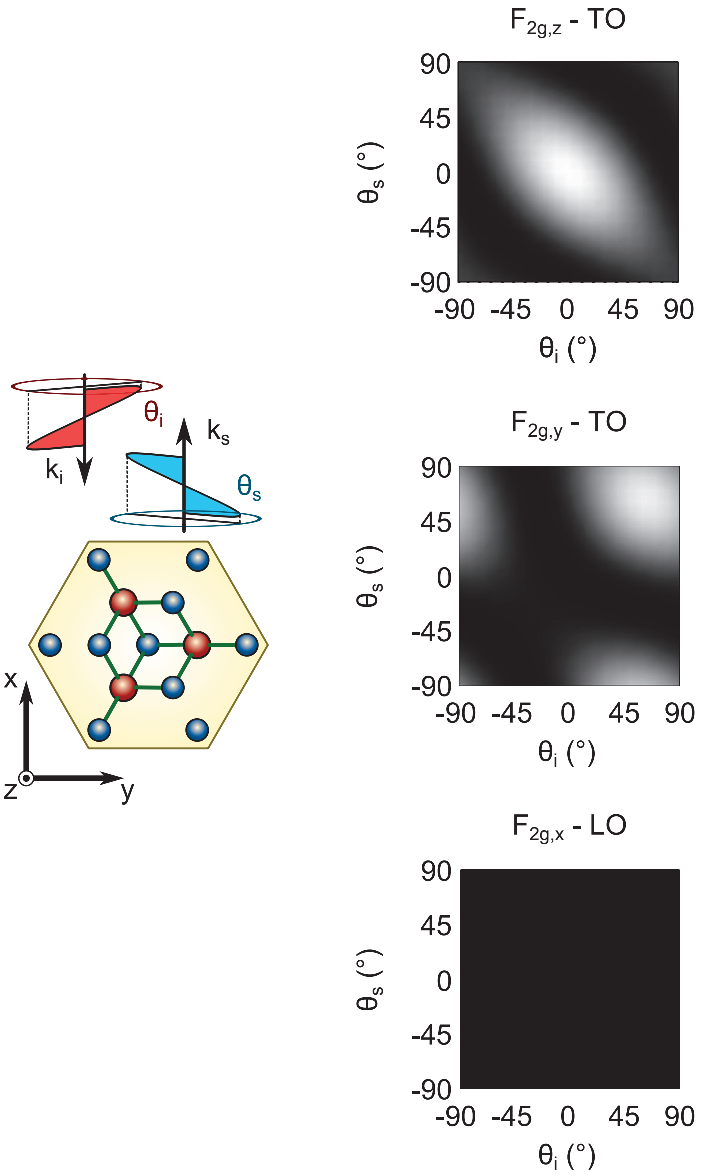

Figure 4.8: Raman scattering selection rules for Zincblende. The scattering geometry is sketched on the left: the z-axis is oriented along [111], the x-axis along $[1\bar{1}0]$ and the y-axis along $[11\bar{2}]$. The scattering intensity for the TO phonons, with displacement along z and y, and LO phonon, with displacement along x, is represented in gray-scale as a function of the incoming and scattered polarization angle. The LO phonon is strictly forbidden in this scattering geometry.

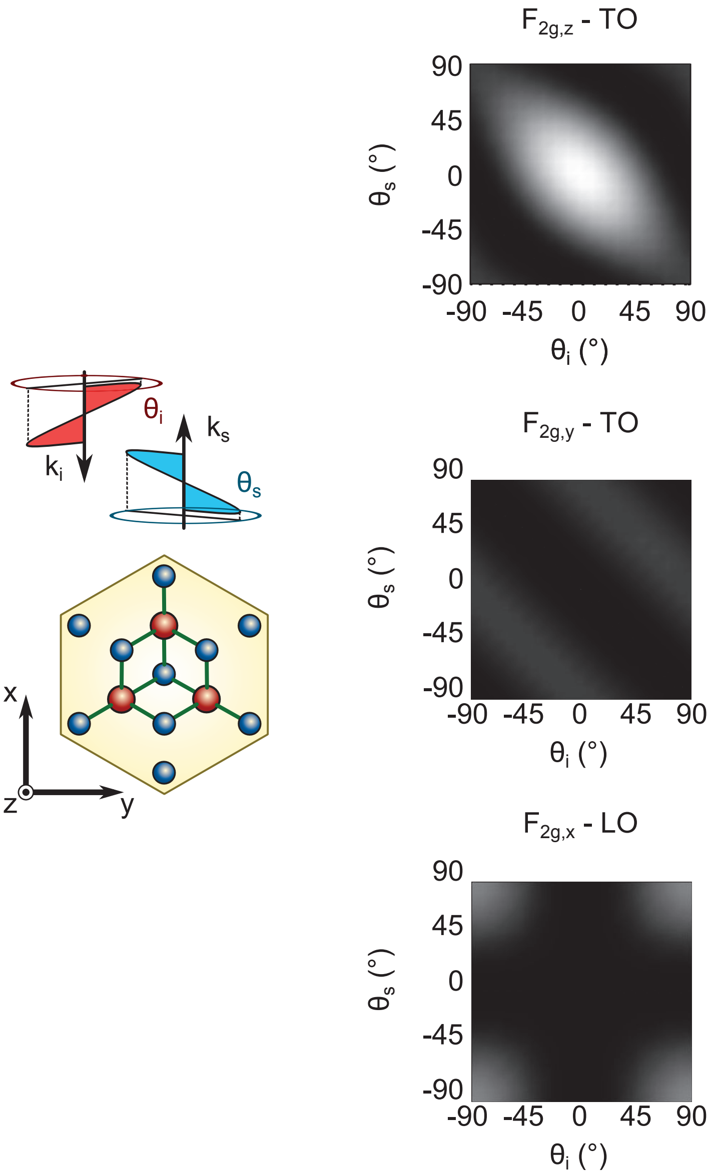

Figure 4.9: Raman scattering selection rules for Zincblende. The scattering geometry is sketched on the left: the z-axis is oriented along [111], the x-axis along $[11\bar{2}]$ and the y-axis along $[1\bar{1}0]$. The scattering intensity for the TO phonons, with displacement along z and y, and LO phonon, with displacement along x, is represented in gray-scale as a function of the incoming and scattered polarization angle. All phonon modes are visible in this scattering configuration.

facets of a nanowire, while in figure 4.9 we represent the selection rules calculated rotating the nanowire by 30°, i.e. with the laser beam directed along $[11\bar{2}]$ and impinging on a nanowire edge. In both configurations, the TO phonon oriented along [111] provides the highest intensity contribution when both incoming and scattered light are polarized along [111]. The displacement of this phonon is also not affected by any rotation along the z-axis and, therefore, its $I(\theta_i, \theta_s)$ colorplot remains unchanged between figure 4.8 and figure 4.9. The remaining two phonons, with displacement in the x-y plane, show instead a dependence on the crystal orientation. In particular, if the laser and detected light have wave-vector along the $[11\bar{2}]$, the LO phonon is visible if the polarizer and the analyzer are oriented orthogonally to the z-axis. The same phonon is instead strictly forbidden, i.e. does not provide any signal for any polarizer configuration, if the excitation and detection wave-vectors are oriented along the $[1\bar{1}0]$ direction. In this same scattering configuration the TO phonon with displacement along y provides instead maximum intensity. We can conclude that, to resolve the energy difference between the two TO phonons under applied stress, it is important to choose correctly the backscattering orientation so that the signals from the different phonons are maximized. The polarization dependence can also be exploited to resolve which phonon contributes to which part of the Raman spectrum.

4.4.3 Raman Scattering Selection Rules in Wurtzite Crystals

In §2.3.2 we have explained that optical phonons of Wurtzite crystals can be decomposed into a combination of phonons with symmetry A_1, E_1, E_2 and B_1. However, only vibrations with the first three symmetries are Raman active and are associated to a Raman tensor different than zero. Choosing z along the c-axis, and x and y in the hexagonal plane of the Wurtzite unit cell, we can express the Raman tensor with the following relations[101]:

$$\mathfrak{R}_x^{E_1} = \begin{bmatrix} 0 & 0 & 0 \\ 0 & 0 & c \\ 0 & c & 0 \end{bmatrix}, \quad \mathfrak{R}_y^{E_1} = \begin{bmatrix} 0 & 0 & -c \\ 0 & 0 & 0 \\ -c & 0 & 0 \end{bmatrix}, \quad \mathfrak{R}_z^{A_1} = \begin{bmatrix} a & 0 & 0 \\ 0 & a & 0 \\ 0 & 0 & b \end{bmatrix},$$

$$\mathfrak{R}_x^{E_2} = \begin{bmatrix} d & 0 & 0 \\ 0 & -d & 0 \\ 0 & 0 & 0 \end{bmatrix}, \quad \mathfrak{R}_y^{E_2} = \begin{bmatrix} 0 & d & 0 \\ d & 0 & 0 \\ 0 & 0 & 0 \end{bmatrix}. \tag{4.24}$$

As in the Zincblende case, the Raman tensors in equation (4.24) posses third rank tensor properties and because of the Wurtzite symmetry, $\mathfrak{R}$ will be defined by four costants a, b, c and d. The crystallographic reference system corresponds to the scattering reference system and, unlike the Zincblende case, rotations of the Raman tensors are not necessary. For simplicity we will treat only one single scattering configuration geometry, shown in figure 4.10, and represent the contribution to the Raman spectrum $I(\theta_i, \theta_s)$ of the different phonons in a two-dimensional plot. To the best of our knowledge, the relations between the coefficients a, b, c and d that define the Raman tensor of Wurtzite GaAs have not been determined yet. We therefore highlight their contribution to the Raman intensity with different colors in figure 4.10. The polarization dependence can be used to identify the different phonon contributions. Similarly to the Zincblende case, the TO phonon with symmetry A_1, i.e. with displacement along the z-axis, has maximum intensity with polarizer and the analyzer aligned parallel to the z-axis and the LO phonon with symmetry E_1, i.e. with displacement along the x-axis, is strictly forbidden. The TO phonon with symmetry E_1, i.e. with displacement along the y-axis, provides maximum contributions if the polarizer and analyzer are orthogonal to each other, and the two E_2 phonons provide maximum intensity if both polarizer and analyzer are orthogonal to the z-axis.

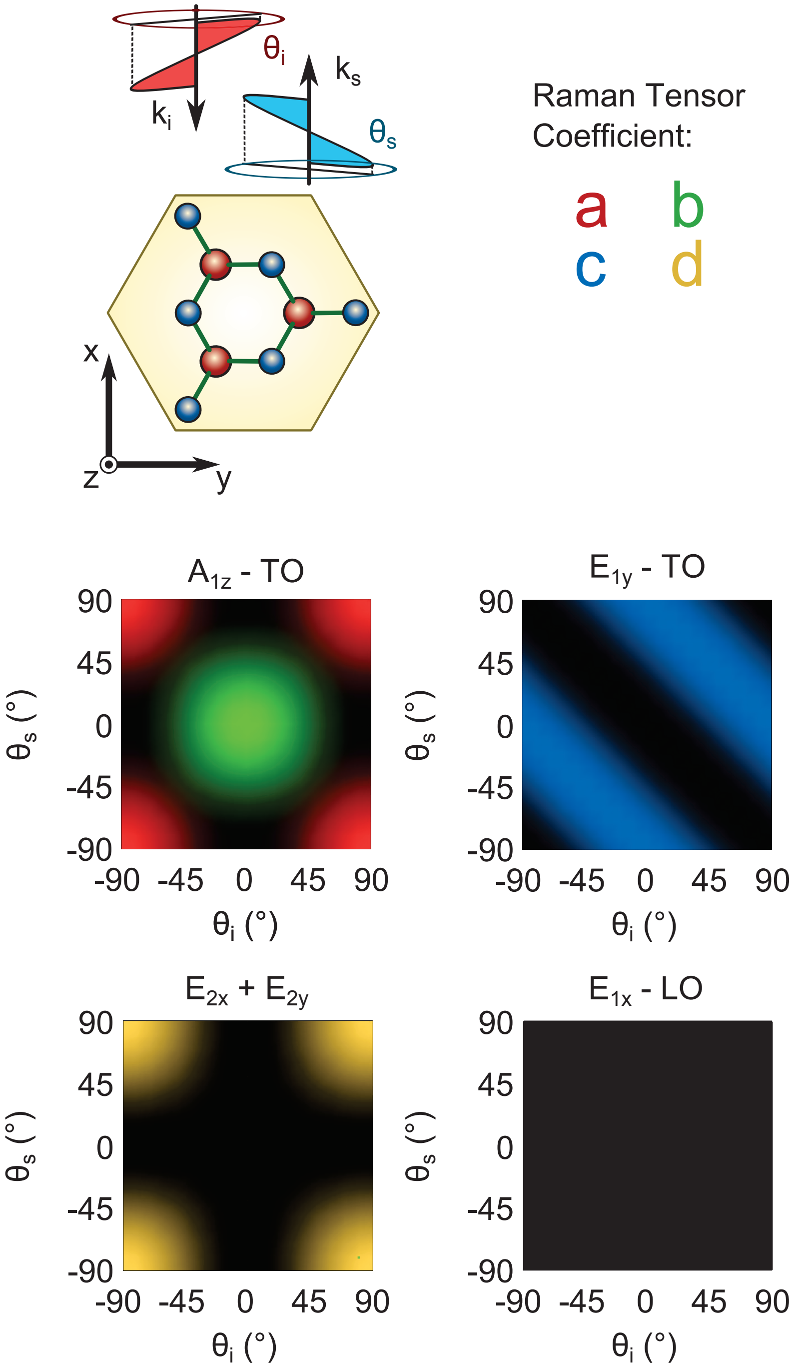

Figure 4.10: Raman scattering selection rules for Wurtzite crystals. The scattering geometry is sketched on the upper left corner: the x, y and z-axis are defined in §2.1. The contributions to the Raman spectrum of the A_1, E_1 and E_2 phonons are represented with color plots. The contributions of the five different coefficients of the Raman tensor is represented with four different colors. For the polar phonons, the transversal or longitudinal nature is specified.

5

Uniaxial Stress Effects on Nanowires: Experimental Methods

"Genius is one percent inspiration, ninety-nine percent perspiration."

Thomas Alva Edison

This chapter is dedicated to the description of the experimental techniques used in our strain experiments: the next sections will provide a description of all the elements used to perform the measurements. We describe briefly the methods used to grow Zincblende and Wurtzite nanowires, providing information about their crystal structure by Transmission Electron Microscopy (TEM), and describe the design principles and the nanofabrication steps necessary to manufacture a strained nanowire device. We then shift our focus to the setup used to apply strain to the nanowire devices and give an overview of the optical spectroscopy setup, with particular attention on the optical units that made possible the control of the polarization in the excitation and analytic path. We conclude the chapter with an overview of the size dependence effects that are expected on our strain experiment.

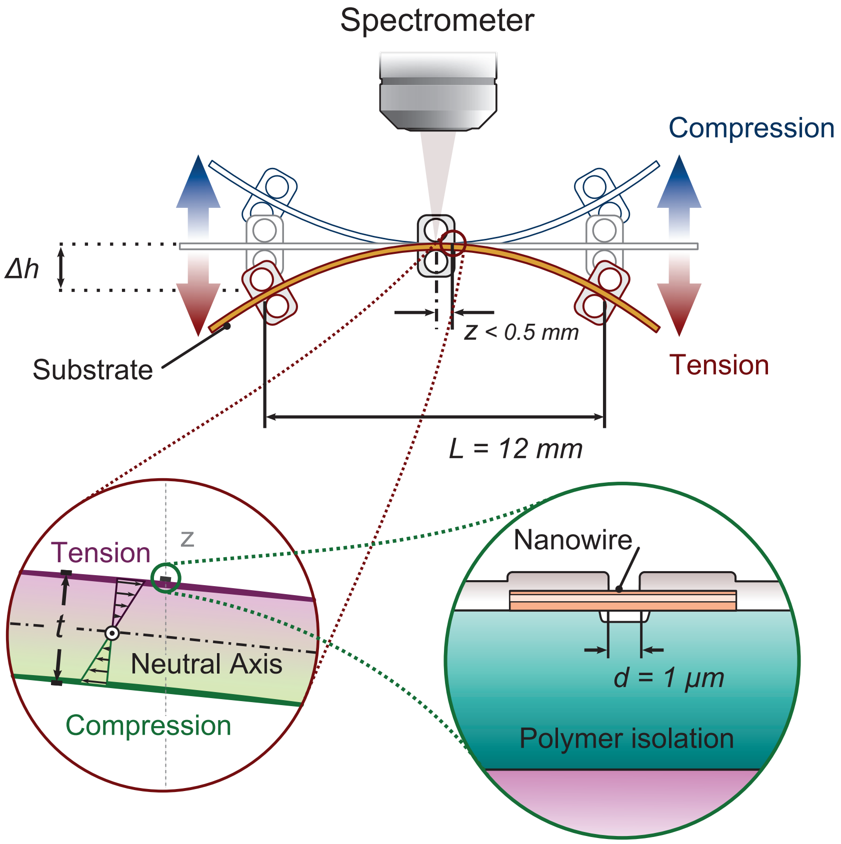

Figure 5.1: Schematic representation of the three-point bending mechanism.

5.1 How to Apply Uniaxial Stress to a Nanowire

Uniaxial stress is applied on a single nanowire by a mechanical microstructure in which the nanowire is embedded. This device is realized on a flexible substrate that is subject to a mechanical deformation in a three-point-bending mechanism. When the lateral supports of the bending mechanism are displaced downwards compared to the central one, as shown in figure 5.1 by the red arrows, the substrate is bent in a convex fashion, creating a tensile strain on its top surface. This surface extension is then transferred to the nanowire by a compliant polymer layer and by the metal contacts that keep the nanowire solidly connected to the substrate surface. By moving the lateral supports in the opposite direction, as shown by the blue arrows, a concave bending of the substrate can be achieved and compressive stress can be induced in the nanowire. The effects of strain on the electronic and vibrational properties of the nanowire are studied using optical spectroscopy techniques as photoluminescence spectroscopy and Raman scattering.

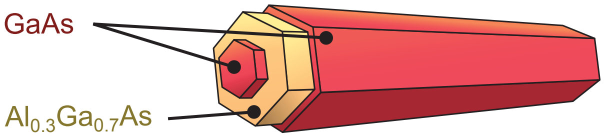

Figure 5.2: Schematic illustration of the core-shell structure of the GaAs-$Al_xGa_{1-x}As$-GaAs nanowires.

5.2 Nanowire Growth and Characterization

Both Wurtzite and Zincblende nanowires used in the strain experiments share a particular core-shell structure, represented schematically in figure 5.2. The nanowires have a GaAs core of hexagonal cross section and diameter ranging between 40 nm and 50 nm. The core is surrounded by a uniform $Al_xGa_{1-x}As$ shell, with a thickness of 50 nm, that ensures the passivation of the interface states between GaAs and $Al_xGa_{1-x}As$ and enables a stable photoluminescence[34,102–107]. The shell does not introduce any strain on the core because, in the Zincblende phase, the difference between the lattice constant of AlAs and the one of GaAs is smaller than 0.0078 Å. The formation of strain at the core-shell interface is also excluded when strain is applied. In the Zincblende phase, the compliance matrix elements follow a linear dependence on the aluminum concentration, increasing by 14 MPa/% for C_{11}, 32 MPa/% for C_{12} and −5 MPa/% for C_{44}[88]. For an aluminum concentration of 30 %, all compliance matrix elements have values within a few percent of the one of GaAs. As for the Wurtzite nanowires, information with this level of detail is not yet available. However, one can relate the mechanical properties of these crystals to the ones of Zincblende using Martin's relations[87]. It is therefore reasonable to assume that the absence of strain at the core-shell interface holds also for Wurtzite nanowires. The outer GaAs shell, the thickness of which is 3 nm, was grown to prevent oxidation of the AlGaAs shell under ambient conditions. This enables measuring the optical spectra of the nanowires even at room temperature over weeks without any degradation.

Both Wurtzite and Zincblende nanowires were grown with Vapour-Liquid-Solid (VLS) technique[108]: group III and group V chemical species are supplied in gas phase and are absorbed at the surface of a metal nanoparticle, which acts as catalyst for the growth reaction. Upon continuous supply, the metal nanoparticle reaches a condition of supersaturation. At this point the chemical constituents of the nanowire precipitate at the interface between the liquid-metal and the solid substrate, beginning to form a nanowire. When the metal catalyst dimensions are macroscopic, GaAs crystallize with the Zincblende structure. However, as the cross-sectional dimension of the metal particle decrease, the surface-to-volume ratio increases. Interestingly, the surface energy of the Wurtzite {110} planes is lower than {110} and {111}A/B planes of Zincblende: because of this property, the Wurtzite phase becomes the most stable crystal structure at the nanoscale[36,37]. For nanowire dimensions of a few tens of nanometers every small perturbations can change the delicate balance between bulk and surface energy, introducing variations in the stacking sequence, and causing a randomly alternated segments of Wurtzite and Zincblende. However, by tailoring the temperature, pressure and supply of group III and V species, it is possible to shift the balance of the reaction towards the growth of a single Wurtzite or Zincblende crystals: although very challenging, it is possible to synthesize single crystalline GaAs nanowires with both structures.

The two different techniques, used to grow the nanowires of this work, are shown schematically in figure 5.3: Metallo-Organic Chemical Vapour Deposition (MOCVD) was the technique of choice to grow Zincblende nanowires, while Molecular Beam Epitaxy (MBE) has been employed to grow nanowires with the Wurtzite structure.

5.2.1 MOCVD Growth of Zincblende Nanowires

MOCVD has become a standard growth technique for III-V alloys and is used to manufacture commercially available lasers and light emitting diodes. In this technology the growth species are introduced in a reactor in the form of metal-organic complexes, like trimethylgallium (TMGa), trimethylaluminum (TMAl) and tertiarybutylarsine (TBAs). These gases are combined in the reactor at elevated temperatures and undergo a chemical interaction that results in the deposition of materials on the substrate. The reactor chamber is made of stainless steel or other materials that withstand high temperatures and do not react with the chemicals. Its walls are kept at a low temperature by a closed loop cooling system, ensuring that the growth occurs on the substrate surface. The substrate is kept at a controlled temperature by a susceptor, that is the primary origin of heat in the reactor. The metal-organic species are stored in liquid phase in devices called bubblers: hydrogen carrier gas is introduced in these devices and bubbles through the liquid, forming a metal-organic vapour that can be transported in the reaction chamber.

The core-shell nanowires with Zincblende structure used in our strain experiments were grown in a Veeco Turbodisc P125LDM MOCVD system by Mikael Björk at IBM Research - Zurich. The GaAs nanowires core were grown on a GaAs [111]B substrate, using colloidal gold nanoparticles, a TMGa molar flow of 10 µmol/min and a V/III ratio of 15, at a temperature

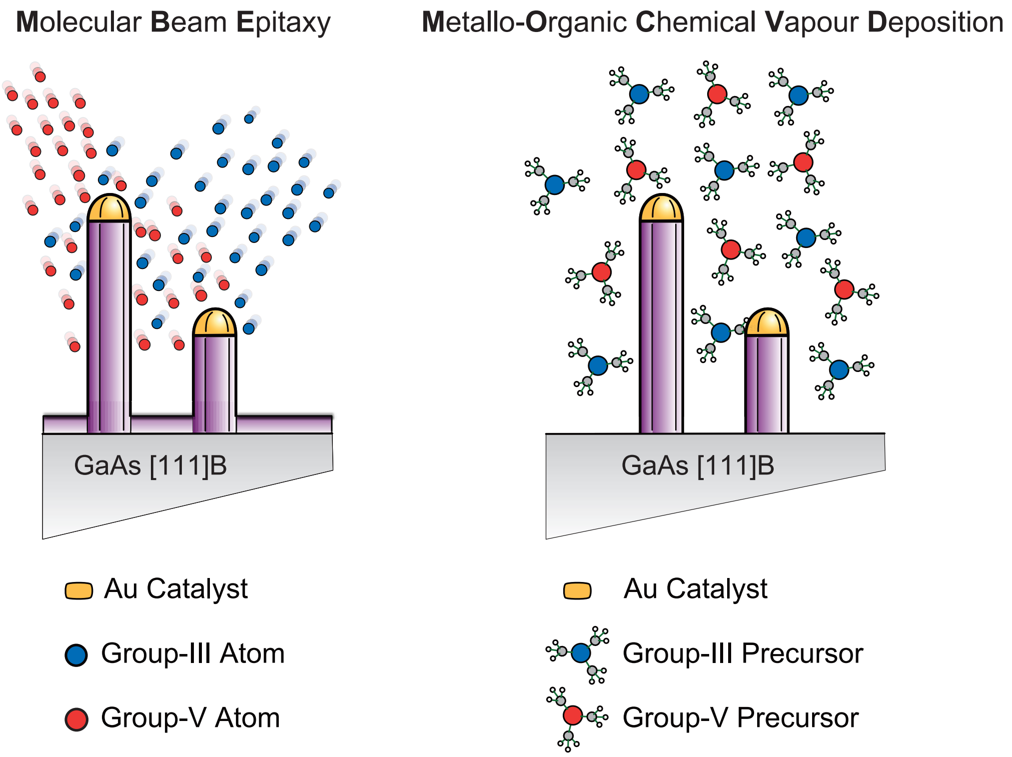

Figure 5.3: Different techniques employed to grow nanowires, i.e. MBE (left) and MOCVD (right). In both cases the vapour-liquid-solid growth was applied.

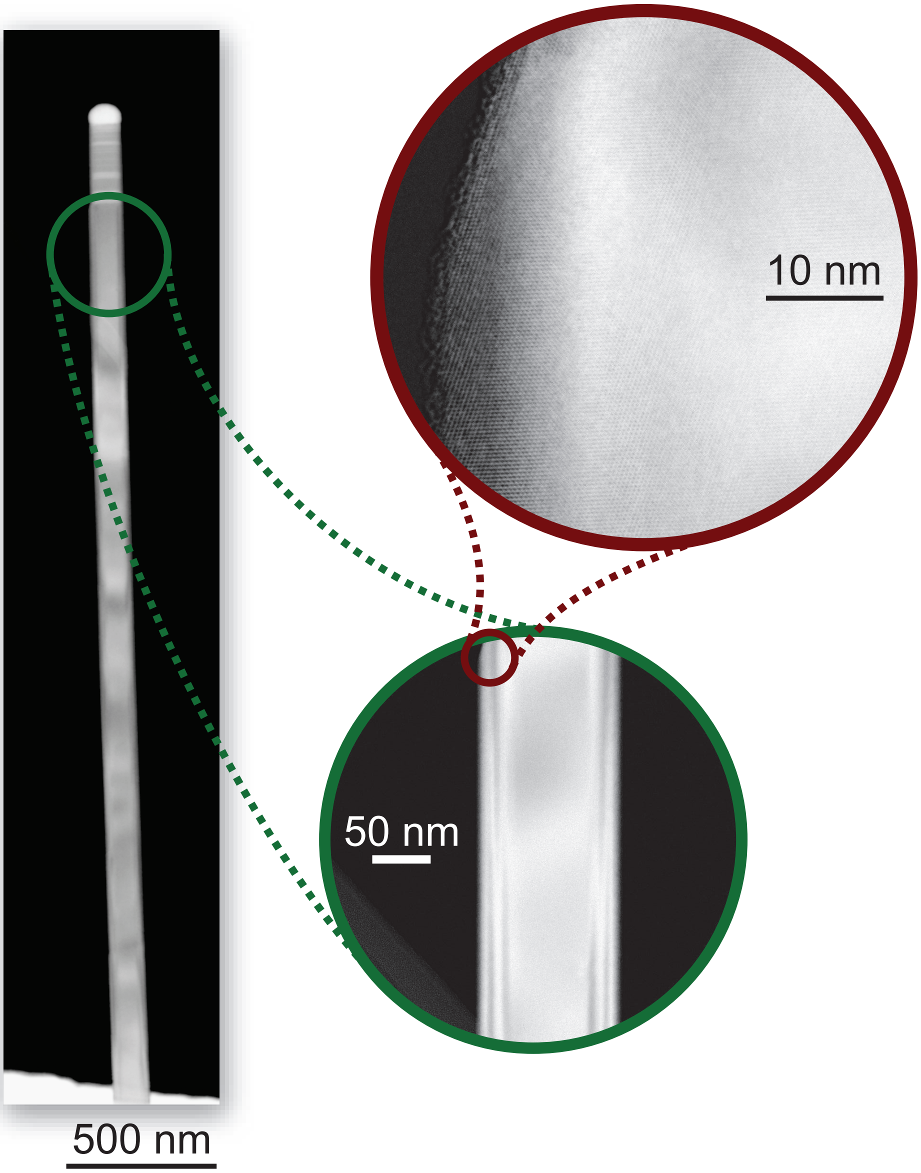

Figure 5.4: TEM micrograph of a typical Zincblende nanowire. No stacking faults could be observed in the nanowire body. Courtesy of Teya Topuria and Philip Rice at IBM Research - Almaden.

of 360 °C and a total pressure of 80 mbar. The $Al_{0.3}Ga_{0.7}As$ and GaAs shells were both grown at 650 °C with the addition of TMAl at a flow rate of 10 µmol/min for the inner shell, 6.66 µmol/min for TMGa and 3.33 µmol/min for TMAl. The wires have a uniform cross section and a length ranging between 7 µm and 8 µm.

T. Topuria and P. Rice at IBM Research - Almaden have performed high-resolution transmission-electron microscopy (HRTEM) on many of these nanowires. A typical HRTEM micro-graph, shown in figure 5.4, reveals that the crystal structure of the nanowires is Zincblende and almost free of twin defects: the stacking fault density is less than one per micrometer.

5.2.2 MBE Growth of Wurtzite Nanowires

Molecular beam epitaxy (MBE) is a technique that relies on the deposition of atoms, or clusters of atoms, produced at high temperatures by a solid source. This technique was invented in the late 1960s at Bell Telephone Laboratories by J. R. Arthur and A. Y. Cho[109]. To obtain high quality materials in terms of purity, uniformity and abruptness of the hetero-interfaces, the growth chamber is kept in UHV conditions. The control of the substrate temperature ensures that atoms and clusters can diffuse on the substrate surface and incorporate into the growing film, maintaining with it the desired epitaxial relations. The most critical component of the MBE system is the effusion cell, which must provide excellent flux stability, uniformity and material purity. The growth chamber is connected to the load-lock module via a preparation chamber, where substrates are introduced from environmental conditions and degassed prior to the growth.

The core-shell nanowires with Wurtzite structure were grown by Dasa Dheeraj, in the group of Helge Weman at the Technical University of Trondheim (NTNU)[107], using a Riber 32 system equipped with Ga dual filament cell and cracker cells for As and Al. Colloidal nanoparticles were not used to prevent the contamination of the MBE chamber with the hydrocarbons that stabilize the nanoparticles. Instead, the surface of the GaAs [111]B substrate was deoxidized at 620 °C, capped with an amorphous As layer to avoid oxidation during its transfer in ambient conditions, and coated with a 1 nm thick gold film deposited by electron-beam evaporation. The sample was then loaded into the MBE system and the As cap was desorbed at 280 °C, at a pressure of 1×10^{-7} mbar. Under an As flux of 6×10^{-6} mbar, the substrate temperature was increased to 540 °C. At this stage, Au alloys with the substrate forming nanoparticles that catalyze the nanowire growth. The temperature of the Ga effusion cell was preset to yield a nominal planar growth rate of 0.7 ML/s. The GaAs nanowires, grown for 25 min, have a uniform hexagonal cross section along the length, and a diameter distribu-

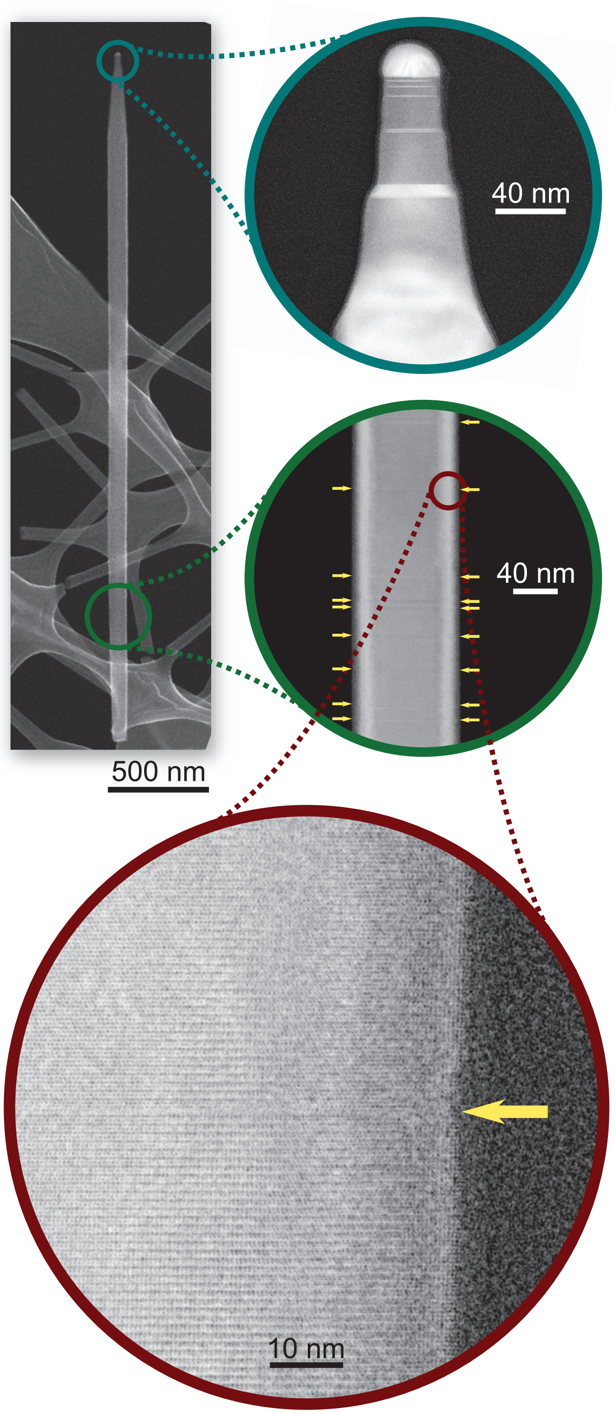

Figure 5.5: HRTEM micro-graph of a typical Wurtzite nanowire. The yellow arrows indicate the presence of a stacking fault. Courtesy of Teya Topuria and Philip Rice at IBM Research - Almaden.

tion ranging from 30 nm to 100 nm. To grow the AlGaAs shell, the Al flux was initiated and the temperature of the respective effusion cell was preset to yield the growth of $Al_{0.3}Ga_{0.7}As$ on planar GaAs (001) substrates. The V/III flux ratio was kept constant by adjusting the As flux. After a growth time of 15 min, the Al, Ga and As fluxes were shut down simultaneously and the substrate temperature immediately ramped down to room temperature.

An example of a typical nanowire HRTEM micro-graph is given, at different magnifications, in figure 5.5. Images like this reveal that the longest wires, which have a diameter of about 150 nm, have a predominant Wurtzite structure with low density of stacking faults, which are highlighted with yellow arrows in figure 5.5. The average stacking fault density is less than $35\,\mathrm{nm}^{-1}$.

5.3 Sample Nanofabrication

In this section we will describe the mechanical, optical, electrical and fabrication requirements imposed by the strain experiment on the substrate, and provide an overview on the fabrication steps used to realize the flexible substrates. We will then illustrate the design of the stress device and describe the steps involved in its fabrication. All nanofabrication steps have been developed by the author of this thesis at IBM Research - Zurich.

5.3.1 Flexible Substrate Design and Fabrication

For the specific application targeted by our strain experiment, a substrate material has to comply with different mechanical, optical, electrical and fabrication requirements.

A detailed analysis of the mechanics of a bending beam, provided in appendix D, suggests that the substrate has to be flexible, elastic and as thick as possible, so that very large axial stress values can be achieved. The Youngs modulus of the substrate material has to be small, so that bending can be easily achieved with the available actuators and motors. Plastic deformation is the preferred mode of failure of the substrate under high deformation. Brittle substrate materials have been avoided, especially when working in UHV conditions: with this choice we avoid that, upon failure, parts of the substrate can damage the turbo-molecular pumps used to achieve the low pressures necessary to work at cryogenic temperatures. Stainless steel or phosphor-bronze sheets, with thickness around 250 µm, have been selected as substrate material of choice: both materials are elastic over a large range of deformations and allow to apply large amounts of stress without brittle failure. Sheets of these materials can also be cut to any desired shape using laser cutting technology. To comply with the fabrication tools used later on, we realized disks of 10 cm (4-inch) in diameter.

The substrate surface is then coated with a flexible polymer that allows to electrically insulate the top surface from the metal substrate, achieve a good planarity, and preserve the compatibility with the lithography and nanofabrication steps performed later on. To comply with the optical requirements, the material must be as "inert" as possible upon excitation with the laser, providing the smallest possible PL or Raman features. Polymers used traditionally in electronics packaging, like polyimide, do not comply with such requirement as they provide a strong photoluminescence when excited in the visible range of the spectrum. On the other end, optical adhesives and polymers used in optoelectronic packaging fulfill the optical requirements but fail when the fabrication requirements are considered. These materials are elastic and stable only below 120 °C: this is a very tight limitation, which strongly affects later fabrication steps like lithography or metal deposition. The surfaces of these materials do not comply well with the metalization steps, too. Evaporated or sputtered films of metals or oxides do not have good adhesion with the polymer surface, and can easily delaminate, especially when in contact with organic solvents.

Different kind of optical adhesives and polymers have been tested and their transmission spectra have been acquired to identify the most inert in the visible to infra-red range. Out of a selection of these materials, different kind of curing methods (UV, vacuum oven, hotplate) and surface preparation steps have been tested, in order to achieve the best transparency together with a good processability. The overview of the processing steps needed to fabricate the substrates is shown in figure 5.6 and summarized in the following list.

- Stainless steel or phosphor-bronze disks are polished until a low surface roughness, that enables the observation of the nanowires, is achieved.
- The insulating polymer is spin-coated on the substrate surface to a thickness of about 12 µm. The sample is cured, using a flat exposure UV lamp.
- The sample is introduced in a vacuum oven, to remove traces of solvent.
- Optical lithography is performed to define metal markers on the substrate surface. A two layer resist recipe is used (LOR5B and AZ6612). The resist thicknesses obtained are about 500 nm for the bottom layer and 1.2 µm for the top layer.
- The photoresist is developed using a solution of AZ400K developer, diluted 4:1 in de-ionized water (DI). After the development, the sample

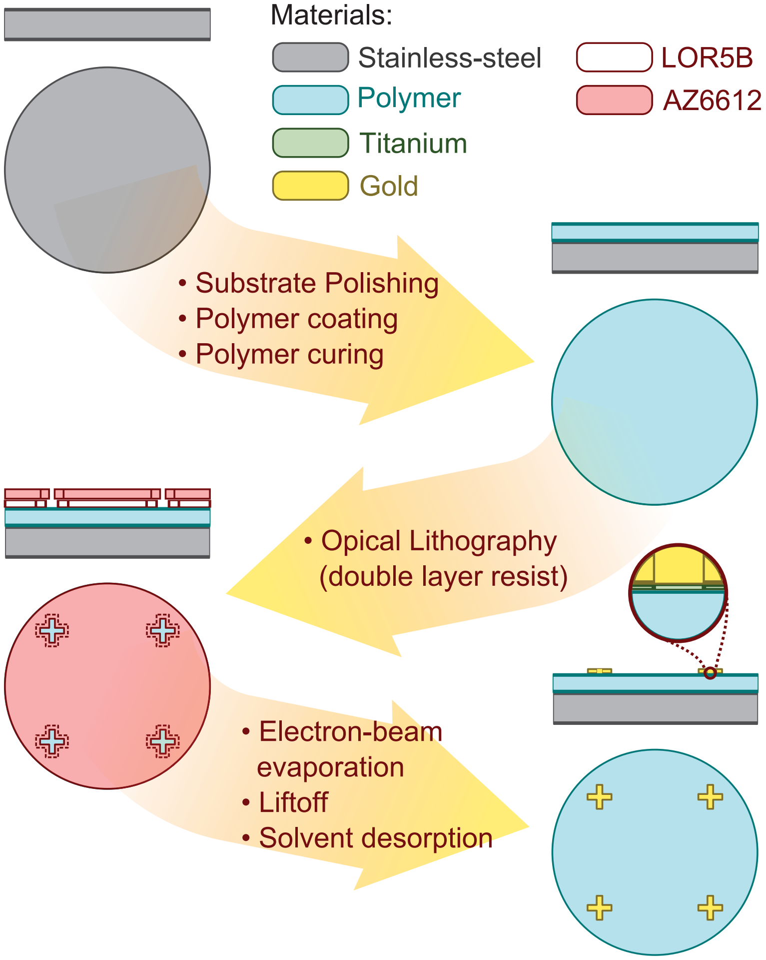

Figure 5.6: Fabrication steps used to realize the flexible substrates.

is rinsed in DI water. Care must be taken that the bottom layer of resist is fully developed and a good undercut is formed.

- The sample is treated in oxygen plasma to remove eventual contaminations and activate the substrate surface, enabling a stable bond formation later on with the metal deposited.
- Metal is deposited in an Electron Beam Physical Vapor Deposition (EBPVD) evaporator. Typically 30 Å of titanium (Ti) and 500 Å of gold (Au) are deposited.
- The metal is lift-off by removing the remaining AZ resist in acetone. To accelerate the process, the sample is immersed in an ultrasonic bath. When the lift-off is complete, the sample is rinsed with acetone and Isopropanol (IPA).
- The sample is introduced in a convection oven, to remove traces of solvent.
- The LOR5B layer is removed in a bath of N-Methyl-2-pyrrolidone (NMP). The substrate is then rinsed in DI water for 3 min and dried in a convection oven at 200 °C for 5 min.
- Using a metal cutter, the substrates can then be cut in smaller pieces, on which the nanowire device fabrication can be performed.

5.3.2 Nanowire Strain Device: Design and Fabrication

Before describing the fabrication steps used, we would like to spend a few words on the design of a strain nanowire device and, in particular, consider how to transmit the surface strain, generated by the substrate bending, to the nanowire under investigation. This function can be performed by a simple mechanical structure, consisting of two metal clamps at the two ends of the nanowire. We will show that, with a simple design, it is possible to concentrate the structure elongation in the nanowire and mechanically amplify the nanowire strain beyond the value defined by the surface expansion.

Let us consider the structure in figure 5.7a and study the distribution of stress and strain upon its elongation. For simplicity, we can represent the structure with a lump element model and each component can be described by a spring and its associated spring constant: k_{clamp} will describe the spring constant of the metal clamps, and k_{nw} will instead describe the nanowire. The strain on the substrate surface will define the total elongation of the device Δl_{dev}, which is given by the sum of the elongation of the contacts Δl_{clamp} plus the one of the nanowire Δl_{nw}. Considering that the axial forces

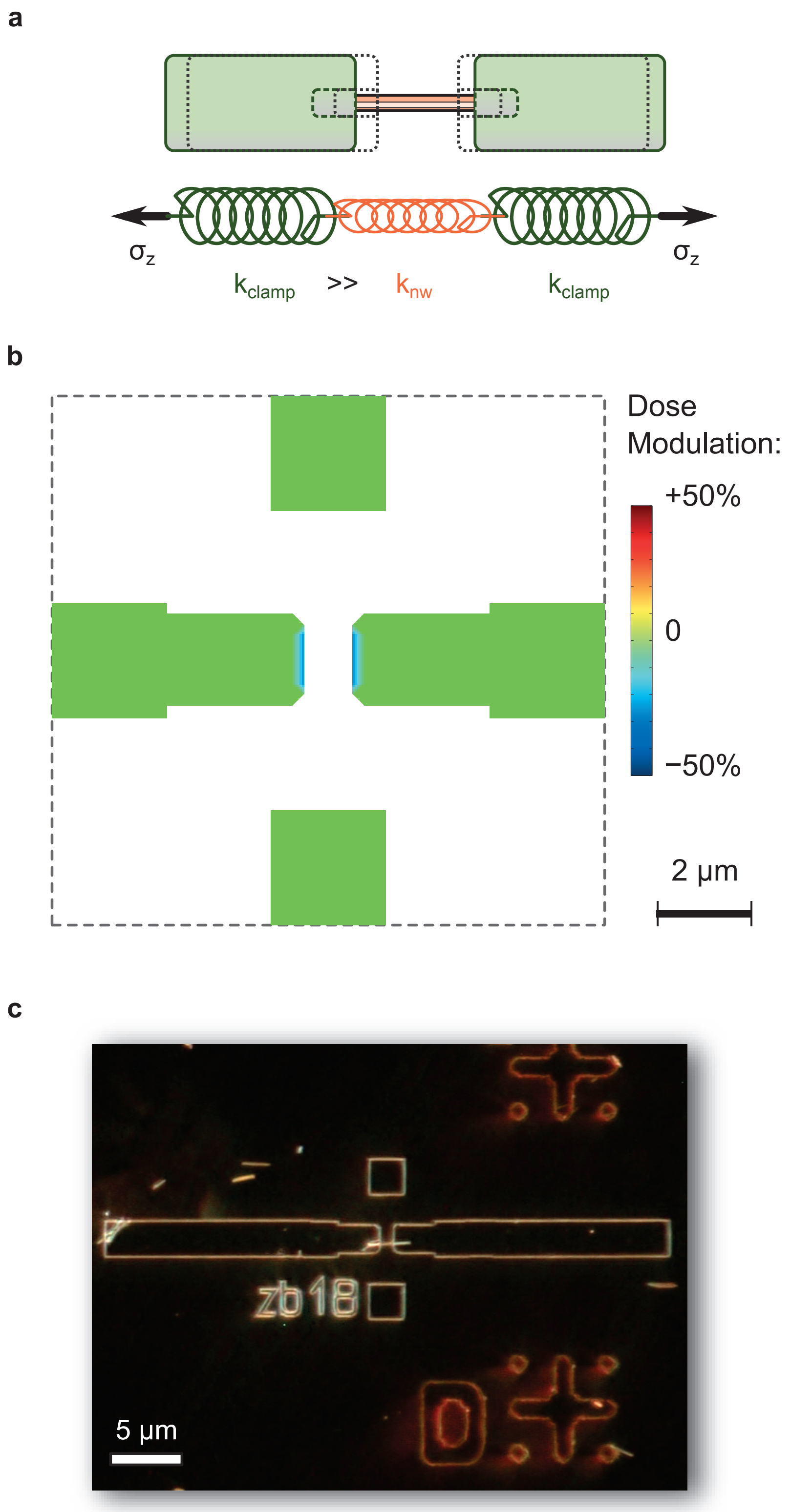

Figure 5.7: Nanowire strain device. (a) Lumped elements model of the mechanical structure. (b) Electron-beam lithography design and dose modulation pattern, shown with a colour scale. (c) Dark-field optical image of a device after the lift-off of the metal clamps.

that induce stress on each spring are the same for all the components of the structure, the relation between the elongation of the nanowire and the one of the whole structure can simply be obtained:

$$\Delta l_{\mathrm{nw}} = \frac{k_{\mathrm{clamp}}}{k_{\mathrm{clamp}} + 2\,k_{\mathrm{nw}}} \Delta l_{\mathrm{dev}} \tag{5.1}$$

If the spring constant of the mechanical clamp is much higher than the one of the nanowire, the elongation of the structure and the one of the nanowire become equal. The mechanical strain of the structure can be therefore concentrated on the nanowire, and the strain of the nanowire can be mechanically amplified:

$$\varepsilon_{\mathrm{nw}} = \frac{k_{\mathrm{clamp}}}{k_{\mathrm{clamp}} + 2\,k_{\mathrm{nw}}} \left(1 + \frac{2\,l_{\mathrm{clamp}}}{l_{\mathrm{nw}}}\right) \varepsilon_{\mathrm{dev}} \tag{5.2}$$

Different parameters can be optimized to achieve a high mechanical amplification. The elastic modulus of the metal used to realize the mechanical clamps should be maximized and, preferably, higher than the one of GaAs. The spring constant of the contacts is proportional to the thickness and width of the contact: both should be as large as possible. The mechanical clamp thickness, however, is limited by the fabrication method and should be smaller than one-third of the thickness of the resist for a good lift-off process. The width of the contact can instead be defined in the electron beam lithography layout. Wide contacts provide the high spring constant needed and, at the same time, are more tolerant against the uncertainty of the nanowire position. Finally, the length of the clamps should be as large as possible. The final e-beam design is shown in figure 5.7b. Each contact has a thickness of 180 nm and lateral dimensions of 3 µm × 20 µm, while the width of the nanowire segment left uncovered by the clamps is 1 µm.

To realize the final device some processing challenges of different nature had also to be overcome. The polymer coating has a poor electrical conductivity and the exposure to the electron beam during the lithography step results in strong charge build-up on the surface, which can deflect the electron beam and impair the achievement of the desired geometry. For beam voltages of 20 kV, normally used in our lithography system, the charge build-up is so severe that dielectric breakdown of the polymer coating occurs and cracks develop across its entire thickness. Higher acceleration voltages can be used to enlarge the penetration depth of the electrons in the polymer: with an acceleration voltage of 30 kV, the electrons have enough energy to reach the stainless steel surface, where charges can therefore be drained. To limit the remaining charging effects the e-gun aperture was decreased to 10 µm and dose modulation profiles, like the one shown in figure 5.7b,

Metal	Modulus of Elasticity (GPa)	Specific Heat ($\mathrm{J\,kg^{-1}\,K}$)	Melting Temperature (°C)
Chromium (Cr)	279	448	1907
Nickel (Ni)	200	445	1445
Titanium (Ti)	116	520	1668
Molybdenum (Mo)	329	251	2623
Gold (Au)	78	129	1064
AlGaAs [111]	142		

Table 5.1: Elastic and thermal properties of metals that can be evaporated with by EBPVD. The elastic modulus of AlGaAs alloys along the [111]-direction is given as a reference value.

had to be implemented in the smallest constrictions of the device design. Finally, to obtain a good contrast, the beam dose had to be increased by a factor of two compared to the normal dose used on silicon substrates, up to $370\,\mathrm{\mu C\,cm^{-2}}$.

The mechanical clamps have been fabricated using different metals, like the ones shown in table 5.1. Titanium was elected as the material of choice as it provided the easiest lift-off process, the best contact with the nanowire, and maintained the highest substrate integrity after processing. The nanofabrication steps necessary to manufacture the final strained nanowire device are shown schematically in figure 5.8 and are described in the following list:

- The core-shell nanowires are harvested from their growth substrate using a small piece of clean-room paper. The nanowires are then deposited on the flexible substrate by putting the paper in contact with the substrate. By “brushing” the surface along one direction a good alignment can be achieved for many nanowires.

- The substrate surface is then imaged using a high magnification (100X) optical microscope in dark field mode. The longest nanowires with the desired orientation are identified and images are acquired with a Charge-Coupled Device (CCD) camera.

- With the aid of Computer-Aided Design (CAD) software, an electron beam lithography pattern is designed specifically for each nanowire. The optical microscope images are used to locate the nanowires on the substrate: the metal markers on the substrate are used to correctly identify the nanowire position.

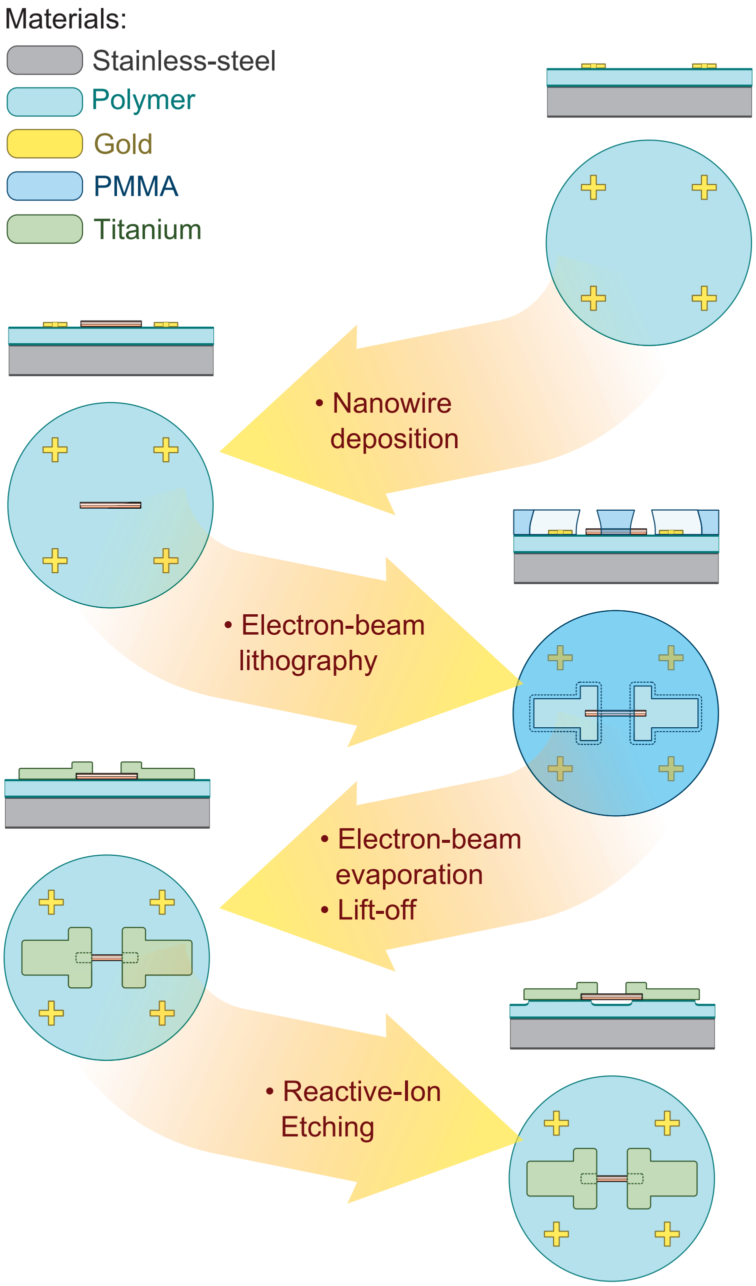

Figure 5.8: Fabrication steps used to fabricate a doubly clamped nanowire device.

- The sample is spin-coated with electron beam resist, consisting of a solution of PMMA 950K with 4% concentration in Anisole, at 2500 rpm for 40 s.

- The sample is baked on a hotplate at 195 °C for 90 s to allow the evaporation of solvents.

- Electron beam lithography is performed in a Raith e-line system, which is based on the electron optics system of a Zeiss Supra 35 Scanning Electron microscope (SEM). The column voltage is set to 30 kV and the gun aperture to 10 µm. The beam current has a value close to 35 pA. The dose was set to 370 µC/cm^2 to obtain good contrast.

- The sample is developed in a solution of Methyl-Isobutyl-Ketone (MIBK) 1:3 in IPA for 50 s. The sample is then rinsed in IPA.

- A short oxygen plasma step is performed to activate the polymer surface. This step is performed in a partial oxygen pressure of 1.5 mbar at 200 W for 20 s.

- A 180 nm thick film of titanium is deposited on the sample with a EBPVD evaporator, at a pressure of 5×10^{-7} mbar and with a deposition rate of 100 Å/min.

- The metal is lifted-off in acetone over night. To ensure a good contact between the metal and the nanowire, no ultrasonic bath must be performed.

- To release the acetone absorbed by the polymer, the sample is introduced in a convection oven at 70 °C for 5 min. A typical sample optical image is shown in figure 5.7c.

- The sample is cut in the final shape, to fit in the bending mechanism. A metal cutter is used for this purpose.

- A Reactive-Ion Etching (RIE) step is performed for less than a minute to etch the polymer underneath the nanowire, decoupling it mechanically from the substrate. The step is performed using a mixture of oxygen and sulfur hexafluoride (SF_6), with fluxes of 5 and 50 sccm, at a partial of pressure 150 mbar. The reactor delivers 20 W of power at a voltage of 200 V.

The SEM image of a typical completed device is shown in figure 5.9a. The sample is now ready to be mounted on the three-point bending mechanism to perform the strain measurement.

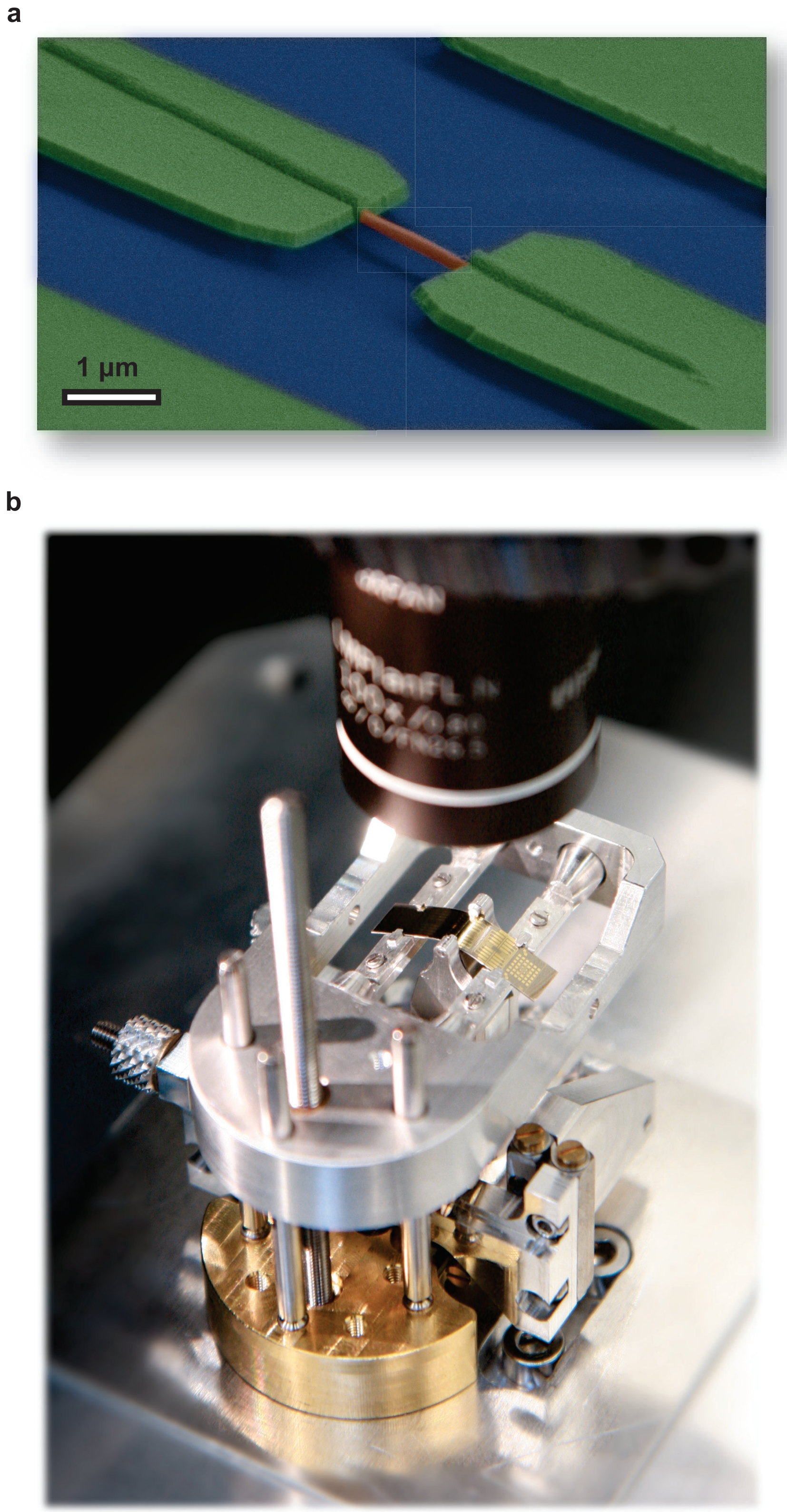

Figure 5.9: Strain nanowire device ready to be measured. (a) SEM image of finalized nanowire device. (b) A sample is mounted and bent on a three-point bending mechanism.

5.4 Three-point Bending Mechanism

To apply uniaxial stress and measure the effect of strain on the nanowire devices, the samples are mounted and bent in a three point bending mechanism, like the one sketched in figure 5.9b. This mechanism has been designed by Emanuel Lörtscher and realized by Lukas Schuler, Marcel Buerge, Meinrad Tschudy and the mechanical workshop team at IBM Research - Zurich. A detailed theoretical treatment of the continuum mechanics of a beam undergoing this kind of deformation is provided in appendix D. Here we will just summarize the most important features of the mechanics.

The three point bending mechanics allows to span a very large dynamic range of surface strain, as high as 10 %, with an accuracy of the order of one part in 10^9, without inducing plastic deformation of the substrate. With our sample geometry, a bending angle smaller than 8×10^{-5} degrees is induced by every percent of elongation of the nanowire. The three-point bending is therefore particularly suitable to induce purely uniaxial stress on the nanowire. As shown in appendix D, the surface strain of the substrate is proportional to the local value of bending moment on the substrate, which is maximum at the center of the beam and decreases linearly to zero to the lateral clamps. It is therefore best practice to locate the nanowire in the central region of the substrate, where it will experience the maximum elongation possible. At this location the nanowire is coupled to an optical spectrometer using a long-working distance objective: since the center clamp is kept at constant height, the working distance of the objective does not have to be corrected significantly when strain is varied. The relative displacement between the central clamp and the lateral supports is controlled using a differential thread, which is constituted by two segments of different diameter and pitch: as the thread is rotated, a relative displacement is induced between the block on which the central clamp is attached and the block on which the lateral supports are connected.

For the experiments of this work, two mechanisms based on the same design have been used, as shown in figure 5.10: one mechanism allows to perform low temperature measurements while the second has been used for room temperature measurements. The low temperature bending mechanism is attached to the cold finger of a liquid-helium flow cryostat, custom made by Cryovac. Using this system it is possible to perform strain measurements as function of temperature, from 325 K down to 8 K. To allow to achieve cryogenic temperatures, the system is located inside a UHV chamber, where pressures of 1×10^{-5} mbar can be reached. The differential thread of this system is attached to a high precision motorized rotational stage (Newport RGV100) through a vacuum rotational feed-through.

The optical spectra of the device are acquired by a high numerical aper-

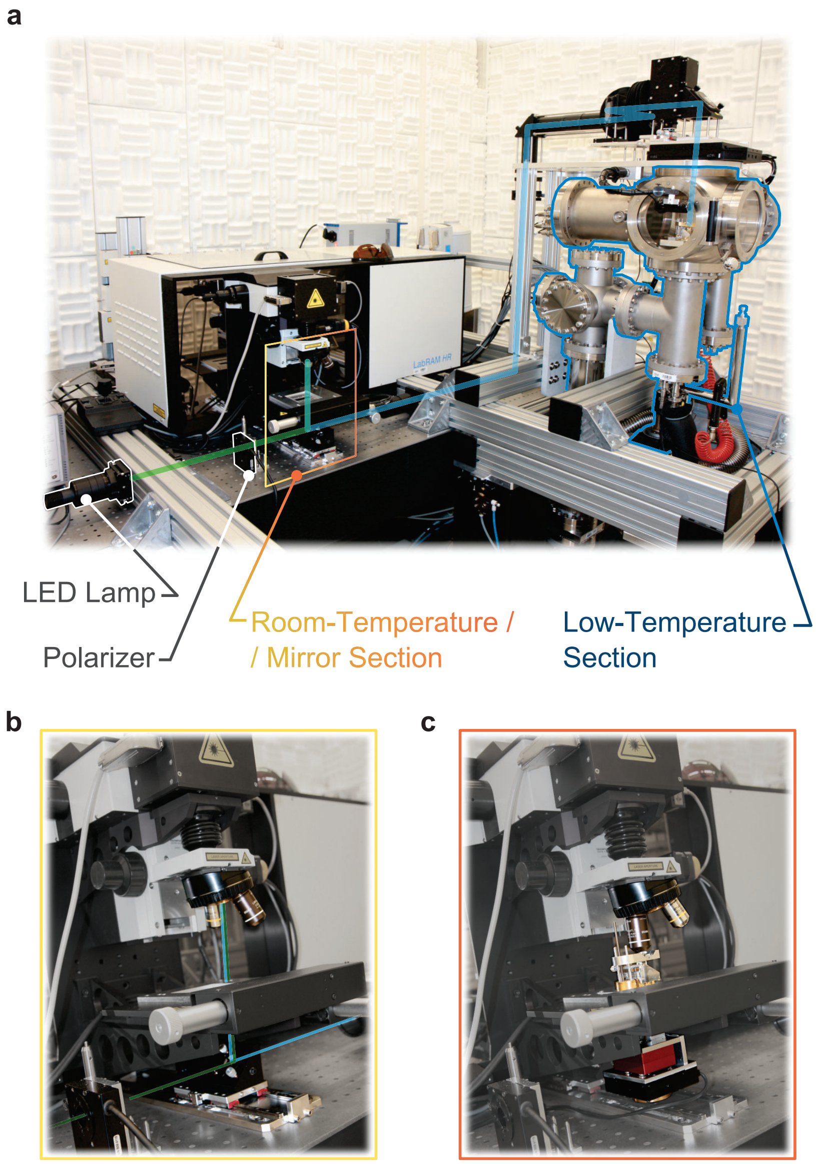

Figure 5.10: Overview of the experimental setup. (a) The optical path from the spectrometer to the low temperature section of the setup is shown in blue. The LED lamp and motorized polarizer used to characterize the polarization control units are highlighted and the corresponding optical path is shown in green. (b) A mirror system attached on rails couples the spectrometer to the LED lamp or to the low temperature section of the setup. (c) The room-temperature bending mechanism is mounted on the Raman spectrometer stage.

ture objective, like the Olympus LMPlanFL 100X or the Leica N Plan L 100X, which is maneuvered inside the vacuum chamber by a set of three piezoeletric actuators. The working distance of the objective is larger than 3.4 mm, allowing imaging and optical measurements to be performed for the whole stress range without interfering with the mechanics. The objective was coupled to the optical spectrometer using a set of 6 aluminum mirrors. The three mirrors closest to the objective, shown on the top-right corner of figure 5.10a, are assembled on a x-y stage, which is programmed to follow the movements of the objective inside the vacuum chamber.

A second bending mechanism, used to perform room temperature measurements, can be mounted directly on the table of the Raman spectrometer. The mechanism is actuated by a smaller and slower rotational stage (Newport SR50). To ensure a faster actuation, a 5:1 gearbox has been mounted between the motor and the differential thread. This mechanical system was realized by Meinrad Tschudy based on the design of the author. To ensure a quick installation and alignment of the low temperature mechanism, one of the mirrors is mounted on a rail system and can be displaced when the room temperature mechanism is installed as shown in figure 5.10b and 5.10c.

5.5 Optical Spectrometer

To acquire the PL and Raman spectra we have used a commercial optical spectrometer (Horiba scientific Labram HR) that has been customized to control the polarization orientation of the laser excitation and of the detected light. A representation of the optical path and of the optical components of the spectrometer is shown in figure 5.11.

The spectrometer is designed to work with a set of different lasers, which are equipped with a plasma-line filter to allow the transmission of single well defined wavelength:

- a He-Ne laser, emitting at 632 nm, is built in the spectrometer and is used as a alignment reference;
- a III-V solid state laser, emitting at 784 nm;
- an Nd:YVO_4 diode pumped laser, emitting at 532 nm;
- an Ar-ion laser, emitting at 363 nm.

These lasers allow the spectrometer to be used in many different applications, from materials characterization, to temperature sensing, to nano-plasmonics. However, the strain experiments discussed here have been performed exclusively with the He-Ne laser. Its emission wavelength is slighly higher than

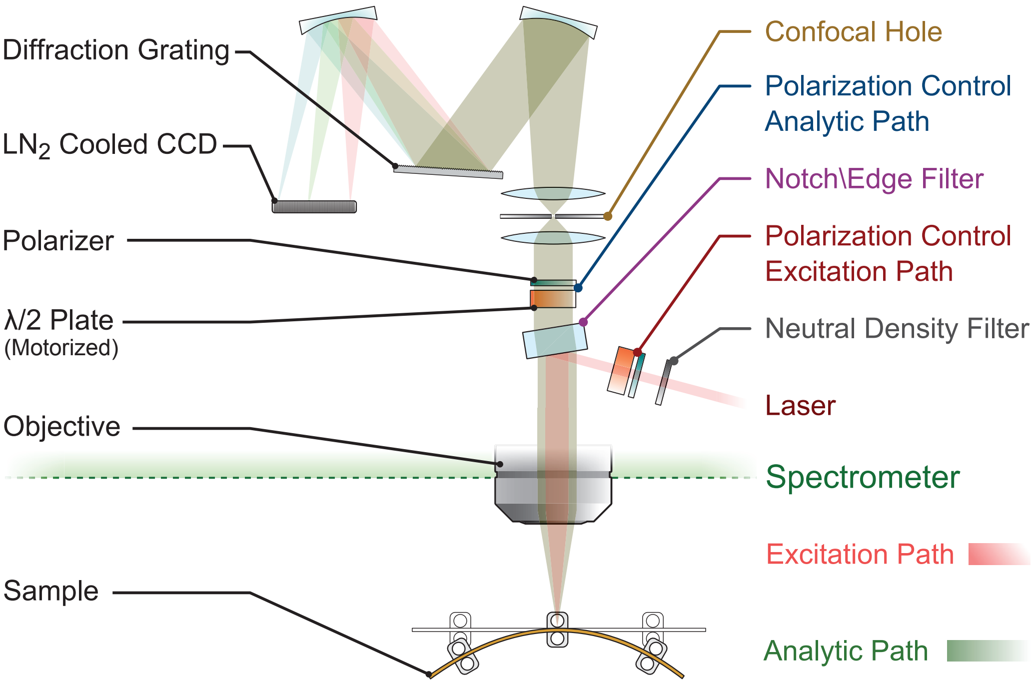

Figure 5.11: Schematic representation of the optical path and of the optical components in the spectrometer.

the bandgap of Zincblende and Wurtzite GaAs and permits to measure the PL of this materials with high efficiency as well as the Raman spectra in the exact same excitation conditions.

After traversing a variable neutral density filter, which can damp the intensity up to a factor of 10^4, the laser light impinges on the polarization control unit, which consists of a polarizer in cascade with a motor-controlled half-wave plate: the first of these optical elements sets the linear polarization of the laser excitation in the vertical direction and increases the polarization ratio beyond 10^2; the second optical element is used to rotate the beam polarization in any desired direction. The laser excitation is then redirected to the objective using a notch or a edge filter, whose spectral response is designed on the specifications of the laser light: the filter acts as a mirror for the laser light and transmits light of different wavelength. The light generated by the sample upon laser excitation is collected by the objective, transmitted by the notch or edge filter, and impinges on a second polarization control system, which selects linearly polarized light ofthe desired orientation and aligns its polarization direction to the high efficiency axis of the spectrometer. Finally, the light to be analyzed is focused on a confocal hole, which performs a double function in this system: it acts as incoming slit of the spectrometer, determining the spectral resolution, and sets the depth of focus of the system, determining the volume of material where the signal is collected.

Because of the strong rejection of the laser line by the notch or edge filter, the spectrometer is equipped with a single diffraction grating. For the acquisition of the photoluminescence spectra we have used a grating of 300 groves per millimeter, with a blasing angle optimized for 600 nm[110]. This grating is characterized by a small angular dispersion and permits to span a wide spectral range on a single acquisition, with a spectral resolution lower than $2\,\mathrm{cm}^{-1}$. For the acquisition of the Raman spectra, a higher resolution is necessary: using a grating of 1800 groves per millimeter, with a blasing angle optimized for 850 nm, enables to achieve a spectral resolution higher than $0.4\,\mathrm{cm}^{-1}$. The optical signal is finally detected by a liquid-nitrogen-cooled CCD. All the polarization-dependent measurements have been performed with a silicon Horiba Symphony open electrode CCD, which is sensitive in the UV-VIS range down to 1.2 eV. For some experiments, which required to extend the range of sensitivity down to 0.77 eV, a Peltier-cooled InGaAs CCD (Horiba Synapse 1700) was used.

5.5.1 Design of the Polarization Control Units

We have seen in the previous section that polarizers and half-wave plates are placed in the optical path to control the orientation of the linear polarization

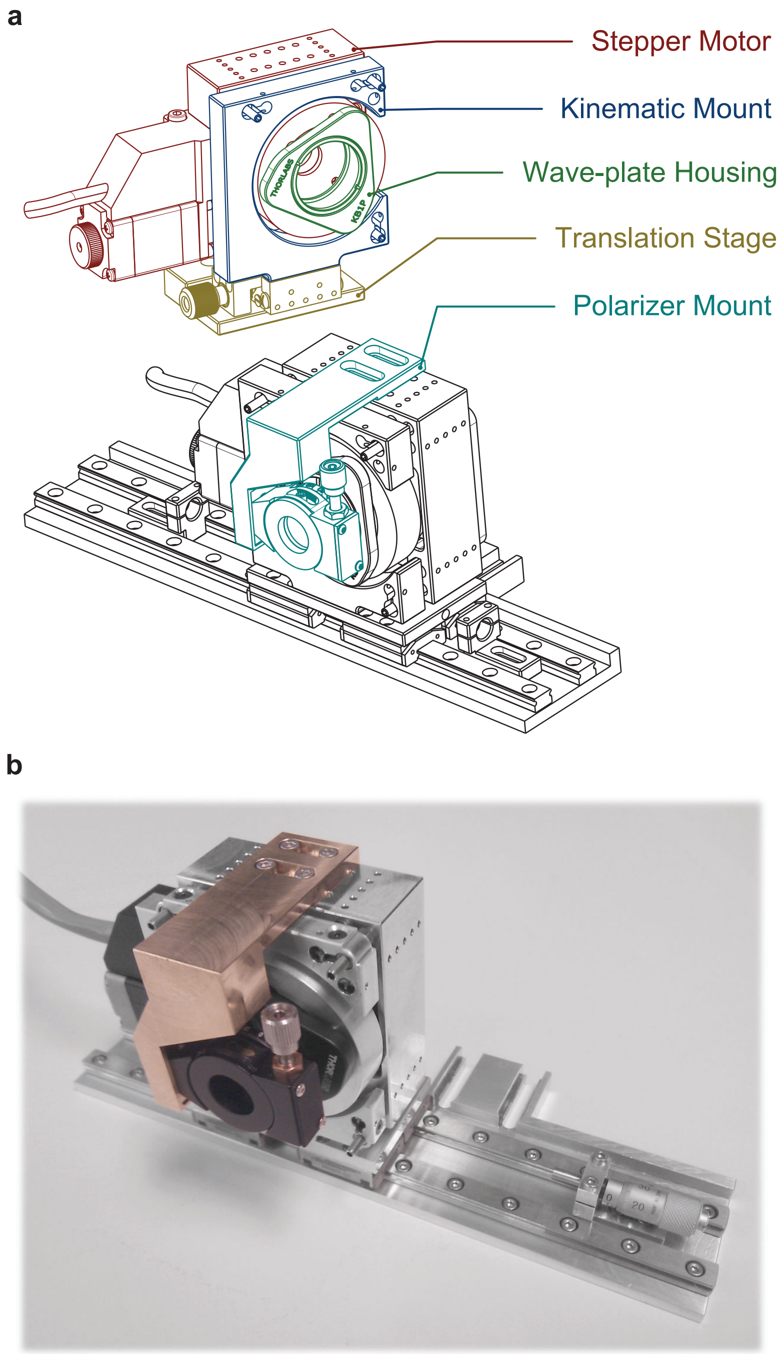

Figure 5.12: Custom-made polarization control unit. (a) CAD drawing of the unit for the excitation path (top) and for the analytic path (bottom). The polarizer mount is shown only in unit for the analytic path. (b) Picture of the assembled unit for the analytic path.

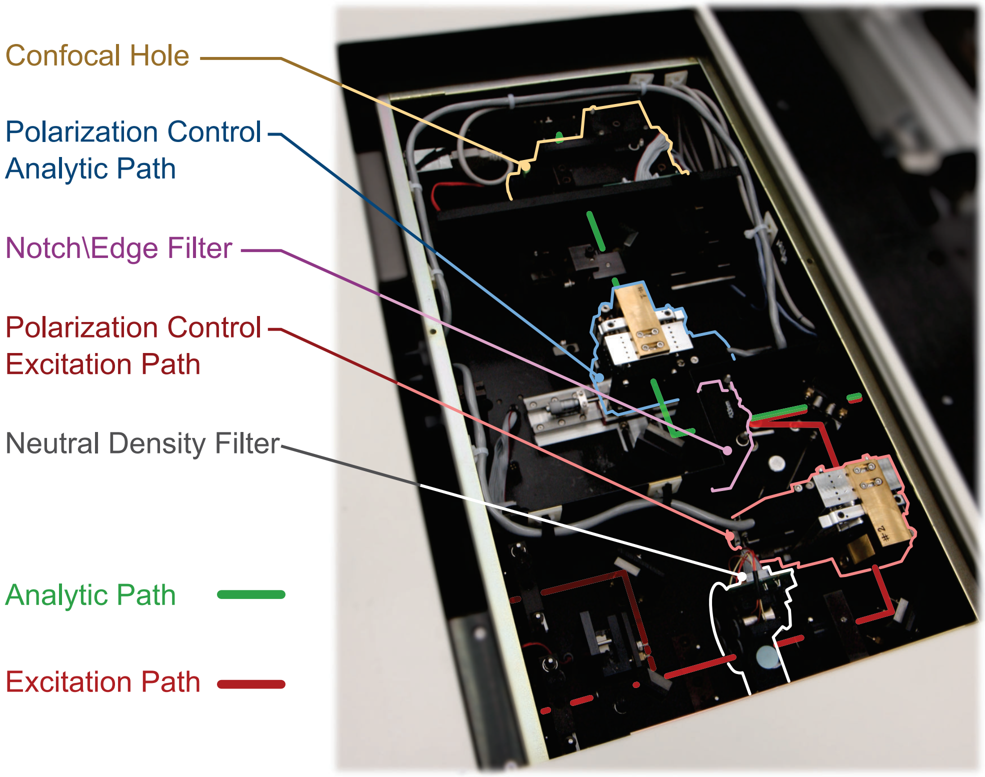

Figure 5.13: Optical components and optical path of the Raman spectrometer. The polarization control unit for the excitation path and for the analytic path are shown respectively in red and blue.

in the excitation and analytic path. Such systems were not provided together with the optical spectrometer and had to be designed and built to enable the polarization-resolved measurements. The polarizer and half-wave plate used in the units have to specifically fit the wavelength of the excitation and spectral range of detection.

The achromatic half-wave plates (B.Halle Nachfl.) used ensure an optical path difference between the ordinary and the extraordinary rays of 0.5±0.02 in the range between 633 nm and 1 µm. Nanoparticle linear film polarizers (Thorlabs LPNIR) allow to achieve an extinction ratio greater than 10^4 between 630 nm and 1 µm and are thin enough so that the mis-orientation of the rotation mount does not produce a significant offset of the beam. In this way no separate mechanics is needed to adjust the orientation of the polarizer, allowing a very compact design.

Since the system is equipped with different lasers and can detect over a broad spectral range, the possibility of exchanging easily the optical components of the polarization units is an important functionality to achieve in the design of the mounts. Figure 5.12 shows the design and realization of the two units, which were manufactured by Marcel Buerge and Meinrad Tschudy at IBM Research - Zurich, following the design and specifications provided by the author. The lambda half plate of each unit is mounted on a quick-release support (Thorlabs KB1F), shown in green in figure 5.12. This part is attached by magnetic supports to the rotating platform of a rotational stage (Standa 8MR174-11-20), shown in red: this rotation stage allows to control the half-wave plate orientation with an accuracy higher than 0.015° and has a very small form factor, necessary to fit in the small space available in the optical section of the spectrometer. The polarizer is mounted on a high precision rotation mount (Thorlabs PRM05/M) shown in teal-blue, which is solidly connected to the stepper motor. The rotation stage and all the components connected to it are attached to a kinematic mirror mount, which permits to adjust the orientation of the rotation axis of the half-wave plate and of the polarizer, aligning them to the excitation path. The two parts of the kinetic mount are kept together by springs, custom made by Spiral AG, and their distance is regulated using fine hexagonal adjusters that are in contact with sapphire supports (Standa) and housed on phosphor-bronze threaded bushings (Thorlabs). The unit designed for the excitation path is mounted on a linear stage (Standa) that permits to precisely align the unit with the optical path. The unit for the analytic path, shown in figure 5.12b , is mounted on a rail system (Schneeberger), which permits to align the unit to the optical path as well as displacing the whole system away from the optical path. This system enables to easily switch between measurements with and without the polarization control unit. Figure 5.13 shows the two polarization control units finally assembled in the

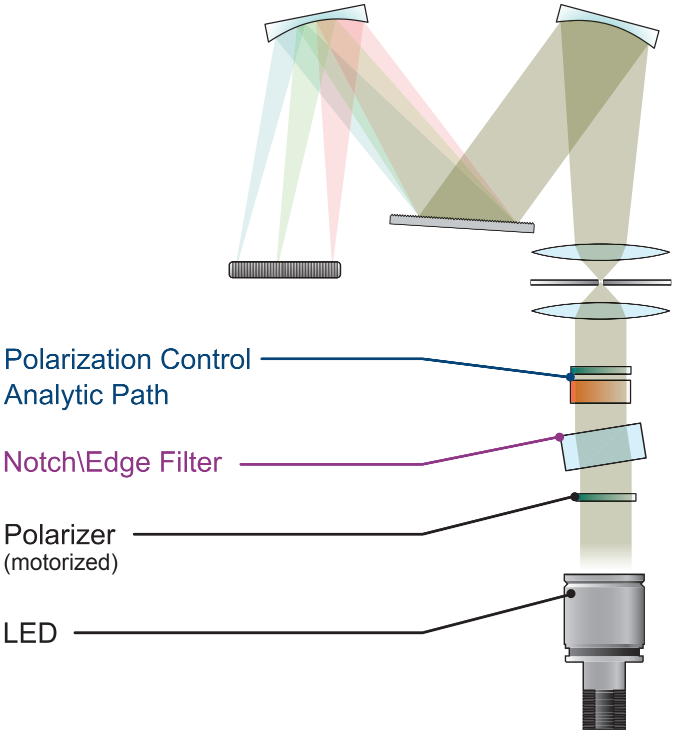

Figure 5.14: Optical setup used for the characterization of the polarization control systems in the analytic path.

optical path of the spectrometer. To ensure the correct operation of the polarization control units, we have carried different characterization tests, which will be described in the next section.

5.5.2 Characterization of the Polarization Control Units

The optical spectrometer Horiba Labram HR, used in our experiments, relies on notch or edge filters to deflect the excitation beam to the sample, as well as selectively reject the laser wavelength and transmit the optical signal to the detection section of the spectrometer. These functions are realized by constructive or destructive interference induced by the multiple reflections occurring at the interface between the different dielectric layers the filter is constituted of. Because of their principle of operation, these filters can also affect the polarization of the light which traverses them away from normal incidence[110]. It is therefore important to control that the use of the edge or of the notch filter does not interfere with the control of the polarization, ensuring that:

- the light transmitted by the filter to the detection section of the spectrometer maintains its initial polarization;

- the excitation light reflected by the filter, acting as a mirror, maintains the linear polarization in the direction set by the control unit.

To control the correct function of the polarization optics on the analytic path, we have modified a section of the optical path as shown in figure 5.14, introducing a red LED lamp (Thorlabs M625L3) and a motorized polarizer (Melles Griot FPG-12.5-4.0). The LED emits an unpolarized beam of light with a peak at 1.984 eV with Full Width at Half Maximum (FWHM) of 45 meV. This light beam is transmitted by the polarizer and optically coupled to the spectrometer using the mirror system shown in figure 5.10. Using this configuration, we can measure the optical spectra of the LED light as a function of the polarization orientation with or without the insertion of the filter. By comparing the two different transmission measurements we can characterize how a filter modifies the linear polarization of the transmitted light.

We first consider the case on which no filter is inserted in the optical path. Figure 5.15a shows the optical spectra acquired for different values of the half-wave plate orientation, with the polarizer offset from the vertical orientation by an angle of $\theta_{\text{pol}} = 50^\circ$. As expected, the spectra have the same line-shape for all analyzer orientations and the peak intensity of the spectrum is modulated by the wave-plate orientation. The peak intensity is maximized when the polarization control unit induces a rotation of the polarization θ_{ana} of 50°, in parallel configuration with the polarizer in front of the LED, and minimized when the polarization control unit induces a rotation of the polarization of -40°, setting the polarization control unit in orthogonal configuration with the polarizer in front of the LED. Figure 5.15b shows how the maximum of the spectrum varies as a function of θ_{pol} and θ_{ana}, respectively plotted in abscissa and ordinate. As expected, the response reproduces well the following cosine squared dependence :

$$I(\theta_{\text{p}}, \theta_{\text{a}}) \propto \cos(\theta_{\text{pol}} - \theta_{\text{ana}})^2 \tag{5.3}$$

The rejection ratio, i.e. the ratio between the maximum and the minimum intensity measured by varying θ_{pol}, was characterized for each value of θ_{ana}. Its maximum, equal to 3×10^3, is measured when the polarizer in front of the LED and the half-wave plate, with its ordinary or extraordinary axis, have the same orientation of the polarizer in the polarization control unit. The rejection ratio can decrease to 4.7×10^2 when the half-wave plate and the LED polarizers have different orientations.

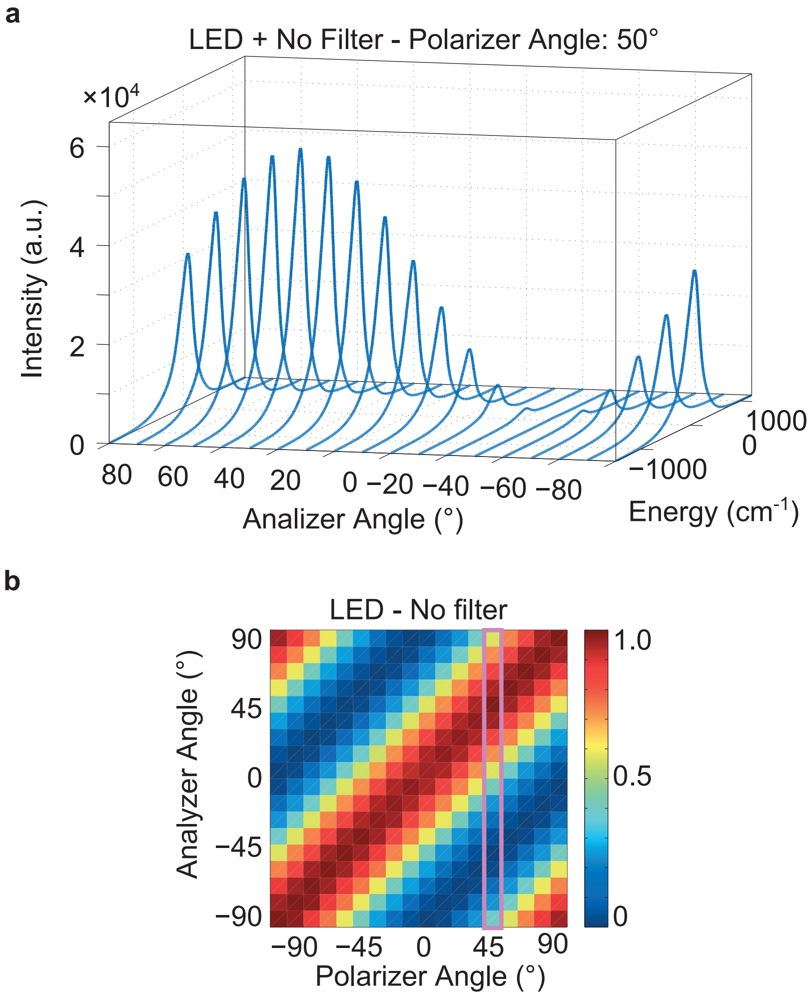

Figure 5.15: Optical spectra of the LED lamp, measured as a function of polarization, without the insertion of any notch or edge filter. (a) Optical spectra measured for different orientations of the half-wave plate, with the polarizer angle of 50° from the vertical direction. (b) The maximum intensity of the spectrum is represented with a color-map and plotted as a function of the LED polarization (abscissa) and of the polarization rotation angle induced by the half-wave plate (ordinate). The data extracted from the spectra shown in (a) are highlighted with a purple rectangle.

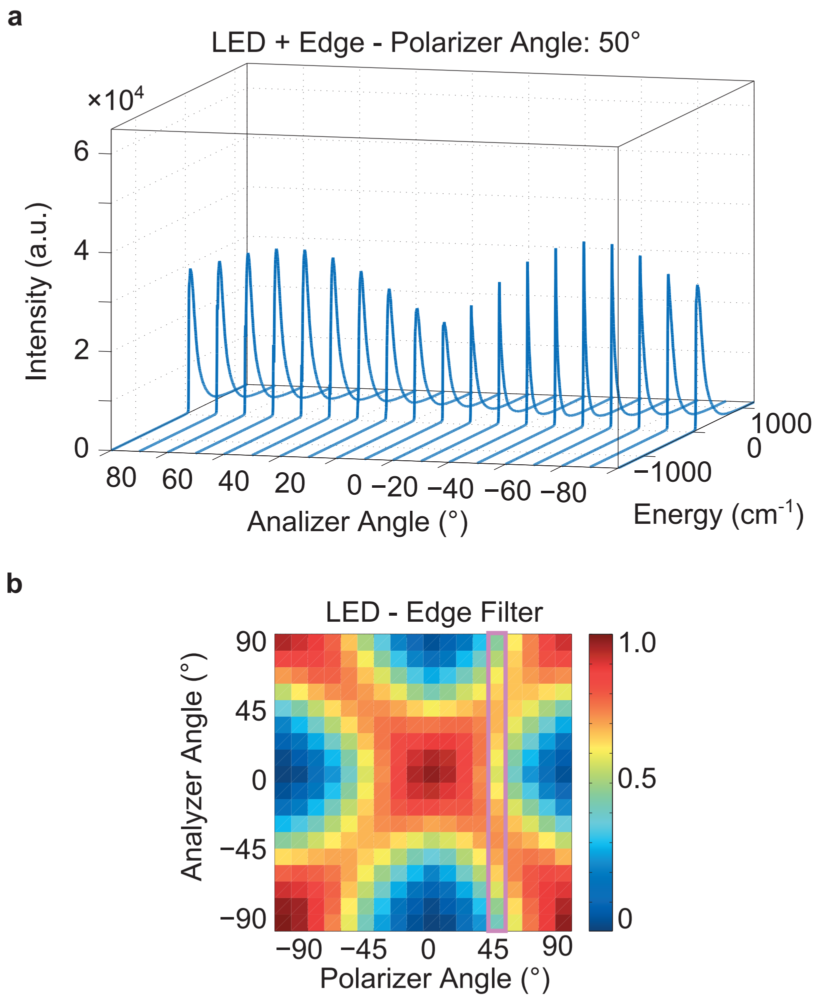

Figure 5.16: Optical spectra of the LED lamp, measured as a function of polarization, with the 633 nm edge filter inserted. (a) Optical spectra measured for different orientations of the half-wave plate, with the polarizer angle of 50° from the vertical direction. (b) The maximum intensity of the spectrum is represented with a color-map and plotted as a function of the LED polarization (abscissa) and of the polarization rotation angle induced by the half-wave plate (ordinate). The data extracted from the spectra shown in (a) are highlighted with a purple rectangle.

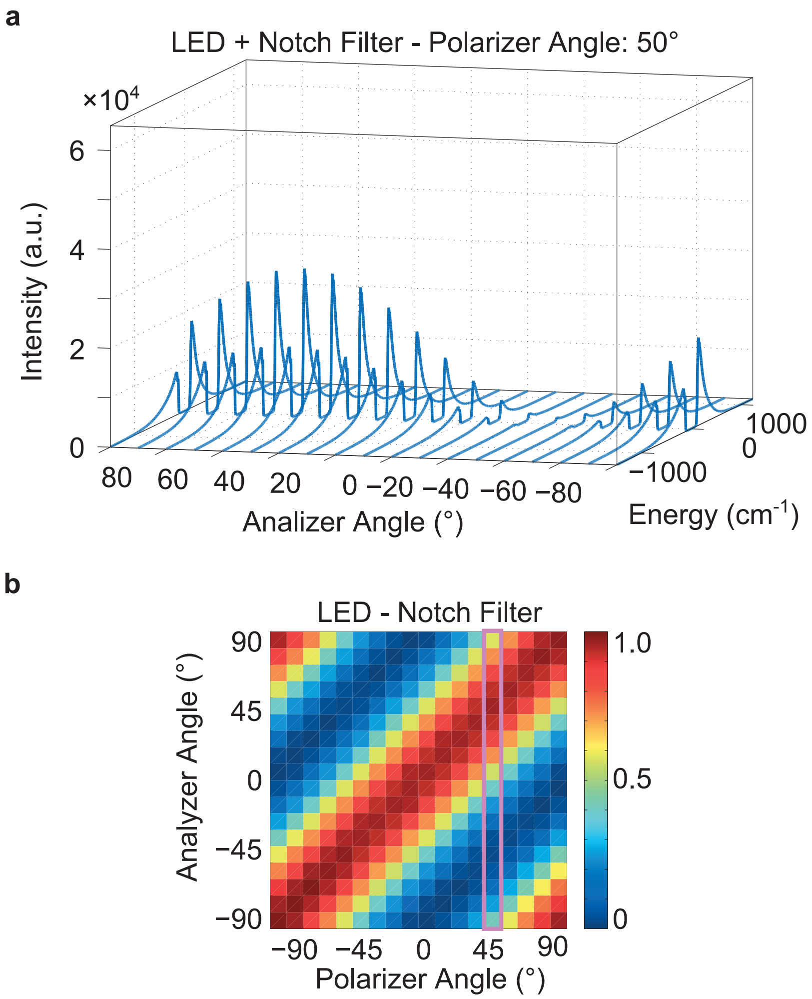

Figure 5.17: Optical spectra of the LED lamp, measured as a function of polarization, with the 633 nm notch filter. (a) Optical spectra measured for different orientations of the half-wave plate, with the polarizer angle of 50° from the vertical direction. (b) The maximum intensity of the spectrum is represented with a color-map and plotted as a function of the LED polarization (abscissa) and of the polarization rotation angle induced by the half-wave plate (ordinate). The data extracted from the spectra shown in (a) are highlighted with a purple rectangle.

We now proceed with inserting in the optical path the edge filter used together with the He-Ne laser, and measure the optical spectra as a function of the polarizer and half-wave plate orientation. Figure 5.16a shows the series of spectra measured with the polarizer and half-wave plate in the same configurations used for figure 5.15a. The spectra show that the edge filter is rejecting the high energy tail of the LED spectrum and transmitting the low energy one, for every configuration of the analyzer. The transmission edge is found at $75.4\,\mathrm{cm}^{-1}$ above the He-Ne emission energy. Unlike the measurements in figure 5.15a, the maximum transmitted intensity does not modulate down to zero for any value of the analyzer angle. The color plot of the maximum intensity as a function of the LED polarizer and analyzer configuration is shown in figure 5.16b and clearly shows that linearly polarized light can become circularly polarized when transmitted by the edge filter, depending on the polarizer orientation. We can conclude that the edge filter strongly modifies the polarization of the transmitted light and cannot be used to perform optical spectroscopy measurements as function of polarization.

Figure 5.17 shows the series of spectra measured with the insertion of the notch filter designed for 632 nm. Figure 5.17a, shows in particular the measurements performed with the polarizer and half-wave plate in the same configurations used for figure 5.15a. A spectral window of few hundreds cm^{-1} is rejected by the edge filter and is suppressed in the LED spectrum. The remaining part is fully transmitted, for all analyzer orientations. Unlike the edge filter, the maximum intensity of the transmitted spectrum can be modulated to almost zero: the notch filter induces some degree of elliptical polarization to the transmitted beam but this effect is not as severe as in the case of the edge filter. Figure 5.17b shows the maximum transmission as a function of the LED polarizer and analyzer orientations: unlike in the case of the edge filter, this color plot shows a pattern that looks very similar to the one in figure 5.15b. The insertion of the notch filter however reduces the minimum rejection ratio of the system to 43, which is an acceptable value for the polarization-dependent spectroscopy measurements we need to perform.

We complete our setup characterization by studying how the notch filter affects the orientation of polarization of the reflected laser light. The sketch of the optical path and elements involved in the test is shown in figure 5.18a: without any attenuation by the neutral density filter, the light of the He-Ne laser impinges directly on a polarizer that ensures its alignment in the vertical direction. After this element, the light traverses the half-wave plate, is reflected by the notch filter, impinges on the motorized polarizer, and finally is detected by an optical power measurement head. The characterization of the filter consists in measuring the laser power as a

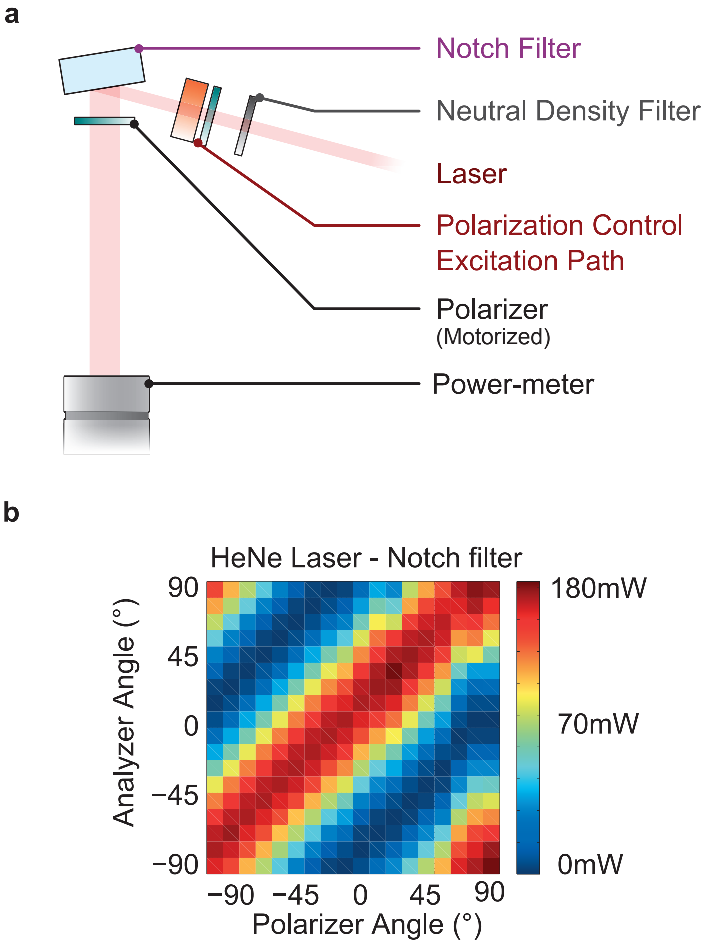

Figure 5.18: Polarization dependence of the laser excitation when the notch filter is used. (a) Optical path and components used for the characterization. (b) The measured laser power is represented with a color-map and plotted as a function of the analyzer orientation (abscissa) and of the polarization rotation angle induced by the half-wave plate (ordinate).

function of the polarization rotation induced by the half-wave plate before the filter, and as a function of the orientation of the polarizer located after the filter. The results of the measurements are shown in figure 5.18b. An optical power of 180 mW can be detected whenever the polarizer in front of the head is aligned parallel to the polarization orientation set by the control unit. The power decreases below 8 µW instead when the polarizers are in crossed configuration. A polarization ratio bigger than 1.2×10^2 is therefore ensured for all orientations of the half-wave plate. We can conclude that, unlike the edge filter, the notch filter does not influence significantly the polarization of light in transmission or reflection. This property makes it suited to perform polarization-dependent measurements on a Labram HR optical spectrometer.

5.6 Size Effects on Mechanical, Optical and Vibrational Properties

Research performed in recent years has shown that nanowires can assume novel mechanical properties, size quantization effects can vary the electronic, the optical and the vibrational properties, and surface effects can become dominant when the cross-section dimensions shrink below few hundred nanometers[70,73,111–116]. These effects can induce substantial deviations from the bulk-like picture we have provided in the previous chapters, when discussing electronic, optical and vibrational properties. Before proceeding with the description of the experimental results, we will give a brief overview of how size-effects can modify mechanical, electronic and vibrational properties of nanowires, specifying also the expected effect in the specific case of the nanowires studied in this work.

5.6.1 Size Effects on the Mechanical Properties

The components of the compliance and stiffness tensor of GaAs have been measured, to the best of our knowledge, only in bulk samples and their values are shown in table 3.1. However, mechanical experiments performed in semiconducting and metallic nanowires[70,73,111–113], have shown that variation of the mechanical properties can occur when the wire dimensions shrink down to the nanometer scale.

Wang et al.[73] imaged Zincblende GaAs nanowires by TEM during mechanical testing, under uniaxial compression and bending, as shown in figure 5.19. Analyzing these deformations with finite element models, it was possible to demonstrate a significant variation of the effective Young's Modulus, which increases from 86 GPa in bulk samples to 180 GPa for wires of 50 nm

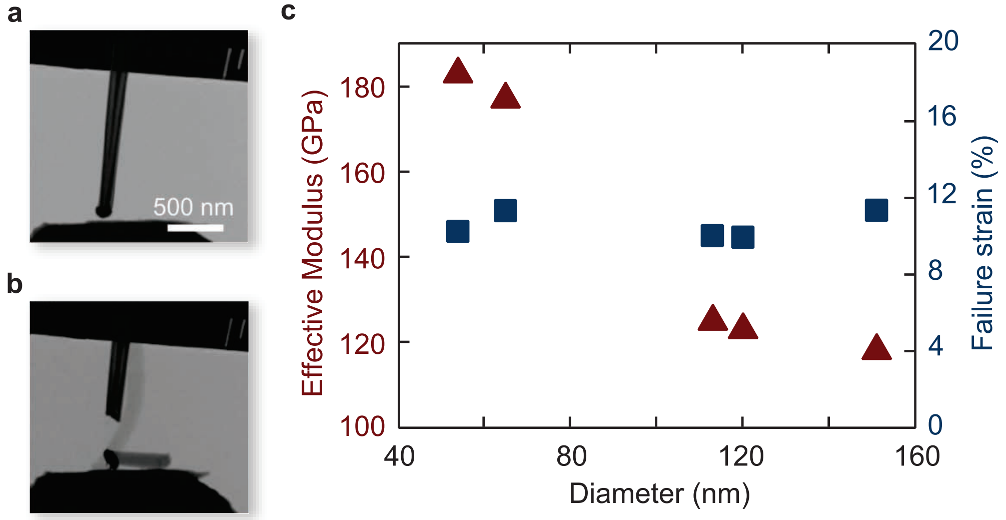

Figure 5.19: Mechanical testing of GaAs Zincblende nanowires. TEM images of a nanowire before (a) and after (b) testing. The effective Young's modulus and yield strength (c) were extracted by finite element simulations. Adapted from Wang et al.[73].

of diameter. These results provide a strong indication of the influence of the surface effects on the mechanical properties of the nanowires and, most importantly, warn us that tensor properties such as stiffness and compliance might deviate strongly from bulk values and cannot be used to accurately describe the nanowire mechanics.

5.6.2 Size Effects on the Band Structure

In chapter 4 we have treated radiative transitions using the single particle picture of electron and holes. To take into account size quantization effects on the electron-hole pairs one has to consider also their mutual interaction through the Coulomb potential, which leads to the formation of electron-hole complexes called excitons[76]. Such states can be described using the effective mass approximation and decoupling the Schrödinger equation of electron and hole into one for their center of mass and one to describe their internal degrees of freedom. Because of the Coulomb nature of electron-hole interaction, this last equation resembles closely the one of the hydrogen atom. Pushing further the analogy, it is possible to define an exciton Bohr radius, i.e. the most probable electron-hole distance, with the following relation:

$$a_{\mathrm{Bohr}} = \frac{4\pi\varepsilon_0\hbar^2}{\mu \mathrm{e}^2} \tag{5.4}$$

where ε_0 is the low frequency permittivity of the material and μ is the reduced effective mass of electrons and holes, already introduced in equation (4.6). The exciton Bohr radius, which in GaAs is as large as 11.2 nm, sets the scale below which quantization effects play a role in optical recombination processes. The smallest nanowire dimension in our experiment, i.e. the core diameter of 50 nm, is more than four times larger than the GaAs exciton Bohr radius and, therefore, size-quantization excitonic effects are not expected to play a significant role.

5.6.3 Size Effects on the Lattice Dynamics

As the nanowire dimensions decrease, also the lattice dynamics can be affected by surface effects. Because of the small nanowire size, the momentum conservation along the nanowire cross section can be relaxed and phonons, normally associated with non-zero wave-vectors, can contribute to the Raman scattering spectrum[117]. Optical phonons localized at the surface of the nanowire, called surface optical phonons, have been observed in GaAs nanowires and have been shown to depend strongly on the nanowire size and on the dielectric constant of the surrounding medium[114]. Even though very little experimental results are available on how strain affects these phenomena, much can be learned from the computational side.

Christian Tuma and coworkers analyzed with molecular dynamics the optical modes of silicon nanowires and their size dependence under uniaxial stress in the [111] direction and other strain conditions[118,119]. The energy of the zone center optical phonon in unstrained conditions was shown to dependend significantly on the nanowire cross-section, decreasing by more than 7 cm^{-1} for wires of 4 nm in diameter. Surprisingly, the hydrostatic and deviatoric phonon deformation potentials have been shown to be practically size independent, with deviations smaller than 5 % compared to bulk values in wires of 4 nm of diameter. These very important results indicate that the phonon deformation potentials derived in bulk can describe accurately the strain dependence of the optical phonons of very small nanowires. Unless surprising size-dependent effects affect the macroscopic electric field of optical phonons, it is easy to imagine that these results can be also be extended to III-V compounds. Raman scattering can therefore be considered as a reliable, size-insensitive technique to measure strain in semiconducting nanostructures.

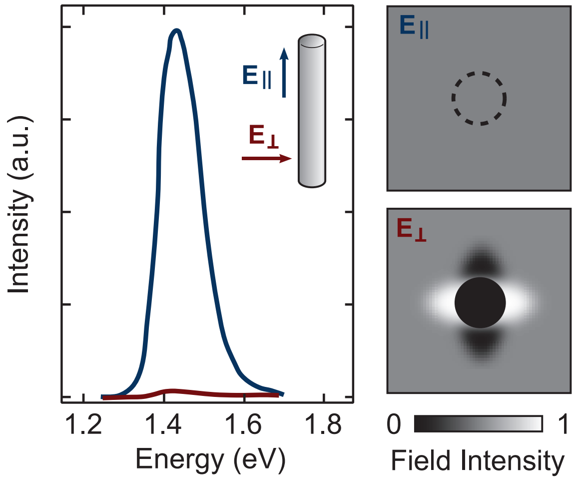

Figure 5.20: Dielectric mismatch effects in InP nanowires. Adapted from Wang et al.[120].

5.6.4 Size Effects on the Optical Coupling: the Dielectric Mismatch Effect

The light emitted by an unstrained GaAs nanowire has a wavelength of approximately 800 nm, which is roughly one order of magnitude bigger than the nanowire diameter. Wang et al. showed in nanowires of similar dimensions that the optical coupling between the environment and the nanowire has a strong polarization anisotropy, caused by the dielectric constant mismatch between the semiconductor and the environment[120]. When the light is polarized perpendicular to the nanowire, the electric field amplitude inside the nanowire is attenuated according to the following relation:

$$E_{\text{internal}} = \left(\frac{2}{\varepsilon_{\text{r}}+1}\right) E_{\text{external}} \tag{5.5}$$

where ε_{r} is the relative permittivity of the semiconductor. If instead the incident light is polarized parallel to the nanowire axis, the electric field perceives a bulk-like medium and is not attenuated. The total intensity can be decomposed in two orthogonal components in the following way:

$$I_{\text{internal}} = \left|E_{\text{int},\parallel} + E_{\text{int},\perp}\right|^2 = \left|\cos\theta + \frac{2}{\varepsilon_{\text{r}}+1}\sin\theta\right|^2 I_{\text{external}} \tag{5.6}$$

Under normal incidence conditions and polarized illumination, the coupling efficiency η will therefore depend on the angle θ between the electric field and the nanowire axis:

$$\eta = \frac{I_{\mathrm{internal}}}{I_{\mathrm{external}}} = \left(\cos\theta + \frac{2}{\varepsilon_{\mathrm{r}} + 1}\sin\theta\right)^2 \tag{5.7}$$

The maximum coupling efficiency of 1 is obtained under parallel alignment with the nanowire, while its minimum, given by the expression:

$$\eta_{\mathrm{min}} = \left(\frac{2}{\varepsilon_{\mathrm{r}} + 1}\right)^2 \tag{5.8}$$

is obtained under orthogonal configuration. Since the relative permittivity of GaAs is 12.9, the coupling efficiency can be as low as 2.3 %. Dielectric mismatch effects will therefore strongly affect how laser light can be coupled inside the nanowires, as well as how the light coming from photoluminescence and Raman scattering processes can be coupled out to the environment.

6

Uniaxial Stress Effects in GaAs Zincblende Nanowires

6.1 Motivation

Strain engineering has proved to be a powerful strategy to enhance the performance of electronic as well as optoelectronic devices. In CMOS technology, the significant increase in charge-carrier mobility gained by the application of strain has facilitated the continued performance increase during scaling, especially below the 90 nm node[5]. In optoelectronics, especially in quantum-well lasers, strain has been used to improve and tailor the device characteristics by shifting the bandgap and thus the spectrum to a wavelength that may not be achievable otherwise[21,27,121,122]. Furthermore, the density of states (DOS) was changed by strain to improve laser performance, increasing the gain and reducing the lasing threshold[23]. Recently it has been shown that strain in Ge can induce a direct bandgap transition and hence allows achieving PL and electroluminescence over a broad spectrum that covers several optical communication windows[28,29,31], thus potentially enabling new integrated photonic applications.

Nanostructures and in particular nanowires benefit from increased yield strength and exotic mechanical properties as compared to their bulk counterparts[70,72,123]. Higher tensile stress levels can be applied elastically to nanostructures, making nanowires a very attractive system for large modifications of the energy band structure. Large shifts of the bandgap and increased emission intensity have been observed in core-shell nanowires of GaAs/GaInP[124] or GaAs/GaP[125], in which, as in most device applications, strain is induced by growing epitaxially lattice-mismatched films or by depositing films with an intrinsic stress. However, the stress achievable with this method is limited by the material system selected and remains fixed once the device has been fabricated. To investigate how different values of strain affect the electronic and optical properties of a device, it is desirable to apply stress mechanically and continuously vary its amount. This has been achieved using, for example, wafer-bending tests[126] or diamond anvil cells[127]. Whereas in the latter high stress levels can be achieved only in the compressive hydrostatic regime, in the former both tensile and compressive stress are possible, but the maximum stress range accessible is limited. For example, for typical Si wafer-bending experiments, only 300 MPa can be applied before the die breaks[8].

In this chapter we investigate the influence of uniaxial tensile and compressive stress on the optical properties of Zincblende GaAs nanowires, a model system for light-emitting materials. In particular, we show that uniaxial stress can be used to tune the emission spectrum of GaAs nanowires over a broad range in a continuous way. By straining the nanowire from $-1.0\,\%$ to $+3.5\,\%$ along its axis, a shift of the PL peak by more than 180 nm was achieved. Such a remarkable PL shift is possible because of the favorable mechanical properties of nanowires which allow a large strain to be applied elastically and reversibly.

6.2 Experiment

The experiments described in this chapter were performed using Zincblende GaAs-$Al_{0.3}Ga_{0.7}As$-GaAs core-shell nanowires grown via VLS technique in a MOCVD system using gold as a catalyst. The GaAs nanowires are grown along the [111] direction with a diameter of 50 nm. The uniform 50 nm thick $Al_{0.3}Ga_{0.7}As$ shell was grown to properly passivate the surface states on the GaAs core to enable a stable PL[102,104]. Finally, the 3 nm thick GaAs outer shell was grown to prevent oxidation of the $Al_{0.3}Ga_{0.7}As$ shell under ambient conditions. Strain effects induced by the $Al_{0.3}Ga_{0.7}As$ shell should be negligible because of the almost perfect lattice match with the GaAs core. The wires have a uniform cross section and a length ranging between 7 and 8 µm. HRTEM analysis of many wires reveals the crystal structure to be Zincblende and almost free of twin defects (on average less than one defect per micrometer). Further details about the nanowire growth and properties have been provided in §5.2.1.

To investigate the influences of strain on the optical properties, we fabricated doubly clamped nanowire structures on flexible stainless-steel substrates coated with a transparent polymer. Selected nanowires, transferred onto the substrate in the uniaxial stress direction, were fixed to the substrate surface by 180 nm thick Ti metal clamps, fabricated using electron-beam lithography and lift-off. Finally, oxygen reactive-ion etching was performed to underetch and release the nanowire segment left uncovered by the metal clamps. Further details about the sample fabrication can be found in §5.3.

The sample was installed into a three-point bending mechanism located in the low temperature section of the setup, described in §5.4. Care was taken to couple the metallic clamp to the cold finger of the cryostat with a good thermal contact. Unless mentioned otherwise, PL and Raman spectra were measured with the cryostat at a temperature of 100 K. The light emitted at 632.8 nm by a HeNe laser was focused by a 100x objective (numerical aperture = 0.8) to a diffraction-limited spot of 0.7 µm FWHM and used to excite the free-standing nanowire. The laser power was reduced by the neutral density filter and kept constant at 450 µW to minimize heating of the nanowire and to achieve a good signal-to-noise ratio. PL and Raman spectra were measured with a single-stage confocal Raman spectrometer (Horiba Scientific LabRam HR), equipped with a custom-made system consisting of motor-controlled rotatable achromatic half-wave plates and nanoparticle linear film polarizers to control the polarization in the excitation and the analytic path. The notch filter installed in the spectrometer rejects the light with energy above 1.95 eV. More details about the optical setup can be found in §5.5.

6.3 Optical Spectroscopy on Unstrained Nanowires

In figure 6.1 we show the PL spectrum of a GaAs-$Al_{0.3}Ga_{0.7}As$-GaAs nanowire device measured at a cryostat temperature of 100 K without any stress applied: a single sharp peak positioned at 1.482 eV±5 meV with a FWHM of 30±5 meV is observed. A small luminescence background, originating jointly from the nanowire shell and from the polymeric substrate, is visible in the range between 1.6 and 1.8 eV. The peaks at higher energies are generated by Raman and Rayleigh scattering processes.

The PL data has been fit with a line-shape model based on bulk-like joint density of states populated by a Boltzmann distribution, broadened with a Gaussian function. Details about the line-shape model are described in §4.3. The value of energy gap inferred from the fitting corresponds well with the bandgap of bulk GaAs at a temperature of 160 K (see figure 6.2a). This temperature is in good agreement with the value estimated from the high energy tail of the PL, confirming that thermal equilibrium between charge

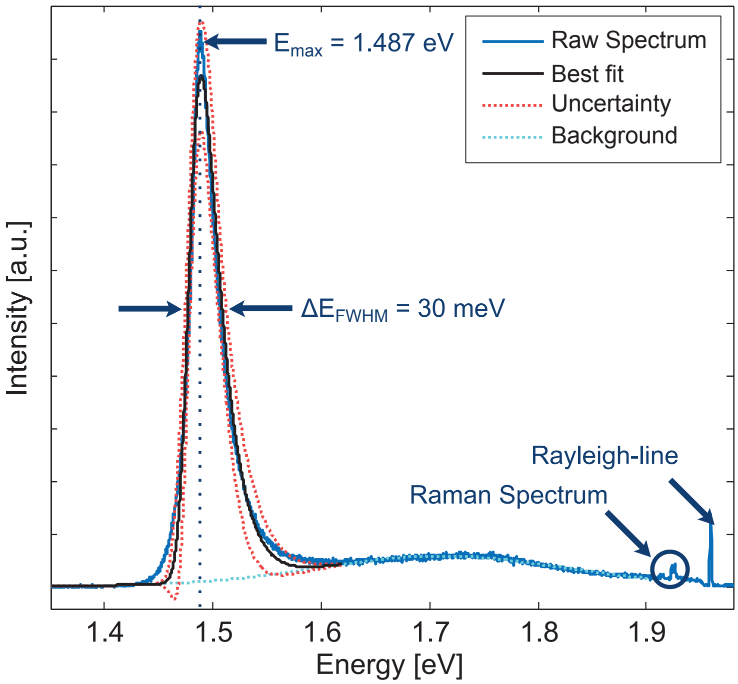

Figure 6.1: Photoluminescence spectrum of a Zincblende nanowire measured with the cryostat at a temperature of 100 K.

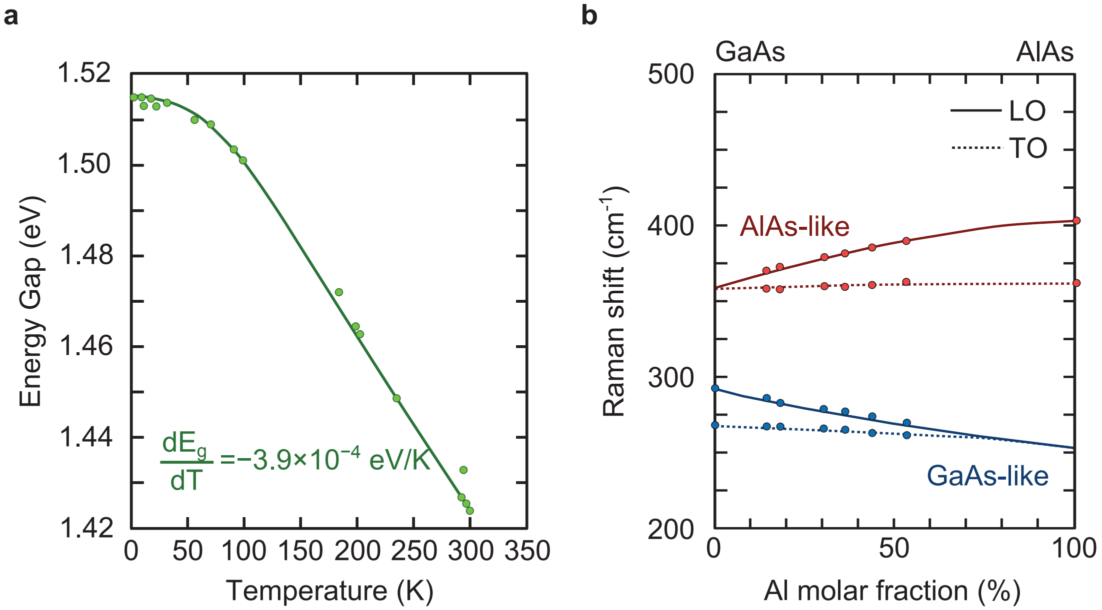

Figure 6.2: Optical and vibrational properties of bulk GaAs and $\mathrm{Al}_x\mathrm{Ga}_{1-x}\mathrm{As}$ alloys. (a) Temperature dependence of energy bandgap of GaAs[128]. (b) Vibrational energy of the optical phonons of $\mathrm{Al}_x\mathrm{Ga}_{1-x}\mathrm{As}$ alloys as function of the aluminum concentration x[88].

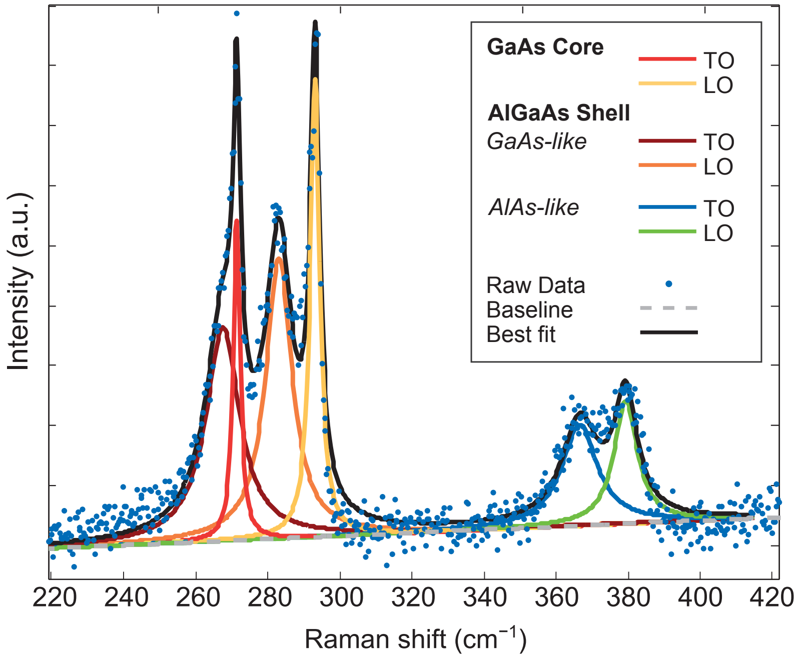

Figure 6.3: Raman spectrum measured (blue dots) for the same wire as in figure 6.1 and deconvolution of the optical phonon contributions, obtained by least-squares fitting. The optical phonon peaks are fitted with Lorentian line-shapes and represented with different colors. A linear background is also considered in the fitting and represented as a dashed line. The black line represents the outcome of the fitting.

carriers and the crystal is reached under laser illumination. We believe that the nanowire temperature is higher than the one of the cryostat because of laser-induced heating and restricted thermal coupling to the substrate. The relatively small FWHM of 30 meV and the high emission intensity, even at room temperature, are evidence of the small non radiative defect density and the high quality of the wires studied here[102,104].

The Raman spectrum of the same Zincblende nanowire has been measured under the same illumination conditions, using a higher resolution grating, and is shown in figure 6.3. This spectrum exhibits the characteristic peaks of the GaAs and $Al_{0.3}Ga_{0.7}As$ optical phonons. The GaAs transverse optical (TO) and longitudinal optical (LO) phonon peaks are located at 271.6 cm^{-1} and 293.1 cm^{-1}, within a few wavenumbers from the values of bulk. Further peaks attributed to the AlGaAs shell are positioned at 267.8 cm^{-1} (GaAs-like TO), 283.2 cm^{-1} (GaAs-like LO), 365.5 cm^{-1} and 378.2 cm^{-1} (AlAs-like

TO and LO)[88]. By comparing the measured phonon energies with the one of $Al_xGa_{1-x}As$ alloys, shown in figure 6.2b, it is possible to infer valuable information about the AlGaAs shell. The energy of the optical phonons depend on the aluminum molar fraction in the alloy: the GaAs-like phonons decrease in energy while the AlAs-like phonon energy increases. The GaAs-like and AlAs-like TO energies have a modest variation on the aluminum concentration. This property is expected, since the lattice constant and the volume of the unit cell of AlGaAs alloys does not vary significantly with the aluminum content. On the other end, because of the difference in electron affinity between gallium and aluminum, we can expect a stronger effect on the macroscopic electric field and on the LO-TO splitting. Indeed, the GaAs-like and AlAs-like LO phonon energy are more sensitive to the aluminum concentration. This strong dependence can be exploited to quantify the alloy composition of the shell, which is estimated to be 30±1 % and in agreement with the growth conditions.

The PL and Raman spectra shown in figure 6.1 and figure 6.3 have been reproduced on tens of different nanowires, indicating the high quality and uniformity of the growth process.

6.4 Strain Effects on Photoluminescence and Raman Spectra

The effect of the crystal deformation on the emission properties of the Zincblende nanowires is presented in figure 6.4, in which the normalized PL spectra of an individual wire are plotted as a function of energy for different values of uniaxial stress. The spectrum plotted right above the dashed line corresponds to the signal of the unstrained wire. Under compression, the peak originally found around 1.48 eV shifts to slightly higher energies with increasing stress and exhibits a maximum of 1.50 eV. Increasing the stress further broadens the spectrum and decreases the peak energy slightly. A much stronger peak shift towards lower energies is observed when tensile stress is applied. For moderate applied tension, a splitting of the PL peak into two components can be resolved. The component with the lowest energy experiences a strong red shift of up to 256 meV with increasing stress.

To understand the significantly asymmetric effect of strain it is important to quantify how much strain is induced in the nanowire. For this, we analyze the Raman spectra in detail and use them to gauge the strain. The corresponding spectra are plotted in figure 6.5 as a function of the Raman shift, for different stress values. All Raman peaks are observed to shift linearly with applied uniaxial stress in the regime we investigated. Tensile stress decreases the energy of all phonons, whereas compressive stress causes

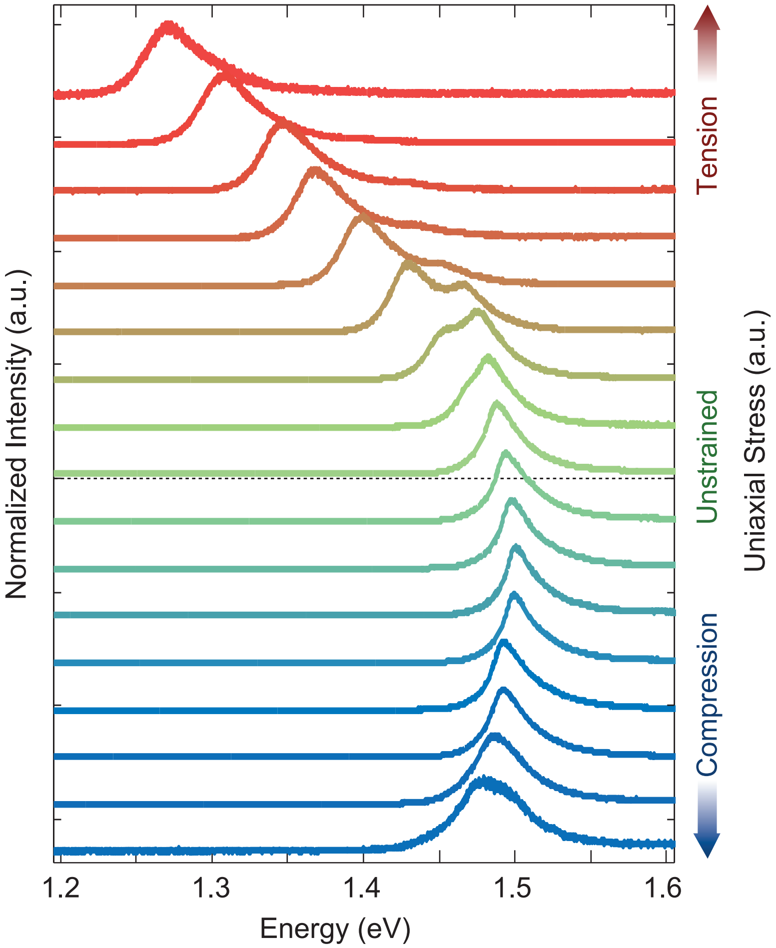

Figure 6.4: Effect of tensile and compressive stress on the PL spectra of the a single core-shell GaAs-$Al_{0.3}Ga_{0.7}As$-GaAs nanowire.

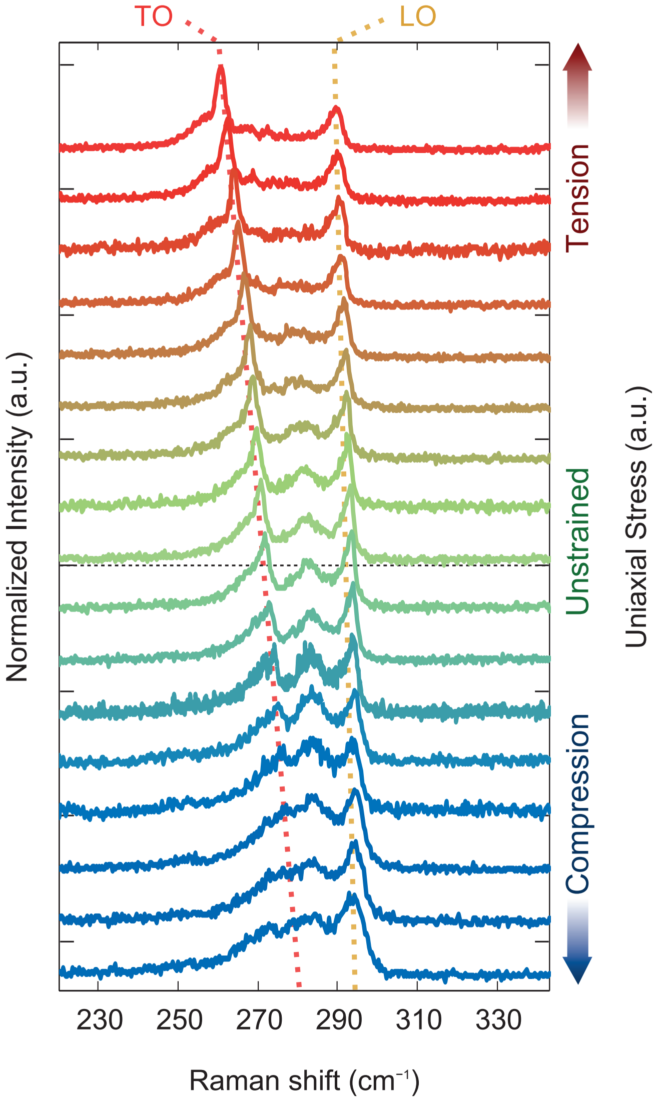

Figure 6.5: Effect of tensile and compressive stress on the Raman spectra of a single core-shell GaAs-$Al_{0.3}Ga_{0.7}As$-GaAs nanowire. A guide to the eye is included for the peak position of the TO and LO of the GaAs core.

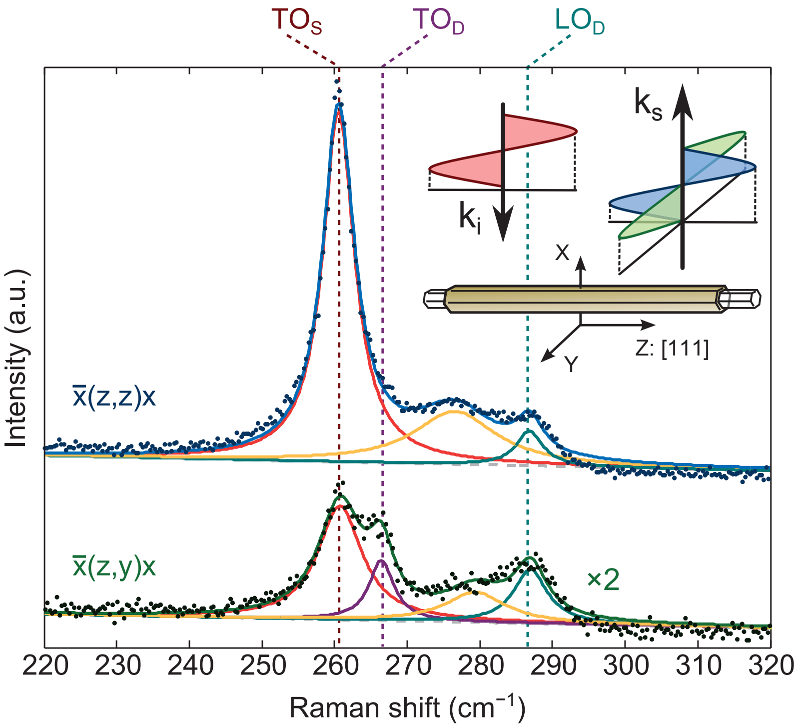

Figure 6.6: Room-temperature Raman spectra of a nanowire under high tensile stress in two distinct scattering configurations.

their energies to increase. As we are interested in the strain effects of the nanowire core, we concentrate on the peak shift of the phonons assigned to the GaAs core: we find that the TO phonon experiences a stronger energy shift ($15\,\mathrm{cm}^{-1}$) than the LO peak ($5\,\mathrm{cm}^{-1}$). The observed stress effects on the PL and Raman spectra are fully reversible and reproducible for all nanowires in the regime tested.

6.5 Resolving the Phonon Contributions

To evaluate the axial strain applied to the wire from the Raman spectra, the predominant phonon contributions have to be identified. To this end, it is worth inspecting the back-scattering geometry used in our experiment, shown in the inset of figure 6.6. In this configuration the momentum of the phonons observed in the Raman spectra is directed with good approximation parallel to the incoming laser photon direction, along the x-axis direction. Only one of the two TO phonons has an atomic displacement along the direction of the nanowire axis, the z-axis. The atomic displacements of the remaining TO and LO lie instead in the nanowire cross-section plane, with the TO oriented along the y-axis and the LO along the x-axis.

At zero applied stress, the two TO phonons are degenerate. When uniaxial stress is applied, the resulting anisotropic deformation reduces the crystal symmetry and lifts the TO degeneracy. In particular, the TO phonon with atomic displacement along the nanowire axis is a non-degenerate singlet and is labeled $\mathrm{TO_S}$ after Cerdeira et al.[95,96]. This phonon is expected to experience a larger energy shift with strain than the doublet constituted by the two other phonons, labeled $\mathrm{TO_D}$ and $\mathrm{LO_D}$. To identify which of the two TO phonons dominates the spectrum in figure 6.5, we can use the polarization dependence given by the Raman selection rules, discussed extensively in §4.4.2. In particular, we can study two distinct configurations shown in figure 6.6. In both cases, the incoming laser light is polarized along the nanowire axis, i.e. the z-axis, to avoid dielectric mismatch effects and maximize the interaction of light with the nanowire[129]. In the first scattering configuration, indicated as $\bar{x}\,(z,y)\,x$, the light is detected orthogonal to the nanowires axis and hence only the $\mathrm{TO_D}$ should be visible[96]. In the second scattering configuration, and indicated as $\bar{x}\,(z,z)\,x$, we collect light polarized along the nanowire axis and hence expect only the $\mathrm{TO_S}$ to be visible. In figure 6.6 are shown two Raman spectra acquired at room temperature on a nanowire under high tensile stress, using these two scattering configurations. The lower curve (green) has been measured with the first scattering configuration and both $\mathrm{TO_S}$, plotted in red, and $\mathrm{TO_D}$, shown in purple, can be observed at $260\,\mathrm{cm}^{-1}$ and at $266\,\mathrm{cm}^{-1}$, respectively. The $\mathrm{TO_S}$ phonon could not be completely suppressed in this configuration because of the finite rejection ratio of our polarization system and the finite angle of collection our objective, which is equal to 53°[130,131]. In the upper curve (blue), the spectrum acquired in the second configuration is shown. The TO peak is located at the same energy as the contribution assigned to the $\mathrm{TO_S}$ phonon, whereas the $\mathrm{TO_D}$ contribution is completely suppressed. The agreement between the measured Raman spectral intensities and the expected polarization dependencies confirms the assignment of $\mathrm{TO_D}$ and $\mathrm{TO_S}$. In both spectra the $\mathrm{LO_D}$ peak , plotted in turquoise, is observed at $286.4\,\mathrm{cm}^{-1}$. We can therefore conclude that $\mathrm{TO_S}$ and $\mathrm{LO_D}$ provide the dominating phonon contributions in the Raman spectra of figure 6.5.

6.6 Axial Strain and Poisson-ratio Estimation

The shift of the $\mathrm{TO_S}$ and $\mathrm{LO_D}$ phonon energy can be used to estimate the nanowire axial strain $\varepsilon_{\parallel}$ and Poisson ratio ν. Our estimation is based on the assumption, discussed in 5.6.3, that the phonon deformation potentials of bulk crystals can be used to describe the shifts observed in the nanowires[119]. This assumption is supported, at least for hydrostatic stress, by independent measurements performed by Zardo et al.[132,133] on GaAs wires: the value of hydrostatic deformation potential extracted matched the bulk value within 30 %. Using the deformation potentials extracted in bulk uniaxial stress experiments[96] and the results in §3.3.1, we can express the relative energy shift of the $\mathrm{TO_S}$ and $\mathrm{LO_D}$ phonons in terms of the axial strain $\varepsilon_\parallel$ in the nanowire in the following set of equations:

$$\begin{cases} \frac{\Delta\omega_{\mathrm{TO_S}}}{\omega_{\mathrm{TO_S}}} = [-3\gamma_T h + r'_T(1-h)]\varepsilon_\parallel \\ \frac{\Delta\omega_{\mathrm{LO_D}}}{\omega_{\mathrm{LO_D}}} = [-3\gamma_L h - \frac{1}{2}r'_L(1-h)]\varepsilon_\parallel \end{cases} \tag{6.1}$$

where $\gamma_T = 1.35$ and $\gamma_L = 1.07$ are the hydrostatic mode Grüneisen parameters, while $r'_T = -0.88$ and $r'_L = -0.53$ are the deviatoric mode Grüneisen parameters for the GaAs TO and LO phonons. The difference between the transversal deformation potentials, labeled with T, and the longitudinal deformation potentials, labeled with L, resides in the strain variation of the microscopic electric field, which is at the origin of the LO-TO splitting. The factor h represents the portion of nanowire elongation caused by the isotropic component of the Zincblende unit-cell deformation and has been defined in equation (3.14), in terms of the Poisson ratio ν for the [111] direction:

$$h = \frac{1-2\nu}{3}$$

The factor $(1-h)$ represents the remaining fraction of elongation due to the shear deformation of the Zincblende unit cell. To estimate the axial strain we note that equation (6.1) can be written in matrix form as:

$$\begin{bmatrix} \frac{\Delta\omega_{\mathrm{TO}_S}}{\omega_{\mathrm{TO}_S}} \\ \frac{\Delta\omega_{\mathrm{LO}_D}}{\omega_{\mathrm{LO}_D}} \end{bmatrix} = \begin{bmatrix} -3\gamma_T & r'_T \\ -3\gamma_L & -\frac{1}{2}r'_L \end{bmatrix} \begin{pmatrix} h \\ 1-h \end{pmatrix} \varepsilon_\parallel \tag{6.2}$$

Multiplying both terms of this equation by the inverse of the matrix containing the deformation potentials, we obtain the vector $\begin{pmatrix} h \\ 1-h \end{pmatrix} \varepsilon_\parallel$. The sum of its two components returns directly the axial strain $\varepsilon_\parallel$ and the ratio contain information about the nanowire Poisson ratio ν in the [111] direction. Interestingly, the Poisson ratio estimated for the nanowire, equal to 0.16±0.04, is smaller than the value of 0.186, expected in bulk GaAs for the same stress direction. We believe that both the nanoscale diameter and the core-shell structure of the nanowire contribute to the discrepancy in mechanical properties compared to bulk.

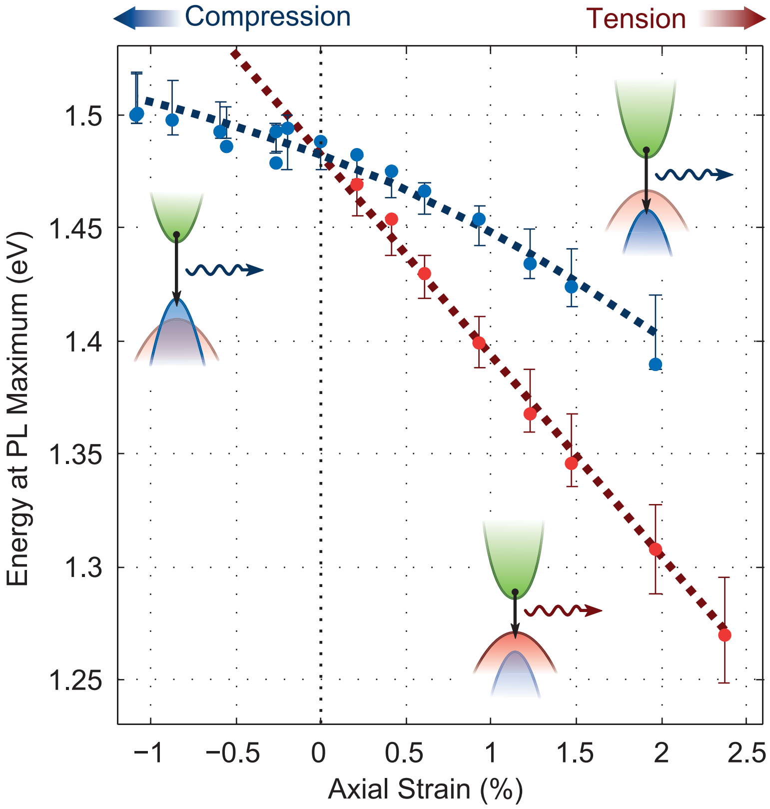

Figure 6.7: PL peak energy and simulated energy shifts of the conduction and valence band edges as a function of the quantified axial strain applied to the core-shell GaAs-$Al_{0.3}Ga_{0.7}As$-GaAs nanowire.

6.7 Band Structure Modification with Strain

Using the axial strain estimation, we proceed to analyze the PL spectra of figure 6.4 quantitatively. In particular, we plot in figure 6.7 the photoluminescence peak energies as a function of the estimated axial strain. The nanowire experiences a compressive strain of up to $-1.0\,\%$ and a tensile strain of up to $2.4\,\%$. These values are within the expected limits imposed by buckling[134] and plastic deformation. In compression, the peak wavelength varies only weakly, whereas in tension a much stronger dependence together with a peak splitting can be observed. Both peaks red shift significantly under tension, by $85\,\mathrm{meV}/\%$ for the lower energy peak and by approximately $56\,\mathrm{meV}/\%$ for the higher energy one.

The shift of the PL peaks vs. axial strain are directly related to the energy shifts of the conduction and valence band edges, which can be described us-

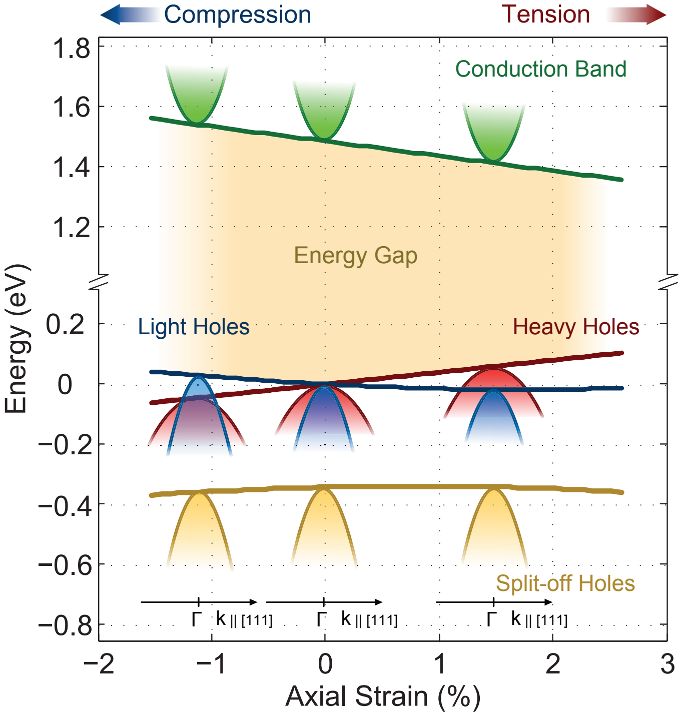

Figure 6.8: Expected shift of the band edges of a strained Zincblende nanowire, according to an 8-band $k \cdot p$ model.

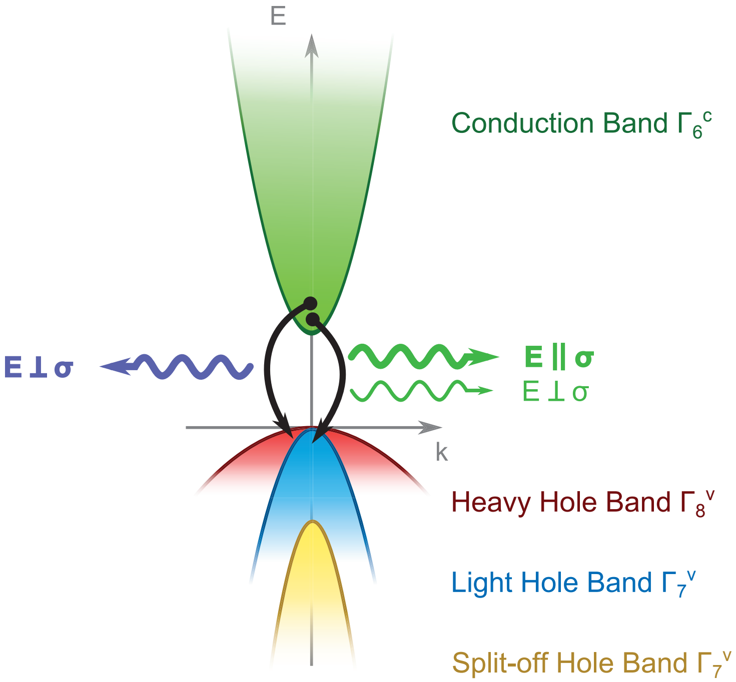

Figure 6.9: Optical selection rules in strained Zincblende crystals.

ing an 8-band $k{\cdot}p$ model that includes the Pikus-Bir strain Hamiltonian[78,93]: the expected energy-shifts induced by the strain are plotted in figure 6.8 while details about the model are provided in §3.2.2. As soon as uniaxial stress is applied to the nanowire, the valence band degeneracy between light hole and heavy hole is lifted because of the symmetry-breaking deviatoric deformation of the Zincblende unit cell. The conduction band will shift because of the isotropic deformation component of the strain. The conduction band edge, represented in green, and the heavy hole band, represented in red, shift linearly with strain with opposite slopes whereas the light hole band, represented in blue, follows a non-linear behavior because of the mix with the split-off band, represented in yellow, and the combined effect of strain and spin-orbit interaction.

The optical selection rules, presented in §4.2 and shown in figure 6.9, identify which optical transitions are allowed for a specific light polarization: recombination into the heavy hole can generate light only with polarization perpendicular to the strain axis[135], while light emitted from the recombination into the light hole states can have polarization either parallel or perpendicular to the stress axis. The nanowire geometry influences the

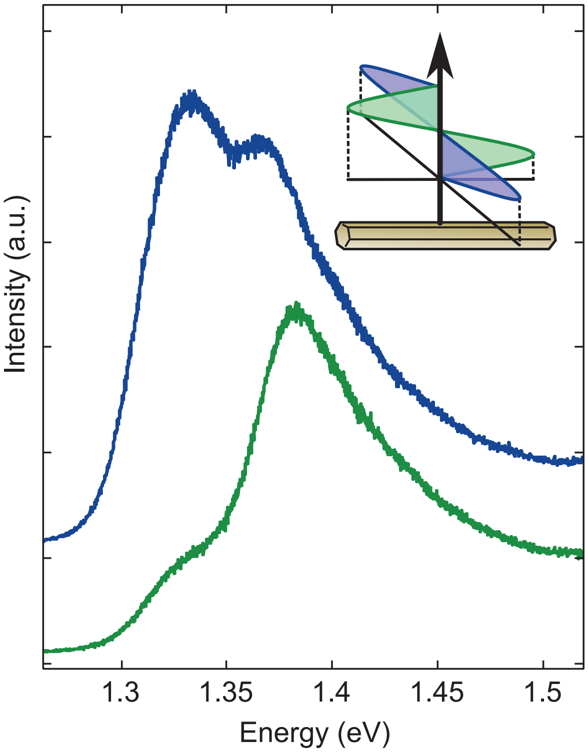

Figure 6.10: Polarization dependence of the PL in a tensile strained Zincblende nanowire. The measurement has been performed at 300 K.

polarization properties of the PL as discussed in §5.6.4: because of the high dielectric mismatch between the nanowire and the environment, the light emitted perpendicular to the nanowire axis will couple out with an efficiency lower than one order of magnitude compared to the light polarized parallel to the nanowire axis[120,136]. For our specific case, the luminescence originating from the heavy hole recombination will therefore be strongly suppressed, while the one coming from the light hole will be less affected. To validate this model, we have measured and plotted in figure 6.10 the PL spectra of Zincblende nanowires under tensile strain, using two different polarization configurations and the same color coding of figure 6.9. The spectrum acquired with polarization aligned to the nanowire axis is shown in green: the high energy peak, assigned to the recombination into the light hole states, is clearly dominating the spectrum. The spectrum acquired with polarization orthogonal to the nanowire axis is shown in purple. In this configuration, the highest intensity is observed for the low energy peak, assigned to the recombination of the heavy hole.

We now can consider jointly the effect of strain, dielectric mismatch effects and optical selection rules on the PL spectra. Under tension, both the light hole band and the conduction band shift down in energy, whereas the heavy hole band shifts up. In this stress regime, the band gap is defined by the heavy hole band and the conduction band. These bands shift towards each other and generate the large red shift of the PL. For high values of stress only the recombination from heavy hole states can be observed, even though affected by the dielectric mismatch effects. For small values of stress that induce a valence-band splitting smaller than a few kT, both heavy and light hole states can be populated and the respective recombination processes observed as a peak splitting. The light hole band will be populated with fewer holes but the photons generated by the recombination into this band will not suffer from dielectric mismatch effects. Conversely, the higher population of the heavy hole is balanced by the poorer coupling of its luminescence due to dielectric mismatch.

Under compression, both the light hole band edge and the conduction band edge shift towards higher energies, whereas the heavy hole band shifts down in energy[92]. The light hole states are therefore energetically favored and populated with highest density, while the corresponding luminescence is efficiently coupled to the environment. Heavy hole states will instead be poorly populated and the corresponding luminescence attenuated because of dielectric mismatch effects. As a consequence only the PL peak due to light hole recombination can be observed. Note that the conduction band and the light hole band undergo similar shifts under strain and, consequently, the energy gap does not vary substantially under compression.

The variation of the energy difference between the conduction band and the two valence bands as a function of the axial strain, $\varepsilon_{\parallel}$, can be approximately expressed with the following set of relations, introduced in §3.2.2:

$$\begin{cases} \Delta E^{\text{cb-hh}} = \left[3ah + \frac{\sqrt{3}}{2} d_v (1-h)\right] \varepsilon_{\parallel} \\ \Delta E^{\text{cb-lh}} = \left[3ah - \frac{\sqrt{3}}{2} d_v (1-h)\right] \varepsilon_{\parallel} - \frac{1}{2\Delta_0} \left[\sqrt{3} d_v (1-h)\, \varepsilon_{\parallel}\right]^2 \end{cases} \tag{6.3}$$

where $\Delta E^{\text{cb-hh}}$ is the energy of the transitions into the heavy hole band, $\Delta E^{\text{cb-lh}}$ is the energy of the transitions into the light hole band, a and d are the hydrostatic and shear optical deformation potentials, and Δ_0 is the spin-orbit splitting. Using this model, as well as the axial strain and Poisson ratio obtained from the Raman spectra, we can extract the values of the hydrostatic deformation potential $a = -8.6 \pm 0.7$ eV and the shear deformation potential $d = -5.2 \pm 0.7$ eV. Both values are very similar to those observed in bulk GaAs, and provide the final confirmation of the integrity of our assumptions and of the axial strain estimation[92,137]. We also note that the finite nanowire size plays an important role in determining the PL shifts because of its effect on the mechanical properties. As the Poisson ratio decreases, the factor h increases and with it the hydrostatic deformation component of the nanowire elongation. As a consequence, the hydrostatic deformation potential a, which is larger than the shear deformation potential d, will increase its influence in the weighted sums in equation (6.3), resulting in an amplification of the PL shift with strain. Finite-size effects can therefore be used to tune the mechanical properties of the nanowire and to boost strain effects.

6.8 Maximum Strain and Photoluminescence Shift

To highlight any variation of the observed phenomena with temperature, we have repeated the same strain measurement on a different nanowire at room temperature. In figure 6.11 we show the energy shift observed in the PL of different nanowires, measured at different temperatures in the tensile regime. The blue squares are extracted from the low-temperature data already presented, whereas the red squares are derived from measurements of the same wire at room temperature. Both datasets follow the same trend, suggesting that the deformation potentials and the elastic constants exhibit no substantial temperature dependence between 160 K and room temperature. To measure the effect of higher strain, we used an InGaAs detector to expand the spectral range of sensitivity beyond 1.2 eV, which is the sensitivity limit of the silicon detector. The corresponding shift in PL peak energy,

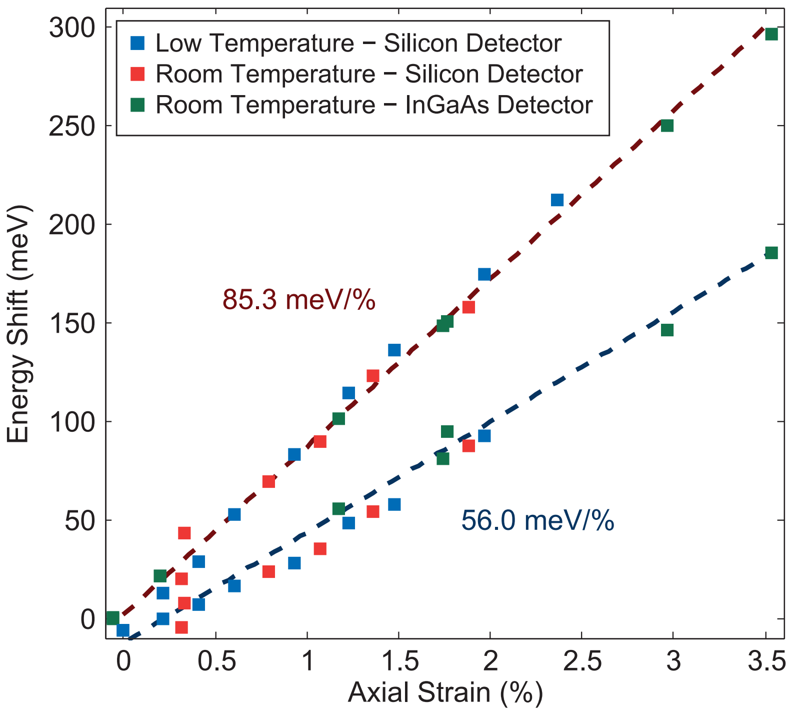

Figure 6.11: Reproducibility and maximum energy shift for the light hole and heavy hole band transitions, as a function of tensile strain in the nanowire.

measured on a different wire, is shown as green squares in Fig. 6. We were able to induce a remarkably high strain of 3.5 % and achieve a maximum red shift of 296 meV. This is, to our knowledge, the highest tensile strain ever reported on a working GaAs nanostructure. Upon further stretching, the PL shifted back to its relaxed position. This could be related to a rupture of the wire or to the slippage of the nanowire under the metal clamps.

6.9 Conclusion

In summary, we investigated the effect of strain on the PL and Raman spectra of core-shell GaAs-$Al_{0.3}Ga_{0.7}As$-GaAs nanowires. Uniaxial stress was applied mechanically to the nanowire in a continuous and reversible way, both in compression and tension. Upon application of tension, we observed a highly asymmetric shift of the PL and a remarkable decrease of the band gap of 296 meV at 3.5 % of strain. Fingerprints of symmetry breaking due to the anisotropic nature of the nanowire deformation were found in the PL and in the Raman spectra, in which polarization-dependent measurement allowed us to univocally identify the distinct phonon contributions. Because of its linear relation with stress, the energy shift of the Raman peaks was used to determine the axial strain induced in the nanowire and to infer information about the Poisson ratio in the [111] direction. The significant change in the electronic bandstructure is explained using an 8-band $k \cdot p$ model and deformation potentials consistent with those of the bulk were extracted. Given the high value for the yield strength and the high elongation that can be elastically induced, GaAs semiconducting nanowires are the ideal platform to realize optoelectronic devices that leverage on strain effects to tune the optical properties over a broad wavelength range.

7

Uniaxial Stress Effects in GaAs Wurtzite Nanowires

Semiconductors are typically classified either as direct-bandgap materials, known for their efficient light-emission properties, or as indirect-bandgap materials, often used in light-harvesting applications and photo-detectors[76]. Wurtzite semiconductors can also have a pseudodirect bandgap configuration[138], in which electron and hole states overlap strongly, but optical transitions between them are impaired by symmetry. Switching a material between these configurations would enable novel photonic applications[139]. However, a large anisotropic strain is needed to induce any of these band structure transitions[140].

In this chapter we show that by applying small uniaxial stress to Wurtzite GaAs nanowires, their light-emission properties can be switched on and off as stress induces a transition from the direct to the pseudodirect configuration. By varying the strain continuously from tension to compression, we could clarify its band structure and resolve a controversial discussion about the energy and symmetry of the valence and conduction band states. We envisage a new generation of devices that can simultaneously serve as efficient light emitters and efficient photodetectors by leveraging the strain degrees of freedom, with a strong impact on the electronic and photonic industries[13,141,142].

7.1 Motivation

In semiconductors, efficient light emission occurs when two conditions are met: the electron and the hole wavefunctions must overlap strongly in the wave-vector space, and the symmetry of the states involved in the radiative process must be compatible with the dipole transitions (see §4.1). Semiconductors with a direct bandgap configuration, such as Zincblende GaAs, fulfill both conditions and have empowered the photonic and optoelectronic industries. Indirect bandgap semiconductors, such as silicon or germanium, also have electron and hole states at the center of the Brillouin zone, whose symmetry is compatible with light emission. However, electrons occupy lower energy states at the edge of the Brillouin zone, causing a reduction of the overlap with the hole wavefunction, which suppresses the light emission. To realize nano-photonic devices directly integrated on silicon, considerable efforts have been made to induce a direct bandgap configuration in germanium. However, the fact that an anisotropic strain of more than 4 % is needed to induce such a transition hampers the development of such photonic applications[32,140].

By reducing the semiconductor dimension down to the nanowire geometry, high values of strain can be accommodated[47,73], and precise control of the morphology[143] and crystal structure[45,46] have made possible to grow pure single-crystal Wurtzite nanowires, not available in bulk or thin film form[50,144]. These crystals are characterized by the peculiar band structure, discussed in detail §2.2.2 and shown in figure 7.1: unlike the case of Zincblende, the heavy, light and split-off holes are non degenerate and the conduction band consists of two states at the Γ-point. One state corresponds to the conduction band of Zincblende crystals (symmetry Γ_7^c in double group notation, shown in green) and is indicated as the "bright" conduction band, whereas the other is related to the states found at the L-point in Zincblende (symmetry Γ_8^c in double group notation, shown in brown) and is indicated as the "dark" conduction band[138].

Understanding which conduction state is lower in energy has important consequences on the electronic transport and optical properties of Wurtzite materials. In some III-V alloys, the dark and the bright conduction band are well separated in energy and the alloy ionicity alone can determine which of them is energetically favored[138]. However, this is not the case for GaAs. Experiments were able to define the value of the energy bandgap[144,145], but the energy difference between the two conduction states could not be determined. Indirect measurements merely provided hints of their proximity[144]. Theoretical investigations addressing this topic have provided only limited insight. Some density functional theory (DFT) studies[138] predicted a direct bandgap configuration in Wurtzite GaAs, in which the bright con-

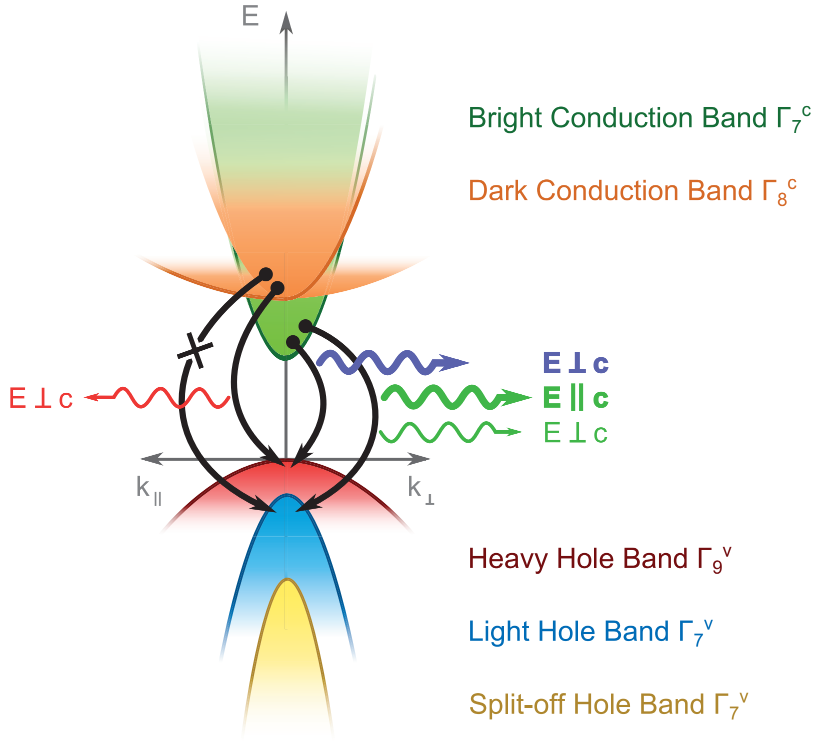

Figure 7.1: Band structure and symmetry of the states for Wurtzite GaAs. The symmetry of the states at the Γ-point are given in the double group notation[80], i.e. including the spin-orbit interaction. Optical transitions between conduction and valence bands are indicated with a black arrow connecting the bands involved, a colored wavy arrow and a label that indicates the polarization of the photon emitted. When the polarization label is indicated in bold, the transition is allowed even if the spin-orbit interaction is disregarded. If the polarization is indicated with thin fonts and arrows, the corresponding transition is allowed only if the spin-orbit interaction is taken into consideration (Wurtzite double group notation). Transitions indicated with a cross are strictly forbidden.

duction band is energetically favored. Other *ab-initio* calculations[80] that included spin-orbit interactions, predicted a pseudodirect bandgap configuration, in which the dark conduction band has the lowest energy. This band alignment imparts interesting optical properties to Wurtzite crystals: the conduction and valence band wavefunctions have a strong overlap at the Γ-point, but light emission is weak because of symmetry reasons discussed in §4.2. The two apparently conflicting theoretical results indicate instead that the bright and the dark conduction band of Wurtzite GaAs are so close in energy that small perturbations, like a spin-orbit interaction or strain, can switch their order, making this material system an ideal platform to study direct-to-pseudodirect transitions. Studying the effect of uniaxial stress on the light emission of a single Wurtzite nanowire would clarify its bandstructure. Because of the large range of elastic deformation of Wurtzite nanowires[73], significant energy level shifts and bandstructure splittings can be induced, enabling a clear interpretation.

7.2 Experiment

To investigate the direct-to-pseudodirect transition in Wurtzite GaAs upon the application of uniaxial stress, we fabricated free-standing structures by clamping single nanowires to a flexible substrate. We used single core-shell GaAs-AlGaAs-GaAs nanowires grown along the *c*-axis. By gradually bending the substrate, in concave or convex fashion, a continuous compressive or tensile deformation can be induced on the substrate surface and transferred to the nanowire. The nanowires have been excited with a low-power (16 µW) He-Ne laser at room temperature. The light from the nanowire has been collected using a 100X long-working-distance objective and detected by a liquid-nitrogen-cooled silicon CCD. The PL spectra were measured with a 300 lines/mm grating to obtain information on the band structure. A 1800 lines/mm grating has been used instead to measure the Raman spectra and locally gauge the strain applied to the nanowire. Further experimental details are available in chapter 5.

7.3 Optical Spectroscopy on Unstrained Wurtzite Nanowires

Figure 7.2 shows the typical PL spectra acquired on a single Wurtzite core-shell GaAs-$Al_{0.3}Ga_{0.7}As$-GaAs nanowire, without the application of any stress. While the laser linear polarization was oriented along the nanowire axis, the polarization orientation of the light detected by the spectrometer (from now on called analyzer) was set along two orthogonal directions.

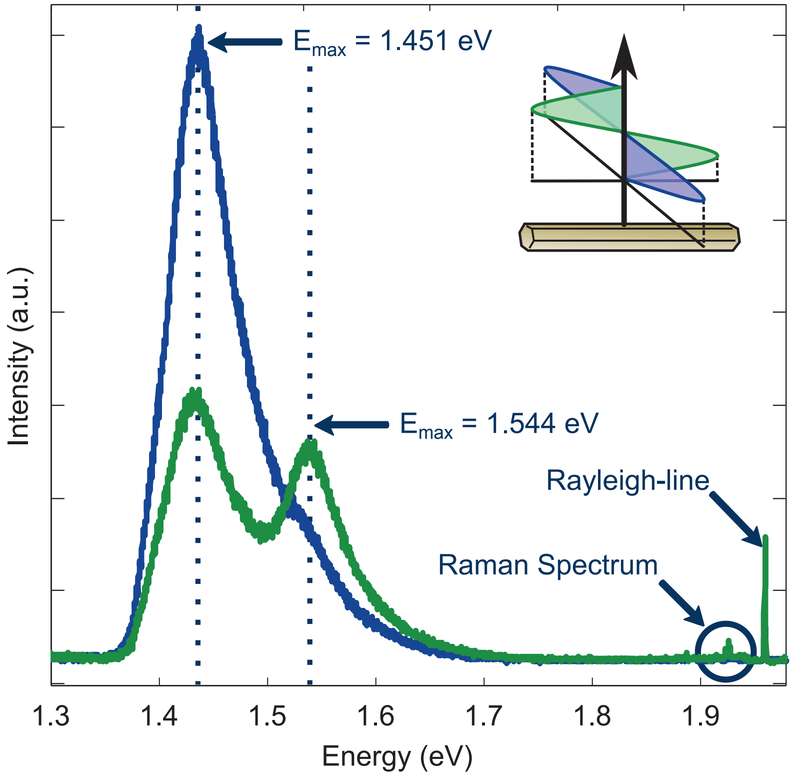

Figure 7.2: Photoluminescence spectra acquired on a single Wurtzite core-shell GaAs-Al$_{0.3}$Ga$_{0.7}$As-GaAs nanowire, with the polarizer parallel to the nanowire axis. The analyzer was oriented parallel to the nanowire axis (green curve) or orthogonal to the nanowire axis (purple curve), as indicated by the sketch.

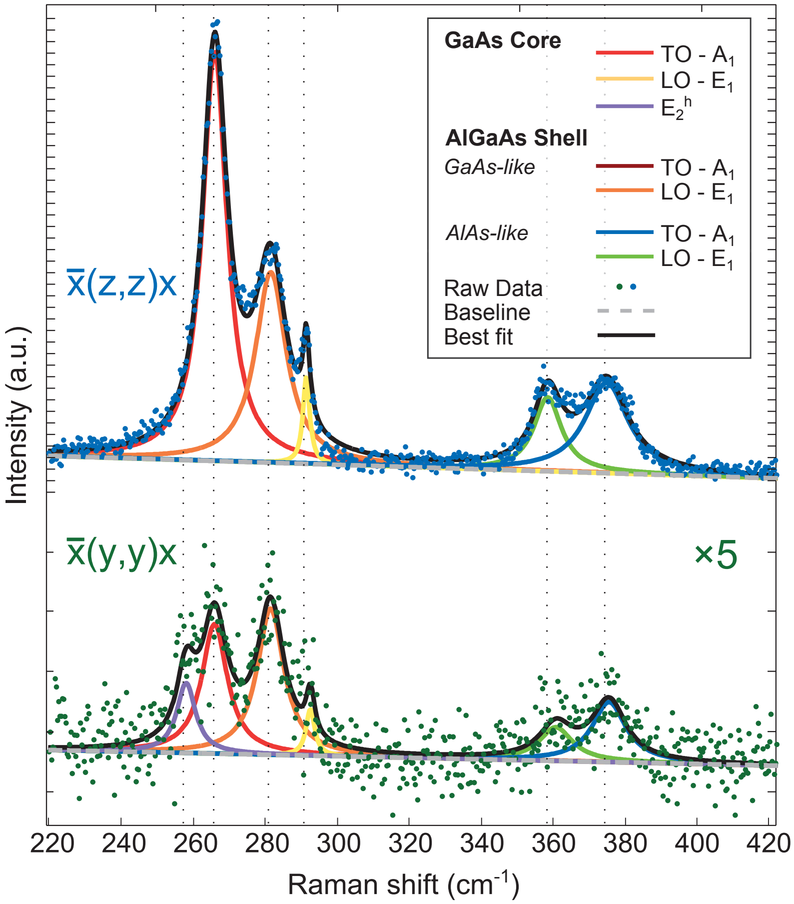

Figure 7.3: Raman spectrum of a single Wurtzite core-shell GaAs-$Al_{0.3}Ga_{0.7}As$-GaAs nanowire under high laser excitation of 160 µW. The spectrum shown in blue was measured with both the polarizer and the analyzer parallel to the nanowire axis. The spectrum shown in green was measured with polarizer and analyzer oriented orthogonally to the nanowire axis. Both scattering configurations are labeled with the Damen's notation.

When the analyzer is oriented orthogonally to the nanowire, as shown in the purple spectrum, the PL shows a predominant peak at 1.451 eV and only a small shoulder around 1.544 eV. When the analyzer is instead oriented along the nanowire axis, the two PL peaks have comparable intensities and their energy difference can be clearly resolved.

The Raman spectrum of the same nanowire under a tenfold higher laser excitation power (1.6 mW) is shown in figure 7.3. Under this illumination conditions it is possible to observe the characteristic peaks of optical phonons of the GaAs core and of the $Al_{0.3}Ga_{0.7}As$ shell[85]. The spectrum shown in blue, in the upper part of the figure, has been acquired with both polarizer and analyzer aligned parallel to the nanowire axis. The GaAs transverse optical (TO) phonon with symmetry A_1 provides the highest peak intensity and is located at $265.6\pm0.1\,\mathrm{cm}^{-1}$. The longitudinal optical (LO) phonon, with symmetry E_1, is also visible $290.9\pm0.1\,\mathrm{cm}^{-1}$. Further peaks, attributed to the $Al_{0.3}Ga_{0.7}As$ shell, are positioned at $281.1\pm0.1\,\mathrm{cm}^{-1}$ (GaAs-like LO), $358.0\pm1\,\mathrm{cm}^{-1}$ and $373.6\pm0.2\,\mathrm{cm}^{-1}$ (AlAs-like TO and LO). The spectrum shown in green, in the lower part of the figure 7.3, has been acquired instead with both polarizer and analyzer aligned perpendicular to the nanowire axis. In this scattering configuration the E_2^{high} phonon becomes observable with a peak, shown in purple, centered at $257.8\pm0.1\,\mathrm{cm}^{-1}$ and provides a fingerprint of the Wurtzite single crystalline structure of the nanowire[85].

To correlate the bandstructure information extracted from the PL spectra with the strain information contained in the Raman spectra, it is very important that the exact same illumination conditions are used to acquire both optical spectra. Our focus in this chapter is understanding the bandstructure modification with strain, which is best captured at low laser illumination. By decreasing the laser power to the nominal 16 µW also for the acquisition of the Raman spectra, some of the optical phonon peaks fall below the detection limit and only the GaAs TO and LO remain clearly observable. These two phonon lines provide anyhow enough information to investigate the strain in the nanowire core.

7.4 Strain Effects on Raman and Photoluminescence Spectra

The effect of strain on the Raman spectrum of the nanowire is shown in figure 7.4. All spectra have been acquired under low laser power (16 µW) by aligning the polarization of both the laser excitation and the light collected by the spectrometer to the nanowire axis. This configuration minimizes dielectric mismatch effects and ensures the highest optical coupling with the nanowire[120]. The curve in green at the center of the panel, close to

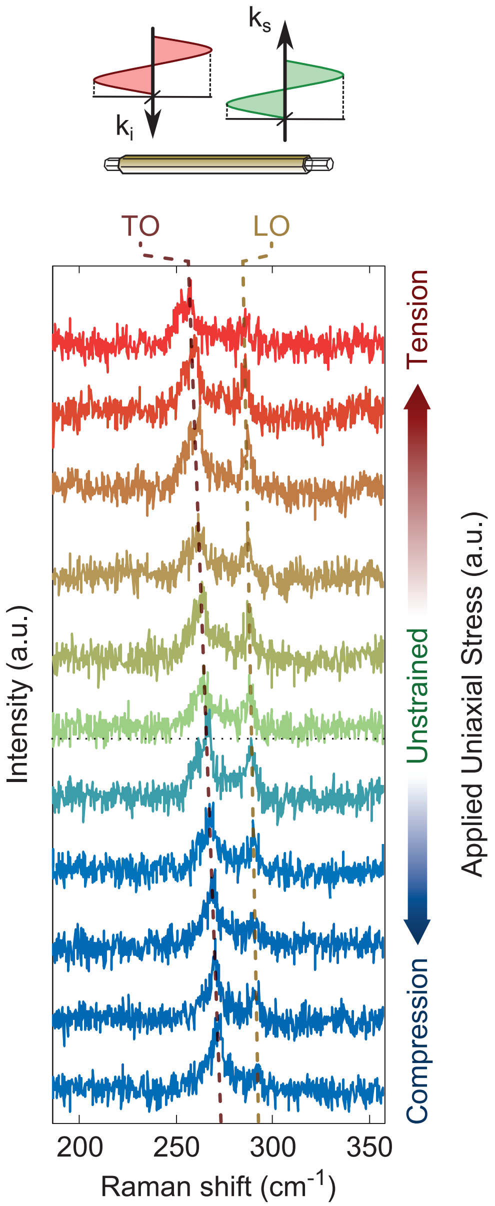

Figure 7.4: Effect of uniaxial stress on the Raman spectrum of a single Wurtzite core-shell GaAs-$Al_{0.3}Ga_{0.7}As$-GaAs nanowire. The spectra are collected with both the laser and the detector polarization aligned with the nanowire axis. The scattering configuration sketch is shown on top. The dotted lines are a guide-to-the-eye for the positions of the phonon peaks attributed to the GaAs TO and LO phonons.

the dashed line, was measured without application of stress. Two peaks, namely, the transversal optical (TO) phonon (symmetry A_1) and the longitudinal optical (LO) phonon (symmetry E_1) of the GaAs core, are observed at $265.5\pm0.28\,\mathrm{cm}^{-1}$ and $289.2\pm0.36\,\mathrm{cm}^{-1}$, respectively. The Raman spectra measured upon application of tensile stress are shown in red in the upper part of the graph, whereas the spectra measured upon compression are shown in blue in the lower part. Both TO and LO phonons experience a linear shift with applied stress. The energy shift of the TO phonon peak is larger than that of the LO phonon peak, shifting down to $256.6\,\mathrm{cm}^{-1}$ with tension and up to $272.2\,\mathrm{cm}^{-1}$ with compression. In contrast, the LO phonon shifts downward in energy to $286.6\,\mathrm{cm}^{-1}$ under tension and upwards to $292.2\,\mathrm{cm}^{-1}$ under compression. As in Zincblende nanowires[146], the energy shift of the TO and LO phonons are expected to depend linearly on the strain of the nanowire[97] and follow different slopes depending on the direction of atomic displacement, providing information about the strain tensor components. The linear dependence between the applied axial strain and the phonon shifts indicates that the nanowire undergoes elastic deformations. However, as no phonon deformation potentials have been determined yet for Wurtzite GaAs, the peak shifts can only be used to measure the relative strain of the nanowire.

Figure 7.5 and 7.6 show the PL spectra measured as function of stress with polarization orthogonal and parallel to the nanowire axis, respectively. The spectra acquired upon increasing tension are shown in red, offset towards higher ordinates. The low-energy PL peak shifts by 200 meV towards lower energies. The peak found at higher energy shifts in the same direction, but its energy difference with the other peak increases from 93 meV with no stress up to 110 meV under maximum tension. Tensile stress affects also the PL intensity, increasing that of the low-energy peak more than eightfold in both polarizer orientations and that of the high-energy peak up to fivefold. The efficiency of the silicon detector drops dramatically below 1.2 eV, limiting the maximum energy shift and tensile strain detectable in our experiment. We expect that, before the elastic deformation limit of the material is reached, larger shifts towards longer wavelengths can be obtained, as we have observed in Zincblende GaAs nanowires[146]. The PL spectra acquired with increasing compressive stress, shown in blue and offset towards lower ordinates, follow the same trends as observed under tensile stress. The peaks shift towards higher energies above 1.57 eV, whereas their energy separation decreases to a few meV[*]. The intensity of the two peaks decreases drastically and is suppressed by more than three orders of magnitude across the entire stress range, from tension to compression.

---

[*] This observation can be clearly seen in figure 7.9.

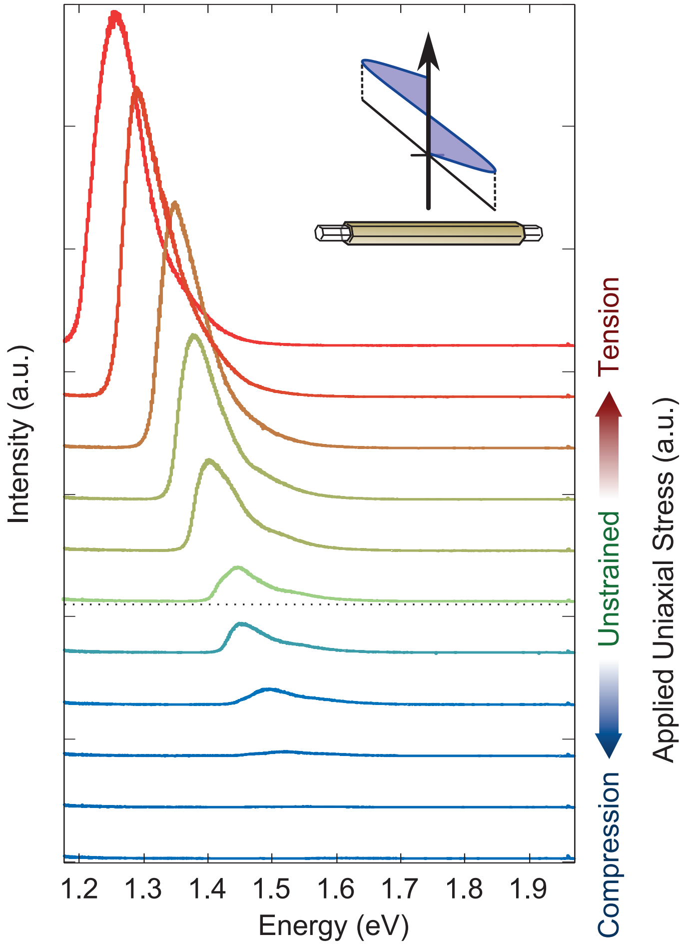

Figure 7.5: Effect of uniaxial stress on the PL spectrum of a single Wurtzite core-shell GaAs-$Al_{0.3}Ga_{0.7}As$-GaAs nanowire. The laser is polarized parallel to the nanowire axis. Linearly polarized photoluminescence, orthogonal to the nanowire axis, was transmitted to the spectrometer. The analyzer configuration is sketched in the inset.

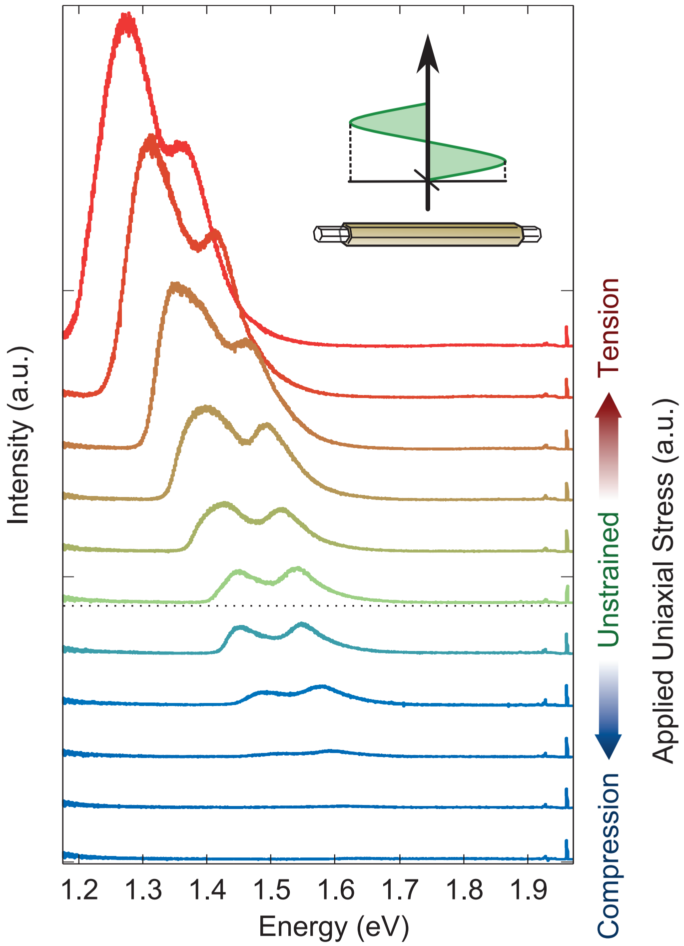

Figure 7.6: Effect of uniaxial stress on the PL spectrum of a single Wurtzite core-shell GaAs-$Al_{0.3}Ga_{0.7}As$-GaAs nanowire. The laser is polarized parallel to the nanowire axis. Linearly polarized photoluminescence, parallel to the nanowire axis, was transmitted to the spectrometer. The analyzer configuration is sketched in the inset.

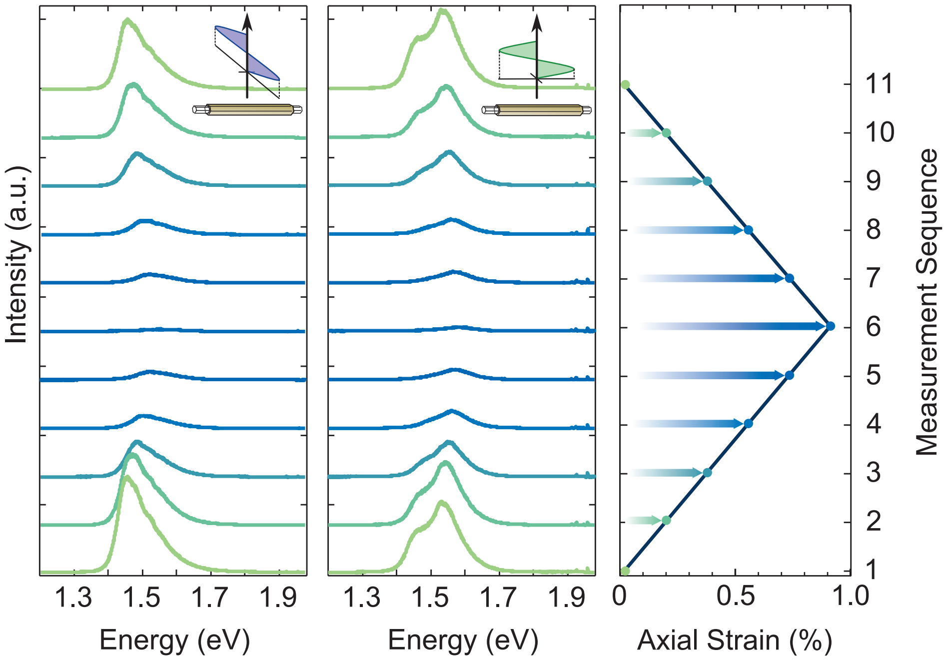

Figure 7.7: PL spectra of a Wurtzite GaAs nanowire under compressive stress during a loading-unloading cycle. The measurements have been performed under high laser illumination (160 µW).

7.5 Reversibility of the Photoluminescence Quenching

To prove that the PL quenching is induced by the elastic deformation of the nanowire, we measured the PL spectra during a loading-unloading cycle, increasing the nanowire compression and returning back to the unstrained condition. Figure 7.7 shows the spectra acquired under unstrained conditions with green color, and the spectra acquired upon increasing compression with a color gradually changing to blue. The left and the center panel show the PL measured with the analyzer aligned perpendicular and parallel to the nanowire axis, respectively. The right panel shows the value of compressive stress applied during the measurement sequence. Figure 7.7 clearly demonstrates that the PL intensity is suppressed by increasing the nanowire compression, and recovered it when returning to the unstrained condition.

7.6 Modeling the Effect of Strain on the Band Structure

The experimental observations discussed so far can be rationalized by considering the theoretical $k\cdot p$ model, which is discussed in detail in §3.2.3. The Wurtzite GaAs nanowire is subject to uniaxial stress parallel to the c-axis, elongates along this direction and shrinks in cross section because of the finite Poisson ratio ν. The corresponding strain preserves the symmetry of the unit cell over the entire stress range. The relations of the energy difference between the valence and conduction band states and the strain applied to the nanowire assume simple analytical expressions in the framework of the cubic approximation[93,94]:

$$\begin{aligned}
E_\mathrm{d} - E_\mathrm{b} &= \Delta E_c + (\Xi_{d,h} - \Xi_{b,h})\, h\varepsilon_\parallel + \Xi_{d,u}(1-h)\varepsilon_\parallel \\
E_\mathrm{b} - E_\mathrm{hh} &= E_\mathrm{gap} + (\Xi_{b,h} - D_1 - 2D_2)\, h\varepsilon_\parallel - \tfrac{1}{2}D_3(1-h)\varepsilon_\parallel \\
E_\mathrm{hh} - E_\mathrm{lh} &= \tfrac{1}{2}\left\{\Delta'_\mathrm{cr} + \Delta_\mathrm{so} - \sqrt{(\Delta'_\mathrm{cr} + \Delta_\mathrm{so})^2 - \tfrac{8}{3}\Delta'_\mathrm{cr}\Delta_\mathrm{so}}\right\} \\
E_\mathrm{hh} - E_\mathrm{so} &= \tfrac{1}{2}\left\{\Delta'_\mathrm{cr} + \Delta_\mathrm{so} + \sqrt{(\Delta'_\mathrm{cr} + \Delta_\mathrm{so})^2 - \tfrac{8}{3}\Delta'_\mathrm{cr}\Delta_\mathrm{so}}\right\} \\
\Delta'_\mathrm{cr} &= \Delta_\mathrm{cr} + \tfrac{3}{2}D_3(1-h)\varepsilon_\parallel
\end{aligned} \tag{7.1}$$

The quantities E_d, E_b, are the energy of the dark and bright conduction band, E_hh, E_lh and E_so are the energy of the heavy hole, light hole and split-off hole bands, evaluated at the Γ-point. The constants $\Xi_{d,h} = \Xi_{d\parallel} + 2\Xi_{d\perp}$, $\Xi_{b,h} = 3\Xi_b$ and $(D_1 + 2D_2)$ are the hydrostatic deformation potentials for the dark and the bright conduction band and for the valence band states (in Pikus-Birr notation[93]). The constants $\Xi_{d,u} = \left(\Xi_{d\parallel} - \Xi_{d\perp}\right)$ and D_3 are, respectively, the deviatoric deformation potentials of the dark conduction band and of the valence bands. Different *ab-initio* methods have been used to quantify these constants and provide values, shown in table 3.5, that are robust and consistent within a few percent[81]. The factor h represents the percentage of isotropic deformation, which causes a variation of the volume of the unit cell but maintains its aspect ratio constant, and can be expressed in terms of the Poisson ratio ν as described in §3.1.5. The factor $(1-h)$ represents instead the percentage of deviatoric deformation, which captures the deformation of the unit-cell aspect ratio occurring at constant volume.

The energy level shifts predicted by the model are plotted in figure 7.8 and, together with the selection rules for the optical transitions shown in

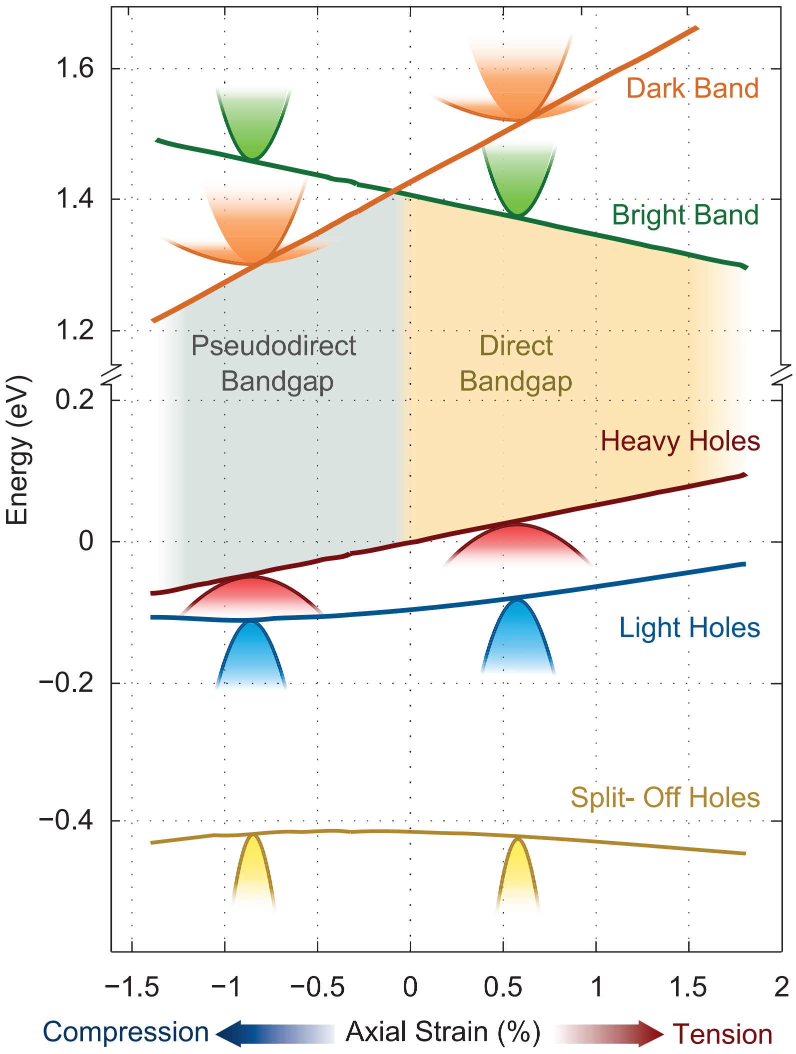

Figure 7.8: Expected shift of the band edges of a strained Wurtzite nanowire, according to a $k \cdot p$ model. The nanowire bandstructure has a direct bandgap configuration (shaded area in yellow) when the bright conduction band has the lowest energy among the conduction band states, and a pseudodirect bandgap configuration (shaded area in gray) when the dark conduction band is lowest. The direct-to-pseudodirect transition occurs when compressive stress is higher than $-0.12\,\%$.

figure 7.1, provide a framework to interpret the experimental observations.

The bright conduction band decreases linearly in energy when tensile stress is applied. The heavy hole band and the dark conduction band follow the opposite trend and increase their energy with tension. The light and split-off hole bands, which share the same symmetry character, will start to mix upon the application of strain and undergo nonlinear shifts because of the combined effect of strain and spin-orbit interaction. When tensile stress is applied to the nanowire, the bright conduction band becomes energetically favorable, and electronic transitions towards both the heavy and light hole bands can occur with high oscillator strength. The low-energy PL peak (1.451 eV under zero stress) can be attributed to the transitions between the bright conduction band and the heavy hole band. These photons are highly polarized in the direction orthogonal to the nanowire axis, as expected from the model shown in 7.1. In contrast, the high-energy photons (1.544 eV under zero stress) are generated by transitions between the bright conduction band and the light hole band and, as expected, have a strong polarization component aligned in the same direction as the nanowire axis. When increasing tensile stress is applied, the energy difference between the heavy and light hole band edges increases, holes tend to populate the heavy hole states with higher density, and the intensity of the corresponding heavy hole PL peak becomes larger. However, the optical coupling of such photons to the environment is low because of dielectric mismatch effects[120]. Because of this bottleneck, holes can populate the light hole band and, by recombining with electrons of the bright conduction band, generate photons polarized along the nanowire axis, which are not damped by dielectric mismatch effects. When increasing compressive stress is applied to the nanowire, the dark conduction band becomes energetically favorable, achieving a pseudodirect bandgap configuration. The electrons populate these states with high density, but cannot easily recombine towards any valence band state. Optical transitions from this band towards the heavy hole band can occur with polarization perpendicular to the nanowire's *c*-axis, but have only small oscillator strength. All other transitions are completely forbidden[99]. When the dark conduction band decreases in energy, below the bright conduction band minimum, the PL intensity decreases accordingly.

7.7 Fingerprint of the Dark Transitions

To investigate the weak PL generated by the weak optical transitions in the pseudodirect configuration, we plot in figure 7.9 the intensity of the PL spectra normalized to unity and acquired with the uniaxial stress ranging from unstrained (green data points) to compression (blue data points). With

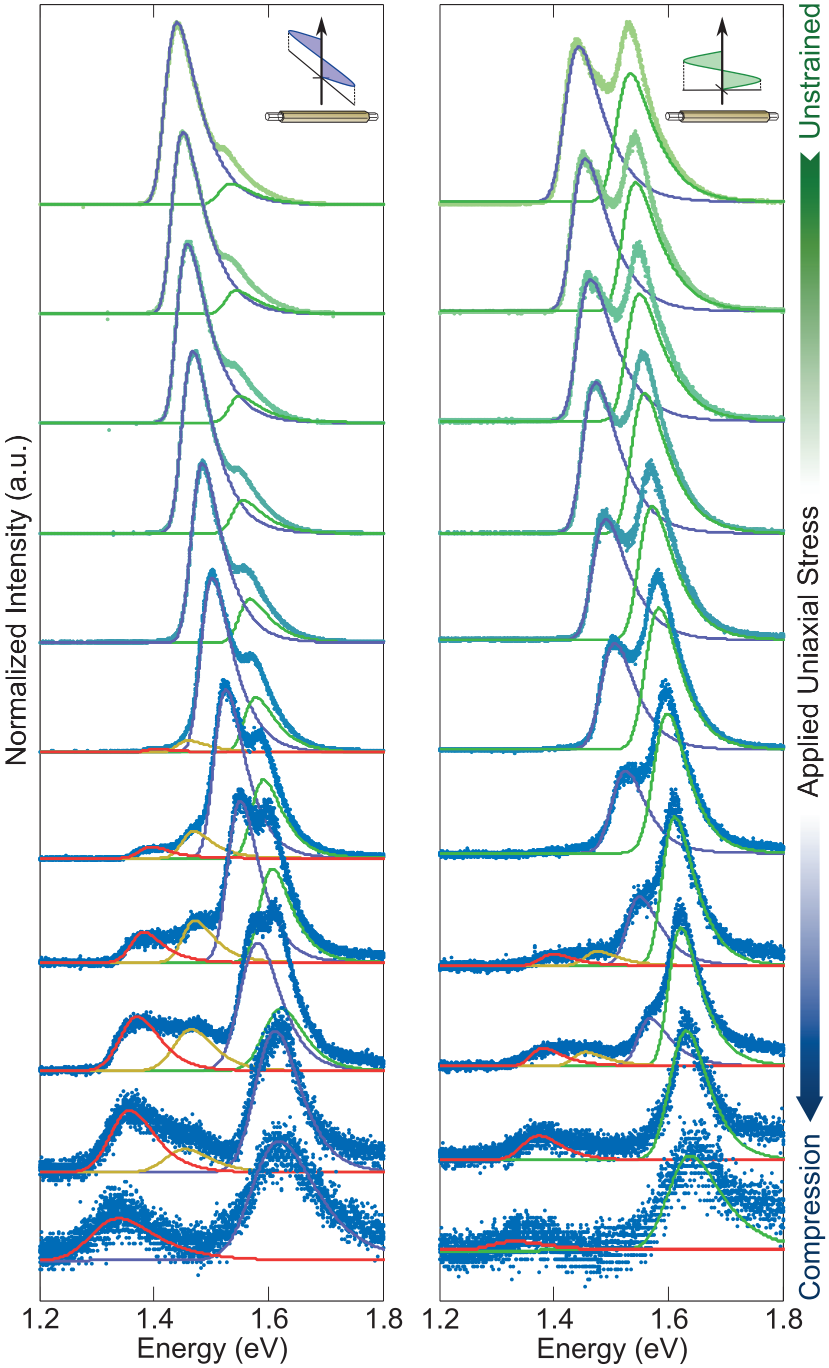

Figure 7.9: Normalized PL spectra acquired under increasing compression, under different analyzer configurations, sketched in the insets. Each spectrum has been fitted with four peaks that correspond to the optical transitions shown in figure 7.1.

increasing compressive stress, the PL peaks shift towards high energy, as already shown in figure 7.5 and 7.6. However, as soon as the low-energy peak reaches 1.47 eV, a shoulder appears around 1.38 eV. If the compressive stress is increased further, this PL component increases in intensity and shifts towards lower energy, exhibiting the opposite trend compared to the other peaks. This PL component is also strongly polarized perpendicularly to the nanowire axis. Both observations are characteristic of a transition between the dark conduction band and the heavy hole band. To support this interpretation, we fit the PL spectra with line-shapes that match the theoretical model shown in figure 7.1 and also follow the color scheme therein. Further details about the fitting are described in §4.3. The purple and green peaks correspond to the photons emitted by the transitions between the bright conduction band electrons and heavy holes or light holes, respectively[†]. The red peak corresponds to the transitions between the electronic states of the dark conduction band and heavy holes. A fourth dark transition, whose origin is not clear, is shown in yellow. The energy values of the observed optical transitions, obtained with this fitting, can be combined with the Raman data to provide a clear picture of the bandstructure and estimate the strain in the nanowire.

7.8 Inferring Strain and Bandstructure Parameters

The energy difference between the conduction and valence bands, obtained by fitting the data from two different nanowire devices (squares and circles), have been plotted in figure 7.10 together with the corresponding TO peak position, which provides a relative measure of the nanowire strain. Compared to the unstrained condition[‡], a lower TO phonon energy characterizes a state of tensile strain whereas a higher TO energy corresponds to a state of compression. We fit the joint PL-Raman data points with the stress dependence predicted from the $k \cdot p$ model shown in figure 7.8: the result of the fit is plotted with continuous lines. This methodology permits us to estimate the axial strain induced in the nanowire as well as the parameters that define the bandstructure in unstrained conditions.

The range of axial strain is comparable to the one estimated in identical experiments made on Zincblende nanowire devices, with the very same

---

[†] A line broadening in the range between 10 meV and 35 meV and an effective temperature ranging between 300 K and 480 K had to be used for an accurate fit. The estimated nanowire temperature increase, between 0 K and 180 K, agrees well with the one measured in identical experiments in Zincblende GaAs nanowires and can be assigned to laser-induced heating.

[‡] The zero-strain position has been identified by measuring the average of the TO peak position ($265.49 \pm 0.28\,\mathrm{cm}^{-1}$) for three different unclamped nanowires lying on the substrate surface.

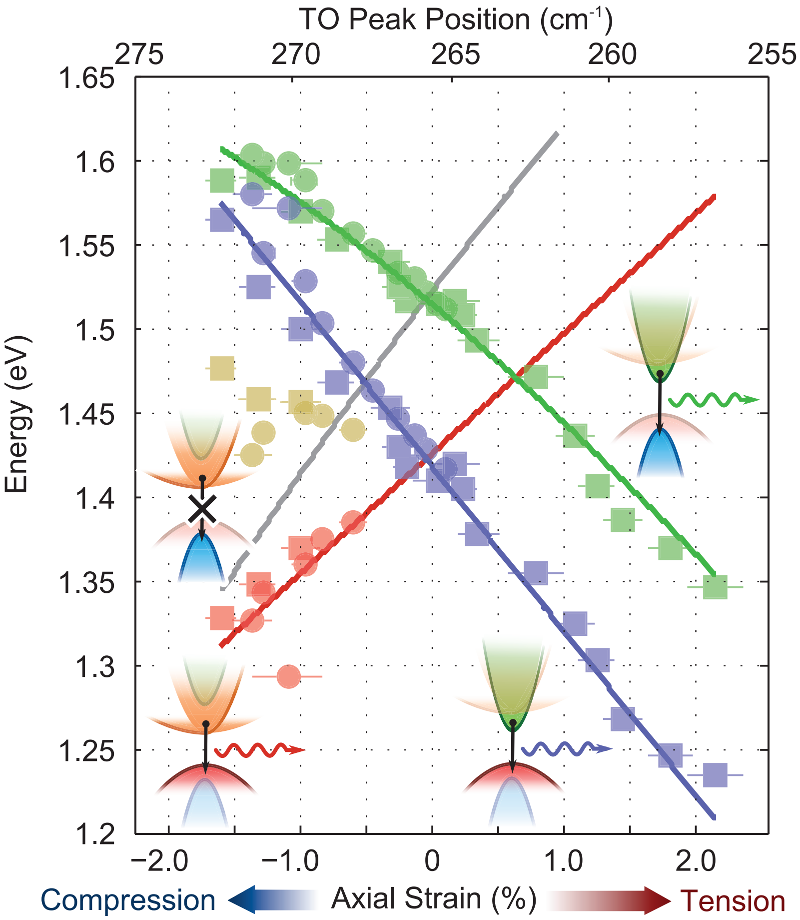

Figure 7.10: The energy of the optical transitions as a function of the TO phonon peak position (top abscissa) and of the inferred axial strain (bottom abscissa). Continuous lines correspond to the strain dependence of the photon energy expected from the $k \cdot p$ model. The energy uncertainties are smaller than the symbol dimensions. Squares and circles represent the values obtained from two different nanowire devices.

core-shell structure and alloy composition. As the mechanical properties of Zincblende and Wurtzite crystals are expected to be similar[87], the excellent agreement between the strain in these two experiments confirms the accuracy of the band-edge deformation potentials used. Although with high uncertainty, the estimated Poisson ratio ν =0.17±0.17 agrees with the value expected (0.188) using Martin's relations[87] and the elastic properties of bulk GaAs. The optical bandgap of the unstrained nanowire is found to be E_{gap} =1.417 eV±8 meV, in agreement with the value expected[144] at a temperature of 398 K±32 K, which has been estimated from the PL fit. This value is bigger than that of Zincblende GaAs at the same temperature (1.376 meV±15 meV), in good agreement with other experimental results[144,145,147]. For the first time we can determine the energy difference between the bright and the dark conduction band, which is equal to 33 meV±47 meV in unstrained conditions, in agreement with most recent theoretical predictions[81]. The bright conduction band is energetically favorable in unstrained conditions, even if only by few tens of meV. The crystal field splitting and spin-orbit splitting of the unstrained nanowires are found to be Δ_{cr} =197 meV±50 meV and Δ_{so} =293 meV±129 meV, respectively. Both of these values agree well with theoretical predictions (the crystal field splitting ranges from 180 meV and 212 meV in different *ab-initio* methods) and other experimental determinations (Δ_{so} =379 meV)[148,149].

7.9 Split-off Hole Transitions: a Consistency Check of the $\mathbf{k} \cdot \mathbf{p}$ Model

To further confirm our estimation of the spin-orbit splitting, we investigated the high-energy region of the PL spectra, to observe if transitions that involved the split-off hole band could be observed directly. Figure 7.11 shows the PL and Raman spectra measured in close proximity of the laser polarization (1.962 eV), which were collected with the laser excitation parallel to the nanowire axis and as a function of uniaxial stress. The spectra are colored according to the value of strain estimated, following the same rules of figure 7.4, 7.5 and 7.6, and are shifted in ordinate to match the value of estimated axial stress. The energy difference between the bright conduction band and the split-off hole band, predicted by the $k \cdot p$ model, is shown by a yellow line superimposed onto the PL spectra.

For tensile strain higher than 1.0 %, these optical transitions become directly observable in PL at the energy predicted by the model, between 1.72 eV and 1.88 eV. As the light hole band and the crystal-field split-off band share the same symmetry character Γ_7^v, we expect the transitions between bright conduction band and split-off band to follow the same selection

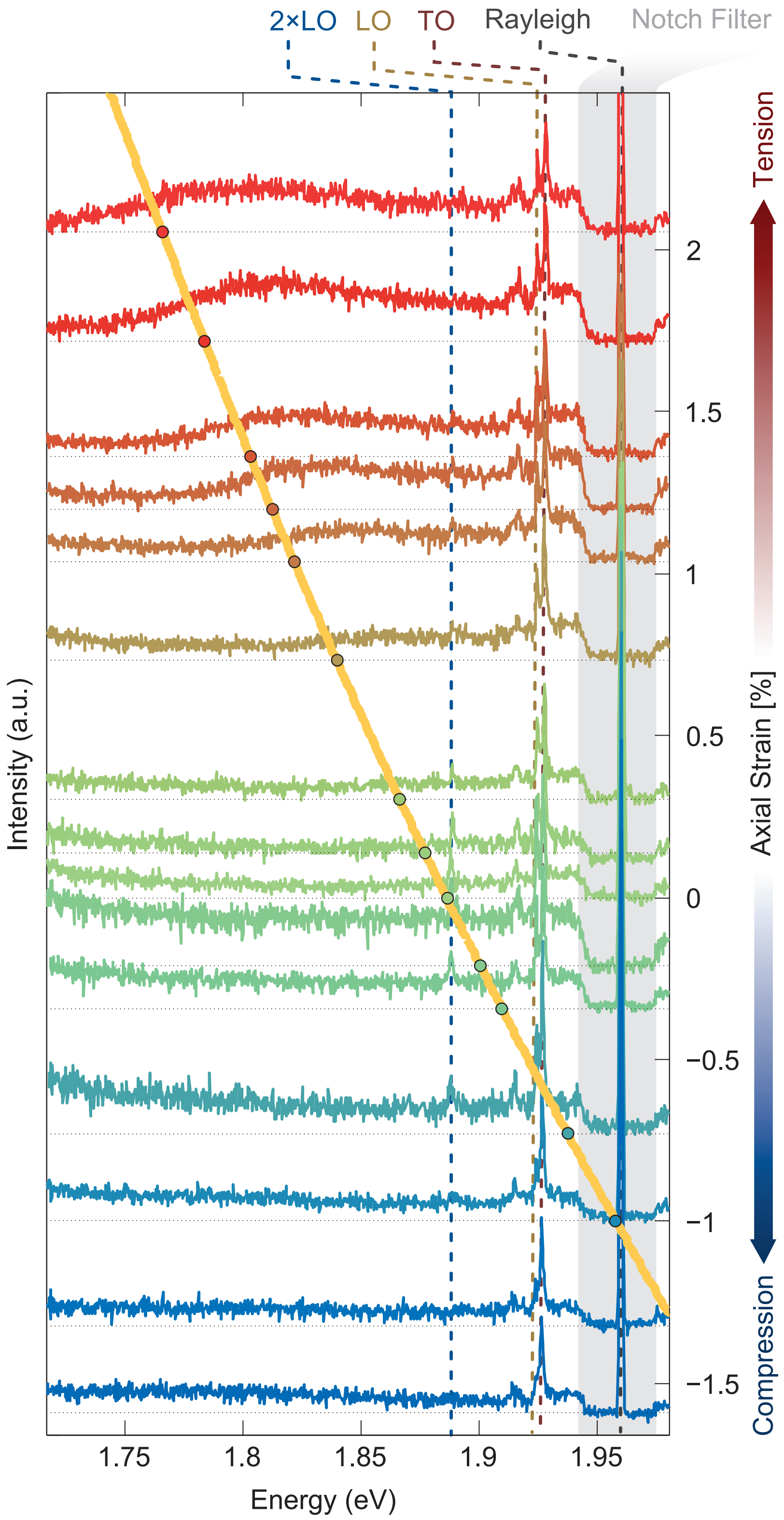

Figure 7.11: Axial strain dependence of the high energy region of the optical spectra of Wurtzite GaAs nanowires. The measurements have been performed with linear polarization excitation and detection aligned parallel to the nanowire axis. Fingerprints of the transition to the split-off holes are observed.

rules as those describing transitions from the bright conduction band to the light hole band. Indeed, the observed PL peaks show a strong polarization parallel to the nanowire axis (data not displayed here). For strain values between 0.5 % and −1.0 %, the optical transitions between the bright conduction band and the split-off hole band are in resonance with the photon energy (LO outgoing resonance around 1.927 eV; incoming resonance at 1.960 eV). In these conditions, the electron-phonon Fröhlich interaction[150] allows the observation of the LO phonon, which otherwise is not observable in this scattering configuration because of the Raman selection rules[85]. The resonant enhancement can therefore explain the intensity modulation of the LO phonon line observed in figure 7.4. The Fröhlich interaction also enables the scattering of LO overtones visible around 1.888 eV. A similar type of resonant behavior has already been observed in bulk Zincblende GaAs[150].

These set of observations provides a further consistency check for the extracted band structure parameters inferred by fitting the experimental data. The GaAs $k \cdot p$ model can therefore explain all optical transitions observed in our experiment, with the exception of the photons identified by the yellow peaks in figure 7.9 and 7.10. Further investigations are needed to elucidate the nature of these peaks and are currently ongoing.

7.10 Determination of the Phonon Deformation Potentials

Now that we have established a method to predict the uniaxial stress experienced by the Wurtzite nanowire, we can shift our focus to its Raman spectrum and study the uniaxial stress effects on the optical phonons of the GaAs core and AlGaAs shell. The polarization dependence of the Raman scattering can be used to clearly identify the symmetry of the optical phonons and, with the complementary information provided by the PL spectra, the phonon deformation potentials can be determined.

Figure 7.12 shows the Raman spectra measured on a single Wurtzite GaAs-AlGaAs-GaAs core-shell nanowire as a function of stress. To enable the observation of distinct phonon modes, the spectra have been measured in four different polarization configurations: the spectra shown in figure 7.12a and 7.12b were measured with laser polarization parallel to the nanowire, while 7.12c and 7.12d were measured with laser polarization in orthogonal configuration. The polarization orientation of the detected light was varied, too: the spectra shown in 7.12a and 7.12c were measured in configuration parallel to the nanowire, while the spectra in 7.12b and 7.12d were acquired under orthogonal configuration. The four different scattering configurations

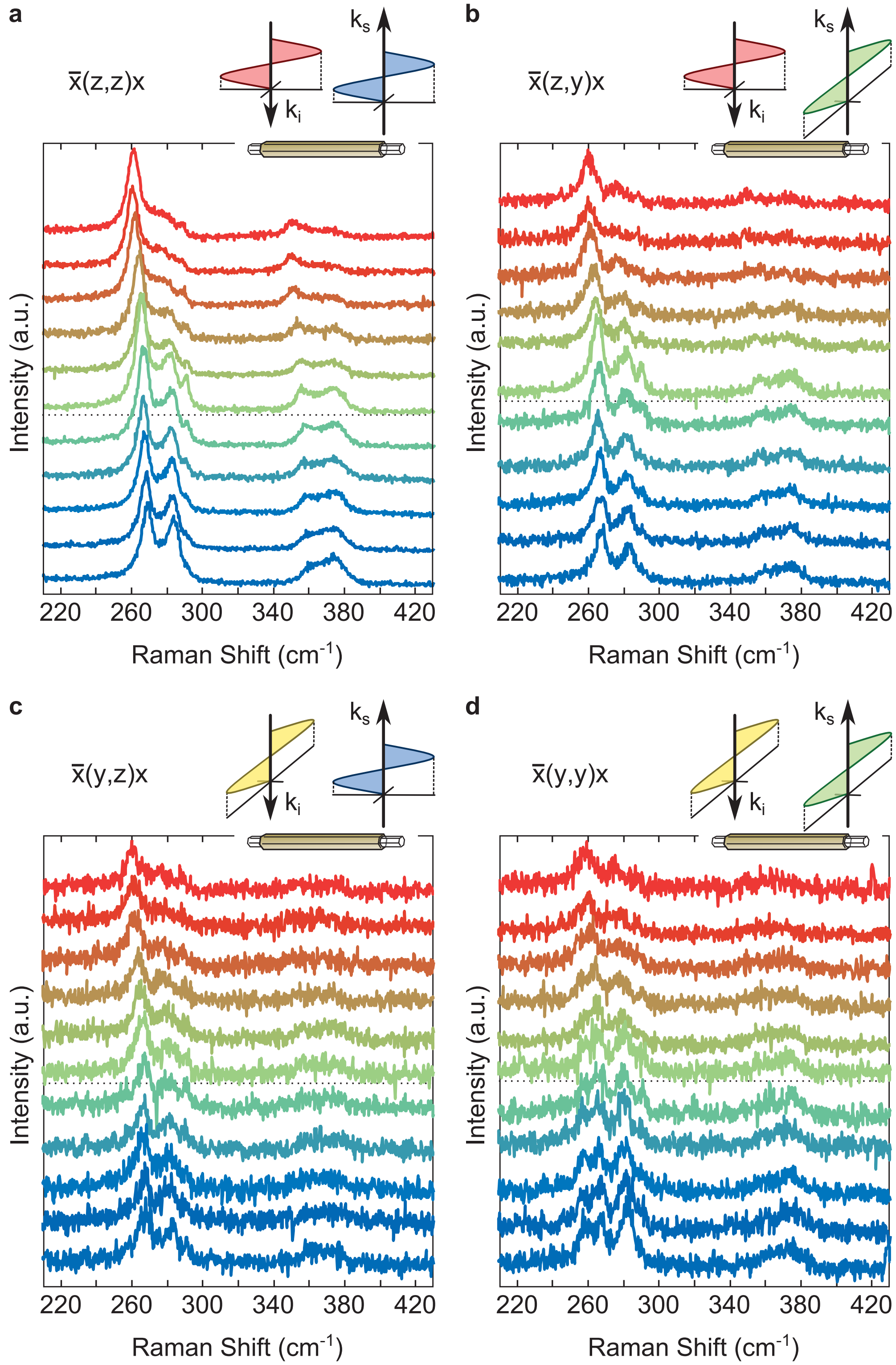

Figure 7.12: Uniaxial stress dependence on the Raman spectrum of a Wurtzite GaAs nanowire. The spectra are color coded according to the applied uniaxial stress, following the same convention of figure 7.4. Linearly polarized excitation and detection was used to measure the spectra. Each polarization configuration is sketched in the inset and labeled with Damen's notation[100].

are shown as insets and labeled using the notation of Damen[§], which has been discussed in §4.4.1. The spectra were acquired under a ten-fold higher laser excitation power (1.6 mW) compared to the spectra in figure 7.4: under this illumination conditions the Raman features of the optical phonons of both core and shell could be clearly resolved. Similarly to figure 7.4, different colors have been assigned to the spectra depending on the stress applied to the nanowire: the spectra acquired under unstrained conditions, located at the center of each plot in proximity of the dashed line, are shown in green; the spectra measured under tension are displaced towards the top part of each plot and their color gradually fades to red; the spectra acquired under compression are displaced towards the bottom and their color fades to blue. The overall intensity of the spectra strongly depends on the polarizer and analyzer configuration: the signal is highest when both excitation and detection are set in parallel configuration with the nanowire axis, and decreases as soon as the polarizer and analyzer deviate from such alignment. We relate this observation to the dielectric mismatch effect, which introduces a penalty in terms of the optical coupling to and from the nanowire as soon as excitation and detection deviate from the parallel configuration with the nanowire axis.

In all four polarization configurations, the energies of all optical phonons follow the general trend observed in figure 7.4, shifting towards lower values upon tension and towards higher values upon compression. We can now consider in detail the effect of strain on the energy and Raman scattering intensity of the optical phonons of the GaAs core and AlGaAs shell. The polarization dependence for each mode, expected from the Raman selection rules (discussed in §4.4.3), is used to confirm the assignment of the phonons to a particular symmetry. The A_1 TO phonon of the GaAs core, located at $265.2\pm0.2\,\mathrm{cm}^{-1}$ in unstrained conditions, experiences the biggest energy shift, up to $268.9\pm0.2\,\mathrm{cm}^{-1}$ under compression and down to $260.5\pm0.2\,\mathrm{cm}^{-1}$ under tension. Because of its symmetry, this phonon is expected to have the highest intensity when both excitation and detection are parallel to the nanowire axis. Indeed, this phonon provides the most intense feature of the Raman spectrum in the configuration of figure 7.12a and is observed also in all other three scattering configurations, because of the limited rejection ratio of the system and the finite numerical aperture of the objective. The E_1 LO phonon of the GaAs core, located at $290.4\pm0.5\,\mathrm{cm}^{-1}$ in unstrained conditions, undergoes moderate shifts with strain, up to $288.4\pm0.5\,\mathrm{cm}^{-1}$ un-

---

[§] The scattering configurations refer to a reference system of axis shown in figure 4.7. The x axis is orthogonal to the nanowire, i.e. $\bar{x}$ and x indicate respectively the wave-vector direction of the incoming and scattered photon. The z axis is oriented along the nanowire direction while the y axis lays in the cross section plane of the wire and is orthogonal to x and z.

der tension and down to 291.4±0.5 cm^{-1} under compression. The intensity of this phonon, which is theoretically forbidden for all polarization configurations, is visible with highest intensity in proximity of the unstrained conditions and becomes less intense whenever compressive or tensile stress is applied. This modulation of the peak intensity reproduces the observations of figure 7.4 and agrees with the Fröhlich interaction and resonant alignment explanation given in §7.9. The E_2^{High} optical phonon of the GaAs core could be identified at 257.3±2.6 cm^{-1} in unstrained conditions. Its energy could be varied up to a maximum, under compression, of 259.3±2.6 cm^{-1} and to a minimum, under tension, of 254.4±2.6 cm^{-1}. As predicted by the scattering selection rules, this particular phonon was visible exclusively in the polarization configuration shown in figure 7.12d: its intensity is shown to increase with increasing compressive stress, and decrease below the detection limit under tension. The E_1 TO phonon of the GaAs core, whose energy is similar to the A_1 TO, could not be resolved.

Raman peaks attributed to the AlGaAs shell could also be observed. The AlAs-like A_1 TO phonon could be identified at 357.3±1.0 cm^{-1} in unstrained conditions, and a large shift down to 350.4±0.8 cm^{-1} under tension and up to 360.0±0.8 cm^{-1} under compression could be measured. The intensity of this Raman peak is insensitive to the uniaxial stress applied and, as expected from the selection rules, is maximized when polarizer and analyzer are both parallel to the nanowire axis. The AlAs-like E_1 LO phonon could be measured at 374.2±0.8 cm^{-1} in unstrained conditions. This phonon undergoes a smaller shift compared to the A_1 TO, down to 371.4±1.0 cm^{-1} under tension and up to 375.5±1.0 cm^{-1} under compression. Its intensity was observed to depend on strain and increase with compression. The GaAs-like E_1 LO phonon of the AlGaAs shell was observed at 280.7±0.3 cm^{-1} in unstrained conditions. This phonon undergoes large shifts in energy, down to 275.7±0.3 cm^{-1} under tension and up to 283.4±0.3 cm^{-1} under compression, and its intensity, which is maximum when polarizer and analyzer are parallel to the nanowire axis, was observed to increase with compression like for the E_1 LO phonon.

The energy of the different optical phonons, measured in the four scattering configurations, is plot as a function of strain in figure 7.13a. The optical phonon energies were determined by fitting each Raman spectrum with a sum of Lorentzian line-shapes: typical fittings look like in figure 7.4. Each spectrum contributes with up to six different data points, which have been colored differently to distinguish the original polarizer and analyzer configuration used in the measurement. The red data-points are estimated from the measurement performed with polarizer and analyzer parallel to the nanowire axis, in configuration $\bar{x}(z,z)x$. Blue and green data-points have been estimated from the measurement performed with crossed polarizer and analyzer,

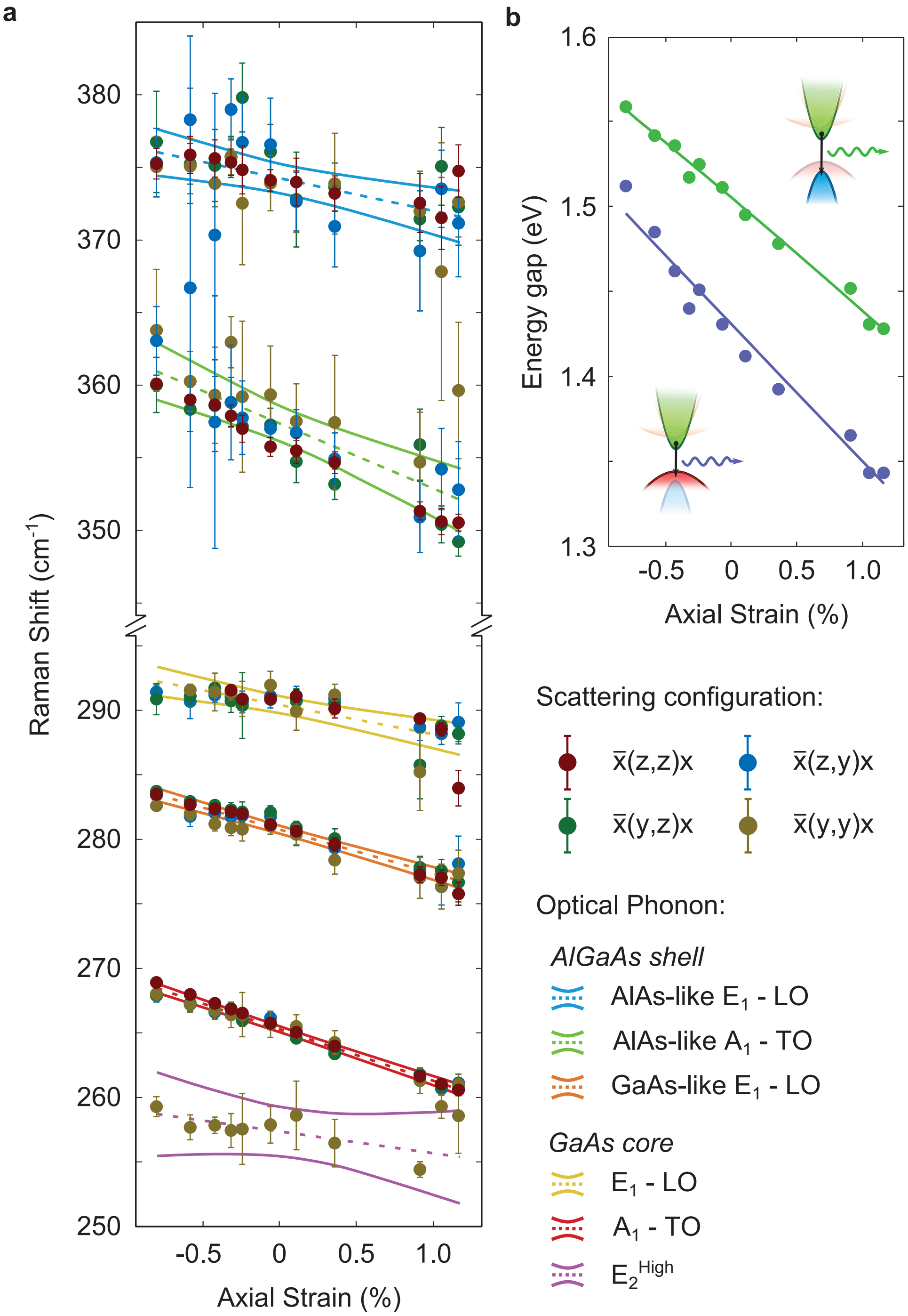

Figure 7.13: Uniaxial stress dependence of the optical phonons of Wurtzite nanowires. (a) The energy of the optical phonons, inferred from the Raman spectra in figure 7.12, is plot as a function of uniaxial stress; the strain dependence is modeled by a linear dependence using a least squares method. (b) The axial strain experienced by the nanowire is deduced from the analysis of the PL spectra.

respectively in configuration $\bar{x}(z,y)x$ and $\bar{x}(y,z)x$. The data-points shown yellow have been acquired with polarizer and analyzer orthogonal to the nanowire, in configuration $\bar{x}(y,y)x$. To complete this information with an estimate of the axial strain of the nanowire, we have collected the PL spectra with parallel and orthogonal analyzer configuration in correspondence to each applied stress value. Some of these spectra, i.e. the ones measured under compression, have already been shown in figure 7.7. The axial strain $\varepsilon_\parallel$ experienced by the nanowire was estimated using the $k \cdot p$ model discussed in §3.2.3 and the results of the fitting are shown in figure 7.13b. Finally, the variation of the phonon energies with strain has been modeled by straight lines, providing jointly all the data-points from all scattering configurations as input to a least square algorithm. The results of the fitting have been collected in table 7.1 and plotted in figure 7.13a together with the estimated 3σ confidence intervals. The lowest uncertainty is obtained for the deformation potentials of the GaAs-core A_1 TO, whose fit is represented in red. The E_2^{High} phonon has instead the largest uncertainty. We notice also that the A_1 phonons of GaAs core and AlGaAs shell are always associated with the highest slopes, in the range between -4.0 and $-4.5\,\mathrm{cm}^{-1}/\%$. This phenomenon is expected in phonons whose atomic displacement is aligned to the direction of stress: the deviatoric and isotropic components of strain contribute to the slope with the same sign. The opposite occurs with the E_1 and E_2 phonons, in which isotropic and deviatoric stress contribute with opposite sign: their slopes are lower than $-3.5\,\mathrm{cm}^{-1}/\%$.

These results represent a first contribution to the complete characterization of the phonon deformation potential tensors of Wurtzite GaAs and AlGaAs alloys. To this end, further uniaxial stress experiments, along different stress directions, and hydrostatic stress experiments need to be performed and analyzed.

7.11 Conclusions

In conclusion, we performed PL and Raman measurements on single Wurtzite GaAs nanowires under both tensile and compressive uniaxial stress. We demonstrated a remarkable energy shift of the PL due to transitions between the bright conduction band and the heavy hole band (345 meV) and the light hole band (257 meV), respectively. A direct-to-pseudodirect transition was observed for the first time through a reversible quenching of the PL. The splitting between the dark and bright conduction bands could be tuned continuously over a range of more than 230 meV. Using the Raman scattering spectra as relative strain gauge and fitting the PL energies to a $k \cdot p$ model, we were able to determine all band-structure parameters of the Wurtzite

Optical Phonon	Phonon Energy (cm^{-1})	Deformation Potential ($\mathrm{cm}^{-1}/\%$)
AlAs-like E_1 - LO	374.2±0.8	-2.3 ± 1.2
AlAs-like A_1 - TO	357.3±1.0	-4.5 ± 1.5
GaAs-like E_1 - LO	280.7±0.3	-3.4 ± 0.4
GaAs E_1 - LO	290.4±0.5	-2.3 ± 0.9
GaAs A_1 - TO	265.2±0.2	-4.0 ± 0.3
GaAs E_2^{High}	257.3±2.6	-1.7 ± 2.4

Table 7.1: Phonon energy and deformation potential of the GaAs and AlGaAs Optical phonons estimated from the strain measurements performed in core-shell Wurtzite nanowires.

GaAs nanowire in unstrained conditions, i.e., the crystal field and spin-orbit splitting, the bandgap and, most importantly, the splitting between the bright and the dark conduction bands. Mechanical properties, such as the Poisson ratio of the nanowire, and the phonon deformation potentials of the GaAs and AlGaAs optical phonons have also been determined. The possibility to induce a direct or pseudodirect transition in Wurtzite GaAs nanowires, and on other ad-hoc designed Wurtzite III-V alloys, promises to have profound implications on a wide range of applications: we envisage, for example, a new generation of devices that can simultaneously serve as efficient light emitters and efficient photodetectors by leveraging the strain degrees of freedom.

8

Conclusions and Outlook

> *"You can't connect the dots looking forward;*
> *you can only connect them looking backwards.*
> *So you have to trust that the dots will*
> *somehow connect in your future."*
>
> Steve Jobs

Conclusions

We embarked on this research journey, inspired by the two biggest challenges that the semiconductor industry faces today, i.e. the future of CMOS scaling and the limits in bandwidth and energy efficiency of the current technology of interconnects. Studying uniaxial stress effects on III-V nanowire devices seemed to have all the ingredients necessary to solve both of these issues: the paradigm shift towards non-planar nanoscale structures, the introduction of novel materials and strain engineering. Rather than contributing to the solution of a specific technological problem, we decided to explore the synergistic interplay between nanoscale devices and strain effects, and get inspired by our observations. Nanowires promised exceptional mechanics and a large range of elastic deformation, which can have unexpected effects on their electronic and optical properties.

We decided to apply uniaxial stress to single nanowires, because of the possibility to re-organize the energy order of the different conduction and valence band states with such type of strain. Optical spectroscopy was identified as the technique that could provide most information in the characterization of the strain effects. The bandstructure of III-V semiconductors can be inspected by photoluminescence spectroscopy, while information about the lattice dynamics and strain can be obtained by Raman spectroscopy. Studying such spectra as a function of the polarization could further broaden our understanding of the physics of the strain effects. Polarization-dependent photoluminescence provides rich information to resolve the symmetry of the conduction and valence band states involved in the light emission processes. In Raman spectroscopy, controlling the polarization of the laser and of the detected light allows the identification of the contribution of individual phonons. This information can be translated into an estimate of the axial strain and Poisson ratio of the nanowire, which provide together the full characterization of the strain tensor.

A series of challenges had to be overcome so that all these ideas and concepts could be combined together in a single experiment. We exploited the mechanical degrees of freedom that the substrate could offer to apply strain on the nanowire. Continuum mechanics teaches us that perfectly uniaxial stress and reproducible mechanical deformations can be obtained and controlled with sub-nanometer resolution by bending a thick substrate on the millimeter scale. We have identified a substrate material which is flexible, insulating, and which did not provide significant luminescence or Raman features upon laser excitation. Furthermore, we developed a set of processing steps and conditions to realize strain nanowire devices on these flexible surfaces. A bending mechanism that could enable strain experiments from room temperature to cryogenic temperatures was designed and manufactured. In this way, it was possible to apply uniaxial stress mechanically to the nanowire in a continuous and reversible way, both in compression and tension. To enable polarization-dependent measurements, our optical spectrometer had to be modified too, by introducing two optical units that allow the full control over the polarization orientation in the excitation and analytic path. We have shown that the insertion of these optical elements has to be done with some care: the control of the polarization can interfere with the notch or edge filter of the spectrometer, resulting in the excitation or the detection of light with undesired state of polarization. Eventually, we could identify a filter that is compatible with polarization dependent spectroscopy and offers the best performance in terms of rejection ratio ($>1.2 \times 10^2$).

GaAs was chosen as the ideal material system to study, for many reasons:

Zincblende GaAs is considered as the material that enabled the foundations of semiconductor based solid state lasers and light-emitting devices; when grown at nanoscale dimensions, novel crystal structures like Wurtzite can be synthesized and new degrees of freedom to tailor electronic and optoelectonic properties are available. Our experiments have shown that, indeed, the nanowire geometry enables the expected enhancement of the strain effects in GaAs.

We have shown that by tuning the strain continuously, from tension to compression and up to 3.5 %, the PL of zincblende GaAs nanowires can be red-shifted by 290 meV. We have observed a much more pronounced PL shift in tension than in compression in these nanowires, and have attributed this phenomenon to the different symmetry character of the top valence band: heavy hole under tension, light hole under compression. Fingerprints of symmetry breaking due to the anisotropic nature of the nanowire deformation were found also in the Raman spectra, in which polarization-dependent measurements allowed the unambiguous identification of distinct phonon contributions. Because of the linear relation with stress, the energy shift of the Raman peaks were used to determine the axial strain induced in the nanowire and to infer information about the Poisson ratio in the [111] direction (0.16±0.04). Using a 8-band $k \cdot p$ model to analyze the measurements, we extracted the band-edge deformation potentials ($a = -8.6\,\mathrm{eV} \pm 0.7\,\mathrm{eV}$ and $d = -5.2\,\mathrm{eV} \pm 0.7\,\mathrm{eV}$), which are consistent with those of bulk GaAs and with our initial assumptions.

Even larger shifts of the PL could be demonstrated by applying stress to Wurtzite nanowires. We demonstrated a remarkable energy shift of the PL due to transitions between the bright conduction band and the heavy hole band (345 meV) or the light hole band (257 meV), by varying the strain over a range of ±2 %. While the tunability of the luminescence is the most remarkable process that takes place in Zincblende GaAs under strain, Wurtzite GaAs shows a richer physics. We demonstrated for the first time that uniaxial stress can be used to induce a transition of the band structure from a direct bandgap to a pseudodirect bandgap configuration. In this last configuration, which is characteristic of Wurtzite crystals, the semiconductor shares some of the properties of direct bandgap and some of indirect bandgap materials. The relation between energy and wave-vector is indistinguishable from the one of direct bandgap materials: the conduction band minimum and valence band maximum are located at the Γ-point and the respective wavefunctions overlap strongly in the wave-vector space. However, because of symmetry reasons, the optical dipole transitions between these states occur with low probability. The material is therefore a poor light emitter, like indirect bandgap materials. Leveraging on the strain degree of freedom, we have shown that both direct and pseudodirect bandgap configurations can

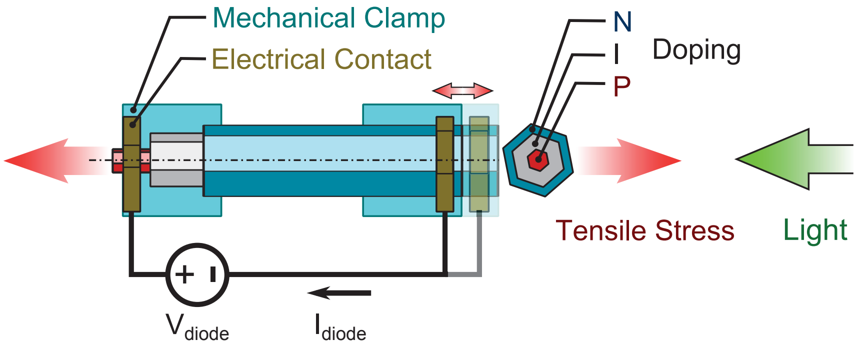

Figure 8.1: Concept of a nanowire p-i-n diode, in which energy bandgap can be tuned by uniaxial stress.

be achieved on a Wurtzite GaAs nanowire. When tensile stress is applied, the direct configuration can be obtained and the nanowires emit light efficiently; upon compression, the pseudodirect configuration is achieved and light emission can be suppressed by more than three orders of magnitude. The splitting between the dark and bright conduction bands could be tuned continuously over a range of more than 230 meV. Using the Raman scattering spectra as relative strain gauge and fitting the optical transition energies to a $k \cdot p$ model, we were able to determine all band structure parameters of the Wurtzite GaAs nanowire in unstrained conditions, i.e., the crystal field (197 meV±50 meV) and spin-orbit splitting (293 meV±129 meV), the bandgap (1.41 eV±8 meV) and, most importantly, the splitting between the bright and the dark conduction bands (33 meV±47 meV). Mechanical properties, such as the Poisson ratio along the c-axis (0.17±0.17), and the phonon deformation potentials of the GaAs and AlGaAs optical phonons have also been determined. Resonant Raman and direct optical transitions involving the bright conduction band and the split-off hole band have been investigated and their analysis provided a consistency check of the band structure parameters extracted.

This body of results constitutes a solid foundation to the understanding of strain effects on the optical and electronic properties of III-V nanowires. Their implications promise to have high technological relevance, which is going to be the focus of our future research and exploration.

Outlook

We believe that the reversibility and reproducibility of the mechanical strain, combined with its effects on the bandstructure, constitute the foundation of a new generation of functional strain devices. As an example, we consider

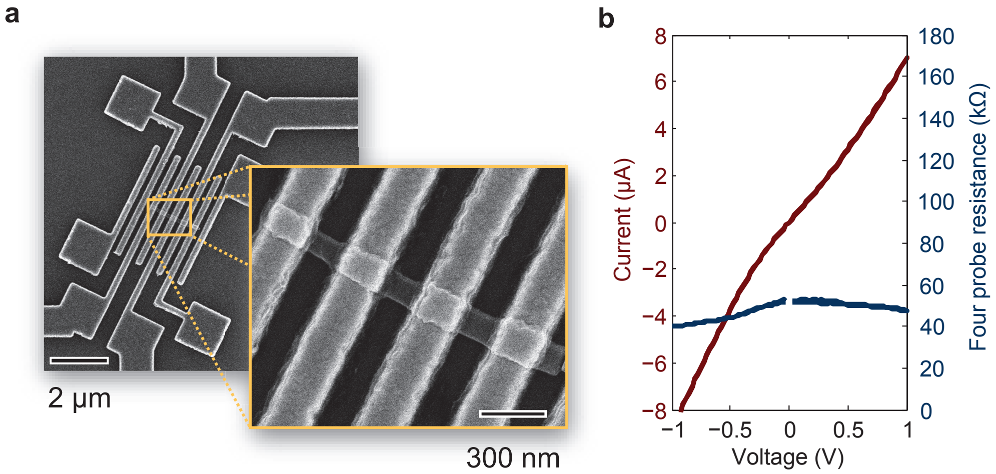

Figure 8.2: Electrical transport measurements on berillium doped Zincblende GaAs nanowires. (b) SEM image of a typical nanowire device. (b) Current-voltage characteristic and four probe resistance measured on the nanowire device .

the bandgap tuning functionality and explore the possibilities that such a strain device would enable. The structure we would like to explore is shown in figure 8.1 and is constituted by a nanowire p-i-n diode mounted on a compact strain mechanics, such as a comb-drive or a mechanically amplified piezoelectric actuator[151]. If the p-i-n structure acts as a light-emitting diode, strain can be used to tune the wavelength of emission and an ultimately scaled tunable light source can be realized. If operated instead as a photo-detector, strain can be used to tune the responsivity of the device to variable wavelength ranges: leveraging on this effect, an ultimately scaled spectrometer can be realized on a single nanowire.

Mastering the growth of different materials for the core and shells, as well as controlling their active doping concentration is going to be essential for the successful realization of these devices. As shown in figure 8.2, we have already taken the first steps in understanding how to dope and achieve good electrical contact to p-doped and n-doped GaAs nanowires. To test the functionality of the devices under strain, it is also important to perform electrical transport measurements as a function of strain. Also in this respect, we have already taken action and, as shown in figure 8.3, we have performed the first studies of this kind on silicon nanowires, to investigate how the nanowire and the contact resistance is affected by the application of strain, or whether the functions of electrical contact and mechanical clamping can be realized jointly using a single structure.

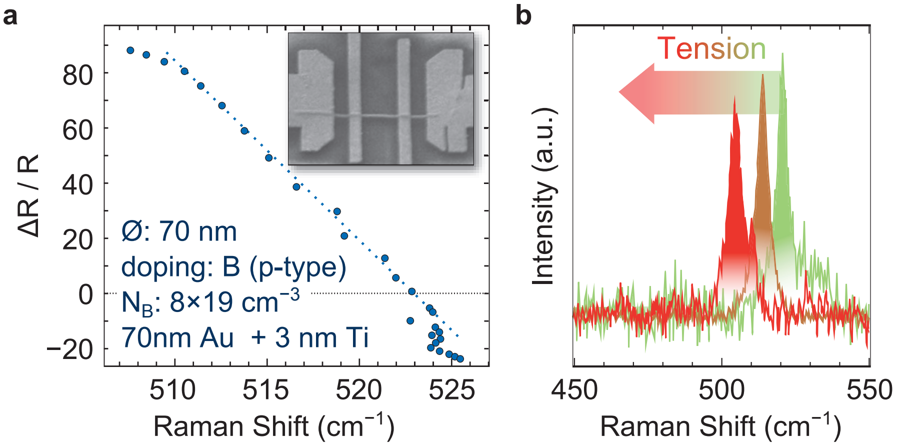

Figure 8.3: Uniaxial tensile stress effects on the charge transport in silicon nanowires. (a) The variation in four-probe resistance is measured as a function of strain. SEM image of the nanowire device is shown in the inset. (b) Raman spectra of a silicon nanowire under uniaxial stress. The energy shift of the F_{2g} modes provide information about the strain in the nanowire.

By combining ultimately scaled tunable light emitters and spectrometers with passive waveguides and modulators, it is easy to imagine the integration of a whole optical spectroscopy lab on a single chip. This could have impact on the many fields of science and technology where optical spectroscopy is used (materials characterization, optical communications, biology, sensing, etc.), and its possible applications are so wide that might very well be beyond anybody's most fervid imagination.

Bibliography

1. Moore, G. E. *International Electron Devices Meeting* , 11–13 (1975).
2. Dennard, R., Gaensslen, F., Rideout, V., Bassous, E., and LeBlanc, A. *IEEE Journal of Solid-State Circuits* **9**(5), 256–268 October (1974).
3. Chu, M., Sun, Y., Aghoram, U., and Thompson, S. E. *Annual Review of Materials Research* **39**(1), 203–229 August (2009).
4. Xu, N., Ho, B., Andrieu, F., Smith, L., Nguyen, B.-Y., Weber, O., Poiroux, T., Faynot, O., and Liu, T.-j. K. *IEEE Electron Device Letters* **33**(3), 318–320 March (2012).
5. Chan, V., Rengarajan, R., Rovedo, N., Hook, T., Nguyen, P., Nowak, E., Lea, D., Chakravarti, A., Ku, V., Yang, S., Steegen, A., Baiocco, C., Shafer, P., and Wann, C. In *IEEE International Electron Devices Meeting 2003*, 3.8.1–3.8.4. IEEE, (2003).
6. Lim, A.-J. and Lee, R.-P. *IEEE Electron Device Letters* **30**(3), 250–253 March (2009).
7. Niquet, Y.-M., Delerue, C., and Krzeminski, C. *Nano letters* **12**(7), 3545–50 July (2012).
8. Choi, Y. S., Numata, T., Nishida, T., Harris, R., and Thompson, S. E. *Journal of Applied Physics* **103**(6), 064510 (2008).
9. Bardeen, J. and Shockley, W. *Physical Review* **80**(1), 72–80 October (1950).
10. Kane, E. O. *Journal of Physics and Chemistry of Solids* **1**(4), 249–261 January (1957).
11. Kane, E. O. *Journal of Physics and Chemistry of Solids* **6**(2-3), 236–241 August (1958).
12. Sun, Y., Thompson, S. E., and Nishida, T. *Journal of Applied Physics* **101**(10), 104503 (2007).

13. Del Alamo, J. A. *Nature* **479**(7373), 317–23 November (2011).

14. Tomioka, K., Yoshimura, M., and Fukui, T. *Nature* **488**(7410), 189–92 August (2012).

15. Miller, D. A. B. *Proceedings of the IEEE* **97**(7), 1166–1185 July (2009).

16. Liang, D. and Bowers, J. E. *Nature Photonics* **4**(8), 511–517 July (2010).

17. Kuo, Y.-H., Lee, Y. K., Ge, Y., Ren, S., Roth, J. E., Kamins, T. I., Miller, D. A. B., and Harris, J. S. *Nature* **437**(7063), 1334–6 October (2005).

18. Yin, T., Cohen, R., Morse, M. M., Sarid, G., Chetrit, Y., Rubin, D., and Paniccia, M. J. *Optics Express* **15**(21), 13965 (2007).

19. Kang, Y., Liu, H.-D., Morse, M., Paniccia, M. J., Zadka, M., Litski, S., Sarid, G., Pauchard, A., Kuo, Y.-H., Chen, H.-W., Zaoui, W. S., Bowers, J. E., Beling, A., McIntosh, D. C., Zheng, X., and Campbell, J. C. *Nature Photonics* **3**(1), 59–63 December (2008).

20. Assefa, S., Xia, F., and Vlasov, Y. A. *Nature* **464**(7285), 80–4 March (2010).

21. Hamada, H., Tominaga, K., Shono, M., Honda, S., Yodoshi, K., and Yamaguchi, T. *Electronics Letters* **28**(19), 1834 (1992).

22. Seki, S. and Yokoyama, K. *Journal of Applied Physics* **76**(6), 3250 (1994).

23. Silver, M. and O'Reilly, E. *IEEE Journal of Quantum Electronics* **30**(2), 547–553 (1994).

24. Beattie, A. R. and Landsberg, P. T. *Proceedings of the Royal Society of London. Series A, Mathematical and Physical Sciences* **249**(1256), 16–29 (2009).

25. Asada, M., Adams, A., Stubkjaer, K., Suematsu, Y., Itaya, Y., and Arai, S. *IEEE Journal of Quantum Electronics* **17**(5), 611–619 May (1981).

26. Chang, C.-S. and Chuang, S. L. *Applied Physics Letters* **66**(7), 795 (1995).

27. Bour, D., Treat, D., Beernink, K., Krusor, B., Geels, R., and Welch, D. *IEEE Photonics Technology Letters* **6**(2), 128–131 February (1994).

28. Sun, X., Liu, J., Kimerling, L. C., and Michel, J. *Applied Physics Letters* **95**(1), 011911 (2009).

29. Huo, Y., Lin, H., Chen, R., Makarova, M., Rong, Y., Li, M., Kamins, T. I., Vuckovic, J., and Harris, J. S. *Applied Physics Letters* **98**(1), 011111 (2011).

30. Gallacher, K., Velha, P., Paul, D. J., Cecchi, S., Frigerio, J., Chrastina, D., and Isella, G. *Applied Physics Letters* **101**(21), 211101 (2012).

31. Saito, S., Oda, K., Takahama, T., Tani, K., and Mine, T. *Applied Physics Letters* **99**(24), 241105 (2011).

32. Camacho-Aguilera, R. E., Cai, Y., Patel, N., Bessette, J. T., Romagnoli, M., Kimerling, L. C., and Michel, J. *Optics express* **20**(10), 11316–20 May (2012).

33. Tomioka, K., Motohisa, J., Hara, S., and Fukui, T. *Nano letters* **8**(10), 3475–80 October (2008).

34. Tomioka, K., Kobayashi, Y., Motohisa, J., Hara, S., and Fukui, T. *Nanotechnology* **20**(14), 145302 April (2009).

35. Kanungo, P. D., Schmid, H., Björk, M. T., Gignac, L. M., Breslin, C., Bruley, J., Bessire, C. D., and Riel, H. *Nanotechnology* **24**(22), 225304 June (2013).

36. Glas, F. *Physical Review B* **74**(12), 121302 September (2006).

37. Glas, F., Harmand, J.-C., and Patriarche, G. *Physical Review Letters* **99**(14), 146101 October (2007).

38. Dubrovskii, V. G. and Sibirev, N. V. *Physical Review B* **77**(3), 035414 January (2008).

39. Björk, M. T., Ohlsson, B. J., Sass, T., Persson, A. I., Thelander, C., Magnusson, M. H., Deppert, K., Wallenberg, L. R., and Samuelson, L. *Nano Letters* **2**(2), 87–89 February (2002).

40. Dick, K. a., Deppert, K., Larsson, M. W., Mårtensson, T., Seifert, W., Wallenberg, L. R., and Samuelson, L. *Nature materials* **3**(6), 380–4 June (2004).

41. Sköld, N., Wagner, J. B., Karlsson, G., Hernán, T., Seifert, W., Pistol, M.-E., and Samuelson, L. *Nano letters* **6**(12), 2743–7 December (2006).

42. Tian, B., Xie, P., Kempa, T. J., Bell, D. C., and Lieber, C. M. *Nature nanotechnology* **4**(12), 824–9 December (2009).

43. Lim, S. K., Crawford, S., Haberfehlner, G., and Gradečak, S. *Nano letters* , 18–23 February (2012).

44. Heiss, M., Fontana, Y., Gustafsson, A., Wüst, G., Magen, C., O'Regan, D. D., Luo, J. W., Ketterer, B., Conesa-Boj, S., Kuhlmann, A. V., Houel, J., Russo-Averchi, E., Morante, J. R., Cantoni, M., Marzari, N., Arbiol, J., Zunger, A., Warburton, R. J., and Fontcuberta i Morral, A. *Nature materials* **12**(2), 1–6 February (2013).

45. Algra, R. E., Verheijen, M. A., Borgström, M. T., Feiner, L.-F., Immink, G., Van Enckevort, W. J. P., Vlieg, E., and Bakkers, E. P. A. M. *Nature* **456**(7220), 369–72 November (2008).

46. Caroff, P., Dick, K. A., Johansson, J., Messing, M. E., Deppert, K., and Samuelson, L. *Nature nanotechnology* **4**(1), 50–5 January (2009).

47. Kuykendall, T., Ulrich, P., Aloni, S., and Yang, P. *Nature materials* **6**(12), 951–6 December (2007).

48. Qian, F., Li, Y., Gradečak, S., Park, H.-G., Dong, Y., Ding, Y., Wang, Z. L., and Lieber, C. M. *Nature materials* **7**(9), 701–6 September (2008).

49. Vu, T. T. T., Zehender, T., Verheijen, M. A., Plissard, S. R., Immink, G. W. G., Haverkort, J. E. M., and Bakkers, E. P. A. M. *Nanotechnology* **24**(11), 115705 March (2013).

50. Assali, S., Zardo, I., Plissard, S., Kriegner, D., Verheijen, M. A., Bauer, G., Meijerink, A., Belabbes, A., Bechstedt, F., Haverkort, J. E. M., and Bakkers, E. P. A. M. *Nano letters* **13**(4), 1559–63 April (2013).

51. Ikonić, Z., Srivastava, G., and Inkson, J. *Physical Review B* **48**(23), 17181–17193 December (1993).

52. Zhao, X., Wei, C. M., Yang, L., and Chou, M. Y. *Physical Review Letters* **92**(23), 236805 June (2004).

53. Van Weert, M. H. M., Akopian, N., Perinetti, U., Van Kouwen, M. P., Algra, R. E., Verheijen, M. A., Bakkers, E. P. A. M., Kouwenhoven, L. P., and Zwiller, V. *Nano letters* **9**(5), 1989–93 May (2009).

54. Reimer, M. E., Van Kouwen, M. P., Hidma, A. W., Van Weert, M. H. M., Bakkers, E. P. A. M., Kouwenhoven, L. P., and Zwiller, V. *Nano letters* **11**(2), 645–50 February (2011).

55. Minot, E. D., Kelkensberg, F., Van Kouwen, M., Van Dam, J. A., Kouwenhoven, L. P., Zwiller, V., Borgström, M. T., Wunnicke, O., Verheijen, M. A., and Bakkers, E. P. A. M. *Nano letters* **7**(2), 367–71 February (2007).

56. Reimer, M. E., Van Kouwen, M. P., Barkelid, M., Hocevar, M., Van Weert, M. H. M., Algra, R. E., Bakkers, E. P. A. M., Björk, M. T., Schmid, H., Riel, H., Kouwenhoven, L. P., and Zwiller, V. *Journal of Nanophotonics* **5**(1), 053502 (2011).

57. Dalacu, D., Mnaymneh, K., Lapointe, J., Wu, X., Poole, P. J., Bulgarini, G., Zwiller, V., and Reimer, M. E. *Nano letters* **12**(11), 5919–23 November (2012).

58. Cao, L., White, J. S., Park, J.-S., Schuller, J. A., Clemens, B. M., and Brongersma, M. L. *Nature materials* **8**(8), 643–7 August (2009).

59. Cao, L., Park, J.-S., Fan, P., Clemens, B., and Brongersma, M. L. *Nano letters* **10**(4), 1229–33 April (2010).

60. Colombo, C., Krogstrup, P., Nygård, J., Brongersma, M. L., and Morral, A. F. I. *New Journal of Physics* **13**(12), 123026 December (2011).

61. Bulgarini, G., Reimer, M. E., Hocevar, M., Bakkers, E. P. A. M., Kouwenhoven, L. P., and Zwiller, V. *Nature Photonics* **6**(7), 455–458 May (2012).

62. Chan, C. K., Peng, H., Liu, G., McIlwrath, K., Zhang, X. F., Huggins, R. A., and Cui, Y. *Nature nanotechnology* **3**(1), 31–5 January (2008).

63. Boukai, A. I., Bunimovich, Y., Tahir-Kheli, J., Yu, J.-K., Goddard, W. A., and Heath, J. R. *Nature* **451**(7175), 168–71 January (2008).

64. Hochbaum, A. I., Chen, R., Delgado, R. D., Liang, W., Garnett, E. C., Najarian, M., Majumdar, A., and Yang, P. *Nature* **451**(7175), 163–7 January (2008).

65. Colombo, C., Heiss, M., Graetzel, M., and Fontcuberta i Morral, A. *Applied Physics Letters* **94**(17), 173108 (2009).

66. Kelzenberg, M. D., Boettcher, S. W., Petykiewicz, J. A., Turner-Evans, D. B., Putnam, M. C., Warren, E. L., Spurgeon, J. M., Briggs, R. M., Lewis, N. S., and Atwater, H. A. *Nature materials* **9**(3), 239–44 March (2010).

67. Mariani, G., Scofield, A. C., Hung, C.-H., and Huffaker, D. L. *Nature communications* **4**, 1497 January (2013).

68. Wallentin, J., Anttu, N., Asoli, D., Huffman, M., Aberg, I., Magnusson, M. H., Siefer, G., Fuss-Kailuweit, P., Dimroth, F., Witzigmann, B., Xu, H. Q., Samuelson, L., Deppert, K., and Borgström, M. T. *Science (New York, N.Y.)* **339**(6123), 1057–60 March (2013).

69. Krogstrup, P., Jørgensen, H. I., Heiss, M., Demichel, O., Holm, J. V., Aagesen, M., Nygard, J., and Fontcuberta i Morral, A. *Nature Photonics* (March), 1–5 March (2013).

70. Han, X., Zheng, K., Zhang, Y., Zhang, X., Zhang, Z., and Wang, Z. *Advanced Materials* **19**(16), 2112–2118 August (2007).

71. Wang, G.-F. and Feng, X.-Q. *Applied Physics Letters* **94**(14), 141913 (2009).

72. Sohn, Y.-S., Park, J., Yoon, G., Song, J., Jee, S.-W., Lee, J.-H., Na, S., Kwon, T., and Eom, K. *Nanoscale research letters* **5**(1), 211–216 January (2009).

73. Wang, Y.-B., Wang, L.-F., Joyce, H. J., Gao, Q., Liao, X.-Z., Mai, Y.-W., Tan, H. H., Zou, J., Ringer, S. P., Gao, H.-J., and Jagadish, C. *Advanced materials (Deerfield Beach, Fla.)* **23**(11), 1356–60 March (2011).

74. Birman, J. *Physical Review* **115**(6), 1493–1505 September (1959).

75. Bergstresser, T. and Cohen, M. *Physical Review* **164**(3), 1069–1080 December (1967).

76. Cardona, M. and Yu, P. Y. *Fundamentals of Semiconductors: Physics and Materials Properties.* Springer, Berlin Heidelberg, (2010).

77. Cardona, M., Christensen, N., and Fasol, G. *Physical Review B* **38**(3), 1806–1827 July (1988).

78. Gershoni, D., Henry, C., and Baraff, G. *IEEE Journal of Quantum Electronics* **29**(9), 2433–2450 (1993).

79. Adachi, S. *GaAs and related materials: bulk semiconducting and superlattice properties.* World Scientific, (1994).

80. De, A. and Pryor, C. E. *Physical Review B* **81**(15), 155210 1–13 April (2010).

81. Cheiwchanchamnangij, T. and Lambrecht, W. R. L. *Physical Review B* **84**(3), 1–8 July (2011).

82. Born, M. and Huang, K. *Dynamical Theory of Crystal Lattices.* Clarendon Press, (1954).

83. Loudon, R. *Advances in Physics* **13**(52), 423–482 October (1964).

84. Ruf, T., Serrano, J., Cardona, M., Pavone, P., Pabst, M., Krisch, M., D'Astuto, M., Suski, T., Grzegory, I., and Leszczynski, M. *Physical Review Letters* **86**(5), 906–909 January (2001).

85. Zardo, I., Conesa-Boj, S., Peiro, F., Morante, J. R., Arbiol, J., Uccelli, E., Abstreiter, G., and Fontcuberta i Morral, A. *Physical Review B* **80**(24), 1–11 December (2009).

86. Nye, J. F. *Physical Properties of Cristals: Their Representation by Tensors and Matrices.* Oxford Science Publications. Oxford University Press, Incorporated, (1985).

87. Martin, R. *Physical Review B* **6**(12), 4546–4553 December (1972).

88. Adachi, S. *Journal of Applied Physics* **58**(3), R1–R29 (1985).

89. Bardeen, J. *The Journal of Chemical Physics* **6**(7), 367–371 (1938).

90. Seitz, F. *The Modern Theory of Solids.* Dover books on hysics and chemistry. Dover Publications, (1987).

91. Bahder, T. *Physical Review B* **41**(17), 11992–12001 June (1990).

92. Chandrasekhar, M. and Pollak, F. F. *Physical Review B* **15**(4), 2127 – 2144 (1977).

93. Bir, G. L. and Pikus, G. E. *Symmetry and Strain-Induced Effects in Semiconductors.* Wiley, (1974).

94. Chuang, S. and Chang, C. *Physical Review B* **54**(4), 2491–2504 July (1996).

95. Cerdeira, F., Buchenauer, C., Pollak, F. F., and Cardona, M. *Physical Review B* **5**(2), 580 (1972).

96. Wickboldt, P., Anastassakis, E., Sauer, R., and Cardona, M. *Physical Review B* **35**(3), 1362 (1987).

97. Briggs, R. and Ramdas, A. *Physical Review B* **13**(12), 5518–5529 June (1976).

98. Bouckaert, L., Smoluchowski, R., and Wigner, E. *Physical Review* **50**(1), 58–67 July (1936).

99. Tronc, P., Kitaev, Y., Wang, G., Limonov, M., Panfilov, A., and Neu, G. *Physica Status Solidi (B)* **216**(1), 599–603 November (1999).

100. Damen, T., Porto, S., and Tell, B. *Physical Review* **142**(2), 570–574 February (1966).

101. Loudon, R. *Proceedings of the Royal Society A: Mathematical, Physical and Engineering Sciences* **275**(1361), 218–232 September (1963).

102. Wolford, D. J. *Journal of Vacuum Science & Technology B: Microelectronics and Nanometer Structures* **9**(4), 2369 July (1991).

103. Noborisaka, J., Motohisa, J., Hara, S., and Fukui, T. *Applied Physics Letters* **87**(9), 093109 (2005).

104. Titova, L. V., Hoang, T. B., Jackson, H. E., Smith, L. M., Yarrison-Rice, J. M., Kim, Y., Joyce, H. J., Tan, H. H., and Jagadish, C. *Applied Physics Letters* **89**(17), 173126 (2006).

105. Demichel, O., Heiss, M., Bleuse, J., Mariette, H., and Fontcuberta i Morral, A. *Applied Physics Letters* **97**(20), 201907 (2010).

106. Tomioka, K., Motohisa, J., Hara, S., Hiruma, K., and Fukui, T. *Nano letters* **10**(5), 1639–44 May (2010).

107. Zhou, H. L., Hoang, T. B., Dheeraj, D. L., Van Helvoort, A. T. J., Liu, L., Harmand, J. C., Fimland, B. O., and Weman, H. *Nanotechnology* **20**(41), 415701 October (2009).

108. Wagner, R. S. and Ellis, W. C. *Applied Physics Letters* **4**(5), 89 (1964).

109. Cho, A. Y. and Arthur, J. R. *Progress in Solid State Chemistry* **10**(0), 157–191 (1975).

110. Pedrotti, F. L., Pedrotti, L. S., and Pedrotti, L. M. *Introduction to Optics.* Pearson Prentice Hall, (2007).

111. Paulo, A. S., Arellano, N., Plaza, J. A., He, R., Carraro, C., Maboudian, R., Howe, R. T., Bokor, J., and Yang, P. *Nano letters* **7**(4), 1100–4 April (2007).

112. Hoffmann, S., Utke, I., Moser, B., Michler, J., Christiansen, S. H., Schmidt, V., Senz, S., Werner, P., Gösele, U., and Ballif, C. *Nano letters* **6**(4), 622–5 April (2006).

113. Lugstein, A., Steinmair, M., Steiger, A., Kosina, H., and Bertagnolli, E. *Nano letters* **10**(8), 3204–8 August (2010).

114. Spirkoska, D., Abstreiter, G., and Fontcuberta i Morral, A. *Nanotechnology* **19**(43), 435704 October (2008).

115. Zangwill, A. *Physics at Surfaces.* Cambridge University Press, (1988).

116. Lüth, H. *Solid surfaces, interfaces and thin films.* Graduate texts in physics. Springer Berlin Heidelberg, (2010).

117. Richter, H., Wang, Z. P., and Ley, L. *Solid State Communications* **39**(5), 625–629 (1981).

118. Tuma, C. and Curioni, A. *Applied Physics Letters* **96**(19), 193106 (2010).

119. Tuma, C. and Curioni, A. In *Materials Research Society Fall Meeting,* (2011).

120. Wang, J., Gudiksen, M. S., Duan, X., Cui, Y., and Lieber, C. M. *Science (New York, N.Y.)* **293**(5534), 1455–7 August (2001).

121. Kikuchi, A., Kishino, K., and Kaneko, Y. *Japanese Journal of Applied Physics* **30**(Part 1, No. 12B), 3865–3872 December (1991).

122. Tanaka, S.-I. and Lundstrom, M. *Solid-State Electronics* **37**(3), 401–410 March (1994).

123. Gordon, M. J., Baron, T., Dhalluin, F., Gentile, P., and Ferret, P. *Nano letters* **9**(2), 525–9 February (2009).

124. Sköld, N., Karlsson, L. S., Larsson, M. W., Pistol, M.-E., Seifert, W., Trägårdh, J., and Samuelson, L. *Nano letters* **5**(10), 1943–7 October (2005).

125. Montazeri, M., Fickenscher, M., Smith, L. M., Jackson, H. E., Yarrison-Rice, J. M., Kang, J. H., Gao, Q., Tan, H. H., Jagadish, C., Guo, Y., Zou, J., Pistol, M.-E., and Pryor, C. E. *Nano letters* **10**(3), 880–6 March (2010).

126. Thompson, S. E., Suthram, S., Sun, Y., Sun, G., Parthasarathy, S., Chu, M., and Nishida, T. In *2006 International Electron Devices Meeting*, 1–4. IEEE, (2006).

127. Goñi, A. and Syassen, K. In *High Pressure in Semiconductor Physics, Volume 1*, chapter 4, 248–410. Academic Press, London (1998).

128. Shay, J. *Physical Review B* **4**(4), 1385–1386 August (1971).

129. Chen, G., Wu, J., Lu, Q., Gutierrez, H. R., Xiong, Q., Pellen, M. E., Petko, J. S., Werner, D. H., and Eklund, P. C. *Nano letters* **8**(5), 1341–6 May (2008).

130. Bonera, E., Fanciulli, M., and Batchelder, D. N. *Journal of Applied Physics* **94**(4), 2729 (2003).

131. Ossikovski, R., Nguyen, Q., Picardi, G., and Schreiber, J. *Journal of Applied Physics* **103**(9), 093525 (2008).

132. Zardo, I., Yazji, S., Marini, C., Uccelli, E., Fontcuberta i Morral, A., Abstreiter, G., and Postorino, P. *ACS nano* **6**(4), 3284–91 April (2012).

133. Zardo, I. In *Selected Topics of Semiconductor Physics and Technology, vol. 122*, 184. Verein zur Förderung des Walter Schottky Instituts der Technischen Universität München (2010).

134. Fang, W. and Wickert, J. A. *Journal of Micromechanics and Microengineering* **4**(3), 116–122 September (1994).

135. Pollak, F. F., Cardona, M., and Shaklee, K. *Physical Review Letters* **16**(21), 942–944 May (1966).

136. Ruda, H. and Shik, A. *Physical Review B* **72**(11), 1–11 September (2005).

137. Van de Walle, C. and Martin, R. *Physical Review B* **35**(15), 8154–8165 May (1987).

138. Yeh, C.-Y., Wei, S.-H., and Zunger, A. *Physical Review B* **50**(4), 2715–2718 July (1994).

139. Süess, M. J., Geiger, R., Minamisawa, R. A., Schiefler, G., Frigerio, J., Chrastina, D., Isella, G., Spolenak, R., Faist, J., and Sigg, H. *Nature Photonics* **7**(6), 466–472 April (2013).

140. Zhang, F., Crespi, V., and Zhang, P. *Physical Review Letters* **102**(15) April (2009).

141. Ionescu, A. M. and Riel, H. *Nature* **479**(7373), 329–37 November (2011).

142. Yan, R., Gargas, D., and Yang, P. *Nature Photonics* **3**(10), 569–576 October (2009).

143. Dick, K. A., Deppert, K., Samuelson, L., Wallenberg, L. R., and Ross, F. M. *Nano letters* **8**(11), 4087–91 November (2008).

144. Ahtapodov, L., Todorovic, J., Olk, P., Mjåland, T., Slåttnes, P., Dheeraj, D. L., van Helvoort, A. T. J., Fimland, B.-O., and Weman, H. *Nano letters* **12**(12), 6090–5 December (2012).

145. Kusch, P., Breuer, S., Ramsteiner, M., Geelhaar, L., Riechert, H., and Reich, S. *Physical Review B* **86**(7), 075317 August (2012).

146. Signorello, G., Karg, S., Björk, M. T., Gotsmann, B., and Riel, H. *Nano letters* **13**(3), 917–24 March (2013).

147. Spirkoska, D., Arbiol, J., Gustafsson, A., Conesa-Boj, S., Glas, F., Zardo, I., Heigoldt, M., Gass, M. H., Bleloch, A. L., Estrade, S., Kaniber, M., Rossler, J., Peiro, F., Morante, J. R., Abstreiter, G., Samuelson, L., and Fontcuberta i Morral, A. *Physical Review B* **80**(24), 1–9 December (2009).

148. Ketterer, B., Heiss, M., Livrozet, M., Rudolph, A., Reiger, E., and Fontcuberta i Morral, A. *Physical Review B* **83**(12), 1–6 March (2011).

149. Ketterer, B., Heiss, M., Uccelli, E., Arbiol, J., and Fontcuberta i Morral, A. *ACS nano* **5**(9), 7585–92 September (2011).

150. Trommer, R. and Cardona, M. *Physical Review B* **17**(4), 1865–1876 February (1978).

151. Bell, D. J., Lu, T. J., Fleck, N. A., and Spearing, S. M. *Journal of Micromechanics and Microengineering* **15**(7), S153–S164 July (2005).

152. Jancu, J.-M., Gauthron, K., Largeau, L., Patriarche, G., Harmand, J.-C., and Voisin, P. *Applied Physics Letters* **97**(4), 041910 (2010).

153. Ganesan, S., Maradudin, A., and Oitmaa, J. *Annals of Physics* **56**(2), 556–594 February (1970).

154. Humphreys, L. and Maradudin, A. *Physical Review B* **6**(10), 3868–3886 November (1972).

155. Maradudin, A., Ganesan, S., and Burstein, E. *Physical Review* **163**(3), 882–895 November (1967).

156. Carpinteri, A. *Structural mechanics: a unified approach*. Taylor & Francis, (1997).

A

Crystal Structure of Zincblende and Wurtzite Crystals

The body of a generic crystal can be represented by the copy of a set of atoms, called basis, in the three dimensions of space. The set of translation vectors that are needed to define the position of each copy forms a periodic structure called Bravais lattice **R**, which is a linear combination with integer coefficients n_i of three unit vectors $\mathbf{a}_i$ that span the three dimensions of space:

$$\mathbf{R} = n_1\mathbf{a}_1 + n_2\mathbf{a}_2 + n_3\mathbf{a}_3 \ . \tag{A.1}$$

Zincblende and Wurtzite crystals can be defined with two different Bravais lattices. The face centered cubic lattice (FCC), used for the Zincblende structure, is generated by a set of primitive vectors shown in figure A.1a, defined by the following relations:

$$\mathbf{a}_1^{\mathrm{FCC}} = \frac{a}{2}\left(\widehat{\mathbf{y}} + \widehat{\mathbf{z}}\right) \ , \quad \mathbf{a}_2^{\mathrm{FCC}} = \frac{a}{2}\left(\widehat{\mathbf{z}} + \widehat{\mathbf{x}}\right) \ , \quad \mathbf{a}_3^{\mathrm{FCC}} = \frac{a}{2}\left(\widehat{\mathbf{x}} + \widehat{\mathbf{y}}\right) \ , \tag{A.2}$$

where $\hat{x}$, $\hat{y}$ and $\hat{z}$ represents the standard set of orthogonal vectors of unitary length. The definition (A.2) highlights that only one lattice parameter a, i.e. the length of the edge of the cube, is needed to define the FCC lattice. The Wurtzite structure is created instead with the hexagonal Lattice (Hex), shown in figure A.1b. This Bravais lattice is obtained by stacking

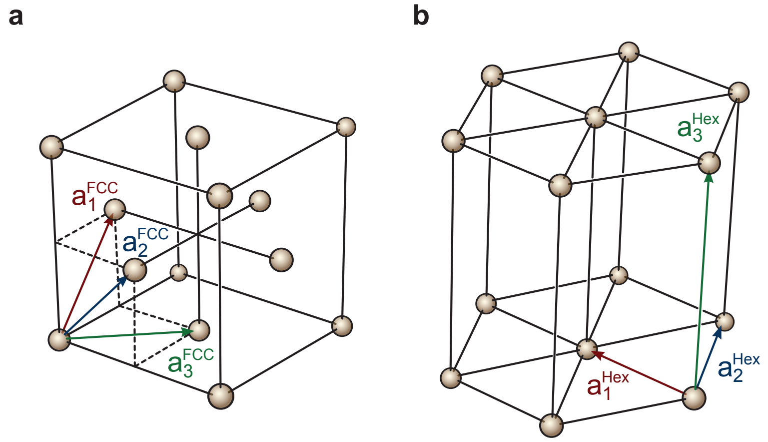

Figure A.1: Unit cell and base vectors of (a) the face centered cubic lattice and of (b) the hexagonal lattice.

two triangular nets on top of each others and its set of primitive vectors is:

$$\mathbf{a}_1^{\mathrm{Hex}} = a\widehat{\mathbf{x}}\,, \quad \mathbf{a}_2^{\mathrm{Hex}} = \frac{a}{2}\widehat{\mathbf{x}} + \frac{\sqrt{3}a}{2}\widehat{\mathbf{y}}\,, \quad \mathbf{a}_3^{\mathrm{Hex}} = c\widehat{\mathbf{z}}\,. \tag{A.3}$$

Unlike the FCC lattice, two parameters, namely the length of the edge of the hexagon a and the height of the parallelepiped c, are needed to define an hexagonal lattice.

To represent the final crystal structure of III-V materials in the Zincblende phase, we attach to each node of the FCC lattice a basis set of two atoms, one of the group III, like Gallium (Ga), and one of the group V, like Arsenic (As). The two atoms will have position $\mathbf{u}_1$ and $\mathbf{u}_2$ defined by:

$$\begin{aligned} \mathbf{u}_1 &= 0\mathbf{a}_1^{\mathrm{FCC}} + 0\mathbf{a}_2^{\mathrm{FCC}} + 0\mathbf{a}_3^{\mathrm{FCC}} = a(0,0,0)\,, \\ \mathbf{u}_2 &= \tfrac{1}{4}\mathbf{a}_1^{\mathrm{FCC}} + \tfrac{1}{4}\mathbf{a}_2^{\mathrm{FCC}} + \tfrac{1}{4}\mathbf{a}_3^{\mathrm{FCC}} = \tfrac{a}{4}(1,1,1)\,. \end{aligned} \tag{A.4}$$

For Wurtzite crystals, each node of the hexagonal lattice is associated to a base set of four atoms. The two atoms of the group III are located at position $\mathbf{u}_1$ and $\mathbf{u}_2$ given by:

$$\begin{aligned} \mathbf{u}_1 &= 0\mathbf{a}_1^{\mathrm{Hex}} + 0\mathbf{a}_2^{\mathrm{Hex}} + 0\mathbf{a}_3^{\mathrm{Hex}} = a\left(0,0,0\right)\,, \\ \mathbf{u}_2 &= \tfrac{1}{3}\mathbf{a}_1^{\mathrm{Hex}} + \tfrac{1}{3}\mathbf{a}_2^{\mathrm{Hex}} + \tfrac{1}{2}\mathbf{a}_3^{\mathrm{Hex}} = a\left(\tfrac{1}{2}, \tfrac{\sqrt{3}}{6}, \tfrac{1}{2}\tfrac{c}{a}\right)\,, \end{aligned} \tag{A.5}$$

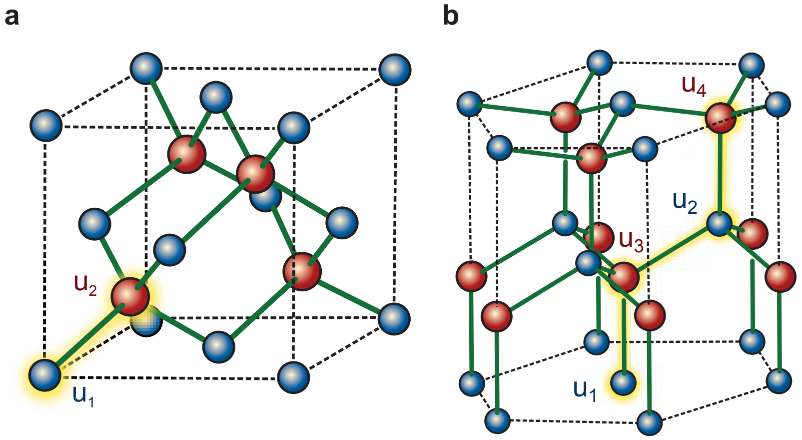

Figure A.2: Crystal structures of Zincblende (a) and Wurtzite (b) crystals. The basis set of atoms is highlighted in yellow.

while the groups V atoms are instead located at position $\mathbf{u}_3$ and $\mathbf{u}_4$:

$$\mathbf{u}_3 = 0\mathbf{a}_1^{\text{Hex}} + 0\mathbf{a}_2^{\text{Hex}} + u\mathbf{a}_3^{\text{Hex}} = a(0, 0, u\tfrac{c}{a}) ,$$

$$\mathbf{u}_4 = \tfrac{2}{3}\mathbf{a}_1^{\text{Hex}} + \tfrac{2}{3}\mathbf{a}_2^{\text{Hex}} + \left(\tfrac{1}{2} + u\right)\mathbf{a}_3^{\text{Hex}} = a\left(\tfrac{1}{2}, \tfrac{\sqrt{3}}{6}, \left(\tfrac{1}{2} + u\right)\tfrac{c}{a}\right) . \tag{A.6}$$

The resulting Zincblende and Wurtzite crystal lattices are represented in figure A.2. The two crystal structures are identical up to the first neighbour coordination: in both structures every atom of group III is located at the center of a regular tetrahedron, forming bonds with four atoms of the group V. The similarity between the two structures becomes even more evident if one rotates the zincblende unit cell according to the rotation matrix defined in equation (B.9). By orienting the z-axis is parallel to the cubic [111] direction, we can see how both crystals are formed by stacking the coordination tetrahedra in triangular lattices. The only difference between the two structure resides therefore in the stacking sequence that, in both cases, ensures the highest possible packing density: in other words, Zincblende and Wurtzite crystals are both are hexagonal close packed (HCP) structures. In table A.1 we have collected the lattice parameters for the case of GaAs in both Zincblende and Wurtzite structure. Notice that the experimental value of the c-a ratio deviates slightly from the value expected from ideal HCP structures:

$$\frac{c}{a} = \sqrt{\frac{8}{3}} \approx 1.633 \,. \tag{A.7}$$

Lattice parameter	Zincblende	Wurtzite
u		0.374
$\frac{c}{a}$		1.648
a	5.653 Å	3.983 Å

Table A.1: Experimental lattice parameters of GaAs with Zincblende and Wurtzite crystal structures[88 152].

B

Basics Concepts of Continuum Mechanics

This section is devoted to some basic concept of tensor calculus. We will describe the direction cosines scheme, used to perform transformations and rotations of tensor of any rank. We briefly describe the Einstein notation, which has been used throughout the thesis, as well as the Voigt notation, which has been used to deal with fourth rank tensor properties such as compliance, stiffness and phonon deformation potentials. We will conclude with deriving the expression of the strain tensors in Zincblende and Wurtzite crystals under uniaxial stress.

B.1 Direction Cosines and Tensor Transformation

Field tensors, like stress and strain, or tensor properties, like the piezoelectric tensor or the compliance, are always defined in reference to a set of orthogonal axis $\mathbf{n}_i$. The axis choice is often arbitrary, i.e. tensors have different expressions on different coordinate systems. It is very important to be able to express tensors in different reference systems and establish a law of transformation.

Let's indicate with $\xi_{ij..k}$ the tensor of rank k to be transformed, and with A the rotation matrix that transforms the old reference system $\mathbf{n}_i$ into the into the new one $\mathbf{n}'_i$. It is easy to see that the elements a_{ij} of the rotation matrix are costituted by the cosine of the angle that the new axis $\mathbf{n}'_i$ forms with the old reference system $\mathbf{n}_j$. Because of this property, the coefficients

a_{ij} are often called direction cosines. It is possible to demonstrate that a tensor of rank k can be expressed in a new reference system with following law of transformation^{86}:

$$\xi_{i'j'..k'} = \sum_{i,j,..,k=1}^{3} a_{i'i}\, a_{j'j}\, ..a_{k'k}\, \xi_{ij..k} \, . \tag{B.1}$$

For second rank tensors, like the stress tensor σ_{ij}, the law of transformation becomes:

$$\sigma_{i'j'} = \sum_{i,j=1}^{3} a_{i'i}\, a_{j'j}\, \sigma_{ij} \, . \tag{B.2}$$

To transform fourth rank tensors, like the stiffness tensor C_{ijkl}, one can use the following expression:

$$C_{i'j'k'l'} = \sum_{i,j,k,l=1}^{3} a_{i'i}\, a_{j'j}\, a_{k'k}\, a_{l'l}\, C_{ijkl} \, . \tag{B.3}$$

B.2 Einstein Notation

To define transformations like the one in (B.1), one must sum over indices like i, j, or k that are always repeated twice. Because of this property, these indices are also known as dummy indices. Albert Einstein introduced a notation in which the summation sign is omitted, implying that the sum will occur only between dummy indices. In this new notation, the relation (B.1) reads:

$$\xi_{i'j'..k'} = a_{i'i}\, a_{j'j}\, ..a_{k'k}\, \xi_{ij..k} \, . \tag{B.4}$$

B.3 Voigt Notation

Tensors of rank higher than two are often cumbersome to handle. For example, compliance and stiffness tensors should be represented by $3 \times 3 \times 3 \times 3$ arrays: this is not the easiest mathematical entity to handle.

Woldemar Voigt noticed that, when dealing with tensor properties that relate any physical quantity to stress or strain, it is possible to reduce the dimension of the representation matrices by exploiting the symmetry properties of the stress or strain tensors. Stress and strain tensors are symmetric upon index permutation and only six parameters are needed to fully define σ_{ij} and ε_{ij}. Voigt introduced a matrix notation and wrote, in form of column vector, only the independent components of these tensors. In the new notation, the double index (i, j) are replaced by a single matrix index I, ranging from 1 to 6, using the following convention:

$$\begin{array}{lcl} i,j = 1,1 & \rightarrow & I = 1\,, \\ i,j = 2,2 & \rightarrow & I = 2\,, \\ i,j = 3,3 & \rightarrow & I = 3\,, \\ i,j = 2,3 \text{ or } 3,2 & \rightarrow & I = 4\,, \\ i,j = 1,3 \text{ or } 3,1 & \rightarrow & I = 5\,, \\ i,j = 1,2 \text{ or } 2,1 & \rightarrow & I = 6\,. \end{array}$$

In this notation the stress tensor can be expressed as:

$$\begin{bmatrix} \sigma_{11} & \sigma_{12} & \sigma_{13} \\ \sigma_{12} & \sigma_{22} & \sigma_{23} \\ \sigma_{13} & \sigma_{23} & \sigma_{13} \end{bmatrix} \rightarrow \begin{bmatrix} \sigma_1 & \sigma_6 & \sigma_5 \\ \sigma_6 & \sigma_2 & \sigma_4 \\ \sigma_5 & \sigma_4 & \sigma_3 \end{bmatrix} . \tag{B.5}$$

The strain tensor will instead be represented as (notice the factors of $\frac{1}{2}$):

$$\begin{bmatrix} \varepsilon_{11} & \varepsilon_{12} & \varepsilon_{13} \\ \varepsilon_{12} & \varepsilon_{22} & \varepsilon_{23} \\ \varepsilon_{13} & \varepsilon_{23} & \varepsilon_{13} \end{bmatrix} \rightarrow \begin{bmatrix} \varepsilon_1 & \frac{1}{2}\varepsilon_6 & \frac{1}{2}\varepsilon_5 \\ \frac{1}{2}\varepsilon_6 & \varepsilon_2 & \frac{1}{2}\varepsilon_4 \\ \frac{1}{2}\varepsilon_5 & \frac{1}{2}\varepsilon_4 & \varepsilon_3 \end{bmatrix} . \tag{B.6}$$

For the compliance matrix, factors are introduced in the following way:

- $S_{ijkl} \rightarrow S_{IJ}$ when both I and J are 1, 2 or 3;
- $2S_{ijkl} \rightarrow S_{IJ}$ when either I or J is 4, 5 or 6;
- $4S_{ijkl} \rightarrow S_{IJ}$ when both I and J are 4, 5 or 6.

Using the Voigt notation, the compliance and stiffness tensors can be represented by 6×6 matrices, in a more compact way that the full tensor notation. The relation between stress and strain becomes a simple matrix product:

$$\varepsilon_I = S_{IJ}\,\sigma_J\ . \tag{B.7}$$

In terms of the stiffness matrix, strain and stress are related in the following way:

$$\sigma_J = C_{IJ}\varepsilon_I\ . \tag{B.8}$$

However, something gets lost in the translation from tensor to Voigt notation, i.e. the possibility to transform the tensors using the direction cosines scheme.

B.3.1 Strain Tensor in Zincblende Nanowires

In this thesis, Zincblende nanowires were grown and uniaxially stressed along the [111] direction axis, which is not aligned to the cubic crystallographic reference system. It is convenient to be able to express the stress and strain tensors in a stress reference system, which can be defined using the FCC lattice vectors: the [111] direction will be our new z-axis; the x and y-axis can be chosen in any direction orthogonal to z, for example along the $[1\bar{1}0]$ and $[11\bar{2}]$ directions. To perform the tensor transformation between these two reference systems, one can use the law of transformation of equation (B.3). The corresponding direction cosines are the elements of the following matrix:

$$a_{ij} = \begin{bmatrix} \frac{1}{\sqrt{2}} & \frac{1}{\sqrt{6}} & \frac{1}{\sqrt{3}} \\ -\frac{1}{\sqrt{2}} & \frac{1}{\sqrt{6}} & \frac{1}{\sqrt{3}} \\ 0 & -\frac{2}{\sqrt{6}} & \frac{1}{\sqrt{3}} \end{bmatrix} . \tag{B.9}$$

In the stress reference system the stress tensor has the expression shown in equation (3.10). To calculate the corresponding strain, two distinct methods are possible. Using the direction cosines scheme of equation (B.3), the compliance tensor is transformed from the crystallographic reference system, where it is defined, to the stress reference system and the strain tensor is obtained by normal tensor product. The alternative method, illustrated here, consist in the following steps. The stress is transformed from stress reference system to the crystallographic one using the direction cosines scheme of equation (B.2):

$$\sigma_{ij}^{\text{Stess}} = \begin{bmatrix} 0 & 0 & 0 \\ 0 & 0 & 0 \\ 0 & 0 & \sigma_{\|} \end{bmatrix} \xrightarrow{\text{Stess}\to\text{Cubic}} \sigma_{i'j'}^{\text{Cubic}} = \begin{bmatrix} 1 & 1 & 1 \\ 1 & 1 & 1 \\ 1 & 1 & 1 \end{bmatrix} \frac{\sigma_{\|}}{3} = \begin{bmatrix} 1 \\ 1 \\ 1 \\ 1 \\ 1 \\ 1 \end{bmatrix} \frac{\sigma_{\|}}{3} . \tag{B.10}$$

The strain tensor is obtained by the tensor product between the stress tensor and the compliance tensor:

$$\varepsilon_J^{\text{Cubic}} = \begin{bmatrix} S_{11}+2S_{12} \\ S_{11}+2S_{12} \\ S_{11}+2S_{12} \\ S_{44} \\ S_{44} \\ S_{44} \end{bmatrix} \frac{\sigma_{\|}}{3} = \begin{bmatrix} 2(S_{11}+2S_{12}) & S_{44} & S_{44} \\ S_{44} & 2(S_{11}+2S_{12}) & S_{44} \\ S_{44} & S_{44} & 2(S_{11}+2S_{12}) \end{bmatrix} \frac{\sigma_{\|}}{6} . \tag{B.11}$$

If necessary, the strain tensor can be also expressed back in the stress reference system, where it assumes again a diagonal form:

$$\varepsilon_{ij}^{\text{Cubic}} = \begin{bmatrix} 2(S_{11}+2S_{12}) & S_{44} & S_{44} \\ S_{44} & 2(S_{11}+2S_{12}) & S_{44} \\ S_{44} & S_{44} & 2(S_{11}+2S_{12}) \end{bmatrix} \frac{\sigma_{\parallel}}{6} \xrightarrow{\text{Cubic}\rightarrow\text{Stess}}$$

$$\rightarrow \varepsilon_{ij}^{\text{Stess}} = \begin{bmatrix} 2(S_{11}+2S_{12})-S_{44} & 0 & 0 \\ 0 & 2(S_{11}+2S_{12})-S_{44} & 0 \\ 0 & 0 & 2(S_{11}+2S_{12})+2S_{44} \end{bmatrix} \frac{\sigma_{\parallel}}{6} \, . \tag{B.12}$$

B.3.2 Strain Tensor in Wurtzite Nanowires

The Wurtzite nanowires used in our experiments are characterized by a growth direction parallel to the c-axis of the unit cell. The uniaxial stress direction is therefore aligned parallel to the hexagonal lattice reference system. The stress tensor can be expressed directly in the form of equation (3.10) in the crystallographic reference system and the strain tensor can be obtained by the tensor product with the Wurtzite compliance tensor:

$$\varepsilon_J = \begin{bmatrix} S_{13} \\ S_{13} \\ S_{33} \\ 0 \\ 0 \\ 0 \end{bmatrix} \sigma_{\parallel} \leftrightarrow \varepsilon_{ij} = \begin{bmatrix} \varepsilon_{xx} & 0 & 0 \\ 0 & \varepsilon_{yy} & 0 \\ 0 & 0 & \varepsilon_{zz} \end{bmatrix} = \begin{bmatrix} S_{13} & 0 & 0 \\ 0 & S_{13} & 0 \\ 0 & 0 & S_{33} \end{bmatrix} \sigma_{\parallel} \, . \tag{B.13}$$

C

Phonons and Vibrational Modes

In this section we will describe the lattice dynamics of Zincblende and Wurtzite crystals using a formalism established by Max Born and Kun Huang[82], which enables to understand the strain effects on the lattice vibrations. We will follow the work of Alex Maradudin et al.[153][154] to find the expression the strain effects in Zincblende crystals and expand these results in the Wurtzite case.

C.1 Lattice Dynamics in III-V Semiconductors

We have seen in §2.2 that the Hamiltonian can be separated in an ionic lattice part and an electronic part. We now concentrate on the ionic-lattice part of the Hamiltonian $\mathscr{H}_{\text{ion}}$ which, in the adiabatic approximation, can be expressed as a function of the atomic displacements from the equilibrium position, and as function of the electric field. We can identify with $\xi_\alpha\binom{l}{k}$ the component α of the atomic displacement ξ of the atoms k in the unit cell l and, for simplicity, we consider the ideal case of an infinite lattice and allow $l = (l_1, l_2, l_3)$ to assume any integer value. The label k instead has a finite number of values, to cover the n atoms of the unit cell. Finally, we indicate with E_μ the component μ of the electric field vector $\mathbf{E}$.

The equilibrium position is going to be a minimum in energy and, therefore, the Hamiltonian will depend quadratically on E_μ and $\xi_\alpha\binom{l}{k}$, assuming the following expression in the Einstein tensor notation :

$$\mathscr{H}_{\text{ion}} = \mathscr{H}_{\text{ion}}^{(0)} + \frac{1}{2} m_k \dot{\xi}_\alpha\binom{l}{k}\dot{\xi}_\alpha\binom{l}{k} + \frac{1}{2}\Phi_{\alpha\beta}\binom{l\,l'}{k\,k'}\xi_\alpha\binom{l}{k}\xi_\beta\binom{l'}{k'} -$$

$$- M_{\mu\alpha}\binom{l}{k}\xi_\alpha\binom{l}{k}E_\mu - \frac{1}{2}A_{\mu\nu}^{(0)}E_\mu E_\nu \; . \tag{C.1}$$

The first term, $\mathscr{H}_{\text{ion}}^{(0)}$, represents the energy of the lattice in the equilibrium configuration. The second term of the Hamiltonian represents the kinetic energy due to the lattice oscillations, i.e. the variation in time of the displacements ξ_α of the atoms k, with mass m_k, across the unit cells l. The third term of the Hamiltoninan represents a purely elastic contribution to the potential energy and $\Phi_{\alpha\beta}\binom{l\,l'}{k\,k'}$ represent the force constant between the atom k of the unite cell l and the atom k' of the unit cell l'. The dipole moment term $M_{\mu\alpha}\binom{l}{k}$ represents the component α of the force acting on the atom in position $\binom{l}{k}$ because of the presence of a component in direction μ of the electric field $\mathbf{E}$. The polarizability term $A_{\mu\nu}^{(0)}$ represents the energy due to the polarization of the lattice under the electric field $\mathbf{E}$.

By differentiating the potential energy term against the atomic displacement $\xi_\alpha\binom{l}{k}$, we can get the equations of dynamics of the crystal lattice:

$$m_k \ddot{\xi}_\alpha\binom{l}{k} = \Phi_{\alpha\beta}\binom{l\,l'}{k\,k'}\xi_\beta\binom{l'}{k'} - M_{\mu\alpha}\binom{l}{k}E_\mu \; , \tag{C.2}$$

while, by differentiating respect to the electric field E_μ, we obtain the expression of the dielectric polarization:

$$P_\alpha = -M_{\mu\alpha}\binom{l}{k}\xi_\alpha\binom{l}{k} - A_{\mu\nu}^{(0)}E_\nu \; . \tag{C.3}$$

It is interesting to compare this system with the set of equations (3.8) that define the behavior of a piezoelectric material under mechanical and electrical stimuli. In our dynamics system (C.2, C.3) the force constants tensor $\Phi_{\alpha\beta}\binom{l\,l'}{k\,k'}$ and the dipole-moment tensor $M_{\mu\alpha}\binom{l}{k}$ play the role of the compliance tensor and of the piezoelectric tensor, within the microscopic picture of the unit cell.

The energies and modes of vibration can be found by solving the dynamics system, which can be performed in two steps. We first consider the homogenoeus problem, that is the system (C.2,C.3) where the coefficients $M_{\mu\alpha}\binom{l}{k}$ are forced to zero. The solution allows the identification of the vibrational modes in absence of coupling between electric fields and lattice vibrations. This would also be the only problem to solve in semiconductors, like for example Silicon or Germanium, where the unit cell is composed by atoms of the same element. We then enable the coupling of electric field and lattice vibration through the dipole-moment tensor and see how vibrational energies are affected.

C.1.1 Homogenoeus Problem

By forcing to zero the dipole moment tensor $M_{\mu\alpha}\binom{l}{k}$, equation (2.4) simplifies significantly and becomes:

$$m_k \ddot{\xi}_\alpha\binom{l}{k} = \Phi_{\alpha\beta}\binom{l\;l'}{k\;k'}\xi_\beta\binom{l'}{k'}\,. \tag{C.4}$$

We can drammatically reduce the complexity of this system by noticing that $\Phi_{\alpha\beta}\binom{l\;l'}{k\;k'}$ possess the same translational symmetry properties of the crystal. As for the Bloch theorem, we can describe the lattice vibrations as plane waves with wave-vector $\mathbf{q}$, defined in the reciprocal space within the first Brillouin zone. If we also look for solutions that have harmonic behavior in their time dependence, with the atomic displacements that assume the form:

$$\xi_\alpha\binom{l}{k} = \frac{1}{\sqrt{m_k}} w_\alpha(k) e^{i\left[2\pi\mathbf{q}\cdot\mathbf{x}\binom{l}{k}-\omega t\right]}\,, \tag{C.5}$$

we obtain that the equations of dynamics of the crystal lattice can be transformed in an eigenvalue problem:

$$\omega^2 w_\alpha(k) = -C_{\alpha\beta}\binom{\mathbf{q}}{kk'} w_\beta(k')\,, \tag{C.6}$$

where we have introduced the dynamical matrix $C_{\alpha\beta}\binom{\mathbf{q}}{kk'}$, obtained from the force constants $\Phi_{\alpha\beta}\binom{l\;l'}{k\;k'}$ by a mass weighted Fourier transformation:

$$C_{\alpha\beta}\binom{\mathbf{q}}{kk'} = \sum_{l'} \frac{e^{i2\pi\mathbf{q}\cdot\left(\mathbf{x}\binom{l}{k}-\mathbf{x}\binom{l'}{k'}\right)}}{\sqrt{m_k m_{k'}}}\Phi_{\alpha\beta}\binom{l\;l'}{k\;k'}\,. \tag{C.7}$$

Once we have set the value of the wave-vector $\mathbf{q}$ of the lattice vibration we are interested in, we can obtain the square of the vibrational modes ω_j and the atomic displacement of vibrational modes $e_\alpha(k|j)$ as eigenvalues and eigenvectors of the dynamical matrix $C_{\alpha\beta}\binom{\mathbf{q}}{kk'}$. The eigenvectors $e_\alpha(k|j)$ have also the property of constituting a complete basis set to represent the lattice vibrations with wave-vector $\mathbf{q}$: any vibration mode has to satisfy (C.6) and can be expressed as a linear superposition of normal modes of oscillation:

$$w_\alpha(k) = \sum_j a_j e_\alpha(k|j)\,. \tag{C.8}$$

If we now put our focus on the vibrational properties of materials in proximity of the Γ-point, forcing $\mathbf{q} \approx \mathbf{0}$, the dynamical matrix $C_{\alpha\beta}\binom{\mathbf{0}}{kk'}$ becomes:

$$C_{\alpha\beta}\binom{\mathbf{0}}{k\,k'} = \sum_{l} \frac{\Phi_{\alpha\beta}\binom{l\;l}{k\,k'}}{\sqrt{m_k m_{k'}}}\,, \tag{C.9}$$

and practically assumes the form of a $3n \times 3n$ matrix, where n is the number of atoms per unit cell. The lattice dynamics problem has therefore as many solutions as degrees of freedom of the atoms in the unit cell. In any type of crystal these solutions can be divided in two main groups: acoustic and optical vibrational modes. The acoustic modes are characterized by atomic displacements that displace the center of mass of the unit cell, keeping the unit cell undeformed. There can only be three of such kind of phonons, one per degree of freedom that describes the displacement of the unit cell. The corresponding dispersion relation follows a liner dependence on the wave vector $\mathbf{q}$ and therefore, in proximity to the Γ point has negligible angular frequency ω. The remaining $3n-3$ optical vibrational modes are characterized by atomic displacements that preserve the position of the unit cell center of mass but distort the cell geometry. These phonons have finite energy for $\mathbf{q} \approx \mathbf{0}$ and, because of this feature, can be visible in optical experiments.

C.1.2 Inhomogenoeus Problem

We now consider the problem (C.2,C.3), in the case where the $M_{\mu\alpha}\binom{l}{k}$ tensor is not equal to zero and solve it with a particular lattice vibration wave, with atomic displacement $\hat{\xi}_{\alpha}\binom{l}{k}$ of the Bloch form, associated with wave-vector $\mathbf{q} \approx \mathbf{0}$:

$$\hat{\xi}_{\alpha}\binom{l}{k} = \frac{1}{\sqrt{m_k}} \hat{w}_{\alpha}(k) e^{i\left[2\pi \mathbf{q}\cdot\mathbf{x}\binom{l}{k} - \omega t\right]}\,. \tag{C.10}$$

Because of (C.3), we can associate to this vibration mode a dielectric polarization $\hat{P}_{\mu}$ that will share with $\hat{\xi}_{\alpha}\binom{l}{k}$ the same plane wave dependence. Born and Huang[82] have shown that in a medium with macroscopic dielectric polarization

$$\mathbf{P}(\mathbf{x}) = \mathbf{P} e^{i2\pi\mathbf{q}\cdot\mathbf{x}}\,, \tag{C.11}$$

a macroscopic electric field $\mathbf{E}$ develops, the direction of which is oriented along the wave-vector $\mathbf{q}$ according to the following relation:

$$\mathbf{E} = -4\pi \mathbf{P}_{\parallel}(\mathbf{x}) \qquad \rightarrow \qquad E_{\mu} = -4\pi \left(\frac{q_{\mu}}{|\mathbf{q}|}\right) \sum_{\alpha} \left(\frac{q_{\alpha}}{|\mathbf{q}|}\right) P_{\alpha}\,. \tag{C.12}$$

The lattice vibration $\hat{\xi}_{\alpha}\binom{l}{k}$ can induce a macroscopic electric field in the medium that directly enters in the dynamics equation (C.2). We call with $S_{\mu\nu}$ the component of the inverse of the following 3×3 matrix defined from the polarizability tensor $A^{(0)}_{\mu\nu}$ and the wave-vector, so that the following relation applies:

$$S_{\lambda\mu}\left[\delta_{\mu\nu}+4\pi A^{(0)}_{\mu\gamma}\left(\frac{q_\gamma q_\nu}{|\mathbf{q}|^2}\right)\right]=\left[\delta_{\mu\nu}+4\pi A^{(0)}_{\mu\gamma}\left(\frac{q_\gamma q_\nu}{|\mathbf{q}|^2}\right)\right]S_{\lambda\mu}=\delta_{\lambda\nu}\ .$$

Using this expression, we can establish a relation between lattice vibration $\hat{\xi}_\alpha\binom{l}{k}$ and its associated polarization vector $\hat{P}_\alpha$:

$$\hat{P}_\alpha=-S_{\alpha\mu}\,M_{\mu\beta}\binom{l}{k}\frac{1}{\sqrt{m_k}}\hat{w}_\beta(k)\ . \tag{C.13}$$

and, together with the expression of the electric field of equation (C.12), we find that the dynamics equation becomes:

$$\begin{aligned}\omega^2\hat{w}_\alpha(k)=&\sum_{k'\beta}C_{\alpha\beta}\binom{\mathbf{q}}{kk'}\hat{w}_\beta(k')+\\ &+\frac{4\pi}{\sqrt{m_k}}\left\{\sum_\mu M_{\mu\alpha}\binom{l}{k}\left(\frac{q_\mu}{|\mathbf{q}|}\right)\right\}\left\{\sum_{k'l'}\sum_{\lambda\gamma\beta}\left(\frac{q_\lambda}{|\mathbf{q}|}\right)S_{\lambda\gamma}M_{\beta\beta}\binom{l'}{k'}\frac{1}{\sqrt{m_k}}\right\}\hat{w}_\beta(k')\ .\end{aligned} \tag{C.14}$$

The second line in equation (C.14) provides an explicit expression for the contribution of the dynamical matrix $C_{\alpha\beta}\binom{\mathbf{0}}{kk'}$ due to the macroscopic electric field generated by a generic lattice vibration: the interaction of this electric field with the charge generated by the atomic displacement, thought the dipole-moment tensor $M_{\mu\beta}\binom{l}{k}$, has a finite energy and stiffens the force constants for specific combinations of the displacement $\hat{w}_\beta(k')$ and of the wave-vector $\mathbf{q}$. It is important to notice that such contribution can only exist in materials where the tensor $M_{\mu\beta}\binom{l}{k}$ is finite and is therefore a physical manifestation of the piezoelectricity of the material.

C.2 Strain Effects on the Lattice Vibrations

Let us consider the ionic Hamiltonian in equation (C.1) and, following the methodology of L. Humphreys and A. Maradudin[153–155], expand it further to third order powers of the lattice configuration $\xi_\beta\binom{l'}{k'}$ and electric field E_μ:

$$\mathscr{H}_{\text{ion}} = \mathscr{H}^{(0)}_{\text{ion}} + \frac{1}{2} m_k \left(\dot{\xi}_\alpha\binom{l}{k}\dot{\xi}_\alpha\binom{l}{k}\right) + E_\mu P^{(0)}_\mu$$

$$+\frac{1}{2}\left[\Phi^{(0)}_{\alpha\beta}\binom{l\,l'}{k\,k'} + \frac{1}{3}\Phi^{(1)}_{\alpha\beta\gamma}\binom{l\,l'\,l''}{k\,k'\,k''}\xi_\gamma\binom{l''}{k''}\right]\xi_\alpha\binom{l}{k}\xi_\beta\binom{l'}{k'}-$$

$$-E_\mu\left[M^{(0)}_{\mu\alpha}\binom{l}{k} - \frac{1}{2}M^{(1)}_{\mu\alpha\beta}\binom{l\,l'}{k\,k'}\xi_\beta\binom{l'}{k'}\right]\xi_\alpha\binom{l}{k}-$$

$$-\frac{1}{2}E_\mu E_\nu\left[A^{(0)}_{\mu\nu} + A^{(1)}_{\mu\nu\alpha}\binom{l}{k}\xi_\alpha\binom{l}{k}\right] . \tag{C.15}$$

As a result of the application of stress, the crystal lattice will relax in a new equilibrium position. The atomic displacement $\xi_\alpha\binom{l}{k}$ can therefore be decomposed in a static term $v_\alpha\binom{l}{k}$, that describes the new equilibrium configuration, and a dynamic term $u_\alpha\binom{l}{k}$, that represents the dynamic displacement of the lattice measured from the new equilibrium configuration:

$$\xi_\alpha\binom{l}{k} = v_\alpha\binom{l}{k} + u_\alpha\binom{l}{k} . \tag{C.16}$$

If we substitute the displacement expression (C.16) in the Hamiltonian (C.15) and expand up to the second in power in $u_\alpha\binom{l}{k}$ and in E_μ, we can write the Hamiltonian as:

$$\mathscr{H}_{\text{ion}} = \frac{1}{2} m_k \dot{\xi}_\alpha\binom{l}{k}\dot{\xi}_\alpha\binom{l}{k} + \hat{\mathscr{H}}^{(0)}_{\text{ion}} + \hat{F}_\alpha\binom{l}{k}\xi_\alpha\binom{l}{k} + \hat{P}_\mu E_\mu$$

$$-\hat{M}_{\mu\alpha}\binom{l}{k}\xi_\alpha\binom{l}{k}E_\mu + \frac{1}{2}\hat{\Phi}_{\alpha\beta}\binom{l\,l'}{k\,k'}\xi_\alpha\binom{l}{k}\xi_\beta\binom{l'}{k'} - \frac{1}{2}\hat{A}_{\mu\nu}E_\mu E_\nu , \tag{C.17}$$

where the force $\hat{F}_\alpha\binom{l}{k}$ and the modified sping constant $\hat{\Phi}_{\alpha\beta}\binom{l\,l'}{k\,k'}$ are:

$$\hat{F}_\alpha\binom{l}{k} = \Phi^{(0)}_{\alpha\beta}\binom{l\,l'}{k\,k'}v_\beta\binom{l}{k} , \tag{C.18}$$

$$\hat{\Phi}_{\alpha\beta}\binom{l\,l'}{k\,k'} = \Phi^{(0)}_{\alpha\beta}\binom{l\,l'}{k\,k'} + \Phi^{(1)}_{\gamma\alpha\beta}\binom{l\,l'\,l''}{k\,k'\,k''}v_\gamma\binom{l''}{k''} - E_\mu M^{(1)}_{\mu\alpha\beta}\binom{l\,l'}{k\,k'} , \tag{C.19}$$

the modified spontaneous polarization $\hat{P}_\mu$, dipole moment $\hat{M}_{\mu\alpha}\binom{l}{k}$ and the dielectric polarizability $\hat{A}_{\mu\nu}$ are:

$$\hat{P}_\mu = P^{(0)}_\mu - M^{(0)}_{\mu\alpha}\binom{l}{k}v_\alpha\binom{l}{k} , \tag{C.20}$$

$$\hat{M}_{\mu\alpha}\binom{l}{k} = M^{(0)}_{\mu\alpha}\binom{l}{k} + M^{(1)}_{\mu\alpha\beta}\binom{l\,l'}{k\,k'} v_\beta\binom{l'}{k'} \,, \tag{C.21}$$

$$\hat{A}_{\mu\nu} = A^{(0)}_{\mu\nu} + A^{(1)}_{\mu\nu\alpha} v_\alpha\binom{l}{k} \,, \tag{C.22}$$

while the modified constant energy term $\hat{\mathscr{H}}^{(0)}_{\text{ion}}$ is :

$$\hat{\mathscr{H}}^{(0)}_{\text{ion}} = \mathscr{H}^{(0)}_{\text{ion}} + \frac{1}{2}\Phi^{(0)}_{\alpha\beta}\binom{l\,l'}{k\,k'} v_\alpha\binom{l}{k} v_\beta\binom{l'}{k'} \,. \tag{C.23}$$

The new equilibrium configuration $v_\alpha\binom{l}{k}$ can be expressed as the sum of a translation $d_\alpha\binom{l}{k}$ plus a term given by the strain tensor $\varepsilon_{\alpha\beta}$ acting on the unstrained crystal configuration $R_\beta\binom{l}{k}$:

$$v_\alpha\binom{l}{k} = d_\alpha\binom{l}{k} + \varepsilon_{\alpha\beta} R_\beta\binom{l}{k} \,. \tag{C.24}$$

By definition of equilibrium, the force $\hat{F}_\alpha\binom{l}{k}$ acting on the lattice should be zero. Equation (C.18) allows the determination the equilibrium configuration of the unit cell, satisfying to the lowest order in displacement the following equation:

$$\Phi^{(0)}_{\alpha\beta}\binom{l\,l'}{k\,k'} d_\beta\binom{l'}{k'} \approx -\Phi^{(0)}_{\alpha\beta}\binom{l\,l'}{k\,k'} \varepsilon_{\alpha\beta} R_\gamma\binom{l'}{k'} \,. \tag{C.25}$$

Introducing $\Gamma^{(0)}_{\alpha\beta}\binom{l\,l'}{k\,k'}$, the effective inverse of the spring constant tensor $\Phi^{(0)}_{\alpha\beta}\binom{l\,l'}{k\,k'}$ obtained by factoring out the translation degrees of freedom of the unit cell, and the translational invariant factor $G_{\alpha\beta\gamma}\binom{l}{k}$ by:

$$G_{\alpha\beta\gamma}\binom{l}{k} = -\Phi^{(0)}_{\alpha\beta}\binom{l\,l'}{k\,k'} R_\gamma\binom{l'}{k'} = -\Phi^{(0)}_{\alpha\beta}\binom{l\,l'}{k\,k'} \left[R_\gamma\binom{l'}{k'} - R_\gamma\binom{l}{k} \right] \,, \tag{C.26}$$

we can express the new atomic configuration within the unit cell $d_\alpha\binom{l}{k}$, in terms of the strain tensor $\varepsilon_{\gamma\delta}$ by:

$$d_\alpha\binom{l}{k} \approx \Gamma^{(0)}_{\alpha\beta}\binom{l\,l'}{k\,k'} G_{\beta\gamma\delta}\binom{l'}{k'} \varepsilon_{\gamma\delta} \,. \tag{C.27}$$

The new equilibrium configuration can therefore be written as:

$$v_\alpha\binom{l}{k} = \left[\Gamma^{(0)}_{\alpha\beta}\binom{l\,l'}{k\,k'} G_{\beta\gamma\delta}\binom{l'}{k'} + \delta_{\alpha\gamma} R_\delta\binom{l}{k} \right] \varepsilon_{\gamma\delta} \,. \tag{C.28}$$

With this expression, one can go back to equations (C.20), (C.21) and (C.22) to obtain the final expression for the modified spring constant $\hat{\Phi}_{\alpha\beta}\binom{l\,l'}{k\,k'}$, spontaneous polarization $\hat{P}_\mu$, dipole moment $\hat{M}_{\mu\alpha}\binom{l}{k}$ and the dielectric polarizability $\hat{A}_{\mu\nu}$. By using this new set of tensors, the equations of motion and the expression of the dynamic polarization vector assume a form that we have encountered already:

$$m_k\ddot{u}_\alpha\binom{l}{k} = \hat{\Phi}_{\alpha\beta}\binom{l\,l'}{k\,k'}u_\beta\binom{l'}{k'} - E_\mu\hat{M}_{\mu\alpha}\binom{l}{k}\,, \tag{C.29}$$

$$P_\alpha = -\hat{M}_{\mu\alpha}\binom{l}{k}u_\alpha\binom{l}{k} - \hat{A}^{(0)}_{\mu\nu}E_\nu\,. \tag{C.30}$$

This new set of equations reads exactly as like (C.2) and (C.3) and the same methods can be used to identify the solutions to the lattice dynamics problem.

As in section C.1, we first consider the homogenous problem, obtained imposing the dipole moment $\hat{M}_{\mu\alpha}\binom{l}{k}$ to zero. The lattice dynamics equation becomes:

$$m_k\ddot{u}_\alpha\binom{l}{k} = \hat{\Phi}_{\alpha\beta}\binom{l\,l'}{k\,k'}u_\beta\binom{l'}{k'}\,, \tag{C.31}$$

and assumes the exact same form of equation (C.4), with the modified spring-constant tensor $\hat{\Phi}_{\alpha\beta}\binom{l\,l'}{k\,k'}$. This tensor can be written in the following form:

$$\hat{\Phi}_{\alpha\beta}\binom{l\,l'}{k\,k'} = \Phi^{(0)}_{\alpha\beta}\binom{l\,l'}{k\,k'} + \hat{\Phi}^{(1)}_{\alpha\beta\gamma\delta}\binom{l\,l'}{k\,k'}\varepsilon_{\gamma\delta}\,, \tag{C.32}$$

where the first term represents the spring constant without applied stress, while the second shows how the spring constants vary under strain. In this relation the phonon deformation-potential tensor $\hat{\Phi}^{(1)}_{\alpha\beta\gamma\delta}\binom{l\,l'}{k\,k'}$ is introduced: its tensor elements represent the variation in the components α of the force felt by the atom $\binom{l}{k}$ because of the β component of atomic oscillation of the atom $\binom{l'}{k'}$ due to the deformation defined by the strain tensor $\varepsilon_{\gamma\delta}$. Using equations (C.19,C.24,C.27), it can be shown that this tensor is defined by the following relation:

$$\hat{\Phi}^{(1)}_{\alpha\beta\gamma\delta}\binom{l\,l'}{k\,k'} = \Phi^{(1)}_{\alpha\beta\gamma}\binom{l\,l'\,l''}{k\,k'\,k''}R_\delta\binom{l''}{k''} + \Phi^{(1)}_{\alpha\beta\lambda}\binom{l\,l'\,l''}{k\,k'\,k''}\Gamma^{(0)}_{\lambda\zeta}\binom{l''\,l^*}{k''\,k^*}G_{\zeta\gamma\delta}\binom{l^*}{k^*}\,. \tag{C.33}$$

The tensor $\Phi^{(1)}_{\alpha\beta\gamma}\binom{l\,l'\,l''}{k\,k'\,k''}$ represents the an-harmonic variation of the force constant due to a general displacement of the lattice. The first term of the sum, in equation (C.33), represents the variation of the spring constant tensor because of the homogeneous deformation of the unit cell. The second term represents instead the effect on the variation of the elastic constants due to the rearrangement of the atoms within the unit cell: because of the application of stress and deformation of the unit cell, the atoms might find a more stable equilibrium rearranging their relative positions within the unit cell. In literature, one often talks about the rearrangement of the unit cell degrees of freedom as internal strain parameters: it is possible to address these modes of deformation only through the internal rearrangement of the unit cell due to the application of external forces.

Using the same methodology as in section C.1, we can expand the lattice vibrations in terms of plane waves with wave-vector $\mathbf{q}$, defined in the first Brillouin zone of the strained crystal. Using the result of §C.1.1 and defining a mass weighted Fourier transformation of the phonon deformation potential tensor as:

$$C^{(1)}_{\alpha\beta\gamma\delta}\binom{\mathbf{q}}{kk'} = \sum_{l'} \frac{e^{i2\pi\mathbf{q}\cdot\left(\mathbf{x}\binom{l}{k}-\mathbf{x}\binom{l'}{k'}\right)}}{\sqrt{m_k m_{k'}}}\,\hat{\Phi}^{(1)}_{\alpha\beta\gamma\delta}\binom{l\,l'}{k\,k'}\,, \tag{C.34}$$

we can write the dynamics equation as:

$$\sum_j \left(\omega^2-\omega_j^2\right) a_j\, e_\alpha(k|j) = C^{(1)}_{\alpha\beta\gamma\delta}\binom{\mathbf{q}}{kk'}\varepsilon_{\gamma\delta}\sum_j a_j\, e_\beta(k|j)\,. \tag{C.35}$$

The shift in energy of the vibrational modes of the crystal under the application of strain can be found by calculating the eigenvalues of $C^{(1)}_{\alpha\beta\gamma\delta}\binom{\mathbf{q}}{kk'}\varepsilon_{\gamma\delta}$. We will see how these expressions take form in the specific case of Zincblende and Wurtizite crystals.

C.2.1 Uniaxial Stress Effects on the Zone-center Phonons of Zincblende Crystals

The Fourier transformed equations of motion can be written using as a basis the eigenmodes of the zincblende, which consists of the three acoustic modes and three optical modes. $C^{(1)}_{\alpha\beta\gamma\delta}\binom{\mathbf{0}}{kk'}$ can therefore be written in a block diagonal form, each block consists of a 3×3 matrix. As shown in §2.3.1 , all optical modes have translation symmetry and the indexes α,β can be assimilated to normal translation indexes. $C^{(1)}_{\alpha\beta\gamma\delta}\binom{\mathbf{0}}{kk'}$ has therefore the symmetry property of a fourth rank tensor and, like the compliance tensor, it is defined by three coefficients p, q and r:

$$C^{(1)}_{\alpha\beta\gamma\delta}\binom{\mathbf{q}}{kk'} = \begin{bmatrix} p & q & q & & & \\ q & p & q & & & \\ q & q & p & & & \\ & & & r & & \\ & & & & r & \\ & & & & & r \end{bmatrix}\,. \tag{C.36}$$

The angular frequency of vibration of the strained Zincblende crystal can be found as eigenvalues of the following matrix:

$$\begin{bmatrix} {\omega_{F_{2g}}}^2 - \omega^2 & & \\ & {\omega_{F_{2g}}}^2 - \omega^2 & \\ & & {\omega_{F_{2g}}}^2 - \omega^2 \end{bmatrix} + \\ + \begin{bmatrix} p\varepsilon_{xx} + q(\varepsilon_{yy} + \varepsilon_{zz}) & r\varepsilon_{xy} & r\varepsilon_{xz} \\ r\varepsilon_{xy} & p\varepsilon_{yy} + q(\varepsilon_{xx} + \varepsilon_{zz}) & r\varepsilon_{yz} \\ r\varepsilon_{xz} & r\varepsilon_{yz} & p\varepsilon_{zz} + q(\varepsilon_{xx} + \varepsilon_{yy}) \end{bmatrix} . \tag{C.37}$$

C.2.2 Uniaxial Stress Effects on the Zone-center Phonons of Wurtzite Crystals

As in the Zincblende case, the Fourier transformed equations of motion can be written using the eigenmodes of the unstrained Wurtzite as a basis. Since the unit cell consists of four atoms, the base will consists of a $3 \times 4 = 12$ dimensional vector. Three degrees of freedom will correspond to the acoustic modes, while the remaining correspond to the optical modes. If we limit our description to the optical modes, $C^{(1)}_{\alpha\beta\gamma\delta}\binom{\mathbf{0}}{kk'}$ is going to be a $9 \times 9 \times 3 \times 3$ tensor: the indexes α and β can have values from 1 to 9, for the nine optical modes shown in figure 2.9, while γ and δ can have values from 1 to 3, as for the indexes of a strain tensor.

As for the case of Zincblende crystals, the dynamics equation should be expressed in matrix form, writing $C^{(1)}_{\alpha\beta\gamma\delta}\binom{\mathbf{0}}{kk'}$ in a notation resembling the one of Voigt. We have seen in §3.1.3 that, because of the symmetry of $\varepsilon_{\gamma\delta}$ upon permutation of the indexes γ and δ, the strain tensor can be written as a vector of six elements in Voigt notation. $C^{(1)}_{\alpha\beta\gamma\delta}\binom{\mathbf{0}}{kk'}$ is also symmetric upon the permutation of indexes α and β because of Newtons third law of mechanics. The double index (α, β) can be defined by a vector whose number of elements is given by

$$\sum_{k=1}^{9} k = \frac{9}{2}(9+1) = 45 .$$

To fully describe the all optical phonons in Wurtizite we need to express $C^{(1)}_{\alpha\beta\gamma\delta}\binom{\mathbf{0}}{kk'}$ in the form of a 45×6 matrix. To determine which subset of coefficients in this matrix can be different than zero one can use the symmetry properties of Wurtzite, using the methodology of Ganesan et al.[153], and

understand which modes can be coupled by the application of strain. Such treatment is however beyond the scope of this thesis and will be reserved to future work.
We will consider here only the subset of optical phonons that are visible with Raman spectroscopy, in our measurement setup. These optical phonons have symmetry A_1 and E_1, and E_2^{high}:

$$\alpha, \beta \in \left\{ 1 = E_{1x}, 2 = E_{1y}, 3 = A_{1z}, 4 = E_{2x}^{\text{high}}, 5 = E_{2y}^{\text{high}} \right\} . \tag{C.38}$$

Limiting the dynamics equation to these modes, we can expand the Voigt notation to describe (α, β) with a double index:

$$\begin{array}{rcl}
\alpha, \beta = E_{1x}, E_{1x} & \rightarrow & 1 \\
\alpha, \beta = E_{1y}, E_{1y} & \rightarrow & 2 \\
\alpha, \beta = A_{1z}, A_{1z} & \rightarrow & 3 \\
\alpha, \beta = E_{1y}, A_{1z} \text{ or } A_{1z}, E_{1y} & \rightarrow & 4 \\
\alpha, \beta = E_{1x}, A_{1z} \text{ or } A_{1z}, E_{1x} & \rightarrow & 5 \\
\alpha, \beta = E_{1x}, E_{1y} \text{ or } E_{1y}, E_{1x} & \rightarrow & 6 \\
\alpha, \beta = E_{2x}^{\text{high}}, E_{2x}^{\text{high}} & \rightarrow & 7 \\
\alpha, \beta = E_{2y}^{\text{high}}, E_{2y}^{\text{high}} & \rightarrow & 8 \\
\alpha, \beta = E_{2x}^{\text{high}}, E_{2x}^{\text{high}} \text{ or } E_{2y}^{\text{high}}, E_{2x}^{\text{high}} & \rightarrow & 9 \\
\alpha, \beta = E_{2x}^{\text{high}}, A_{1z} \text{ or } A_{1z}, E_{2x}^{\text{high}} & \rightarrow & 10 \\
\alpha, \beta = E_{2y}^{\text{high}}, A_{1z} \text{ or } A_{1z}, E_{2y}^{\text{high}} & \rightarrow & 11 \\
\alpha, \beta = E_{2x}^{\text{high}}, E_{1y} \text{ or } E_{1y}, E_{2x}^{\text{high}} & \rightarrow & 12 \\
\alpha, \beta = E_{2y}^{\text{high}}, E_{1y} \text{ or } E_{1y}, E_{2y}^{\text{high}} & \rightarrow & 13 \\
\alpha, \beta = E_{2x}^{\text{high}}, E_{1x} \text{ or } E_{1x}, E_{2x}^{\text{high}} & \rightarrow & 14 \\
\alpha, \beta = E_{2y}^{\text{high}}, E_{1x} \text{ or } E_{1x}, E_{2y}^{\text{high}} & \rightarrow & 15
\end{array}$$

The deformation potential tensor $C^{(1)}_{\alpha\beta\gamma\delta}\binom{\mathbf{0}}{kk'}$ can be shown to have the following expression

$$C^{(1)}_{\alpha\beta\gamma\delta}\binom{\mathbf{q}}{kk'} = \begin{bmatrix} K_{11} & K_{12} & K_{13} & & & \\ K_{12} & K_{11} & K_{13} & & & \\ K_{13} & K_{13} & K_{33} & & & \\ & & & K_{44} & & \\ & & & & K_{44} & \\ & & & & & K_{66} \\ K_{71} & K_{72} & K_{73} & & & \\ K_{72} & K_{71} & K_{73} & & & \\ & & & & & K_{96} \\ & & & & & \\ & & & & & \\ & & & & & \\ & & & & & \\ & & & & & \\ & & & & & \end{bmatrix}, K_{66} = \kappa_1 K_{11} + \kappa_2 K_{12}. \tag{C.39}$$

The vibration frequency of the selected modes (C.38) of a strained Wurtzite crystal can be found as eigenvalues of the following block diagonal matrix:

$$\begin{bmatrix} \hat{C}^{(A_1,E_1)}_{\alpha\beta} & \\ & \hat{C}^{(E_2^{\text{high}})}_{\alpha\beta} \end{bmatrix}. \tag{C.40}$$

The first block corresponds to the polar phonons, with symmetry A_1 and E_1, and can be written as:

$$\hat{C}^{(A_1,E_1)}_{\alpha\beta} = \begin{bmatrix} {\omega_{E_1}}^2 - \omega^2 & & \\ & {\omega_{E_1}}^2 - \omega^2 & \\ & & {\omega_{A_1}}^2 - \omega^2 \end{bmatrix} +$$

$$+ \begin{bmatrix} K_{11}\varepsilon_{xx} + K_{12}\varepsilon_{yy} + K_{13}\varepsilon_{zz} & K_{66}\varepsilon_{xz} & K_{44}\varepsilon_{xz} \\ K_{66}\varepsilon_{xz} & K_{12}\varepsilon_{xx} + K_{11}\varepsilon_{yy} + K_{13}\varepsilon_{zz} & K_{44}\varepsilon_{yz} \\ K_{44}\varepsilon_{xz} & K_{44}\varepsilon_{yz} & K_{13}\varepsilon_{xx} + K_{13}\varepsilon_{yy} + K_{33}\varepsilon_{zz} \end{bmatrix}. \tag{C.41}$$

while the second block corresponds to the E_2^{high} phonons and has the following expression:

$$\hat{C}^{(E_2^{\text{high}})}_{\alpha\beta} = \begin{bmatrix} {\omega_{E_2^{\text{high}}}}^2 - \omega^2 & \\ & {\omega_{E_2^{\text{high}}}}^2 - \omega^2 \end{bmatrix} + \tag{C.42}$$

$$+\begin{bmatrix} K_{71}\varepsilon_{xx}+K_{72}\varepsilon_{yy}+K_{73}\varepsilon_{zz} & K_{96}\varepsilon_{xz} \\ K_{96}\varepsilon_{xz} & K_{71}\varepsilon_{yy}+K_{72}\varepsilon_{xx}+K_{73}\varepsilon_{zz} \end{bmatrix} .$$

For the particular case of uniaxial stress applied along the c-axis direction, as shown in §3.1.5 and §B.3.2, the strain tensor has diagonal form and preserves the hexagonal symmetry of the semiconductor. As in the previous cases, the strain can be decomposed in isotropic and deviatoric component. For small deformations, the shift in energy of the phonons due to isotropic strain component can be approximated as:

$$\begin{aligned} \Delta\omega_{E_1,\mathrm{iso}} &\approx \frac{\omega^2-{\omega_{E_1}}^2}{2\omega_{E_1}} = \frac{K_{11}+K_{12}+K_{13}}{2\omega_{E_1}}\,h\,\varepsilon_\parallel\,, \\ \Delta\omega_{A_1,\mathrm{iso}} &\approx \frac{\omega^2-{\omega_{A_1}}^2}{2\omega_{A_1}} = \frac{K_{33}+2K_{33}}{2\omega_{A_1}}\,h\,\varepsilon_\parallel\,, \\ \Delta\omega_{E_2^{\mathrm{high}},\mathrm{iso}} &\approx \frac{\omega^2-{\omega_{E_2^{\mathrm{high}}}}^2}{2\omega_{E_2^{\mathrm{high}}}} = \frac{K_{71}+K_{72}+K_{73}}{2\omega_{E_2^{\mathrm{high}}}}\,h\,\varepsilon_\parallel\,. \end{aligned} \tag{C.43}$$

In the same spirit of the definition of the mode Grüneisen parameters, we defined the isotropic phonon-deformation-potentials γ for modes A_1, E_1 and E_2^{high} with the following set of relations:

$$\begin{aligned} \gamma_{E_1} &= \frac{K_{11}+K_{12}+K_{13}}{2{\omega_{E_1}}^2}\,, \\ \gamma_{A_1} &= \frac{K_{33}+2K_{33}}{2{\omega_{A_1}}^2}\,, \\ \gamma_{E_2^{\mathrm{high}}} &= \frac{K_{71}+K_{72}+K_{73}}{2{\omega_{E_2^{\mathrm{high}}}}^2}\,. \end{aligned} \tag{C.44}$$

We now consider the effect of the deviatoric component of strain. Upon this kind of deformation, the dynamical matrix (C.40) also preserves its diagonal form. This type of deformation does not lift any degeneracy of the E_1 and E_2^{high} phonons. The energy shift induced by the deviatoric strain is:

$$\begin{aligned} \Delta\omega_{E_1,\mathrm{dev}} &\approx \frac{\omega^2-{\omega_{E_1}}^2}{2\omega_{E_1}} = \frac{K_{13}-\frac{1}{2}(K_{11}+K_{12})}{2\omega_{E_1}}\,(1-h)\,\varepsilon_\parallel\,, \\ \Delta\omega_{A_1,\mathrm{dev}} &\approx \frac{\omega^2-{\omega_{A_1}}^2}{2\omega_{A_1}} = \frac{K_{33}-K_{13}}{2\omega_{A_1}}\,(1-h)\,\varepsilon_\parallel\,, \end{aligned} \tag{C.45}$$

$$\Delta\omega_{E_2^{\text{high}},\text{dev}} \approx \frac{\omega^2 - \omega_{E_2^{\text{high}}}{}^2}{2\omega_{E_2^{\text{high}}}} = \frac{K_{73} - \frac{1}{2}(K_{71} + K_{72})}{2\omega_{E_2^{\text{high}}}}\,(1-h)\,\varepsilon_\parallel\,.$$

We can therefore define the deviatoric deformation potentials ζ for the strain along the c-axis:

$$\begin{aligned}
\zeta_{E_1} &= \frac{K_{13} - \frac{1}{2}(K_{11} + K_{12})}{2\omega_{E_1}{}^2}\,,\\
\zeta_{A_1} &= \frac{K_{33} - K_{13}}{2\omega_{A_1}{}^2}\,,\\
\zeta_{E_2^{\text{high}}} &= \frac{K_{73} - \frac{1}{2}(K_{71} + K_{72})}{2\omega_{E_2^{\text{high}}}{}^2}\,.
\end{aligned} \tag{C.46}$$

The frequency shift of the optical phonons, due to the compound effect of isotropic and deviatoric strain, can therefore be expressed as function of γ and ζ with the following expressions:

$$\begin{cases}
\Delta\omega_{E_1} = \omega_{E_1}[\gamma_{E_1} h + \zeta_{E_1}(1-h)]\varepsilon_\parallel\,;\\
\Delta\omega_{A_1} = \omega_{A_1}[\gamma_{A_1} h + \zeta_{A_1}(1-h)]\varepsilon_\parallel\,;\\
\Delta\omega_{E_2^{\text{high}}} = \omega_{E_2^{\text{high}}}[\gamma_{E_2^{\text{high}}} h + \zeta_{E_2^{\text{high}}}(1-h)]\varepsilon_\parallel\,.
\end{cases} \tag{C.47}$$

This set of equation describes the effect of uniaxial stress on the vibration modes of a Wurtzite crystal but neglects the force constant stiffening due to the macroscopic electric field, shown in equation (C.14). This term can be fully determined from the terms $\hat{M}_{\mu\alpha}\binom{l}{k}$ and $\hat{A}_{\mu\nu}$. In a similar fashion to the case of Zincblende, one can use the arguments of Wickboldt et al.[96] and define a phonon deformation potential tensor (C.39) and, therefore, constants γ and ζ to distinctively describe transverse and longitudinal modes of the polar modes A_1 and E_1. The difference between the two sets represents the change in transverse effective charge induced by strain. The set of phonon deformation potentials to be used for a particular stress and Raman measurement depends on the orientation of the wave-vector **q**, defined by the details of the scattering configuration.

To our knowledge, a full characterization of the phonon deformation potentials in GaAs Wurtzite has not been object of experimental measurement yet.

D

Continuum Mechanics of a Doubly-clamped Beam

The static problem of a beam subject to a system of applied forces can be described by the equations of equilibrium of the elastic line[156]. The internal reactions of a section of a beam can be decomposed in an axial force N, shear force T and bending moment M, shown schematically in figure D.1a. The axial force is positive when tensile. Shear forces are positive when they tends to rotate a given segment of the beam in clockwise fashion. A bending moment is positive when stretches the lower fibers and compresses the upper fibers of a beam.

In presence of distributed axial loads p, transversal loads q and distributed moment m on a small section of the beam of length dz, the system of forces and moments undergoes variations that are described by the following equations:

$$\begin{cases} \frac{d}{dz}N(z) = -p(z)\,; \\ \frac{d}{dz}T(z) = -q(z)\,; \\ \frac{d}{dz}M(z) = T - m(z)\,. \end{cases} \tag{D.1}$$

The variation of axial load dN at the two ends of the beam segment has to balance the axial distributed load. The variation of shear load dT at the two ends of the beam segment has to balance the transversal distributed

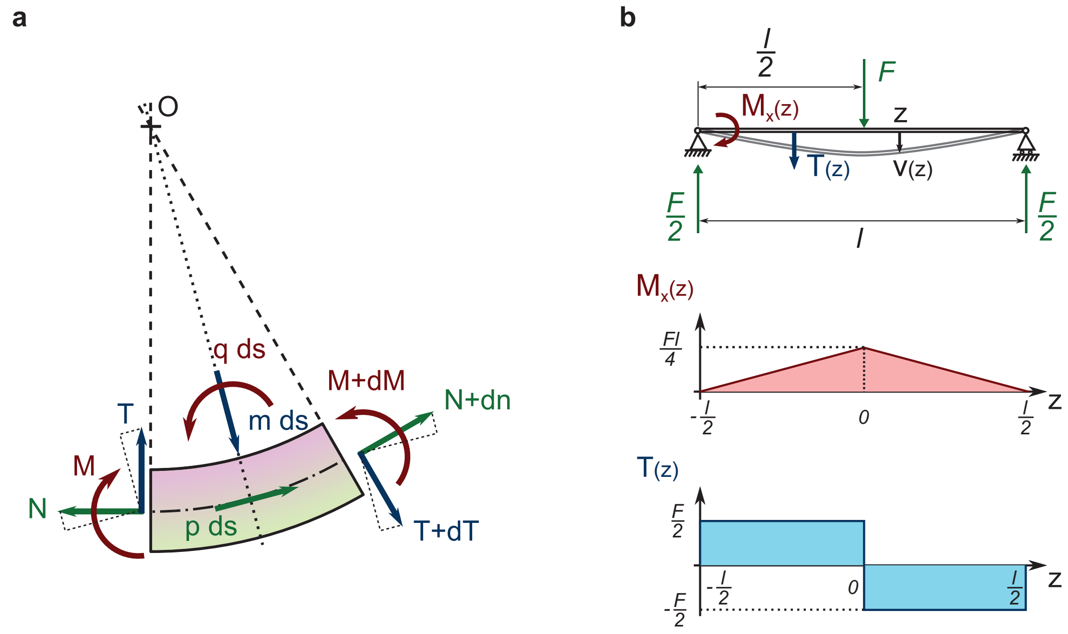

Figure D.1: The static problem of a bent beam. (a) Representation of the characteristics of internal reaction of a beam: axial force N, shear force T and bending moment M and their respective distributed axial loads p, transversal loads q and distributed moment m. (b) Solution of the static equations the three point bending of a beam.

load. Finally, the variation in bending moment M has to balance the distributed momentum minus the shear force. This set of equations completely determines the status of stress of a linear beam.

Let's now consider the stress induced on a flexible beam subject to the forces of a three-point bending mechanism, as shown in figure D.1b. The substrate is supported on the two ends, l is the distance between the supports and F will be the force applied in the middle. No axial load will be present on the substrate. For mechanical equilibrium to be established, each supports will react with a force $\frac{1}{2}F$ at each end, so that the sum of all forces is zero. The profile of shear force and momentum are obtained by solving the equations (D.1) for the system of loads stated above and are represented in figure D.1b. In particular, the bending moment follows the relation:

$$M_x(z) = \frac{Fl}{4}\left(1 - 2\frac{|z|}{l}\right) , \tag{D.2}$$

has its maximum in the center position and decreases linearly along the length of the substrate, reaching zero at the supports.

The displacement profile of the beam can be calculated by integrating the differential equation of the elastic line[156]:

$$\frac{d^2v}{dz^2} = -\frac{1}{E\,I_x} M_x(z)\,. \tag{D.3}$$

This equation states that the beam displacement $v(z)$ from the straight condition is, with good approximation, caused by the bending moment $M_x(z)$ applied to the beam, and is inversely proportional to the Young's modulus E of the beam and to the momentum of inertia I_x.

It can also be shown that the surface strain ε_z of the slab is proportional to the bending moment M_x according to the following relation:

$$\varepsilon_z(z) = \frac{M_x(z)}{EI_x}\frac{t}{2}\,. \tag{D.4}$$

Integrating equation (D.3) for the momentum profile of figure D.1b with the appropriate boundary conditions, we can obtain an expression for the displacement of the beam from the center:

$$v(z) = -\frac{\frac{F}{2}|z|^3}{6\,E\,I_x} + \frac{\frac{Fl}{4}|z|^2}{2\,E\,I_x}\,. \tag{D.5}$$

The maximum deflection of the beam Δh, between the center and the lateral supports, can be expressed with the following relation:

$$\Delta h = \frac{1}{3\,E\,I_x}\frac{F}{2}\left(\frac{l}{2}\right)^3\,. \tag{D.6}$$

Equations (D.2, D.4, D.6) can be combined to provide the relation between the surface strain ε_z of the beam at a position z along the bending coordinate as a function of the maximum displacement of the beam Δh:

$$\varepsilon_z(z) = 6\frac{t}{l^2}\left(1 - 2\frac{|z|}{l}\right)\,\Delta h\,. \tag{D.7}$$

The strain induced on the surface by bending will depend linearly on the displacement Δh of the substrate and on its thickness t and inversely to the square of the distance l between the two outer supports. In our experiment we have used substrates with a thickness t of 250 µm and the supported substrate length is of 12 mm: we therefore estimate that, for every millimeter of travel of the supports, a surface strain of about 1 % is generated and can be transferred to the substrate. Our system uses a differential thread to control the relative displacement of the supports. The thread rotation is induced by a high precision stepper motors that have an accuracy higher than 0.001°. This permits to apply axial strain with high resolution, nominally higher than $3 \times 10^{-7}\,\%$.

From the equation (D.5) we can also calculate the variation in angle between two points, located symmetrically with respect to the center clamp at a distance d from each others:

$$\Delta\theta \approx 2\frac{dv}{dz}|_d = \frac{(2l-d)d}{tl}\varepsilon_z \approx \frac{2d}{t}\varepsilon_z \,. \tag{D.8}$$

This quantity describes how effectively the substrate bending is transmitted to the nanowire, in the case in which the nanowire is located in the center. This quantity scales like the ratio between the substrate thickness and the free-standing segment of the wire: for a freestanding segment of 1 µm and a substrate thickness of 250 µm, an increment in angle of only 8×10^{-5} degrees is induced by every percent of strain generated in the substrate surface.

For the strain range we are interested we can consider the stress applied purely uniaxial.

Acknowledgements

I started dreaming about working in IBM Research back in 2006. After 2 years, 6 failed trials to get my application through human resources, 3 months of search and 4 months of internship in Switzerland, many emails to IBM managers and one night spent at the Nacht der Foschung, I finally could get to know what were going to be my future colleagues. So here I am, seven years after it started, living the last moments of my dream come true. I feel privileged to have had the opportunity to realize my dream. And this story would have never come this far without the people mentioned below. This is the time to say thank you:

Heike (Riel), thank you so much for daring to give the chance to “such an insisting Italian” to realize his dream. Thank you for your humanity, for taking the time to listen to me especially in the moment of discomfort, for sharing smiles, laughs and tears.

Prof. Christian Schönenberger, thank you so much for accepting me in your group as an external PhD student, for your very enlightening scientific discussions, for being such an excellent guidance in the world of the University of Basel, and for allowing me to join your PhD conferences, which have been great source of inspiration.

A big thank you to Prof. Anna Fontcuberta i Morral and Prof. Lars Samuelson, for giving me the honor of taking part of my thesis dissertation, and for sharing their ideas and insights with me during conferences and workshops.

A huge thank you to Walter (Riess), for taking time to discuss about physics and devices, for sharing with me and all the colleagues at IBM his constant good mood and keeping up such a positive spirit in the lab in his very own way: “it’s very simple!”.

Thank you Bernd (Gotsmann) for your contagious joy of research, for discussing with me about physics, about faith, about the meaning of life.

Thank you Manu (Löertscher), for teaching me how important it is to fight for your ideas, for showing me that even the craziest idea, no matter how complicated, can be brought to life with hard work, and for transmitting to me your passion and love for beauty of details of the experimental setups.

Thank you Sigi (Karg), for transmitting your down-to-the-essential approach to physics and sharing your insights about for the big picture and impact of research.

Thank Mikael (Björk), for your great support and scientific discussions, especially when completing my first manuscript, for introducing me to the world of $k \cdot p$ models, for growing so great Zincblende nanowire samples. I wish we had more time to work together: the research world is small, and who knows what will happen in the future.

A great thank you to Petr (Komjakov) and Christian (Tuma), who always found time to answer and discuss my theoretical questions and supported me in building the physics understanding that I have today.

Thank you to Helge Weman and Dong Chul Kim and Dasa Dheeraj, for creating such a great environment of collaboration with NTNU, for sharing your art of Wurtzite nanowire growth and for working together on the GaAs nanowire doping.

A great thank you to Andreas Schenk, Manuel Cardona and Alex Maradudin, for answering my theoretical questions from a distant institute, nation or continent, without even knowing me. Reading your mails makes you feel that the scientific community is indeed alive and ready to support you.

Thousand times thank you to Ute Drechsler and Daniele Caimi, for their tremendous support in the cleanroom and for their precious advices with micro-fabrication and processing issues, and to Meinrad Tschudy, Lukas Schuler, Marcel Buerge and Urs Kloter, for their patience with me and my sloppy 3D designs, for taking time to transform my ideas into working assemblies of aluminum, brass and steel.

Thank you Charlie Rettner, Teya Topuria and Phil Rice, for your support from California with e-beam issues, TEM imaging of the nanowires and for providing your insight and care for detail.

Thank you to Volker Schmidt (“Comandante!”), Kirsten Moselund, Heinz Schmid, Matthias Borg, Cedric Bessire, Hesham Ghoneim, Valentina Troncale, Pratjiush Das Kanugo, Fabian Menges, Peter Nirmalraj, Florian Schwarz, Philipp Mensch and Antje Rey for creating such a joyfull environment in the nanoelectronics team and nice moments during our coffee breaks and stimulating discussions.

Un grazie enorme to Gabriele Raino, Olivier Gallay, Johan Engelen, Antonio La Porta, Daniel Krebs, Tomas Tuma, Philip Shemella, Claudia Santini, Francesco Fusco, Maria Dubovitskaya, Philip Eib, Stefan Abel and Federico Zipoli for sharing discussions about physics and life, music, dance, fun and, most of all, for being friends, and to Franziska Buser and Alessandra Patti for their tremendous support and sharing the highs and lows of the realization of my lifelong dream.

Grazie infinite to Maurizio, Clara e Marco for being there for me, always.

Publications and Presentations

Publications

- **Inducing a Direct-to-Pseudodirect Bandgap Transition in Wurtzite GaAs Nanowires with Uniaxial Stress**

  G. Signorello, E. Lörtscher, P. Khomyakov, S. Karg, D.L. Dheeraj, B. Gotsmann, H. Weman, and H. Riel
  Nature Communications **5**, 3655 (2014)

- **Tuning the Light Emission from GaAs Nanowires over 290 meV with Uniaxial Strain**

  G. Signorello , S. Karg , M.T. Björk , B. Gotsmann , and H. Riel
  Nano Letters **13**, 917 (2013)

- **Comparison of Be-doped GaAs Nanowires Grown by Au- and Ga-assisted Molecular Beam Epitaxy**

  D.L. Dheeraj, A.M. Munshi, O.M. Christoffersen, D.C. Kim, G. Signorello, H. Riel, A.T.J. van Helvoort, H. Weman, B.O. Fimland
  Journal of Christal Growth **12**, 130 (2013)

- **Solid-state Diffusion as an Efficient Doping Method for Silicon Nanowires and Nanowire Field Effect Transistors**

  K.E. Moselund, H. Ghoneim, H. Schmid, M.T. Björk, E. Lörtscher, S. Karg, G. Signorello, D. Webb, M. Tschudy, R. Beyeler and H. Riel
  Nanotechnology **21**, 435202 (2010)

- **Low Capacitance HTS Junctions for Single Electron Transistors**

  D. Gustafsson, T. Bauch, S. Nawaz, M. Mumtaz, G. Signorello, F. Lombardi
  Physica C: Superconductivity **470**, S118 (2010)

Selected Presentations

- **Uniaxial Stress Effects in Zincblende and Wurtzite GaAs Nanowires: an Optical Spectroscopy Study**

  G. Signorello, S. Karg, E. Lörtscher, P. Khomyakov, B. Gotsmann, M. Björk, D.L. Dheeraj, H. Weman, and H. Riel (**invited**)
  School of Engineering, EPFL
  (Lausanne, Switzerland)

- **Tuning the Light Emission from GaAs Nanowires over 290 meV with Uniaxial Stress**

  G. Signorello, E. Lörtscher, S. Karg, M. Björk, B. Gotsmann, and H. Riel (**invited**)
  Dept. of materials science and engineering, MIT
  (Boston, USA)

- **Influence of Uniaxial Stress on the Optical Properties of Wurtzite GaAs Nanowires**

  G. Signorello, S. Karg, E. Lörtscher, M. Björk, H. Schmid, B. Gotsmann, K. Moselund, and H. Riel
  MRS Fall meeting 2012, Materials Research Society
  (Boston, USA)

- **Tuning the Light Emission from GaAs Nanowires over 290 meV with Uniaxial Stress**

  G. Signorello, E. Lörtscher, S. Karg, M. Björk, B. Gotsmann, and H. Riel
  International Conference of Physics of Semiconductors - ICPS 2012
  (Zurich, Switzerland)

- **Uniaxial Stress in Silicon and Core/Shell III-V Nanowires: Correlation to Electronic Properties**

  G. Signorello, S. Karg, E. Lörtscher, M. Björk, H. Schmid,
  B. Gotsmann, K. Moselund, and H. Riel
  MRS Spring meeting 2011, Materials Research Society
  (San Francisco, USA)

- **Effect of Uniaxial Stress on Transport Properties of Silicon Nanowires**

  G. Signorello, E. Lörtscher, S. Karg, B. Gotsmann, H. Schmid,
  M. T. Björk, W. Riess, K. Moselund, D. Obergfell, H. Riel
  SPS Meeting 2010, Swiss Physical Society
  (Basel, Switzerland)

Giorgio Signorello - Curriculum Vitæ

Business Contact and Personal Information

Date and Place of Birth:	11th of February 1983 in Palermo, Italy
Address:	IBM Research - Zurich, Säumerstrasse 4, CH-8803 Rüschlion (CH)
Phone Number:	(+41)44 724 8217
email:	gio@zurich.ibm.com
website:	http://www.linkedin.com/in/signorello

Professional Experience

- April 2009 - Today
  IBM Reseach - Zurich (Rueschlikon, Switzerland)
  - Nano-fabrication of semiconducting nanowire devices on flexible substrates for tunable light emitting applications
  - Device characterization by Raman and Photoluminescence spectroscopy and electrical transport measurement under mechanical strain
- September 2005 - December 2007
  ABB Corporate Research (Baden-Dättwil, Switzerland)
  - Small scale Plasma-arch erosion testing on CuW contact material for High Voltage and Generator Circuit Breakers
  - Microscopic investigation of CuW sintered structure after arching with Scanning Electron Microscopy and EDX spectroscopy
- November 2006 - January 2008
  MC2, Chalmers University of Tecnology (Göteborg, Sweden)
  - Nano-fabrication of High T_C superconducting devices: wet processing, electron beam lithography, metal evaporation, Reactive Ion Etching, Kauffman Source Ar+ Milling
  - Low temperature (300 mK) electrical charaterization

Honors and awards

- IBM Invention Achievement Award 2012
- European Research Council Marie Curie Fellowship 2009
- UNITECH-Internalional fellow 2006
- Excellence Scholarship Politecnico di Milano 2005

Education

- April 2009 - September 2013
  University of Basel Basel, Switzerland
  - PhD awarded summa cum laude in the Nanoscience program, Nanoelectronics group, Prof. C. Schönenberger
  - Scientific activity carried on at IBM Research - Zurich
  - Thesis title: *Uniaxial Stress Effects on Zincblende and Wurtzite GaAs Nanowires: an Optical Spectroscopy Study*
- August 2006 - April 2008
  Chalmers University of Technology Göteborg, Sweden
  - International MSc Degree in Nanoscale Science
  - Thesis title: *Feasibility Study Of An All High-T_C Single Electron Transistor*
- September 2005 - April 2008
  Politecnico di Milano Milan, Italy
  - MSc Degree in Engineering Physics: 110/110 summa cum laude
  - UNITECH-International exchange Student
- October 2001 - July 2005
  Politecnico di Milano Milan, Italy
  - BSc Degree in Engineering Physics: 110/110 summa cum laude
  - Thesis title: *Charge Particle Optics For Microscopy Applications*